Elaboration des membranes d'oxydes par electrospinning pour des applications photocatalytiques

Maryline Nsar

▶ **To cite this version:**

Maryline Nsar. Elaboration des membranes d'oxydes par electrospinning pour des applications photocatalytiques. Chimie. Univ. Montpellier, 2017. Français. NNT : . tel-01681200

HAL Id: tel-01681200
https://hal.umontpellier.fr/tel-01681200v1

Submitted on 11 Jan 2018

THÈSE POUR OBTENIR LE GRADE DE DOCTEUR DE L'UNIVERSITÉ DE MONTPELLIER

En Chimie et Physico Chimie des matériaux

École doctorale Sciences chimiques Balard (ED459)

Unité de recherche Institut Européen des Membranes (IEM)

Elaboration of oxides membranes by electrospinning for photocatalytic applications

Présentée par Maryline NASR
Le 16 octobre 2017

Sous la direction de Philippe MIELE, Roland HABCHI, Mikhael BECHELANY et Cynthia EID

Devant le jury composé de

M. Philippe MIELE, professeur, Université de Montpellier	**Directeur de thèse**
M. Roland HABCHI, professeur, Université Libanaise	**Directeur de thèse**
M. Mikhael BECHELANY, chargé de recherche CNRS, Université de Montpellier	**Co-encadrant**
Mme. Cynthia EID, professeur associé, Université Libanaise	**Co-encadrante**
M. Bilal NSOULI, professeur, CNRS Libanais	**Rapporteur**
M. Philippe KNAUTH, professeur, Université Aix Marseille	**Rapporteur**
Mme. Maguy JABER, professeur, Université Pierre et Marie Curie	**Examinatrice**
Mme. Nissrine EL HASSAN, professeur associé, Université de Balamand	**Examinatrice**

UNIVERSITÉ DE MONTPELLIER

To My Wonderful Parents

To My Precious "Sister and Brother"

Acknowledgment

IEM, PR2N, EC2M for their generosity and cooperation and for maintaining a very friendly environment in the laboratories.

I wish to express my gratitude to the reviewers of this thesis, Mr. Bilal Nsouli, Mr. Philippe Knauth, Mrs. Maguy Jaber and Mrs. Nisrine El Hassan for their effort to revise this manuscript and their insightful comments and remarks.

Last but not least, I deeply thank my parents for their unconditional love and support, without them I would not have been able to succeed in this endeavor. Thank you for being beside me in every critical phase of my life.

Table of Contents

Abstract

Nowadays, industrial toxic chemicals are still not properly treated and these contaminants may directly impact the safety of drinking water. Photocatalysis "a green technology" is an effective and economical approach and plays an important role in solar energy conversion and degradation of organic pollutants. This thesis manuscript reports on developing advanced materials (based on TiO_2 and ZnO) being capable of exploiting renewable solar energy for solving the environmental pollution problems. A part of this work was dedicated to improve the UV and visible light TiO_2 photoresponse. Therefore, rGO/TiO_2, BN/TiO_2 and $BN-Ag/TiO_2$ composties nanofibers were successfully elaborated using the electrospinning technique. The second part focused on ZnO. Novel structures of $ZnO/ZnAl_2O_4$ multi co-centric nanotubes and Al_2O_3 doped ZnO nanotubes were designed by combining the two techniques of atomic layer deposition (ALD) and electrospinning. The morphological, structural and optical properties of all synthesized nanostructures were investigated by several characterization techniques. The results show that the chemical and physical properties have a high impact on the photocatalytic properties of the synthesized materials. Moreover, it was found that the doping effect lead to a more efficient charge separation in the photocatalyst, which is an advantage for photocatalytic activities. In addition, methyl orange and methylene blue were used as model reference. A significant enhancement and a long-term stability in the photocatalytic activity were observed with the doped materials compared to the non-doped ones under both UV and visible light. Antibacterial tests against *Escherichia coli* have also been performed; the results indicate that $BN-Ag/TiO_2$ present interesting photocatalytic properties for both organic compound degradation and bacterial removal.

Résumé

De nos jours, les produits chimiques toxiques industriels ne sont pas toujours traités proprement, et leurs contaminants peuvent directement affecter la sécurité de l'eau potable. La photocatalyse, «une technologie verte» est une approche efficace et économique qui joue un rôle important dans la conversion de l'énergie solaire et la dégradation des polluants organiques. Ce manuscrit de thèse rapporte sur le développement des matériaux avancés (basés sur TiO_2 et ZnO) susceptibles d'exploiter l'énergie solaire renouvelable pour résoudre les problèmes de pollution environnementale. Une partie de ce travail a été consacrée pour l'amélioration de l'activité photocatalytique du TiO_2 sous lumière UV et visible. Par conséquent, les nanofibres composites de rGO/TiO_2, BN/TiO_2 et BN-Ag/TiO_2 ont été élaborées en utilisant la technique d'électrofilage (electrospinning). La deuxième partie porte sur le ZnO, ainsi que les nanotubes multi co-centriques de ZnO/$ZnAl_2O_4$ et les nanotubes de ZnO dopés Al_2O_3 qui ont été synthétisés en combinant les deux techniques : dépôt de couche atomique (ALD) et electrospinning. Les propriétés morphologiques, structurelles et optiques de toutes les nanostructures synthétisées ont été étudiées par différentes techniques de caractérisations. Les résultats ont montré que les propriétés chimiques et physiques ont un effet très important sur les propriétés photocatalytiques des matériaux synthétisés. En outre, il a été constaté que l'effet de dopage conduit à une séparation de charge efficace dans le photocatalyseur, ce qui rend l'activité photocatalytique plus efficace. De plus, le méthyle orange et le bleu de méthylène ont été utilisés comme modèle de référence. Une amélioration significative et une stabilité à long terme de l'activité photocatalytique ont été observées avec les matériaux dopés comparés aux matériaux non-dopés sous lumière UV et visible. Des tests antibactériens contre *Escherichia coli* ont été également effectués; les résultats indiquent que BN-Ag/TiO_2 présente à la fois des propriétés photocatalytiques intéressantes pour la dégradation des composés organiques et pour l'élimination des bactéries.

List of Figures

List of Tables

General Introduction

General Introduction

A combination of a growing population and a rapid development of industry have resulted in a steady increase of water pollution in many parts of the world due to the accelerated release of harmful agents especially organic pollutants, toxic heavy metal ions, and pathogenic microorganisms. Therefore the need for clean water increases the demand for new purification technologies. Photocatalysis is a promising process in the field of green technology because it can use solar energy to degrade organics and inactivate pathogens. This technique requires the absorption of a photon by a semiconductor with an energy equal to or higher than the band gap of the semiconductor, leading to the creation of charge carriers with an oxidizing or reducing power that will accelerate a chemical reaction for the degradation of pollutants. Among many candidates for photocatalysts, TiO_2 is almost the only material suitable for industrial use in the present and probably also in the future. This is because TiO_2 has the most efficient photoactivity, the highest stability, the lowest cost and its safety to humans and the environment has been guaranteed overtime. Titanium dioxide has been used in a wide variety of applications in many fields: glass, ceramics, paper industries, cosmetics, painting, medicine, electronic components and chemical catalysis. Even though, TiO_2 still possesses undesirable disadvantages such as a wide optical band gap (3.2 eV) that leads to limited applications using solar light, and fast recombination of photo-reduced carriers. In order to overcome the above drawbacks, many strategies have been used via further modifying the TiO_2. Recently, combining TiO_2 with metals and/or non-metals has been testified to be effective in strengthening the visible light activity as well as facilitating the charge separation. Zinc oxide , a naturally n-type semiconductor with a wide bandgap (Eg = 3.37 eV), has been a very attractive material for several applications including solar cells, UV-absorbing material in sunscreen, UV light emitters, spin functional devices, gas sensors, transparent electronics and photocatalysis. ZnO nanostructures have been recognized as excellent materials for photocatalytic processes due to their high photosensitivity, high catalytic activity, suitable band gap, low cost, and environmental friendliness. However, enhancing the photocatalytic activity and stability of ZnO nanomaterial to meet the practical application requirements is still a challenge because of the bottleneck of poor quantum yield caused by the fast recombination rate of photogenerated electron-hole pairs and low stability due to photochemical corrosion.

Photo-corrosion leads to a fast decrease in activity, or deactivation, and difficult recycling of the catalyst. It was found that the design and fabrication of high quality ZnO nanocrystals with desired nanostructure or morphology are of great fundamental and technological interest in the enhancement of their photocatalytic activity and stability.

The purpose of this research is to find a way of reducing the recombinaton rate of TiO_2 and ZnO photogenerated charge carriers and to shift the absorption edge of TiO_2 toward visible range in order to improve their photocatalytic activity and stability under UV and visible light. During this work, electrospinning and atomic layer deposition were the two synthesis techniques used for the elaboration of the materials. Methyl orange and methylene blue were used as model pollutant to evaluate the photocatalytic performance of the prepared nanomaterials. The antibacterial properties were evaluated against Escherichia coli bacterium. The morphological, structural and optical properties of the synthesized nanostructures were investigated using different characterization techniques such as scanning electron microscopy, transmission electron microscopy, energy-dispersive X-ray spectroscopy, BET measurements, X-ray diffraction, Raman spectroscopy, Fourier-transform infrared spectrometer, UV–VIS spectrophotometer and photoluminescence.

To achieve the above objectives, the following topics were investigated:

- Chapter 1: a literature review about the recent progress in enhancing the visible light photocatalysis of titanium dioxide, the current synthesis techniques and the different photocatalysis applications.

- Chapter 2: Synthesis of electrospun reduced graphene oxide/TiO_2 composite nanofibers and their photocatalytic performance in the degradation of methyl orange under visible light.

- Chapter 3: Enhanced photocatalytic activity under UV light of Novel Boron Nitride nanosheets/TiO_2 composite nanofibers using electrospinning technique.

- Chapter 4: Elaboration of BN-Ag/TiO_2 composite nanofibers and their photocatalytic performance for bactericidal effect and degradation of pollutants under visible light.

- Chapter 5: Synthesis of Al_2O_3 doped ZnO nanotubes and the effect of their optical and structural properties on their photocatalytic application.

➢ Chapter 6: Elaboration of novel $ZnO/ZnAl_2O_4$ multi co-centric nanotubes by combining the two techniques: atomic layer deposition and electrospinning and their photocatalytic stability.

Chapter 1: Literature Review

Table of Contents

1. Abstract

Recently, many efforts have been devoted to improve the visible-light photocatalytic activity using titanium dioxide as photocatalyst due to its wide range of applications in energy and environment fields. However, the fast charge recombination and the absorption edge in the UV range limits the photocatalytic efficiency of TiO_2 under visible-light irradiation. Many investigations have been carried out in order to overcome the limitations of TiO_2 and therefore enhance its photocatalytic activity under visible light. The present literature review focuses on different strategies used to promote the separation efficiency of the electron-hole pairs and shift the absorption edge of TiO_2 to the visible region. Current synthesis techniques of TiO_2 based material, recent progresses in enhancing visible photocatalytic activity and the different photocatalysis applications will be discussed. Based on the studies reported in the literature, we believe that this review will help in the development of new strategies to further improve the visible photocatalytic performance of TiO_2 based materials.

2. Introduction

In recent years, there has been great concern over many serious environmental problems that we are facing on a global scale [1]. One of them concerns water safety, our most important natural resource [2]. The need for clean water put more stresses on the removal of organic pollutants, and toxic heavy metal ions from water sources [3, 4], therefore new effective and low cost purification technologies are required [5]. Several techniques are already used for the treatment of water such as absorption with or without chemical reaction [6], adsorption [7], condensation [8], biological degradation and photocatalysis [9]. The adsorption techniques on highly porous materials have the disadvantage of transferring the pollutants to another phase without destroying them. Thus, their destruction requires the subsequent use of filters [10], while the ideal solution should be applicable to all types of pollutants and should not consume energy or emit environmentally harmful by-products [11]. Photocatalysis has appeared as an innovative and promising technology for water disinfection [12]. Figure 1.1 describes the principle of a semiconductor photcatalysis. The absorption of a photon by the semiconductor ($hv \geq E_g$) will cause an excitation of an electron from its valence band to its conduction band creating a

positively charged hole (h^+) in the valence band. The electron-hole pairs can migrate separately to the surface of the semiconductor and participate in the redox reactions in order to degrade the pollutants (Equation 1 to 4) [12, 13].

$$SC + hv \longrightarrow h^+ + e^- \qquad \text{(Equation 1)}$$

$$H_2O + h^+_{\text{(valence band)}} \longrightarrow HO^\bullet + H^+ \qquad \text{(Equation 2)}$$

$$h^+_{\text{(valence band)}} + \text{pollutant} \longrightarrow \text{pollutant}^+ \qquad \text{(Equation 3)}$$

$$HO^\bullet + \text{pollutant} \rightarrow H_2O + CO_2 \qquad \text{(Equation 4)}$$

$$h^+ + e^- \rightarrow \text{heat} \qquad \text{(Equation 5)}$$
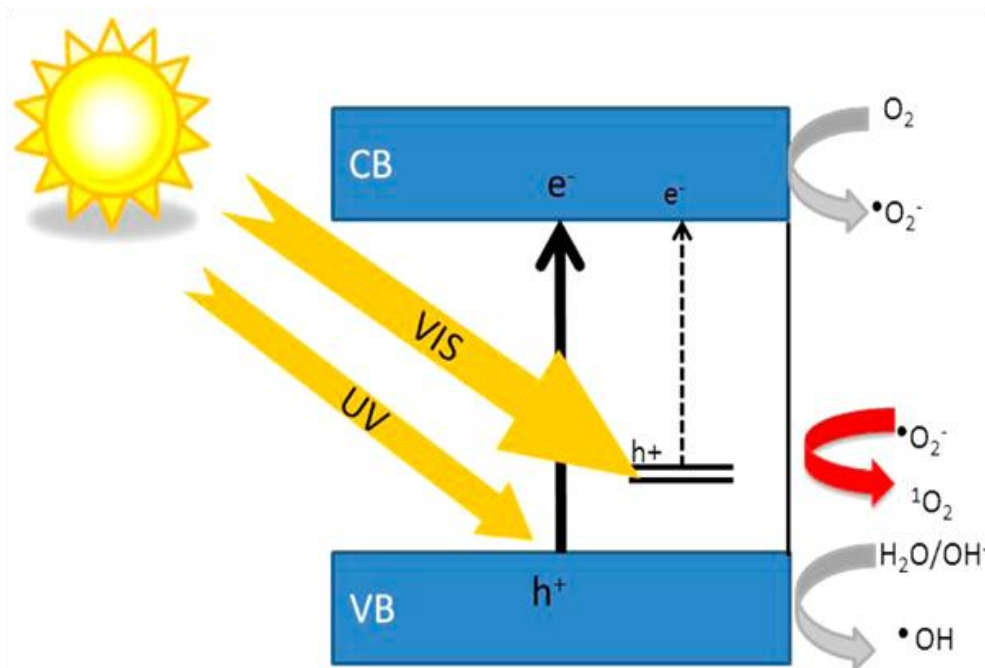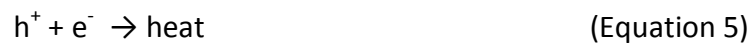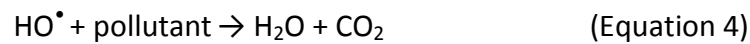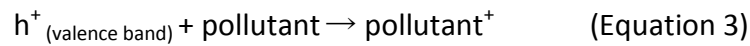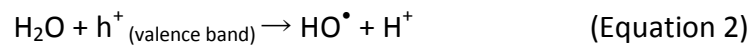
Figure 1.1. Schematic of a semiconductor photocatalysis. [14]

In 1972, Fujishima and Honda [15] observed that under UV irradiation, the use of a TiO_2 electrode in an electrochemical cell lead to water dissociation, even without imposing an external voltage. This experiment demonstrates another property of TiO_2: its photocatalytic activity, thereby opening up a new field of application [16]. Till now, titanium oxide is the most photoactive material [17] due to its oxidizing ability, chemical stability and

low cost [18, 19]. Anatase, rutile and brookite are the main crystalline phases of TiO_2. The three crystalline phases are all made up of oxygen's octahedral around a titanium atom (TiO_6 octahedral) but with a different organization from one phase to another (Figure 2). The rutile is the most abundant form and crystallizes in the quadratic Bravais network. The rutile is formed of oxygen's octahedral connected regularly in the direction [001]. The atoms are well organized in each face and thus contribute to the stability of the rutile phase. The anatase as well has a tetrahedral structure (also called quadratic) in the Bravais network. On the other hand, the anatase consists of irregular oxygens' octahedral giving it an elongated structure. The brookite has an orthorhombic structure which their oxygens' octahedral are organized regularly (Figure 1.2) [20, 21]. According to previous studies, anatase TiO_2 has demonstrated a greater photocatalytic activity compared to other crystalline phases of TiO_2 [22]. However, till now TiO_2 has not yet reached the expected photocatalytic activity due to several limitations including the fast electron-hole pair recombination [23]. In addition, TiO_2 has a large band gap (Eg > 3.2 eV), and it can only be excited by ultraviolet light with a wavelength less than 388 nm (less than 7% of solar light) [24]. To overcome these limitations, several strategies have been adopted to improve the visible-light absorbance and increase the charge carrier's life time of TiO_2-based photocatalyst [25, 26]. The present literature review will focus on tuning the photocatalyst properties to overcome the limitations of TiO_2 and enhance the visible-light photocatalytic activity. Also, the current synthesis techniques of TiO_2 based materials and the recent progresses in this field will be discussed.
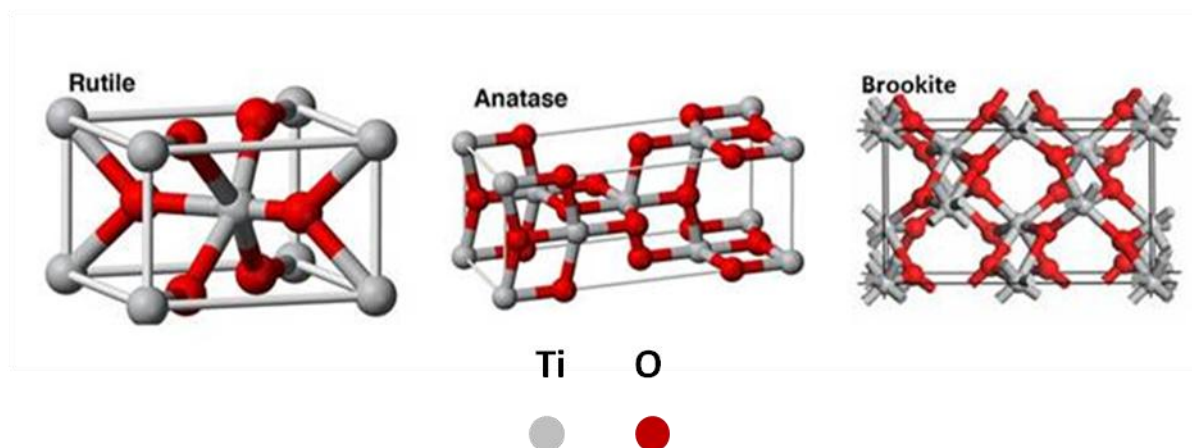
Figure 1.2. Crystalline phases of TiO_2. [27]

1.3. Synthesis methods

Previous studies showed that different morphologies of a photocatalyst may result in different photocatalytic properties [28], those diversities can be achieved by a wide variety of titanium dioxide synthesizing methods [29]. The size, the morphology and the composition of titanium dioxide can be controlled by different parameters, such as titanium precursor concentration, pH, temperature, duration of treatment and the used chemical species [30, 31]. This following section will focus on the most common synthesis techniques used to elaborate different structures of TiO_2 based materials including electrospinning, spin coating, dip coating, hydrothermal, chemical vapor deposition and atomic layer deposition.

1.3.1. Electrospinning technique

Electrospinning is a versatile and cost-effective technique for the production of multi-functional nanofibers from various polymers, composites, sol-gels, ceramics etc. [32, 33] The basic principle of this technique is based on generating the direct movement of charged molecules by applying a high voltage to supply the ejection of a viscous liquid jet through a spinneret [34]. Electrospinning setup consists of three main components; (1) high voltage power supply, (2) syringe pump and (3) collector. Figure 1.3 shows the schematic view of electrospinning. When the electric field is created between the droplet of solution and the grounded collector, it overcomes the surface tension and the polymer jet is then created to begin the fiber formation [35]. The Taylor cone shape starts to be observed at the tip of the needle during the injection [36]. In electrospinning process, the morphology and the uniformity of nanofibers are determined by considering a number of parameters which are investigated under two main parts: (a) polymer/solution properties such as molecular weight, viscosity, conductivity and surface tension; and (b) set-up parameters such as the electric field, the flow rate of solution and the tip-to-collector distance. Moreover, the ambient conditions (temperature, humidity) may affect the formation of nanofibers [37, 38]. In general, the elaboration of TiO_2 nanofibers using electrospinning involves the following three steps: (1) preparation of the electrospun solution with titania precursor and a polymer template; (2) electrospinning of the solution to obtain the composite nanofibers, and (3) calcination of the as-prepared nanofibers to remove the polymer and to obtain the crystalline phase of TiO_2 nanofibers [39]. In order to increase the active surface area of TiO_2 nanofibers, different TiO_2-based composites and co-doped nanofibers were elaborated by

electrospinning such as graphene-TiO$_2$[40], BN-TiO$_2$[41], ZnO/TiO$_2$[42], CuO/TiO$_2$[43], and Ag/TiO$_2$ [44]. The performances of these composites and co-doped materials for photocatalytic application have shown a significant enhancement compared to pure TiO$_2$ nanofibers [44]. Even though electrospinning has a potential for industrial production, though it may not be suitable for mass production, due to the large standard deviations on nanofibers' diameter, and the restricts fiber mat purity by the presence of polymer beads.
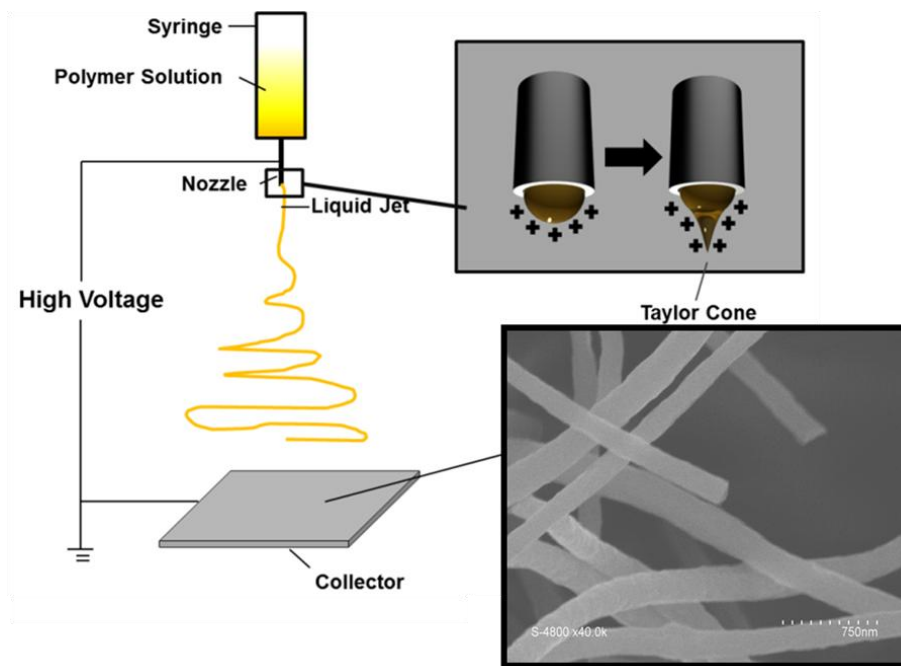
Figure 1.3. Schematic of the electrospinning process.

1.3.2. Spin coating

Spin coating is one of the most common techniques for applying thin films to substrates. It is used in a wide variety of industries and technology sectors [45]. The advantage of spin coating is the ability to quickly and easily produce uniform films with a thickness ranging from a few nanometres to a few microns. A droplet of the coating liquid is applied on the center of the substrate. The substrate is then rotated at high speed in order to spread the coating material by centrifugal force. Alternatively, the liquid solution may be applied while the substrate is spinning [46]. The thickness, morphology and surface topography of the final film obtained from a particular material in a given solvent at a given concentration are highly reproducible. Due to the ability to have high spin speeds, the high airflow leads to fast drying. Different parameters affect the spin-coating deposition process

such as rotational speed, viscosity, spinning time, molecular weight and concentration of the solutes [47]. Pan *et al.* [48] have grown highly ordered cubic mesoporous WO_3/TiO_2 thin films using spin coating method. The optimized doping amount was found at 4 mol % of WO_3 concentration and they showed that the long-range ordering of the mesostructure was appreciably organized. The enhancement of WO_3/TiO_2 photocatalytic activity in the decomposition of 2-propanol was ascribed to the surface acidity of the resultant mesoporous structures. Spin coating insure an easy film thickness control by changing spin speed, or switching to a different viscosity photoresist, while a large substrate cannot be spun at a sufficiently high rate in order to allow the film to thin. Another disadvantage of spin coating is its lack of material efficiency. Spin coating processes use only 2-5% of the material dispensed onto the substrate, while the remaining 95–98% is flung off in to the coating bowl and disposed.

1.3.3. Dip coating

Dip coating is particularly well suited to the production of thin films because it allows the deposition of very homogeneous films on substrates of different sizes [49]. Moreover, this technique is perfectly controlled and it allows to properly adjust the microstructure (porosity, crystalline structure) of the deposition and to control their thickness [50]. This technique is based on immersing a substrate in the coating solution, fixing it for a while inside the solution then pulling it up at a constant speed. The thin layer deposits itself on the substrate while it is pulled up [51]. The assembly must be devoid of any vibration so that the surface of the solution remains immobile during the deposition in order to obtain a good quality of deposition. The slightest disturbance during this step (immersion-pulling up) will cause horizontal streaks on the deposited film [52]. Different parameters should be controlled during the dip-coating process such as the immersion speed and the solution concentration and viscosity [53]. Several studies reported on the synthesis of TiO_2 and TiO_2 based materials via dip coating technique. For example, Janczarek *et al.* [54] elaborated transparent thin films of Cu–TiO_2 on glass surface with different amounts of copper using the simple dip coating method. They concluded that the Cu-TiO_2 photocatalytic activity under visible light is correlated to the optimal content of copper (Cu/Ti ratio = 0.017). Despite the low cost and the easy process of dip coating, this sol gel technique is not able to elaborate completely densified and uniform coatings.

1.3.4. Hydrothermal methods

Hydrothermal technique is usually performed in a stainless steel vessel [55], this technique is the most commonly used for elaboration of powdery nanostructures [56]. It involves the growth of materials from aqueous solutions at high temperature (above the boiling point of water) which produces high pressure [57]. Hydrothermal method is based on mixing the reagent with the precursor to be injected in the solvent which plays a double role: it accelerates the dissolution of the precursor as well as the reaction rate between the precursor and the reagent with the pressure and temperature increasing [58]. Tian *et al.* [59] report on the different 1D nanostructures elaborated by hydrothermal methods such as nanotubes [60], nanorods [61], nanowires [62] and nanobelts [63] as shown in Figure 1.4. It was found that the morphology and the length of the nanotubes affect the photocatalytic performance of TiO_2. Therefore, increasing the length of the TiO_2 nanotubes improves the photocatalytic performance due to the increased specific surface area. In addition, this structure promotes the decomposition of organic pollutants due to the facile diffusion of pollutants into the TiO_2 nanotubes [64]. Different TiO_2 based materials were synthesized by hydrothermal methods and they showed an enhancement in the visible light photocatalytic activity compared with pure TiO_2 such as Fe-TiO_2 [65], N-TiO_2 [66], Co/Cu-TiO_2 [67] and S-TiO_2 [68]. Despite the advantages of hydrothermal technique such as cost-effective, low energy consumption, simple equipment, chemical homogeneity and high dispersibility, the hydrothermal method has some disadvantages such as having long reaction time duration and producing non-uniform particle sizes of samples
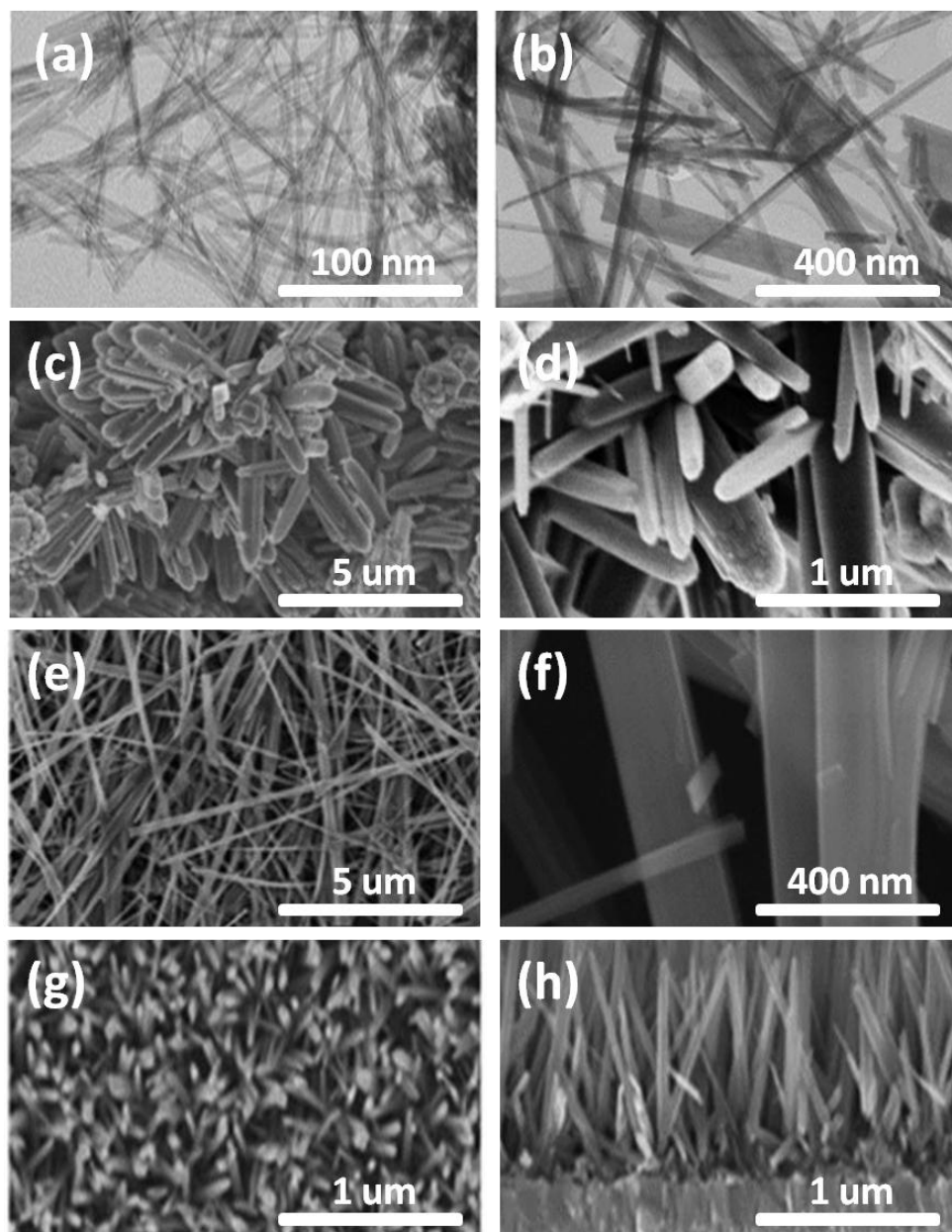
Figure 1.4. Different morphology types of 1D TiO$_2$ nanostructures synthesized through hydrothermal methods: (a, b) TiO$_2$ nanotubes, (c, d) TiO$_2$ nanorods, (e, f) TiO$_2$ nanobelts, (g, h) TiO$_2$ nanowires. [59]

1.3.5. Chemical vapor deposition (CVD)

Chemical Vapor Deposition (CVD) is a low cost technique that consists of growing a solid phase material from a gas phase material [69]. In a typical CVD process, the substrate is exposed to one or more precursors which react and/or decompose in gas phase to produce the final film [70, 71]. The CVD technique can be coupled with a plasma system as activation energy instead of thermal activation and it is called PECVD [72]. Yoshitake *et al.*

[73] elaborated mesoporous titanium dioxide using chemical vapor deposition (CVD) of titanium isopropoxide followed by its decomposition with water vapor. They reported that CVD treatment improved the thermal stability of template-extracted titania in air without changing the chemical composition. Recently, Youssef et *al.* [74] prepared single-oriented pure and N-doped anatase films via PECVD technique using titanium isopropoxide as a precursor and NH$_3$ as a doping agent. They concluded that N-doped TiO$_2$ film is an efficient photocatalyst for the photodegradation of stearic acid under visible light. Chemical vapor deposition is widely used for laboratory and industrial applications due to the conformal coating ability in the micrometric range. Despite those advantages of CVD, the nanoscience and nanotechnology need a deposition technique with a conformal coating ability in the nanometer scale.

1.3.6. Atomic Layer deposition

Many deposition techniques are available to deposit TiO$_2$ thin films on surfaces as explained above. First, these methods cannot deposit conformal films in the nano scale range. In addition, the thick films created using these processes require significant precursor usage relative to alternate thin film solutions [75]. Atomic layer deposition (ALD) is gaining an increased attention in energy and environmental fields as promising method of surface modification and protection [76]. ALD is a vapor deposition method of ultrathin layers. The originality of ALD is given to Professor Aleskovskii and his team in 1960 when they realized the deposition of TiO$_2$ from TiCl$_4$ and H$_2$O [77]. Atomic layer deposition is a deposition technique that derivates from the CVD (Chemical Vapor Deposition) technique, it is based on 2 self-limiting reactions absolutely separated in gas phases. Two precursors A and B react on gas phases during the CVD deposition to produce a thin film on the surface of the substrate; the same precursors react separately in ALD with the substrate surface to produce a uniform coating. ALD is a multi-step gas phase adsorption technique that is an analogue of a one-step CVD reaction. No other thin film technique can approach the conformity achieved by the ALD on high aspect ratio structures [78-80]. One cycle including four steps is needed to be able to perform the 2 self-limiting reactions as presented in Figure 1.5: (1) Pulse precursor 1 (introducing the first precursor to the deposition chamber to react with the substrate surface and form a chemisorbed and physisorbed layer), (2) Purge to eliminate both of the physisorbed layer and the by-products of the reaction, (3)

Pulse precursor 2 (introducing the second precursor to react with the chemisorbed layer resulting by the reaction of the first precursor with the substrate). As for the step 1, the chemisorbed and physisorbed layers were formed and (4) Purge to eliminate both of the physisorbed layer and the by-products of the reaction [81]. For photocatalysis application, various nanostructures of TiO_2 based materials have been obtained using ALD methods including Zn_2TiO_4 nanowires [82], ZnO-TiO_2 core-shell [83], Ag-TiO_2 nanocomposites [84] and Pt-TiO_2, nanoparticles [85]. The potential area of research is increasing in this field due to the accomplishment of ALD in deposition of conformal thin films over complex nanostructures in a precise manner. However, the long deposition time limits the use of ALD in laboratory scale. Therefore, the fabrication in industrial scale is a crucial challenge posed on ALD which could be overcome either by scaling-up or quickening the processes.
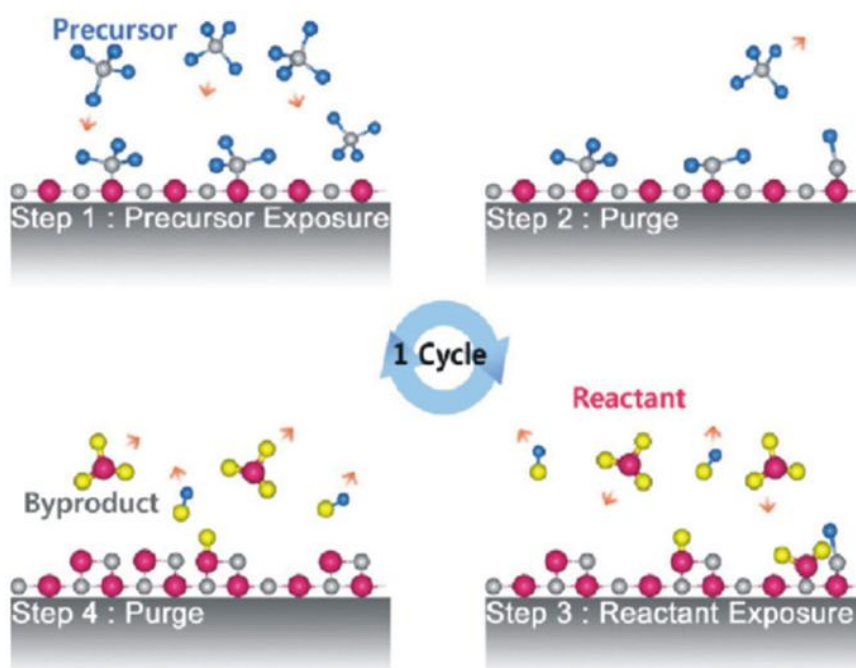
Figure 1.5. Schematics showing the growth process of ALD. [86]

Since the nanostructure's morphology has a high impact on the photocatalytic activity, the most current synthesis techniques used to elaborate different morphologies of TiO_2 nanostructures have been presented. In the next section we will present and discuss the different photocatalysis parameters and how it could be controlled and/or modified in order to improve the photocatalytic performance of TiO_2.

1.4. Photocatalysis parameters

Many factors affect the rate of a photocatalytic reaction; a distinction can be made between the operating parameters and those relating to the characteristics of the photocatalyst. The operating or extrinsic parameters are external factors such as the pH of the solution, the initial concentration of the organic compound, the catalyst concentration, the oxygen content and the temperature. The parameters related to the photocatalyst or intrinsic properties are those related to the properties of the photocatalyst itself such as structure, band gap, crystallite size …) [16, 87, 88].

1.4.1. Operating parameters

In photocatalytic process, the followings are operating parameters which affect the process: the pH of the solution, the initial concentration of the organic compound, the catalyst concentration, the oxygen content and the temperature. These parameters will be considered one after the other as they influenced the photocatalytic processes.

- (1) The concentration of the catalyst: previous studies showed that the catalyst concentration is proportional to the concentration of the electron-hole pairs (generated during the process). Actually, an increase in the amount of catalyst increases the number of active sites on the photocatalyst surface and thus improves the photoreaction rate [89, 90]. It was also found that the reaction rate increases with the concentration of catalyst until a maximum constant value (limit concentration) corresponding to the total absorption. Above this limit concentration, the photoreaction rate could even decrease [91, 92].

- (2) The initial concentration of the pollutant: as in any chemical reaction, the reaction is limited by the concentration of one or more reagents in a heterogeneous medium as follow:

$$r = \frac{dC}{dt} = \frac{kKC}{(1+KC)} \qquad \text{(Equation 6)}$$

In general, the behavior of Langmuir-Hinshelwood type is observed, where r is the degradation rate of the reagent, k represents the kinetic reaction constant, K the adsorption equilibrium constant and C the concentration of the reagent in the aqueous medium. For low value of C ($KC \ll 1$), the reaction follows a first order apparent behavior whereas for high value of C ($KC \gg 1$) the reaction follows a zero order behavior with the reaction rate [16, 93]. Several researches affirmed that the photodegradation efficiency decreased when

the initial concentration of the pollutant increased. In fact, more pollutant molecules were adsorbed on the surface of the catalyst, thus the generation of OH radicals at the catalyst surface was reduced because the active sites were occupied by pollutant cations [94, 95].

- (3) The oxygen content in the medium: The oxygen (from air flow) reacts with the electrons on the surface of the semiconductor and allows the balance of charges to be maintained [90]. Huang *et al.* [96] studied the effect of adding H_2O_2 on the decolorization of methyl orange. They found that the decolorization rate was increased with the increase in H_2O_2 concentration. They reported an optimum concentration of 1.2 mM/L H_2O_2 for photocatalytic decolorization of methyl orange solution by Pt modified TiO_2.

- (4) The pH value plays an important role on the charge surface of both semiconductor and pollutant. On the one hand, it can modify the size of the particles in the aqueous medium; on the other hand, it can modify the adsorption of the pollutant on the surface of the semiconductor. The effects of pH on the photocatalytic degradation of the pollutant have been studied by many researchers and they found that the degradation rate of pollutants is increasing with the decrease in pH [97-99].

- (5) Temperature: previous studies showed that the photocatalytic system does not require heat input because it is a photonic activation process. The majority of photoreactions are not sensitive to small variations of temperature. The decrease in temperature promotes the adsorption which is a spontaneously exothermic phenomenon. When the temperature rises above 80°C, the exothermic adsorption of the pollutants is disadvantaged. Actually, the photocatalysis experiments using high power lamps are equipped with cooling system in order to maintain the temperature of the whole system at 25°C [100, 101].

1.4.2. Modification of TiO_2 properties

One of the limitations of the photocatalytic process in the presence of TiO_2 is the fast recombination of charge carriers [102]. This recombination reduces the quantum efficiency of the photocatalytic process of TiO_2. On the other hand, the non-absorption of visible light limits its applications in sunlight [103, 104]. In order to improve the photocatalytic activity of TiO_2, researches have been carried out on the modification of TiO_2.

1.4.2.1. Metal-doping

Hoffman *et al.* [105] have shown that the substitution of Ti atoms with metallic atoms modify the absorption of TiO_2 by introducing localized energy levels between the valence band and the conduction band of TiO_2. The energy of these levels as well the distribution and the concentration of dopants in the semiconductors play an important role in the photocatalytic process. They introduce extrinsic band gap with lower energy, facilitates the electron-hole separation (formation of Schottky barrier between the semiconductor and the metal) and the hosting of active sites on the surface of TiO_2 [106]. To overcome the limitations of TiO_2 photocatalyst, it was doped with different metals such as silver, iron, palladium, platinum, copper and gold. Among all the noble metals, Ag is promising for extensive applications because of its low cost, facile preparation and antibacterial properties [107]. Until now, many strategies including chemical reduction, UV irradiation, hydrothermal method and electrospinning have been investigated to synthesize different Ag/TiO_2 nanostructures for photocatalytic application [44, 108-111]. These studies show that the presence of Ag nanoparticles can largely prevent the recombination of photo-induced electron-hole pairs in TiO_2. On the other hand, they demonstrated that the fact of introducing Ag leads to a red shift of TiO_2 absorption edge wavelength, thus to an enhancement of the photocatalytic activity of TiO_2 under visible light irradiation [44, 107]. Iron doping was also used to improve the photocatalytic properties of TiO_2. The substitution of Ti atoms by Fe atoms in the TiO_2 network is possible thanks to the similarity of their ionic radii. DFT simulation studies were carried out by Asai *et al.* [112] and more recently by Yalçin *et al.* [113]. In both studies, a slight shift in the energy levels of VB and CB and the creation of intermediate levels are predicted: these results are based on the interaction of the iron 3d orbits with the TiO_2 conduction band. Therefore, Fe-TiO_2 nanoparticles are able to absorb visible radiation. Wang *et al.* [114] have shown that the deposition of Pd on the surface of TiO_2 significantly decreases the rate of depolarization of the particles to such an extent that the accumulation of negative charges in the particles becomes zero. This phenomenon is attributed to the improvement of the mechanism of capture and transport of photo-electrons by Pd to adsorbed O_2. With the decrease of electrons in the particles, the probability of charges recombination decreases and the photocatalytic process is more efficient [114, 115]. The enhancement of the photocatalytic activity with Pt-TiO_2 as photocatalyst was also studied and explained as follow: the electrons are transferred to the

Pt while the deficiency accumulates at the Pt/TiO_2 interface leading to the charges separation and thus reducing the recombination of the electron/hole pairs [116, 117]. The deposition of metals such as Cu [118], Au [119] etc. on the TiO_2 surface enhances its photocatalytic activity, the metal nanoparticles act as electron sensors and improve the separation of charges [120]. Copper-doped nanoparticles, $Cu-TiO_2$ have been frequently applied in antibacterial treatments, and in CO_2 reduction reactions. The nanoparticles doped with gold ($Au-TiO_2$) have interesting applications for the production of H_2. As results, the metal-doping has shown both positive and negative effects: some studies confirm that in this case, metal-doping can act as electron-hole recombination centers which are detrimental to the photocatalytic activity [121]. Others also report that metal-doping reduces the band gap energy of TiO_2 and increases its visible-light photoresponse [122]. Although metal-TiO_2 catalysts have been an efficient photocatalyst under visible light they still suffer from multiple competitive disadvantages, including their high cost, susceptibility to gas poisoning, and detrimental effects on the environment. The cost-effectiveness needed by industrial application usually causes their replacement by more economical transition or non-metals doping.

1.4.2.2. Non-metal doping

Due to problems associated with metal doping, non-metal doping was studied comprehensively in the hope of achieving visible light active stable titanium dioxide [123, 124]. The fact of introducing these elements in the TiO_2 network reduced the excitation energy of TiO_2 either by reducing the band gap energy or by creating intermediate energy levels between the valence band and the conduction band [125, 126].

Carbon doping (CNT, graphene, graphene oxide)

Previous studies showed that non-metal doping are able to shift the optical absorbance of TiO_2 to the visible region [127, 128]. Recently, many attentions were devoted toward TiO_2 doped with carbon materials. Etacheri *et al.* [129] have reported that the observed visible light activity is due to the substitution of carbon atoms in the TiO_2 photocatalyst which introduces a new state (C 2p) close to the valence band of TiO_2 (O 2p). C-doped TiO_2 offers high active surface area which is one of the important parameters leading to the increase of the photocatalytic activity. Several studies were focused on

Carbon nanotubes (CNT)/TiO$_2$ nanocomposites [130, 131]. CNT is considered as a remarkable material due to its unique hollow structure, high electrochemical stability, strong adsorption and high surface-to-volume ratio. It also has an excellent charge transfer ability that contributes to restrain the combination of electron–holes in TiO$_2$ [130, 132]. Single-walled carbon nanotubes (SWCNTs) have shown a synergy effect on enhancing photoactivity over a mixture of SWCNTs and TiO$_2$ [133]. On the other hand, previous studies have also demonstrated that multi-walled carbon nanotubes (MWCNTs) could enhance the visible-light-driven photoactivity of TiO$_2$ by acting as a photosensitizer and promoting the charge transfer in the MWCNT-TiO$_2$:Ni composites [134].

In 2004, the synthesis of graphene was reported for the first time [135]. Graphene is a one-atom-thick sheet of sp^2 bonded carbon atoms packed into a 2D honeycomb structure [136, 137]. Graphene has excellent thermal conductivity, large specific area, high electron mobility and good mechanical strength. These properties of graphene make it an ultimate candidate material for enhancement of TiO$_2$ photoreactivity [138]. Previous studies concluded that graphene enhances the transport of the electron and recombination of the electron and hole gets suppressed. They demonstrated that with the use of graphene-TiO$_2$ composite (with small amount of graphene) agglomeration of TiO$_2$ can be avoided so that higher surface area can be maintained and there will be more active sites for the degradation of pollutants. Graphene-TiO$_2$ composite was doped with different metal and non-metal ions in order to improve the visible-light photocatalysis activity of TiO$_2$ [139, 140].

Due to the high cost of graphene production, most of researchers choose to work with reduce graphene oxide which can be produced at low cost [141, 142]. Graphene oxide (GO) is usually obtained by the oxidation of graphite using the famous Hummers' method and followed with an exfoliation step (high power ultrasound) [143]. Reduced graphene oxide (removal of some oxygen functionalities) can be obtained by thermal or chemical reduction of graphene oxide [144]. Several advantages motivated the researchers to use rGO or GO/TiO$_2$ composites to enhance the visible light photocatalytic activity of TiO$_2$. For example, GO has an excellent carrier mobility, thus the photoelectrons will be rapidly transferred to the GO layers, which reduce the probability of electron-hole recombination. The large surface area of graphene oxide will offer more active adsorption sites of pollutants. In addition, the band gap of graphene oxide can be tuned (from 2.7 to 1.15 eV) by varying the oxidation level (reduced graphene oxide) [145-147]. The key of an effective

visible light photocatalytic activity is to shift the absorbance of TiO_2 from UV range to the visible range by reducing the band gap energy of TiO_2. Many researchers have proved that using graphene oxide as a dopant for TiO_2 will lead to the Ti-O-C bond formation and therefore introduces lower band gap energy which will improve the visible light photoactivity of TiO_2, as shown in Figure 6 [148, 149].

Since the surface complexity, the crystalline phase, the porosity and the size of photocatalyst play an important role in the photocatalysis process enhancement, different morphologies of GO/TiO_2 structures were successfully elaborated [150-152]. Lavanya *et al.* [144] fabricated reduced graphene oxide wrapped with mesoporous TiO_2 nanofibers using the simple electrospinning technique and easy chemical reduction. They demonstrated that the reaction area and the adsorption of dye were increased due to the high surface area of the rGO. As result, the photocatalytic activity of the composites is enhanced compared to TiO_2 nanofibers alone. Li *et al.* [153] showed that the porosity improves the utilization rate of the visible light because the light enters the porous TiO_2 nanotubes and is repeatedly reflected inside the nanotubes until it is completely absorbed.
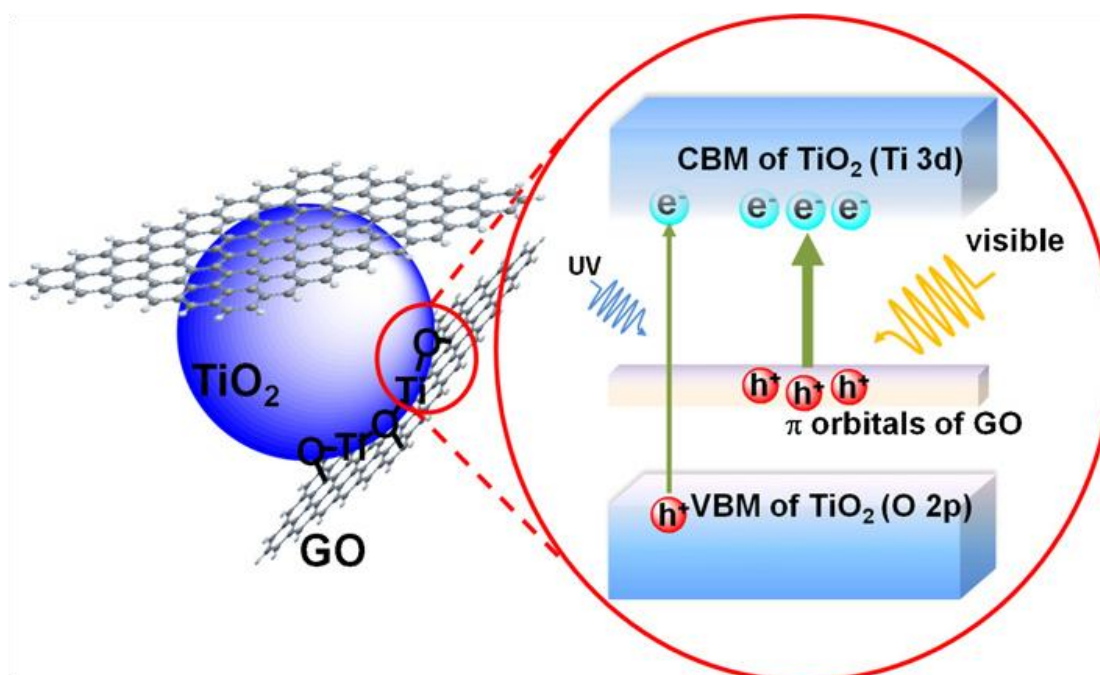
Figure 1.6. Ti–O–C bonding formed through interaction between unpaired π electrons on GO with Ti atoms surface of TiO_2. This bonding narrows the band gap of TiO_2 and extends the light absorption range of TiO_2. [154]

Nitrogen doping

Due to its high stability and small ionization energy, nitrogen was also an element of increased interest over the years with several publications focusing on the N doped TiO_2 for visible light photocatalysis [66, 155, 156]. There are three different explanations regarding modification mechanism of TiO_2 doped with nitrogen:

- (1) Impurity energy levels: Wang *et al.* [157] suggest that after nitrogen doping, N element substitutes the O element in the lattice of TiO_2 and forms isolated impurity energy levels above the valence band. They suggest that Irradiation with UV light excites electrons in both the VB and the impurity energy levels, but illumination with visible light only excites electrons in the impurity energy level.

- (2) Band gap decreasing: Cao *et al.* [158] found that due to their close energies, N 2p state hybrids with O 2p states, leading to the band gap narrowing which made N-TiO_2 active under visible light.

- (3) Oxygen vacancies: Ihara *et al.* [159] affirmed that oxygen vacancies, formed in the grain boundaries, are stabilized by the presence of nitrogen. As a result of charge compensation they improve the visible light response. Till now, no study has demonstrated completely the exact chemical states of N species that are responsible for achieving visible light photocatalytic activity of TiO_2.

Figure 1.7 shows a possible mechanism of photocatalytic reactions of $\dot{O}^-$ radical and the schematic band structure of N-doped TiO_2 under visible light irradiation. The electron transfers directly into the conduction band of TiO_2, reducing O_2 to form superoxide ions (O_2^-). The hole (h^+) then reacts with OH^- group to produce $\dot{O}H$ radical, which are responsible for the degradation of the pollutants under visible light irradiation [160, 161].

As reported for metal-doping, non-metal doped TiO_2 has also its own problems. For example, the doping of nonmetals into the lattice of TiO_2 usually results in the formation of oxygen vacancies in the bulk which can act as massive recombination centers of photo-induced electron-hole pairs and therefore limits the visible light photocatalysis efficiency of doped TiO_2. The stability of non-mental doped TiO_2 is also a concern in regard to the long-term photocatalytic stability. Therefore, other research focuses on the coupling of two semiconductors as it will be discussed in the following section.
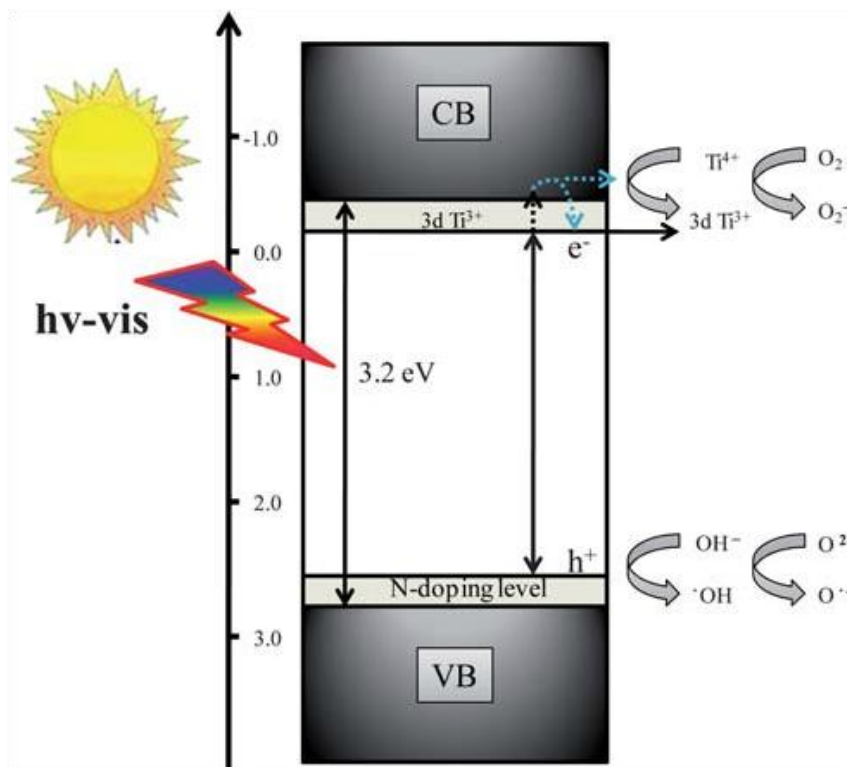
Figure 1.7. A possible mechanism of photocatalytic reactions of $\dot{O}^-$ radical and the schematic band structure of N-doped TiO_2 under visible light irradiation. [155]

1.4.2.3. Coupling with other semiconductors

During the formation of an interface between two different semiconductor's phases, the difference in energy between the conduction and valence bands of the two phases may allow the irreversible spatial separation of the charge carriers as long as this difference in energy is sufficiently large [162]. In addition to the importance of these interfaces between crystalline phases for the efficient separation of charge carriers, the interfaces' structure plays an important role for the interfacial transfer process efficiency [163]. For visible light photocatalysis, the nanoscale coupling is between TiO_2 and another small band gap semiconductor such as WO_3, SnO_2, FeO_3 and CdS [164-167]. The small band gap semiconductor allows the absorption band of TiO_2 to be shifted toward visible wavelengths. These semiconductors with a smaller band gap absorb a part of the visible light and can serve as sensitizers for TiO_2. Thus, many coupled photocatalysts have been used in the field of pollutant degradation [168]. The coupling between TiO_2 and another semiconductor at the nanometric scale leads to the formation of an interface between the two semiconductors, called heterojunction. The existence of this interface under optimum

conditions will make it possible to increase the efficiency of the photocatalytic process by reducing the probability of the photogenerated charges recombination through their spatial separation on the two semiconductors. Therefore, we must consider the relative positions of the energy levels of the valence and conduction bands of the two semiconductors [169]. Figure 8 presents the semiconductors configuration in which a vectorial transfer of photogenerated electron–hole, between corresponding band levels, ensures a spatial separation between them. Previous study shows that it is necessary that the conduction band of TiO_2 be more anodic than the corresponding band of the sensitizer. Thus, under visible irradiation, only the sensitizer is excited and the generated electrons will flow into the conduction band of the adjacent TiO_2 (Figure 1.8. a). Besides, if the valence band of the sensitizer is more cathodic than that of TiO_2, the holes will be lower in the valence band of the sensitizer (Figure 1.8. b) [163]. Subsequently, this phenomenon has been widely studied and discussed. Moreover, for an effective vectorial phenomenon under visible light, the following steps are required: (1) the sensitizer should have a strong absorption threshold in the visible region; (2) the conduction band edge potential of the sensitizer should be higher than the TiO_2 conduction band to facilitate the smooth electron transfer; (3) simultaneous irradiation and excitation of the two semiconductors; and (4) intimate contact between the two types of semiconductor particles. Thus, this physical separation of the photogenerated charges will make it possible to increase their lifetime and improve the efficiency of the visible light photocatalytic phenomenon [170]. Li *et al.* [171] prepared CdS (2.4 eV) sensitized mesoporous TiO_2 photocatalysts. Both the conduction band and the valence band of CdS are higher than their counterparts in TiO_2. The presence of CdS in the TiO_2 framework extended its photoresponse to the visible light region by accelerating the photogenerated electron transfer from the inorganic sensitizer to TiO_2. High photocatalytic activity has been recorded toward the degradation of organic compounds under visible light. Despite all these advantages for using coupled semiconductors, the presence of a large number of unpassivated or partially passivated surface states act as trap centers for holes and electrons, leading to a decrease in the photocatalytic activity.
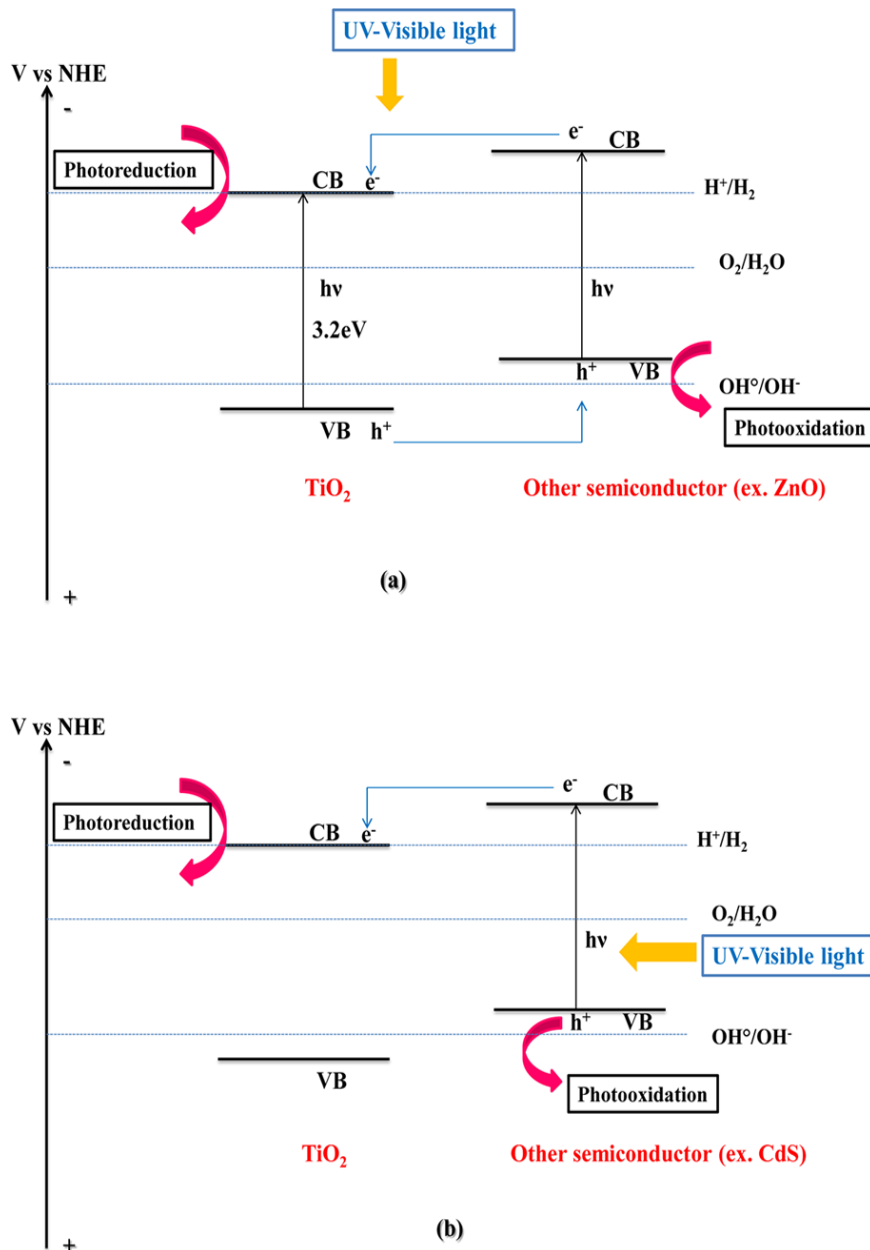
Figure 1.8. Vectorial transfer of electrons−holes in coupled semiconductor system:(a) when the conduction band of TiO$_2$ is more anodic than the corresponding band of the sensitizer and (b) when the valence band of the sensitizer is more cathodic than that of TiO$_2$ one. [172]

1.4.2.4. Multiple functional components

The heterostructure junctions with built-in potential effectively drive the separation and transportation of photogenerated electron-hole pairs [173, 174]. Different rational design and nanoscale integration of multiple functional components were elaborated in order to promote the photogenerated charge carriers and therefore improve the

photocatalytic activity and stability [175, 176]. A list of different multiple functional/TiO_2 based materials; their preparation methods and their photocatalysis application are shown in Table 1.1. The reported studies show that the multiple functional components exhibit a higher photocatalytic performance compared to single - or two-component photocatalysts. For example, Sui *et al.* [24] fabricated Ag-AgBr/TiO_2 heterostructured nanofibers by combining solvothermal technique with photoreduction method. Ag-AgBr/TiO_2 heterostructured nanofibers showed an enhanced photocatalytic activity and good stability (reuse for up to five cycles) for the degradation of methylene blue under visible light compared with TiO_2 nanofibers and Ag-AgBr powder. These results were explained by the surface plasmon resonance effect of Ag nanoparticles and the synergetic effect between the three components of Ag, AgBr powder and TiO_2 nanofibers. Figure 1.9 shows the proposed photogenerated charge separation and migration process in Ag-AgBr/TiO_2 heterostructure.
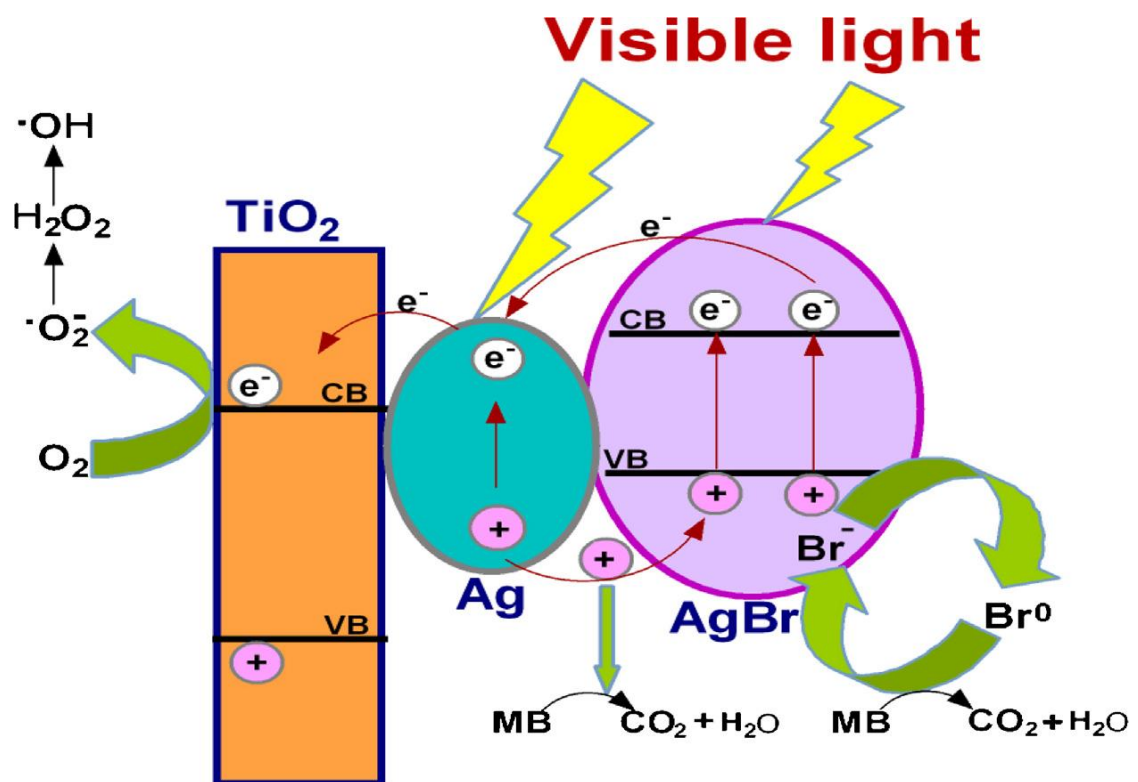
Figure 1.9. Proposed photogenerated charge separation and migration process in Ag AgBr/TiO_2 heterostructured nanofibers under visible light irradiation. [24]

Table 1.1. Different multiple functional/TiO_2 based materials, their preparation methods, their band gap, their photocatalysis application and their photocatalytic efficiency under visible light.

TiO_2 based heterostructures	Preparation method	Band gap (ev)	Photocatalysis application	Photocatalytic efficiency	References
Ag-AgBr/TiO_2 nanofibers	Solvothermal technique and photoreduction method	2.59	Degradation of methylen blue under visible light	2.5 times higher than TiO_2-P25	[24]
3D ordered assembly of Thin-Shell Au/TiO_2 hollow nanospheres	Layer-by-Layer technique	2.53	Decomposition of isopropanol	2.8 times higher than TiO_2-P25	[177]
Heterostructured g-C_3N_4(4%)/Ag/TiO_2 microspheres	Photodeposition method	2.68	Photodegradation of methyl orange	40 times higher than TiO_2 microspheres	[178]
Au-Pd/TiO_2 nanobelts nanostructures	Deposition-precipitation method	2.83	Aerobic oxidation of benzyl alcohol	3 times higher than Au/TiO_2 nanobelts	[179]
Au–Cu nanoparticles supported on $SrTiO_3$/TiO_2 coaxial nanotube arrays	Hydrothermal and solvothermal methods	2.17	Photoreduction of CO_2 into CO	16 times higer than TiO_2 nanotube arrays	[180]
CdS/Pt-TiO_2 hybrids	Chemical precipitation	2.25	Hydrogen production	10 times higher than CdS/TiO_2	[181]
Ag_3PO_4/TiO_2/Fe_3O_4 heterostructure nanospheres	In situ hydrolysis and precipitation method.	2.75	Photodegradation of acid orange 7	5.1 times higher than TiO_2 nanoparticles	[182]

The most efficient strategies and the recent progress to enhance the visible light photocatalytic activity of TiO_2 were discussed in this section. As results, there is a critical necessity to further develop these strategies in the purpose to be used in the industrial field. The TiO_2 based photocatalyst could be used in different photocatalysis applications in energy conversion and environmental remediation purposes as it will be discussed in the following section.

1.5. Photocatalysis applications

Increasing the need of clean water sources due to the rapid development of industries, population growth, science and technology have become issues worldwide. Recently, much attention was devoted to the photocatalysis process in the water depollution process. In addition, the photocatalysis process also concerns the energy storage via the ability to produce hydrogen. In this section, we briefly discuss the implication of TiO$_2$ in the various photocatalysis applications for treatment of water sources (pollutant degradation and bacterial removal) and hydrogen production.

1.5.1. Pollutant degradation

Water pollution, by some industrial, pharmaceutical or agricultural chemicals constitutes a source of environmental degradation and is currently attracting a particular national and international attention [183]. Several types of organic and inorganic pollutants have been identified in industrial effluents such as dyes, heavy metals and pharmaceutical products [3, 184, 185]. The degradation of these pollutants by photocatalysis process will be discussed in this section.

1.5.1.1. Organic compounds

Because the textile industry uses large volume of water, a large number of organic compounds are released into the environment [186]. Organic pollutants are defined by the following properties: (1) Toxicity: they have one or more harmful impacts on human health as well as on the environment [187]; (2) Persistence in the environment: there are molecules that resist natural biological degradation; and (3) Bioaccumulation: the molecules accumulate in living tissues [188]. In addition to their properties of persistence and bioaccumulation, these molecules tend to move along very long distances and they deposit away from their emission sites, such as pesticides, hydrocarbons, dyes, drugs etc [189-192]. Removing organic contaminants via photocatalysis has been shown to be more efficient than conventional waste water treatment such as filtration [193]. Several studies reported on the photodegradation of dyes as model pollutants by TiO$_2$-based photocatalyst under visible light include methylene blue[194], methyl orange[195], rodamine B[196-198], brilliant green[199, 200], phenol[201, 202], acid red [203, 204]. Wand *et al.* [205] elaborated

carbon-sensitized and nitrogen-doped TiO_2 (C/N–TiO_2) using sol-gel method. They obtained a high efficient photodegradation of sulfanilamide (SNM) under visible light due to the incorporated carbon which serves as photosensitizer and the nitrogen doping which is responsible of the absorption edge red shift of C/N–TiO_2. Senthilnathan et al. [206] used lindane, an insecticide, as a target pollutant. They found that lindane was completely degraded under visible light by N-TiO_2 photocatalyst.

1.5.1.2. Heavy metals

Heavy metals are numerous and their toxicity depends on the context in which they are located and their concentration in aquatic environments [207]. In environmental science, heavy metals associated to the pollution and toxicity are generally cadmium (Cd), chromium (Cr), mercury (Hg), manganese (Mn), arsenic (As), nickel (Ni) and plumb (Pb) [208]. When we discuss the problem of heavy metals, it is worth noting that these elements are found in our everyday environment in different chemical forms which can confer a particular property (solubility, toxicity, etc.) on the studied metal [209]. Schrank et al. [210] evaluated the effect of pH and pollutants concentration on the kinetics of the reactions. They concluded that Cr(VI) reduction using TiO_2-P25 as photocatalyst was faster in acidic pH (pH = 2.5) compared to neutral pH. Recently, Sreekantan et al. [211] synthesized Cu-TiO_2 nanotubes using electrochemical anodization. The results showed that the removal of Pb(II) heavy metal by Cu-TiO_2 photocatalyst was up to 97% due to Cu^{2+} ions which play an important role in suppressing the recombination of charge carriers. In 2016, Zhang et al. [212] developed TiO_2-modified sewage sludge carbon (SS-carbon). They reported that the combination of the SS carbon with TiO_2 doubled the adsorption capacity of mercury on the SS carbon, and the photocatalytic removal rate was increased to 151 g/kg compared to 87 g/kg for SS carbon only. In addition, they concluded that Hg(II) removal increased with the increase of pH value.

1.5.2. Bacterial removal for water disinfection

Over the past 35 years, the use of TiO_2 photocatalysis for remediation of contaminated water has been extensively reported [213]. TiO_2-mediated disinfection has been studied for the first time by Matsunaga et al. [214] when they reported the destruction of three different bacterial species (E. coli, Lactobacillus, Acidophilus) using Pt-

TiO$_2$ as photocatalyst. Due to its strong oxidizing power, non-toxicity, and long-term photostability, photocatalytic disinfection is a promising process compared to the chlorination and UV disinfection methods [215]. Matsunaga *et al.* [216] studied the photocatalytic inactivation of E. Coli TiO$_2$. They found an E. coli inactivation of 99% in deionized water. The authors suggested that cell death was caused by the inhibition of its respiratory activity caused by the decrease in coenzyme A. They also reported that no cell wall destruction caused by the semiconductor was observed. Other studies demonstrated that the oxidative damage is initially due to oxidation of the cell wall, where the TiO$_2$ photocatalytic surface allows first contact with the intact cells. Then, the oxidative damage of the cytoplasmic membrane occurs. The photocatalytic action progressively increases the cell permeability and then allows the release of the intracellular content leading eventually to death. These authors also suggested that free particles of TiO$_2$ could also penetrate the membrane of damaged cells and attack intracellular components, which can accelerate the cell death [217]. Nadtochenkoa *et al.* [218] showed that trapping holes in TiO$_2$ by the cell wall is more efficient than photogenerated electrons trapping, leading to a decrease in electron/hole recombination. Several authors have reported that cell wall modification by UV/TiO$_2$ is the main cause of bacterial inactivation [219-221].

1.5.3. Hydrogen generation

The production of hydrogen by photocatalysis is based on the decomposition of many organic species (alcohols, acids ...). The main objective of photocatalysis is to directly use water, or polluted effluents as a source of hydrogen [222]. The following three mechanisms are used for the hydrogen production:

- (1) Mechanism for the dehydrogenation of an alcohol: when the reagent used to produce hydrogen is a pure alcohol, the resulting photocatalytic reaction corresponds to the dehydrogenation of this alcohol [223]. Higashimoto *et al.* [224] reported on the synthesis of CdS/TiO$_2$ photocatalyst modified with a Pd co-catalyst for the selective dehydrogenation of benzyl alcohol to benzaldehyde with high selectivity (>99%) accompanied by the formation of H$_2$ in aqueous solution under visible-light irradiation.

- (2) Water splitting: this mechanism is one of the most attractive reactions for hydrogen production [225]. The objective is to use solar energy to obtain hydrogen from water, and then to use this hydrogen directly to produce electricity via a fuel cell. The chosen

photocatalyst should have a conduction band with an electrochemical potential lower than that of the H^+/H_2 redox couple to reduce the hydrogen. In addition, the electrochemical potential of the photocatalyst's valence band should be greater than that of the O_2/H_2O redox couple to oxidize the water [226]. The photocatalytic hydrogen production by TiO_2 is shown in Figure 1.10. Thus, all the photocatalysts that satisfy the above-mentioned requirements are capable to reduce hydrogen or to oxidize water. TiO_2 [227], $SrTiO_3$ [228], $KTaO_3$ [229, 230] and CdS [231, 232] are the most used candidates for water splitting.

- (3) Mechanism of an alcohol reforming: photocatalytic reforming of organic compounds such as alcohols is another method of hydrogen production. These reactions generally consist of several successive steps leading to the formation of CO_2 and H_2. Various alcohols have been used in this type of photocatalytic reforming reaction such as methanol, and ethanol [233, 234]. The hydrogen produced by photocatalysis is not pure. The species present in the gas phase will be dependent on the organic compounds used for reforming. Thus, hydrogen is accompanied by different species such as CO_2, alkanes and aldehydes [235]. Recently, Kennedy *et al.* [236] produced hydrogen by methanol reforming using Au-Ag/TiO_2 photocatalyst prepared via sol immobilization. They studied the effect of gold loading over Au/TiO_2 catalysts. They showed that the maximum rate of H_2 production was observed for Au loadings of 1–2 wt.%. In addition, they reported that the order of the metal addition is significant for the preparation of active Au–Ag/TiO_2 photocatalysts and in improving the hydrogen production.

Now, it is well-established that energy production and environmental challenges constitute issues worldwide. As conclusion we can assume that the photocatalysis applications with TiO_2 should have a future beneficial impact on the environment, energy production and public health. In addition, the results found from different photocatalytic applications employed in the laboratory scale encourage further research to use photocatalysis to advance in the large scale such as commercial and industrial processes.
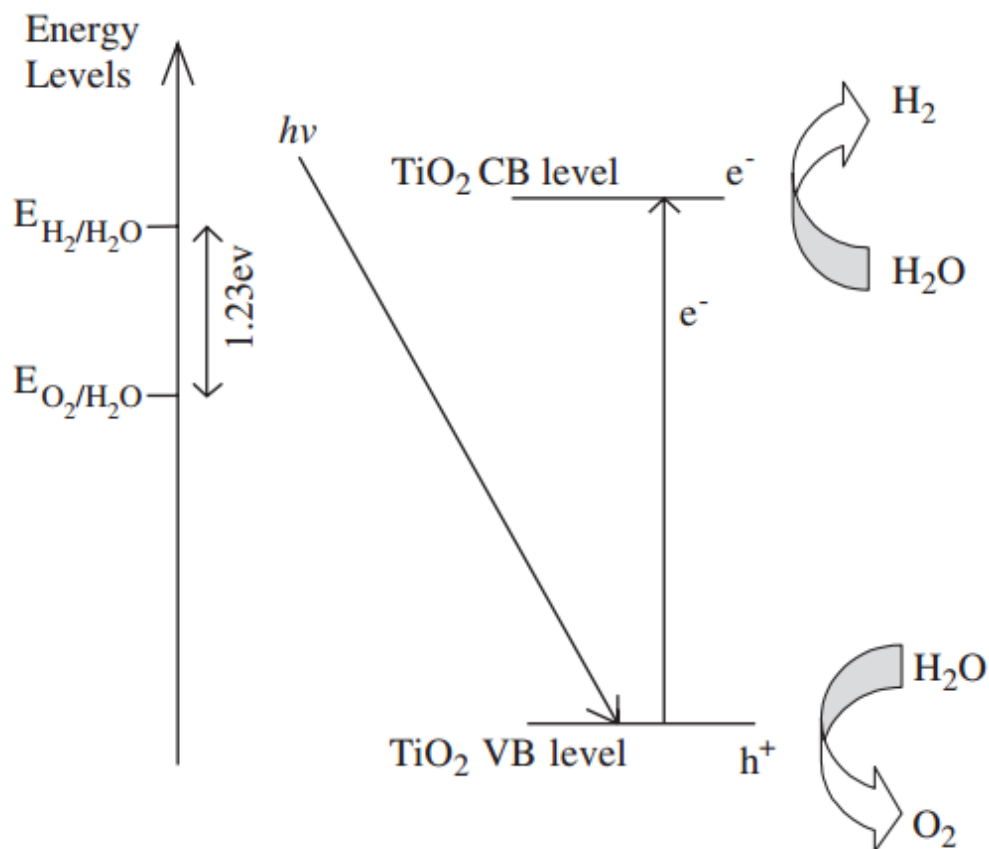
Figure 1.10. Mechanism of TiO$_2$ photocatalytic water-splitting for hydrogen production. [225]

1.6. Conclusion and Perspectives

Since the two principle limitations of TiO$_2$ are the fast charge recombination and the UV absorption edge, many efforts have been devoted to develop a new TiO$_2$ photocatalyst with low charge recombination rate and able to absorb visible light which is the main part of solar spectrum. The present chapter has summarized the recent research development to enhance the photocatalytic activity of TiO$_2$ photocatalyst under visible light and solar irradiation. First, we defined current techniques used to synthesize different morphological structures of TiO$_2$ based materials. In order to promote the charge separation efficiency and improve the visible light photocatalytic activity of TiO$_2$, different strategies were discussed such as metal doping, non-metal doping, coupling of two semiconductors with different energy band gap, metal deposition on the surface of TiO$_2$ and the multiple functional components heterostructure. These strategies promote the charge separation of TiO$_2$ and extend the absorption to the visible region allowing the use of solar light to achieve the photocatalytic process. In addition, we showed the different photocatalysis applications.

Photocatalysis process can be used for the treatment of industrial wastewater for the removal of heavy metals and organic compounds. This technique can be used also for hydrogen production and water disinfection. As perspectives, future research should be focused on the development of new strategies to improve the photocatalytic efficiency of TiO_2. Although the achieved great progress in the TiO_2 photocatalyst under visible light is still at a laboratory scale, the major challenge for the scientific research is to further improve the efficiency of these photocatalysts for industrial use.

1.7. Research Aim

The aim of the present work is to find a way of reducing the recombination of photogenerated charge carriers and to shift the absorption edge of TiO_2. Our research will focus on elaborating titanium dioxide nanofibres, modified with metal doping and/or non-metal doping and to study the effect of structural and optical properties on the photocatalytic properties of the prepared samples. The photocatalytic activity of the prepared photocatalysts will be investigated for the degradation of organic dyes (methylene blue and methyl orange) as well as for the water disinfection against E.coli bacteria under UV and visible light.

References

1. Hoffmann, M.R., et al., Environmental applications of semiconductor photocatalysis. Chemical reviews, 1995. **95**(1): p. 69-96.

2. Zhai, C., et al., Reduced graphene oxide modified highly ordered TiO 2 nanotube arrays photoelectrode with enhanced photoelectrocatalytic performance under visible-light irradiation. Physical Chemistry Chemical Physics, 2014. **16**(28): p. 14800-14807.

3. Le, T.X.H., et al., High removal efficiency of dye pollutants by electron-Fenton process using a graphene based cathode. Carbon, 2015. **94**: p. 1003-1011.

4. Dąbrowski, A., et al., Selective removal of the heavy metal ions from waters and industrial wastewaters by ion-exchange method. Chemosphere, 2004. **56**(2): p. 91-106.

5. Sofianou, M.-V., et al., Solvothermal synthesis and photocatalytic performance of Mn 4+-doped anatase nanoplates with exposed {001} facets. Applied Catalysis B: Environmental, 2015. **162**: p. 27-33.

6. Legrini, O., E. Oliveros, and A. Braun, Photochemical processes for water treatment. Chemical reviews, 1993. **93**(2): p. 671-698.

7. Ali, I. and V. Gupta, Advances in water treatment by adsorption technology. Nature protocols, 2006. **1**(6): p. 2661-2667.

8. Pokhrel, D. and T. Viraraghavan, Treatment of pulp and paper mill wastewater—a review. Science of the total environment, 2004. **333**(1): p. 37-58.

9. Xu, X., et al., Fabrication of one-dimensional heterostructured TiO 2@ SnO 2 with enhanced photocatalytic activity. Journal of Materials Chemistry A, 2014. **2**(1): p. 116-122.

10. Kannan, N. and M.M. Sundaram, Kinetics and mechanism of removal of methylene blue by adsorption on various carbons—a comparative study. Dyes and pigments, 2001. **51**(1): p. 25-40.

11. Jiang, L., Y. Huang, and T. Liu, Enhanced visible-light photocatalytic performance of electrospun carbon-doped TiO 2/halloysite nanotube hybrid nanofibers. Journal of colloid and interface science, 2015. **439**: p. 62-68.

12. Serpone, N. and E. Pelizzetti, Photocatalysis: fundamentals and applications. 1989.

13. Linsebigler, A.L., G. Lu, and J.T. Yates Jr, Photocatalysis on TiO2 surfaces: principles, mechanisms, and selected results. Chemical reviews, 1995. **95**(3): p. 735-758.

14. Fisher, M.B., et al., Nitrogen and copper doped solar light active TiO 2 photocatalysts for water decontamination. Applied Catalysis B: Environmental, 2013. **130**: p. 8-13.

15. Fujishima, A. and K. Honda, Electrochemical photolysis of water at a semiconductor electrode. nature, 1972. **238**(5358): p. 37-38.

16. Konstantinou, I.K. and T.A. Albanis, TiO 2-assisted photocatalytic degradation of azo dyes in aqueous solution: kinetic and mechanistic investigations: a review. Applied Catalysis B: Environmental, 2004. **49**(1): p. 1-14.

17. Liang, P., et al., Immobilisation of TiO2 films on activated carbon fibres by a hydrothermal method for photocatalytic degradation of toluene. Micro & Nano Letters, 2016. **11**(9): p. 539-544.

18. Nasr, M., et al., Enhanced photocatalytic performance of novel electrospun BN/TiO 2 composite nanofibers. New Journal of Chemistry, 2017. **41**(1): p. 81-89.

19. Reddy, K.R., M. Hassan, and V.G. Gomes, Hybrid nanostructures based on titanium dioxide for enhanced photocatalysis. Applied Catalysis A: General, 2015. **489**: p. 1-16.

20. Ye, J., et al., Nanoporous anatase TiO2 mesocrystals: additive-free synthesis, remarkable crystalline-phase stability, and improved lithium insertion behavior. Journal of the American Chemical Society, 2010. **133**(4): p. 933-940.

21. Braun, J.H., Titanium dioxide: A review. JCT, Journal of coatings technology, 1997. **69**(868): p. 59-72.

22. Van der Meulen, T., A. Mattson, and L. Österlund, A comparative study of the photocatalytic oxidation of propane on anatase, rutile, and mixed-phase anatase–rutile TiO 2 nanoparticles: role of surface intermediates. Journal of Catalysis, 2007. **251**(1): p. 131-144.

23. Yang, D., et al., Synthesis of Ag/TiO2 nanotube heterojunction with improved visible-light photocatalytic performance inspired by bioadhesion. The Journal of Physical Chemistry C, 2015. **119**(11): p. 5827-5835.

24. Sui, Y., et al., Ag-AgBr nanoparticles loaded on TiO 2 nanofibers as an efficient heterostructured photocatalyst driven by visible light. Journal of Molecular Catalysis A: Chemical, 2015. **410**: p. 226-234.

25. Ide, Y., et al., h-BN nanosheets as simple and effective additives to largely enhance the activity of Au/TiO2 plasmonic photocatalysts. Physical Chemistry Chemical Physics, 2015. **18**(1): p. 79-83.

26. Wei, Z., et al., Hierarchical heterostructure of CdS nanoparticles sensitized electrospun TiO 2 nanofibers with enhanced photocatalytic activity. Separation and Purification Technology, 2014. **122**: p. 60-66.

27. Hashimoto, K., H. Irie, and A. Fujishima, TiO2 photocatalysis: a historical overview and future prospects. Japanese journal of applied physics, 2005. **44**(12R): p. 8269.

28. Testino, A., et al., Optimizing the photocatalytic properties of hydrothermal TiO2 by the control of phase composition and particle morphology. A systematic approach. Journal of the American Chemical Society, 2007. **129**(12): p. 3564-3575.

29. Nakade, S., et al., Dependence of TiO2 nanoparticle preparation methods and annealing temperature on the efficiency of dye-sensitized solar cells. The Journal of Physical Chemistry B, 2002. **106**(39): p. 10004-10010.

30. Wang, P., et al., Enhance the performance of dye-sensitized solar cells by co-grafting amphiphilic sensitizer and hexadecylmalonic acid on TiO2 nanocrystals. The Journal of Physical Chemistry B, 2003. **107**(51): p. 14336-14341.

31. Atyaoui, A., Elaboration de TiO2 sous forme de couche mince dopée et nanotubulaire: caractérisation électrochimique et performance photocatalytique, 2013, Université Pierre et Marie Curie-Paris VI.

32. MacDiarmid, A., et al., Electrostatically-generated nanofibers of electronic polymers. Synthetic Metals, 2001. **119**(1-3): p. 27-30.

33. Doshi, J. and D.H. Reneker. Electrospinning process and applications of electrospun fibers. in Industry Applications Society Annual Meeting, 1993., Conference Record of the 1993 IEEE. 1993. IEEE.

34. Nasr, M., et al., Photoluminescence: A very sensitive tool to detect the presence of anatase in rutile phase electrospun TiO 2 nanofibers. Superlattices and Microstructures, 2015. **77**: p. 18-24.

35. Chronakis, I.S., Novel nanocomposites and nanoceramics based on polymer nanofibers using electrospinning process—a review. Journal of materials processing technology, 2005. **167**(2): p. 283-293.

36. Yarin, A.L., S. Koombhongse, and D.H. Reneker, Taylor cone and jetting from liquid droplets in electrospinning of nanofibers. Journal of applied physics, 2001. **90**(9): p. 4836-4846.

37. Baji, A., et al., Electrospinning of polymer nanofibers: effects on oriented morphology, structures and tensile properties. Composites science and technology, 2010. **70**(5): p. 703-718.

38. Casper, C.L., et al., Controlling surface morphology of electrospun polystyrene fibers: effect of humidity and molecular weight in the electrospinning process. Macromolecules, 2004. **37**(2): p. 573-578.

39. Onozuka, K., et al., Electrospinning processed nanofibrous TiO2 membranes for photovoltaic applications. Nanotechnology, 2006. **17**(4): p. 1026.

40. Zhang, X., et al., Electrospun TiO2–graphene composite nanofibers as a highly durable insertion anode for lithium ion batteries. The Journal of Physical Chemistry C, 2012. **116**(28): p. 14780-14788.

41. Shahgaldi, S., et al., Characterization and the hydrogen storage capacity of titania-coated electrospun boron nitride nanofibers. International Journal of Hydrogen Energy, 2012. **37**(15): p. 11237-11243.

42. Park, J.Y., et al., Synthesis and gas sensing properties of TiO2–ZnO core-shell nanofibers. Journal of the American Ceramic Society, 2009. **92**(11): p. 2551-2554.

43. Yousef, A., et al., Inactivation of pathogenic Klebsiella pneumoniae by CuO/TiO 2 nanofibers: a multifunctional nanomaterial via one-step electrospinning. Ceramics International, 2012. **38**(6): p. 4525-4532.

44. Nalbandian, M.J., et al., Synthesis and optimization of Ag–TiO 2 composite nanofibers for photocatalytic treatment of impaired water sources. Journal of hazardous materials, 2015. **299**: p. 141-148.

45. Sahu, N., B. Parija, and S. Panigrahi, Fundamental understanding and modeling of spin coating process: A review. Indian Journal of Physics, 2009. **83**(4): p. 493-502.

46. Krebs, F.C., Fabrication and processing of polymer solar cells: a review of printing and coating techniques. Solar energy materials and solar cells, 2009. **93**(4): p. 394-412.

47. Hall, D.B., P. Underhill, and J.M. Torkelson, Spin coating of thin and ultrathin polymer films. Polymer Engineering & Science, 1998. **38**(12): p. 2039-2045.

48. Pan, J.H. and W.I. Lee, Preparation of highly ordered cubic mesoporous WO3/TiO2 films and their photocatalytic properties. Chemistry of Materials, 2006. **18**(3): p. 847-853.

49. Brinker, C., et al., Fundamentals of sol-gel dip coating. Thin solid films, 1991. **201**(1): p. 97-108.

50. Strawbridge, I. and P. James, The factors affecting the thickness of sol-gel derived silica coatings prepared by dipping. Journal of non-crystalline solids, 1986. **86**(3): p. 381-393.

51. Grosso, D., How to exploit the full potential of the dip-coating process to better control film formation. Journal of Materials Chemistry, 2011. **21**(43): p. 17033-17038.

52. Nishio, K., T. Sei, and T. Tsuchiya, Preparation and electrical properties of ITO thin films by dip-coating process. Journal of materials science, 1996. **31**(7): p. 1761-1766.

53. Nandi, B., R. Uppaluri, and M. Purkait, Effects of dip coating parameters on the morphology and transport properties of cellulose acetate–ceramic composite membranes. Journal of Membrane Science, 2009. **330**(1): p. 246-258.

54. Janczarek, M., et al., Transparent thin films of Cu–TiO 2 with visible light photocatalytic activity. Photochemical & Photobiological Sciences, 2015. **14**(3): p. 591-596.

55. Yanagisawa, K. and J. Ovenstone, Crystallization of anatase from amorphous titania using the hydrothermal technique: effects of starting material and temperature. The Journal of Physical Chemistry B, 1999. **103**(37): p. 7781-7787.

56. Ismail, A.A., et al., Application of statistical design to optimize the preparation of ZnO nanoparticles via hydrothermal technique. Materials Letters, 2005. **59**(14): p. 1924-1928.

57. Xu, Y., et al., Self-assembled graphene hydrogel via a one-step hydrothermal process. ACS nano, 2010. **4**(7): p. 4324-4330.

58. Akhtar, J. and N.A.S. Amin, A review on process conditions for optimum bio-oil yield in hydrothermal liquefaction of biomass. Renewable and Sustainable Energy Reviews, 2011. **15**(3): p. 1615-1624.

59. Tian, J., et al., Recent progress in design, synthesis, and applications of one-dimensional TiO 2 nanostructured surface heterostructures: a review. Chemical Society Reviews, 2014. **43**(20): p. 6920-6937.

60. Bavykin, D.V., L. Passoni, and F.C. Walsh, Hierarchical tube-in-tube structures prepared by electrophoretic deposition of nanostructured titanates into a TiO 2 nanotube array. Chemical Communications, 2013. **49**(62): p. 7007-7009.

61. Venkatachalam, S., et al., Preparation and characterization of nanostructured TiO2 thin films by hydrothermal and anodization methods, in Optoelectronics-Advanced Materials and Devices. 2013, InTech.

62. Sheng, X., et al., Understanding and removing surface states limiting charge transport in TiO 2 nanowire arrays for enhanced optoelectronic device performance. Chemical Science, 2016. **7**(3): p. 1910-1913.

63. Mao, M., et al., High electrochemical performance based on the TiO 2 nanobelt@ few-layered MoS 2 structure for lithium-ion batteries. Nanoscale, 2014. **6**(21): p. 12350-12353.

64. Liu, Z., et al., Efficient photocatalytic degradation of gaseous acetaldehyde by highly ordered TiO2 nanotube arrays. Environmental science & technology, 2008. **42**(22): p. 8547-8551.

65. Zhu, J., et al., Characterization of Fe–TiO 2 photocatalysts synthesized by hydrothermal method and their photocatalytic reactivity for photodegradation of XRG dye diluted in water. Journal of Molecular Catalysis A: Chemical, 2004. **216**(1): p. 35-43.

66. Wang, X., et al., Synthesis and characterization of N-doped TiO 2 loaded onto activated carbon fiber with enhanced visible-light photocatalytic activity. New Journal of Chemistry, 2014. **38**(12): p. 6139-6146.

67. Ruiz, A.M., et al., Transition metals (Co, Cu) as additives on hydrothermally treated TiO 2 for gas sensing. Sensors and Actuators B: Chemical, 2005. **109**(1): p. 7-12.

68. Ho, W., C.Y. Jimmy, and S. Lee, Low-temperature hydrothermal synthesis of S-doped TiO 2 with visible light photocatalytic activity. Journal of solid state chemistry, 2006. **179**(4): p. 1171-1176.

69. Chayahara, A., et al., Function of substrate bias potential for formation of cubic boron nitride films in plasma CVD technique. Japanese journal of applied physics, 1987. **26**(9A): p. L1435.

70. Lin, Y. and A. Burggraaf, CVD of solid oxides in porous substrates for ceramic membrane modification. AIChE journal, 1992. **38**(3): p. 445-454.

71. Piccirillo, C., R. Binions, and I.P. Parkin, Synthesis and functional properties of vanadium oxides: V2O3, VO2, and V2O5 deposited on glass by aerosol-assisted CVD. Chemical Vapor Deposition, 2007. **13**(4): p. 145-151.

72. Hess, D.W., Plasma-enhanced CVD: Oxides, nitrides, transition metals, and transition metal silicides. Journal of Vacuum Science & Technology A: Vacuum, Surfaces, and Films, 1984. **2**(2): p. 244-252.

73. Yoshitake, H., T. Sugihara, and T. Tatsumi, Preparation of wormhole-like mesoporous TiO2 with an extremely large surface area and stabilization of its surface by chemical vapor deposition. Chemistry of Materials, 2002. **14**(3): p. 1023-1029.

74. Youssef, L., et al., Optimization of N-doped TiO 2 multifunctional thin layers by low frequency PECVD process. Journal of the European Ceramic Society, 2017.

75. Hass, G., M.H. Francombe, and R.W. Hoffman, Physics of Thin Films: Advances in Research and Development. 2013: Elsevier.

76. Chaaya, A.A., et al., Evolution of microstructure and related optical properties of ZnO grown by atomic layer deposition. Beilstein journal of nanotechnology, 2013. **4**(1): p. 690-698.

77. Sveshnikova, G., S. Kol'tsov, and V. Aleskovskii, Overview of early publications on Atomic Layer Deposition. J. Appl. Chem. USSR, 1967. **40**: p. 2644-2646.

78. Johnson, R.W., A. Hultqvist, and S.F. Bent, A brief review of atomic layer deposition: from fundamentals to applications. Materials today, 2014. **17**(5): p. 236-246.

79. Puurunen, R.L., Surface chemistry of atomic layer deposition: A case study for the trimethylaluminum/water process. Journal of applied physics, 2005. **97**(12): p. 9.

80. George, S.M., Atomic layer deposition: an overview. Chem. Rev, 2010. **110**(1): p. 111-131.

81. Pinna, N. and M. Knez, Atomic layer deposition of nanostructured materials. 2012: John Wiley & Sons.

82. Yang, Y., et al., Multitwinned spinel nanowires by assembly of nanobricks via oriented attachment: a case study of Zn2TiO4. ACS nano, 2009. **3**(3): p. 555-562.

83. Kayaci, F., et al., Selective isolation of the electron or hole in photocatalysis: ZnO–TiO 2 and TiO 2–ZnO core–shell structured heterojunction nanofibers via electrospinning and atomic layer deposition. Nanoscale, 2014. **6**(11): p. 5735-5745.

84. Chen, Q., et al., Enhancing the photocatalytic and antibacterial property of polyvinylidene fluoride membrane by blending Ag–TiO2 nanocomposites. Journal of Materials Science: Materials in Electronics, 2017. **28**(4): p. 3865-3874.

85. Zhou, Y., et al., Optimal preparation of Pt/TiO 2 photocatalysts using atomic layer deposition. Applied Catalysis B: Environmental, 2010. **101**(1): p. 54-60.

86. Kim, H. and W.-J. Maeng, Applications of atomic layer deposition to nanofabrication and emerging nanodevices. Thin Solid Films, 2009. **517**(8): p. 2563-2580.

87. Ahmed, S., et al., Influence of parameters on the heterogeneous photocatalytic degradation of pesticides and phenolic contaminants in wastewater: a short review. Journal of Environmental Management, 2011. **92**(3): p. 311-330.

88. Akpan, U. and B. Hameed, Parameters affecting the photocatalytic degradation of dyes using TiO 2-based photocatalysts: a review. Journal of hazardous materials, 2009. **170**(2): p. 520-529.

89. Saquib, M., et al., Photocatalytic degradation of two selected dye derivatives in aqueous suspensions of titanium dioxide. Desalination, 2008. **219**(1-3): p. 301-311.

90. Chakrabarti, S. and B.K. Dutta, Photocatalytic degradation of model textile dyes in wastewater using ZnO as semiconductor catalyst. Journal of hazardous materials, 2004. **112**(3): p. 269-278.

91. Liu, S., J.-H. Yang, and J.-H. Choy, Microporous SiO 2–TiO 2 nanosols pillared montmorillonite for photocatalytic decomposition of methyl orange. Journal of Photochemistry and Photobiology A: Chemistry, 2006. **179**(1): p. 75-80.

92. Sun, J., et al., Photocatalytic degradation of Orange G on nitrogen-doped TiO 2 catalysts under visible light and sunlight irradiation. Journal of hazardous materials, 2008. **155**(1): p. 312-319.

93. Serpone, N., et al., Standardization protocol of process efficiencies and activation parameters in heterogeneous photocatalysis: relative photonic efficiencies ζr. Journal of photochemistry and photobiology A: Chemistry, 1996. **94**(2-3): p. 191-203.

94. Grzechulska, J. and A.W. Morawski, Photocatalytic decomposition of azo-dye acid black 1 in water over modified titanium dioxide. Applied Catalysis B: Environmental, 2002. **36**(1): p. 45-51.

95. Daneshvar, N., D. Salari, and A. Khataee, Photocatalytic degradation of azo dye acid red 14 in water: investigation of the effect of operational parameters. Journal of Photochemistry and Photobiology A: Chemistry, 2003. **157**(1): p. 111-116.

96. Huang, M., et al., Photocatalytic discolorization of methyl orange solution by Pt modified TiO 2 loaded on natural zeolite. Dyes and Pigments, 2008. **77**(2): p. 327-334.

97. Baran, W., A. Makowski, and W. Wardas, The effect of UV radiation absorption of cationic and anionic dye solutions on their photocatalytic degradation in the presence TiO 2. Dyes and Pigments, 2008. **76**(1): p. 226-230.

98. Sakthivel, S., et al., Solar photocatalytic degradation of azo dye: comparison of photocatalytic efficiency of ZnO and TiO 2. Solar Energy Materials and Solar Cells, 2003. **77**(1): p. 65-82.

99. WEI, C.-h., et al., Preparation, characterization and photocatalytic activities of boron- and cerium-codoped TiO2. Journal of Environmental Sciences, 2007. **19**(1): p. 90-96.

100. Sun, M., et al., Rapid microwave hydrothermal synthesis of GaOOH nanorods with photocatalytic activitytoward aromatic compounds. Nanotechnology, 2010. **21**(35): p. 355601.

101. Lee, S.W., S. Obregón-Alfaro, and V. Rodríguez-González, Photocatalytic coatings of silver–TiO 2 nanocomposites on foamed waste-glass prepared by sonochemical process. Journal of Photochemistry and Photobiology A: Chemistry, 2011. **221**(1): p. 71-76.

102. Wang, J., et al., A high efficient photocatalyst Ag 3 VO 4/TiO 2/graphene nanocomposite with wide spectral response. Applied Catalysis B: Environmental, 2013. **136**: p. 94-102.

103. Kim, D.H., et al., Photocatalytic behaviors and structural characterization of nanocrystalline Fe-doped TiO 2 synthesized by mechanical alloying. Journal of Alloys and Compounds, 2004. **375**(1): p. 259-264.

104. Formo, E., et al., Functionalization of electrospun TiO2 nanofibers with Pt nanoparticles and nanowires for catalytic applications. Nano Letters, 2008. **8**(2): p. 668-672.

105. Choi, W., A. Termin, and M.R. Hoffmann, The role of metal ion dopants in quantum-sized TiO2: correlation between photoreactivity and charge carrier recombination dynamics. The Journal of Physical Chemistry, 1994. **98**(51): p. 13669-13679.

106. Chen, J., et al., Recent progress in enhancing photocatalytic efficiency of TiO 2-based materials. Applied Catalysis A: General, 2015. **495**: p. 131-140.

107. Yao, Y.-C., et al., Synthesis of Ag-decorated porous TiO 2 nanowires through a sunlight induced reduction method and its enhanced photocatalytic activity. Applied Surface Science, 2016. **387**: p. 469-476.

108. Guo, G., et al., Synthesis and photocatalytic applications of Ag/TiO 2-nanotubes. Talanta, 2009. **79**(3): p. 570-575.

109. He, X., et al., Photocatalytic degradation of organic pollutants with Ag decorated free-standing TiO 2 nanotube arrays and interface electrochemical response. Journal of Materials Chemistry, 2011. **21**(2): p. 475-480.

110. Liu, R., et al., UV-and visible-light photocatalytic activity of simultaneously deposited and doped Ag/Ag (I)-TiO2 photocatalyst. The Journal of Physical Chemistry C, 2012. **116**(33): p. 17721-17728.

111. Sangpour, P., F. Hashemi, and A.Z. Moshfegh, Photoenhanced degradation of methylene blue on cosputtered M: TiO2 (M= Au, Ag, Cu) nanocomposite systems: a comparative study. The Journal of Physical Chemistry C, 2010. **114**(33): p. 13955-13961.

112. Umebayashi, T., et al., Analysis of electronic structures of 3d transition metal-doped TiO 2 based on band calculations. Journal of Physics and Chemistry of Solids, 2002. **63**(10): p. 1909-1920.

113. Yalçın, Y., M. Kılıç, and Z. Çınar, Fe+ 3-doped TiO 2: a combined experimental and computational approach to the evaluation of visible light activity. Applied Catalysis B: Environmental, 2010. **99**(3): p. 469-477.

114. Wang, C.M., A. Heller, and H. Gerischer, Palladium catalysis of O2 reduction by electrons accumulated on TiO2 particles during photoassisted oxidation of organic compounds. Journal of the American Chemical Society, 1992. **114**(13): p. 5230-5234.

115. Xie, B., et al., Catalytic activities of Pd–TiO 2 film towards the oxidation of formic acid. Catalysis Communications, 2005. **6**(11): p. 699-704.

116. Sakthivel, S., et al., Enhancement of photocatalytic activity by metal deposition: characterisation and photonic efficiency of Pt, Au and Pd deposited on TiO 2 catalyst. Water research, 2004. **38**(13): p. 3001-3008.

117. Kim, S., S.-J. Hwang, and W. Choi, Visible light active platinum-ion-doped TiO2 photocatalyst. The Journal of Physical Chemistry B, 2005. **109**(51): p. 24260-24267.

118. Zhang, W., et al., Copper doping in titanium oxide catalyst film prepared by dc reactive magnetron sputtering. Catalysis Today, 2004. **93**: p. 589-594.

119. Li, H., et al., Mesoporous Au/TiO2 nanocomposites with enhanced photocatalytic activity. Journal of the American Chemical Society, 2007. **129**(15): p. 4538-4539.

120. Subramanian, V., E.E. Wolf, and P.V. Kamat, Influence of metal/metal ion concentration on the photocatalytic activity of TiO2– Au composite nanoparticles. Langmuir, 2003. **19**(2): p. 469-474.

121. Di Paola, A., et al., Preparation of polycrystalline TiO2 photocatalysts impregnated with various transition metal ions: characterization and photocatalytic activity for the degradation of 4-nitrophenol. The Journal of Physical Chemistry B, 2002. **106**(3): p. 637-645.

122. Yamashita, H., et al., Application of ion beam techniques for preparation of metal ion-implanted TiO2 thin film photocatalyst available under visible light irradiation: metal ion-implantation and ionized cluster beam method. Journal of synchrotron radiation, 2001. **8**(2): p. 569-571.

123. Chen, X. and C. Burda, The electronic origin of the visible-light absorption properties of C-, N-and S-doped TiO2 nanomaterials. Journal of the American Chemical Society, 2008. **130**(15): p. 5018-5019.

124. Ohno, T., T. Mitsui, and M. Matsumura, Photocatalytic activity of S-doped TiO2 photocatalyst under visible light. Chemistry Letters, 2003. **32**(4): p. 364-365.

125. Cong, Y., et al., Synthesis and characterization of nitrogen-doped TiO2 nanophotocatalyst with high visible light activity. The Journal of Physical Chemistry C, 2007. **111**(19): p. 6976-6982.

126. Umebayashi, T., et al., Visible light-induced degradation of methylene blue on S-doped TiO2. Chemistry Letters, 2003. **32**(4): p. 330-331.

127. Choi, Y., T. Umebayashi, and M. Yoshikawa, Fabrication and characterization of C-doped anatase TiO 2 photocatalysts. Journal of Materials Science, 2004. **39**(5): p. 1837-1839.

128. Asahi, R., et al., Visible-light photocatalysis in nitrogen-doped titanium oxides. science, 2001. **293**(5528): p. 269-271.

129. Etacheri, V., et al., A highly efficient TiO2–x C x nano-heterojunction photocatalyst for visible light induced antibacterial applications. ACS applied materials & interfaces, 2013. **5**(5): p. 1663-1672.

130. Dong, H., et al., Synthesis of Multi-Walled Carbon Nanotubes/TiO2 Composite and Its Photocatalytic Activity. Journal of nanoscience and nanotechnology, 2016. **16**(3): p. 2646-2651.

131. Dai, K., et al., Multiwalled carbon nanotube-TiO 2 nanocomposite for visible-light-induced photocatalytic hydrogen evolution. Journal of Nanomaterials, 2014. **2014**: p. 4.

132. Dembele, K.T., et al., Hybrid carbon nanotubes–TiO2 photoanodes for high efficiency dye-sensitized solar cells. The Journal of Physical Chemistry C, 2013. **117**(28): p. 14510-14517.

133. Ahmmad, B., et al., Carbon nanotubes synergistically enhance photocatalytic activity of TiO 2. Catalysis Communications, 2008. **9**(6): p. 1410-1413.

134. Ou, Y., et al., MWNT–TiO 2: Ni composite catalyst: a new class of catalyst for photocatalytic H 2 evolution from water under visible light illumination. Chemical Physics Letters, 2006. **429**(1): p. 199-203.

135. Novoselov, K.S., et al., Electric field effect in atomically thin carbon films. science, 2004. **306**(5696): p. 666-669.

136. Ferrari, A.C., et al., Raman spectrum of graphene and graphene layers. Physical review letters, 2006. **97**(18): p. 187401.

137. Nair, R.R., et al., Fine structure constant defines visual transparency of graphene. Science, 2008. **320**(5881): p. 1308-1308.

138.   Zhu, P., et al., Facile fabrication of TiO2–graphene composite with enhanced photovoltaic and photocatalytic properties by electrospinning. ACS applied materials & interfaces, 2012. **4**(2): p. 581-585.

139.   Yang, M.-Q., N. Zhang, and Y.-J. Xu, Synthesis of fullerene–, carbon nanotube–, and graphene–TiO2 nanocomposite photocatalysts for selective oxidation: a comparative study. ACS applied materials & interfaces, 2013. **5**(3): p. 1156-1164.

140.   Qiu, B., M. Xing, and J. Zhang, Mesoporous TiO2 nanocrystals grown in situ on graphene aerogels for high photocatalysis and lithium-ion batteries. Journal of the American Chemical Society, 2014. **136**(16): p. 5852-5855.

141.   Štengl, V., et al., TiO2-graphene oxide nanocomposite as advanced photocatalytic materials. Chem. Cent. J, 2013. **7**(1): p. 41.

142.   Eid, C., et al., Tunable properties of GO-doped CoFe 2 O 4 nanofibers elaborated by electrospinning. RSC Advances, 2015. **5**(118): p. 97849-97854.

143.   Hummers Jr, W.S. and R.E. Offeman, Preparation of graphitic oxide. Journal of the American Chemical Society, 1958. **80**(6): p. 1339-1339.

144.   Lavanya, T., et al., Superior photocatalytic performance of reduced graphene oxide wrapped electrospun anatase mesoporous TiO 2 nanofibers. Journal of Alloys and Compounds, 2014. **615**: p. 643-650.

145.   Zhou, Y., et al., Hydrothermal dehydration for the "green" reduction of exfoliated graphene oxide to graphene and demonstration of tunable optical limiting properties. Chemistry of Materials, 2009. **21**(13): p. 2950-2956.

146.   Gómez-Navarro, C., et al., Electronic transport properties of individual chemically reduced graphene oxide sheets. Nano letters, 2007. **7**(11): p. 3499-3503.

147.   Zhu, Y., et al., Graphene and graphene oxide: synthesis, properties, and applications. Advanced materials, 2010. **22**(35): p. 3906-3924.

148.   Huang, Q., et al., Enhanced photocatalytic activity of chemically bonded TiO2/graphene composites based on the effective interfacial charge transfer through the C–Ti bond. ACS Catalysis, 2013. **3**(7): p. 1477-1485.

149.   Bukowski, B. and N.A. Deskins, The interactions between TiO 2 and graphene with surface inhomogeneity determined using density functional theory. Physical Chemistry Chemical Physics, 2015. **17**(44): p. 29734-29746.

150.   Lee, J.S., K.H. You, and C.B. Park, Highly photoactive, low bandgap TiO2 nanoparticles wrapped by graphene. Advanced Materials, 2012. **24**(8): p. 1084-1088.

151.   Kim, I.Y., et al., A Strong Electronic Coupling between Graphene Nanosheets and Layered Titanate Nanoplates: A Soft-Chemical Route to Highly Porous Nanocomposites with Improved Photocatalytic Activity. Small, 2012. **8**(7): p. 1038-1048.

152.   Zhang, H., et al., P25-graphene composite as a high performance photocatalyst. ACS nano, 2009. **4**(1): p. 380-386.

153.   Li, Y., et al., Preparation of Graphene–TiO 2 nanotubes/nanofibers composites as an enhanced visible light photocatalyst using a hybrid synthetic strategy. Materials Science in Semiconductor Processing, 2014. **27**: p. 695-701.

154.   Yeh, T.-F., et al., Roles of graphene oxide in photocatalytic water splitting. Materials Today, 2013. **16**(3): p. 78-84.

155.   Yang, G., et al., Preparation of highly visible-light active N-doped TiO 2 photocatalyst. Journal of Materials Chemistry, 2010. **20**(25): p. 5301-5309.

156. Kim, C.H., B.-H. Kim, and K.S. Yang, TiO 2 nanoparticles loaded on graphene/carbon composite nanofibers by electrospinning for increased photocatalysis. Carbon, 2012. **50**(7): p. 2472-2481.

157. Wang, D.-H., et al., One-step hydrothermal synthesis of N-doped TiO 2/C nanocomposites with high visible light photocatalytic activity. Nanoscale, 2012. **4**(2): p. 576-584.

158. Cao, S., et al., Unique double-shelled hollow silica microspheres: template-guided self-assembly, tunable pore size, high thermal stability, and their application in removal of neutral red. Journal of Materials Chemistry, 2011. **21**(47): p. 19124-19131.

159. Ihara, T., et al., Visible-light-active titanium oxide photocatalyst realized by an oxygen-deficient structure and by nitrogen doping. Applied Catalysis B: Environmental, 2003. **42**(4): p. 403-409.

160. Rengifo-Herrera, J., et al., Abatement of organics and Escherichia coli by N, S co-doped TiO 2 under UV and visible light. Implications of the formation of singlet oxygen (1 O 2) under visible light. Applied Catalysis B: Environmental, 2009. **88**(3): p. 398-406.

161. Dong, F., W. Zhao, and Z. Wu, Characterization and photocatalytic activities of C, N and S co-doped TiO2 with 1D nanostructure prepared by the nano-confinement effect. Nanotechnology, 2008. **19**(36): p. 365607.

162. Wang, H., et al., Semiconductor heterojunction photocatalysts: design, construction, and photocatalytic performances. Chemical Society Reviews, 2014. **43**(15): p. 5234-5244.

163. Robert, D., Photosensitization of TiO 2 by M x O y and M x S y nanoparticles for heterogeneous photocatalysis applications. Catalysis Today, 2007. **122**(1): p. 20-26.

164. Kuang, S., et al., Fabrication, characterization and photoelectrochemical properties of Fe 2 O 3 modified TiO 2 nanotube arrays. Applied Surface Science, 2009. **255**(16): p. 7385-7388.

165. Ren, G., et al., Synthesis of high activity TiO2/WO3 photocatalyst via environmentally friendly and microwave assisted hydrothermal process. J. Chem. Soc. Pak, 2011. **33**(5): p. 666.

166. Shang, J., et al., Structure and photocatalytic performances of glass/SnO 2/TiO 2 interface composite film. Applied Catalysis A: General, 2004. **257**(1): p. 25-32.

167. Sun, S., C. Murry, and D. Weller, On the synergistic coupling properties of composite CdS/TiO2 nanoparticle arrays confined in nanopatterned hybrid thin films. 2000.

168. Ouyang, J., M. Chang, and X. Li, CdS-sensitized ZnO nanorod arrays coated with TiO 2 layer for visible light photoelectrocatalysis. Journal of Materials Science, 2012. **47**(9): p. 4187-4193.

169. Zhang, H., G. Chen, and D.W. Bahnemann, Photoelectrocatalytic materials for environmental applications. Journal of Materials Chemistry, 2009. **19**(29): p. 5089-5121.

170. Liqiang, J., et al., Review of photoluminescence performance of nano-sized semiconductor materials and its relationships with photocatalytic activity. Solar Energy Materials and Solar Cells, 2006. **90**(12): p. 1773-1787.

171. Li, G.-S., D.-Q. Zhang, and J.C. Yu, A new visible-light photocatalyst: CdS quantum dots embedded mesoporous TiO2. Environmental science & technology, 2009. **43**(18): p. 7079-7085.

172.   Daghrir, R., P. Drogui, and D. Robert, Modified TiO2 for environmental photocatalytic applications: a review. Industrial & Engineering Chemistry Research, 2013. **52**(10): p. 3581-3599.

173.   Zhou, H., et al., Towards highly efficient photocatalysts using semiconductor nanoarchitectures. Energy & Environmental Science, 2012. **5**(5): p. 6732-6743.

174.   Yang, Z., et al., Electrochemical energy storage for green grid. Chemical reviews, 2011. **111**(5): p. 3577-3613.

175.   Park, H., W. Choi, and M.R. Hoffmann, Effects of the preparation method of the ternary CdS/TiO 2/Pt hybrid photocatalysts on visible light-induced hydrogen production. Journal of Materials Chemistry, 2008. **18**(20): p. 2379-2385.

176.   Tada, H., et al., All-solid-state Z-scheme in CdS–Au–TiO2 three-component nanojunction system. Nature materials, 2006. **5**(10): p. 782-786.

177.   Dinh, C.T., et al., Three-Dimensional Ordered Assembly of Thin-Shell Au/TiO2 Hollow Nanospheres for Enhanced Visible-Light-Driven Photocatalysis. Angewandte Chemie International Edition, 2014. **53**(26): p. 6618-6623.

178.   Chen, Y., et al., Construction of heterostructured g-C3N4/Ag/TiO2 microspheres with enhanced photocatalysis performance under visible-light irradiation. ACS applied materials & interfaces, 2014. **6**(16): p. 14405-14414.

179.   Jiang, T., et al., Gold and gold–palladium alloy nanoparticles on heterostructured TiO 2 nanobelts as plasmonic photocatalysts for benzyl alcohol oxidation. Nanoscale, 2015. **7**(1): p. 209-217.

180.   Kang, Q., et al., Photocatalytic reduction of carbon dioxide by hydrous hydrazine over Au–Cu alloy nanoparticles supported on SrTiO3/TiO2 coaxial nanotube arrays. Angewandte Chemie, 2015. **127**(3): p. 855-859.

181.   Park, H., Y.K. Kim, and W. Choi, Reversing CdS preparation order and its effects on photocatalytic hydrogen production of CdS/Pt-TiO2 hybrids under visible light. The Journal of Physical Chemistry C, 2011. **115**(13): p. 6141-6148.

182.   Xu, J.-W., et al., Synthesis of magnetically separable Ag3PO4/TiO2/Fe3O4 heterostructure with enhanced photocatalytic performance under visible light for photoinactivation of bacteria. ACS applied materials & interfaces, 2014. **6**(17): p. 15122-15131.

183.   Kabra, K., R. Chaudhary, and R.L. Sawhney, Treatment of hazardous organic and inorganic compounds through aqueous-phase photocatalysis: a review. Industrial & engineering chemistry research, 2004. **43**(24): p. 7683-7696.

184.   Doh, S.J., et al., Development of photocatalytic TiO 2 nanofibers by electrospinning and its application to degradation of dye pollutants. Journal of Hazardous Materials, 2008. **154**(1): p. 118-127.

185.   Du, P., et al., Photocatalytic degradation of Rhodamine B using electrospun TiO2 and ZnO nanofibers: a comparative study. Journal of Materials Science, 2013. **48**(24): p. 8386-8392.

186.   Jeswani, H.K., et al., Removal of organic compounds from water: life cycle environmental impacts and economic costs of the Arvia process compared to granulated activated carbon. Journal of Cleaner Production, 2015. **89**: p. 203-213.

187.   Noziere, B., et al., The molecular identification of organic compounds in the atmosphere: state of the art and challenges. Chemical reviews, 2015. **115**(10): p. 3919-3983.

188. Schaider, L.A., et al., Pharmaceuticals, perfluorosurfactants, and other organic wastewater compounds in public drinking water wells in a shallow sand and gravel aquifer. Science of the Total Environment, 2014. **468**: p. 384-393.

189. Yan, Z., et al., Visible-light degradation of dyes and phenols over mesoporous titania prepared by using anthocyanin from red radish as template. International Journal of Photoenergy, 2014. **2014**.

190. Quero-Pastor, M., et al., Degradation of drugs in water with advanced oxidation processes and ozone. Journal of environmental management, 2014. **137**: p. 197-203.

191. Straaten, N., et al. Degradation of hydrocarbons under methanogenic conditions in different geosystems. in EGU General Assembly Conference Abstracts. 2014.

192. von der Ohe, P.C. and W. Goedkoop, Distinguishing the effects of habitat degradation and pesticide stress on benthic invertebrates using stressor-specific metrics. Science of the Total Environment, 2013. **444**: p. 480-490.

193. Van der Bruggen, B. and C. Vandecasteele, Removal of pollutants from surface water and groundwater by nanofiltration: overview of possible applications in the drinking water industry. Environmental pollution, 2003. **122**(3): p. 435-445.

194. Tahir, K., et al., Visible light photo catalytic inactivation of bacteria and photo degradation of methylene blue with Ag/TiO 2 nanocomposite prepared by a novel method. Journal of Photochemistry and Photobiology B: Biology, 2016. **162**: p. 189-198.

195. Dong, S., et al., Visible-light photocatalytic degradation of methyl orange over spherical activated carbon-supported and Er3+: YAlO3-doped TiO2 in a fluidized bed. Journal of Chemical Technology and Biotechnology, 2015. **90**(5): p. 880-887.

196. Kavitha, V., P. Ramesh, and D. Geetha, Synthesis of Cu Loaded TiO2 Nanoparticles for the Improved Photocatalytic Degradation of Rhodamine B. International Journal of Nanoscience, 2016. **15**(05n06): p. 1660002.

197. Prabhu, S., et al., Visible light photocatalytic activity of CeO2-ZnO-TiO2 composites for the degradation of Rhodamine B. Indian Journal of Materials Science, 2014. **2014**.

198. He, M., et al., Synthesis of molecularly imprinted polypyrrole/titanium dioxide nanocomposites and its selective photocatalytic degradation of rhodamine B under visible light irradiation. Express Polymer Letters, 2014. **8**(11).

199. Jain, A.K., S. Benjamin, and R. Ameta, Use of N, S-Codoped Nano Titania As Photocatalyst for Degradation of Brilliant Green. Octa Journal of Environmental Research, 2015. **3**(1).

200. Sood, S., et al., Efficient photocatalytic degradation of brilliant green using Sr-doped TiO 2 nanoparticles. Ceramics International, 2015. **41**(3): p. 3533-3540.

201. Zhang, D., et al., The photocatalytic interaction of Cr (VI) ions and phenol on polymer-modified TiO2 under visible light irradiation. Kinetics and Catalysis, 2015. **56**(5): p. 569-573.

202. Niu, Y., et al., Visible light activated sulfur and iron co-doped TiO 2 photocatalyst for the photocatalytic degradation of phenol. Catalysis Today, 2013. **201**: p. 159-166.

203. Sabar, S., M. Nawi, and W. Ngah, Photocatalytic removal of Reactive Red 4 dye by immobilised layer-by-layer TiO2/cross-linked chitosan derivatives system. Desalination and Water Treatment, 2016. **57**(13): p. 5851-5857.

204. Akpan, U. and B. Hameed, Development and photocatalytic activities of TiO2 doped with Ca–Ce–W in the degradation of acid red 1 under visible light irradiation. Desalination and Water Treatment, 2014. **52**(28-30): p. 5639-5651.

205. Wang, P., et al., Carbon-sensitized and nitrogen-doped TiO 2 for photocatalytic degradation of sulfanilamide under visible-light irradiation. Water research, 2011. **45**(16): p. 5015-5026.

206. Senthilnathan, J. and L. Philip, Photocatalytic degradation of lindane under UV and visible light using N-doped TiO 2. Chemical engineering journal, 2010. **161**(1): p. 83-92.

207. de Vries, W., et al., Critical loads of heavy metals for soils, in Heavy metals in soils. 2013, Springer. p. 211-237.

208. Wong, Y.E., Determination of heavy metals in water, sediment and fishes of Bakun Hydroelectric Reservoir. 2015.

209. Bolan, N., et al., Remediation of heavy metal (loid) s contaminated soils–to mobilize or to immobilize? Journal of Hazardous Materials, 2014. **266**: p. 141-166.

210. Schrank, S., H. José, and R. Moreira, Simultaneous photocatalytic Cr (VI) reduction and dye oxidation in a TiO 2 slurry reactor. Journal of photochemistry and photobiology A: Chemistry, 2002. **147**(1): p. 71-76.

211. Sreekantan, S., et al., Post-annealing treatment for Cu-TiO2 nanotubes and their use in photocatalytic methyl orange degradation and Pb (II) heavy metal ions removal. The European Physical Journal Applied Physics, 2014. **67**(1): p. 10404.

212. Zhang, F.-S., J.O. Nriagu, and H. Itoh, Photocatalytic removal and recovery of mercury from water using TiO 2-modified sewage sludge carbon. Journal of Photochemistry and Photobiology A: Chemistry, 2004. **167**(2): p. 223-228.

213. Keane, D.A., et al., Solar photocatalysis for water disinfection: materials and reactor design. Catalysis Science & Technology, 2014. **4**(5): p. 1211-1226.

214. Matsunaga, T., et al., Photoelectrochemical sterilization of microbial cells by semiconductor powders. FEMS Microbiology letters, 1985. **29**(1-2): p. 211-214.

215. Lee, O.-M., et al., A comparative study of disinfection efficiency and regrowth control of microorganism in secondary wastewater effluent using UV, ozone, and ionizing irradiation process. Journal of hazardous materials, 2015. **295**: p. 201-208.

216. Matsunaga, T., et al., Continuous-sterilization system that uses photosemiconductor powders. Applied and environmental microbiology, 1988. **54**(6): p. 1330-1333.

217. Huang, Z., et al., Bactericidal mode of titanium dioxide photocatalysis. Journal of Photochemistry and photobiology A: Chemistry, 2000. **130**(2): p. 163-170.

218. Nadtochenko, V., et al., Laser kinetic spectroscopy of the interfacial charge transfer between membrane cell walls of E. coli and TiO 2. Journal of Photochemistry and Photobiology A: Chemistry, 2006. **181**(2): p. 401-407.

219. Maness, P.-C., et al., Bactericidal activity of photocatalytic TiO2 reaction: toward an understanding of its killing mechanism. Applied and environmental microbiology, 1999. **65**(9): p. 4094-4098.

220. Kiwi, J. and V. Nadtochenko, New evidence for TiO2 photocatalysis during bilayer lipid peroxidation. The Journal of Physical Chemistry B, 2004. **108**(45): p. 17675-17684.

221. Suwalsky, M., et al., Evidence for the hydration effect at the semiconductor phospholipid-bilayer interface by TiO 2 photocatalysis. Journal of Photochemistry and Photobiology B: Biology, 2005. **78**(3): p. 253-258.

222. Pinaud, B.A., et al., Technical and economic feasibility of centralized facilities for solar hydrogen production via photocatalysis and photoelectrochemistry. Energy & Environmental Science, 2013. **6**(7): p. 1983-2002.

223. Nishimoto, S.-i., B. Ohtani, and T. Kagiya, Photocatalytic dehydrogenation of aliphatic alcohols by aqueous suspensions of platinized titanium dioxide. Journal of the Chemical Society, Faraday Transactions 1: Physical Chemistry in Condensed Phases, 1985. **81**(10): p. 2467-2474.

224. Higashimoto, S., et al., Selective dehydrogenation of aromatic alcohols photocatalyzed by Pd-deposited CdS–TiO 2 in aqueous solution using visible light. Catalysis Science & Technology, 2013. **3**(2): p. 400-403.

225. Ni, M., et al., A review and recent developments in photocatalytic water-splitting using TiO2 for hydrogen production. Renewable and Sustainable Energy Reviews, 2007. **11**(3): p. 401-425.

226. Hisatomi, T., J. Kubota, and K. Domen, Recent advances in semiconductors for photocatalytic and photoelectrochemical water splitting. Chemical Society Reviews, 2014. **43**(22): p. 7520-7535.

227. Liu, E., et al., Plasmonic Ag deposited TiO2 nano-sheet film for enhanced photocatalytic hydrogen production by water splitting. Nanotechnology, 2014. **25**(16): p. 165401.

228. Wang, Q., et al., Core/shell structured La-and Rh-codoped SrTiO3 as a hydrogen evolution photocatalyst in Z-scheme overall water splitting under visible light irradiation. Chemistry of Materials, 2014. **26**(14): p. 4144-4150.

229. Hagiwara, H., et al., Effect of Porphyrin Molecular Structure on Water Splitting Activity of a KTaO3 Photocatalyst. Catalysts, 2016. **6**(3): p. 42.

230. Xu, D., et al., Ag-Decorated ATaO3 (A= K, Na) Nanocube Plasmonic Photocatalysts with Enhanced Photocatalytic Water-Splitting Properties. Langmuir, 2015. **31**(35): p. 9694-9699.

231. Xu, J. and X. Cao, Characterization and mechanism of MoS 2/CdS composite photocatalyst used for hydrogen production from water splitting under visible light. Chemical Engineering Journal, 2015. **260**: p. 642-648.

232. Wang, H., et al., Nickel nanoparticles modified CdS–a potential photocatalyst for hydrogen production through water splitting under visible light irradiation. International Journal of Hydrogen Energy, 2015. **40**(1): p. 340-345.

233. Puskelova, J., et al., Hydrogen production by photocatalytic ethanol reforming using Eu-and S-doped anatase. Applied Surface Science, 2014. **305**: p. 665-669.

234. Nomikos, G.N., et al., Kinetic and mechanistic study of the photocatalytic reforming of methanol over Pt/TiO 2 catalyst. Applied Catalysis B: Environmental, 2014. **146**: p. 249-257.

235. Haryanto, A., et al., Current status of hydrogen production techniques by steam reforming of ethanol: a review. Energy & Fuels, 2005. **19**(5): p. 2098-2106.

236. Kennedy, J., et al., Photocatalytic hydrogen production by reforming of methanol using Au/TiO2, Ag/TiO2 and Au-Ag/TiO2 catalysts. Catalysis, Structure & Reactivity, 2015. **1**(1): p. 35-43.

Chapter 2: Enhanced Visible-Light Photocatalytic Performance of Electrospun rGO/TiO₂ Composite Nanofibers

Table of Contents

1. Abstract

Reduced graphene oxide (rGO) / Titanium dioxide (TiO$_2$) composite nanofibers as photocatalytic materials were successfully elaborated by using electrospinning. The as-spun nanofibers with controlled ratio of rGO were annealed at 500°C under Nitrogen in a tubular furnace. Structural, morphological and optical characterizations demonstrate the success of rGO incorporation in the TiO$_2$ nanofibers. The performances of these nanocomposites for photocatalytic application have been evaluated. The presence of rGO sheets decreases the band gap energy of TiO$_2$ NFs from 3.2 eV to 2.9 eV. Hence, in the photodegradation of methyl orange (MO), a significant enhancement in the reaction rate was observed with rGO/TiO$_2$ (2wt. %) composite NFs compared to commercial TiO$_2$-P25. In addition, the kinetic of MO degradation by rGO/TiO$_2$ (2wt. %) composite NFs is 6 times higher than that by commercial TiO$_2$. Thus, the photocatalytic activity of the composites rGO/TiO$_2$ significantly increases the visible light photo-response and improves the separation of photo-induced electron-hole pairs of TiO$_2$.

2. Introduction

The aim of this chapter was the enhancement of the photocatalytic activity of TiO$_2$ under visible light by doping with reduced Graphene Oxide (rGO) nanosheets. The role of rGO is to shift the absorption edge of TiO$_2$ toward higher wavelengths and to decrease its band gap. As well, rGO plays an important role in the photodegradation process by improving the separation efficiency of the electron/hole pairs in the semiconductor. In this chapter, we will report on the synthesis of Graphene Oxide (GO) using modified Hummer's method and the elaboration of rGO/TiO$_2$ composite nanofibers by electrospinning technique. Different characterisations techniques were used to study the morphological, structural and optical properties of the prepared samples. The photocatalytic activity of TiO$_2$ and rGO/TiO$_2$ composite nanofibers was evaluated by the degradation of Methyl Orange (MO) under visible light irradiation.

3. Materials and methods

3.1. Materials

Commercial graphite powder (99.95%), titanium tetraisopropoxide (TTIP) Ti{OCH(CH$_3$)$_2$} (97%), polyvinylpyrrolidone (PVP) (Mw = 13,00,000), acetic acid (98%), phosphoric acid (H$_3$PO$_4$, 85%), sulfuric acid (H$_2$SO$_4$, 98%), hydrochloric acid (HCl, 30%), potassium permanganate (KMnO$_4$, 98%), hydrogen peroxide (H$_2$O$_2$, 30%), methyl orange (MO), and absolute ethanol were purchased from Sigma Aldrich, and used without any further purification.

3.2. Synthesis of Graphene Oxide

Graphene oxide was synthesized from natural graphite powder, following modified Hummer's method [1]. Briefly, 3g of graphite were dispersed in concentrated H$_2$SO$_4$:H$_3$PO$_4$ (9:1, 400 mL) solution. 18 g of KMnO$_4$ were added gradually to the mixture with stirring for 12 h. Later on, the mixture was cooled down to room temperature and then H$_2$O$_2$ (3 mL) was added. Brown precipitate was observed showing the exfoliation of graphene oxide from graphite. After one hour of stirring, GO was separated by centrifugation at 2697 G for 10 minutes and the supernatant was decanted away. The resultant precipitates were washed several times with 30% hydrochloric acid and absolute ethanol. Finally, the obtained powder was dried at 50°C for 24 hours to obtain the pure graphene oxide.

3.3. Preparation of TiO$_2$ and rGO composite nanofibers

The electrospinning process was used to prepare the rGO-incorporated TiO$_2$ nanofibers. Spun solution was prepared in three steps. In the first one, different amounts of graphene oxide (0, 2, 5, 7 wt. % of mass Ti) and 2 ml of absolute ethanol were sonicated for 12h to disperse the graphene oxide into ethanol solution. In the second step, titanium tetraisopropoxide was dissolved in a mixture of 2 ml of acetic acid and 3 ml of ethanol mixed with 0.3 g of polyvinylpyrrolidone (PVP). The precursor mixture was stirred for 1 h at room temperature to obtain sufficient viscosity required for electrospinning. Finally, the GO solution was added to the precursor solution with vigorous magnetic stirring (150 rpm) for 30 min. The homogeneous dark black solution was loaded into a plastic syringe having a stainless steel needle with a diameter of 0.7 mm at a constant flow rate of 1 ml/h. The feeding rate was controlled by the syringe pump. The temperature level inside the

electrospinning chamber was 38 ± 5°C. Nanofibers were collected on a rotating coil covered with an aluminum foil with a rotation speed of 400 rpm. The distance between the tip of the needle and the aluminum foil was maintained at 20 cm, and a DC voltage of 25 kV was applied. During electrospinning process, the applied electric field overcomes the surface tension of the polymeric solution, thereby ejecting a continuous jet, which upon subsequent solvent evaporation and bending produces nanofibers on the collector surface [2]. The electrospun TiO_2-GO composite nanofibers were collected and then calcined at 500°C with a heating rate of $1°C.min^{-1}$ for 6 h in N_2 environment in a tubular furnace in order to reduce the GO sheets [3] to form rGO/TiO_2 NFs.

3.4. Chemical and structural Characterization

X-ray diffraction (XRD) measurements were carried out using a PANAlytical Xpert-PRO diffractometer equipped with an X'celerator detector using Ni-filtered Cu-radiation (λ= 1.54 ˚A). Fourier-transform infrared (FTIR) spectra were recorded on a Nicolet 370 FTIR spectrometer using an ATR system. Transmission electron microscopy (TEM) images were taken with a PHILIPS-CM 20 (accelerating voltage: 200 KV). Scanning electron microscopy (SEM) images were taken with a Hitachi S4800, Japan (accelerating voltage: 1 KV). The UV–Vis absorbance spectra of methyl orange were recorded by a Jasco V-570 UV–VIS-NIR spectrophotometer. Raman spectra have been obtained from Horiba xplora, λ= 659 nm. Energy-dispersive X-ray spectroscopy analysis (EDX) was taken with Zeiss EVO ED15 microscope coupled with an Oxford X-MaxN EDX detector.

3.5. Photocatalytic activity measurement

Methyl orange was used as a reference of organic pollutant to evaluate the photocatalytic activity of the rGO/TiO_2 composite NFs. The photocatalytic performance of the samples was evaluated by analyzing the decrease in concentration of the MO during exposure to visible light irradiation. The reaction temperature was kept constant at 25 ± 0.2 °C by circulating water in a cylindrical tube surrounding the photo-reactor during the entire experiment. The decomposition was carried out in several beakers containing a suspension of 10 mg of each sample in 25 mL of MO solution (10 mg/L) under visible light irradiation (obtained from a 150 W light source, emission wavelength > 400 nm). The distance between the lamp and the dye solution was maintained at 10 cm. First, the solution

mixture was magnetically stirred for 30 min without irradiation to reach the adsorption–desorption equilibrium of MO [4]. Then, the solution was irradiated with visible light for 2 hours. Each 30 minutes, 3 ml of the sample solution was taken out and centrifuged to remove the catalyst. The centrifuged solutions were analyzed by a UV/Vis spectrometer. The absorbance spectra of MO (major absorption band around 462 nm)[5] were recorded to measure the change in the concentration of MO[6]. After irradiation, the photocatalytic degradation efficiency has been calculated by equation 1:

$$\text{Degradation efficiency (\%)} = (C_0 - C) / C_0 \times 100 \qquad \text{(Equation 1)}$$

where C_0 and C are the initial concentration and the final concentration of dye before and after photo-irradiation respectively. This equation shows the dye photocatalyst degradation percentage [7].

4. Results and discussion

4.1. Morphological properties of TiO$_2$ /rGO nanofibers
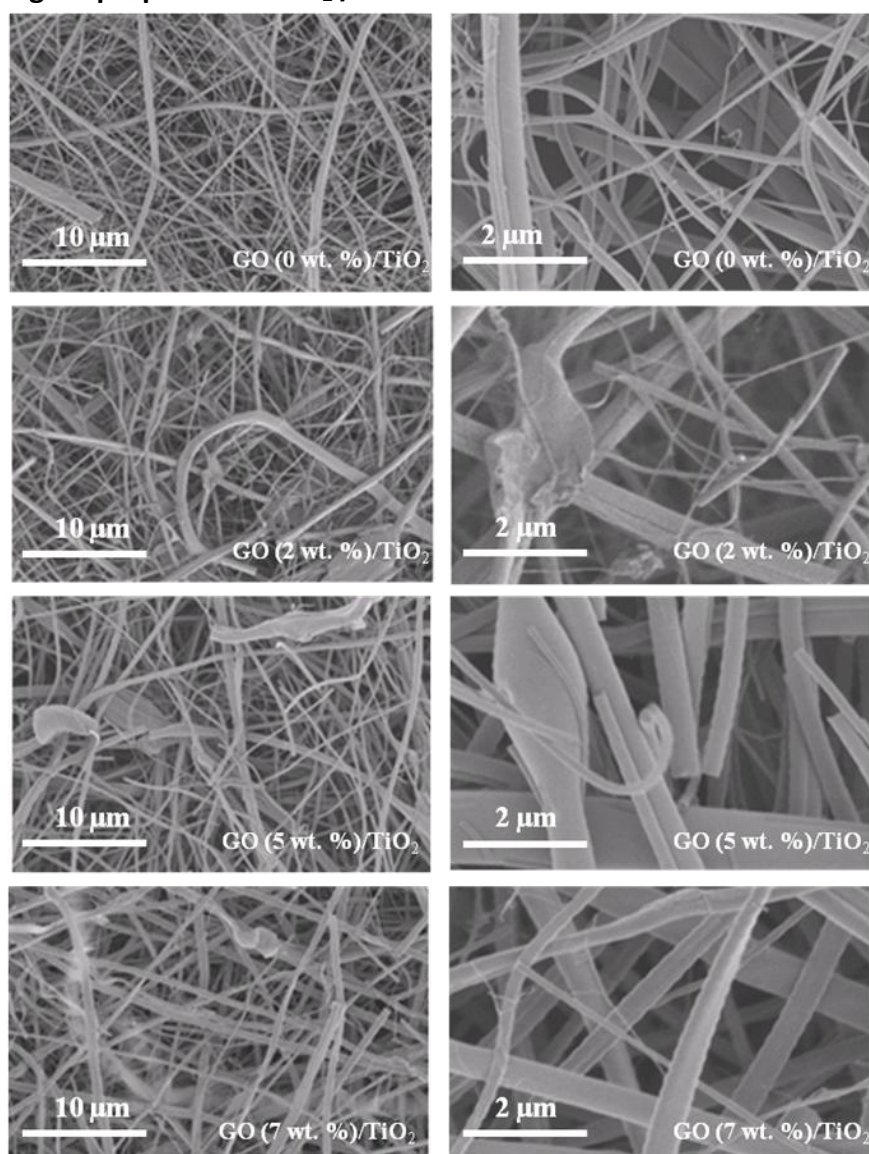
Figure 11. Scanning Electron Microscope images of TiO$_2$ and rGO/TiO$_2$ annealed composite nanofibers under N$_2$ atmosphere for 6h at 500°C.

The TiO$_2$ and TiO$_2$/GO NFs with different amounts of graphene oxide were fabricated by electrospinning of a polymeric solution with titanium tetraisopropoxide as precursor. The morphological and microstructural details of TiO$_2$ and TiO$_2$/GO nanofibers were examined by SEM. Figure 1.1 displays the SEM images of the obtained TiO$_2$ and GO-containing electrospun NFs after calcination at 500°C for 6h under N$_2$ atmosphere. The formation of highly interconnected networks of continuous, randomly oriented nanofibers can be clearly seen. It can also be observed that the incorporation of GO did not affect the nanofibrous

morphology of TiO_2. The diameters have been obtained using the ImageJ, Java-based image processing software. The average diameter was measured on 100 randomly chosen nanofibers of each sample (Figure 1). After calcination, we measured an average diameter of (141 ± 5 nm), (263 ± 7nm), (293 ± 10 nm) and (355 ± 13 nm) for samples with GO weight amount of 0, 2, 5 and 7 wt. % respectively. The average diameter of the nanofibers increases with the increase of the amount of graphene oxide. It can be attributed to the increase of the solution viscosity induced by inclusion of the GO in the electrospinning solution[8]. This increase reveals the successful incorporation of the graphene oxide in the TiO_2 nanofibers. An energy dispersive X-ray spectrum (EDX) of GO/TiO_2 NFs recorded along with elemental mapping is presented in Table 2.1. The EDX analysis revealed the molar ratio of Ti and O to be 1:2 for the above fibers, which is in good agreement with the stoichiometric ratio of TiO_2. Comparing the GO doped fibers to the pure one, we can notice the increase of the carbon content in GO (2 wt. %) /TiO_2, GO (5wt. %) /TiO_2 and GO (7wt. %) /TiO_2.

Table 2.1. EDX data showing the composition of TiO_2, GO (2 wt. %) /TiO_2, GO (5wt. %) /TiO_2 and GO (7wt. %) /TiO_2 annealed nanofibers under N_2 atmosphere.

Samples	Atomic percentages		
	Ti	O	C
TiO_2	30.49	60.76	8.75
GO (2 wt. %)	30.89	58.31	10.8
GO (5 wt. %)	29.29	53.26	17.45
GO (7 wt. %)	24.98	52.07	22.95
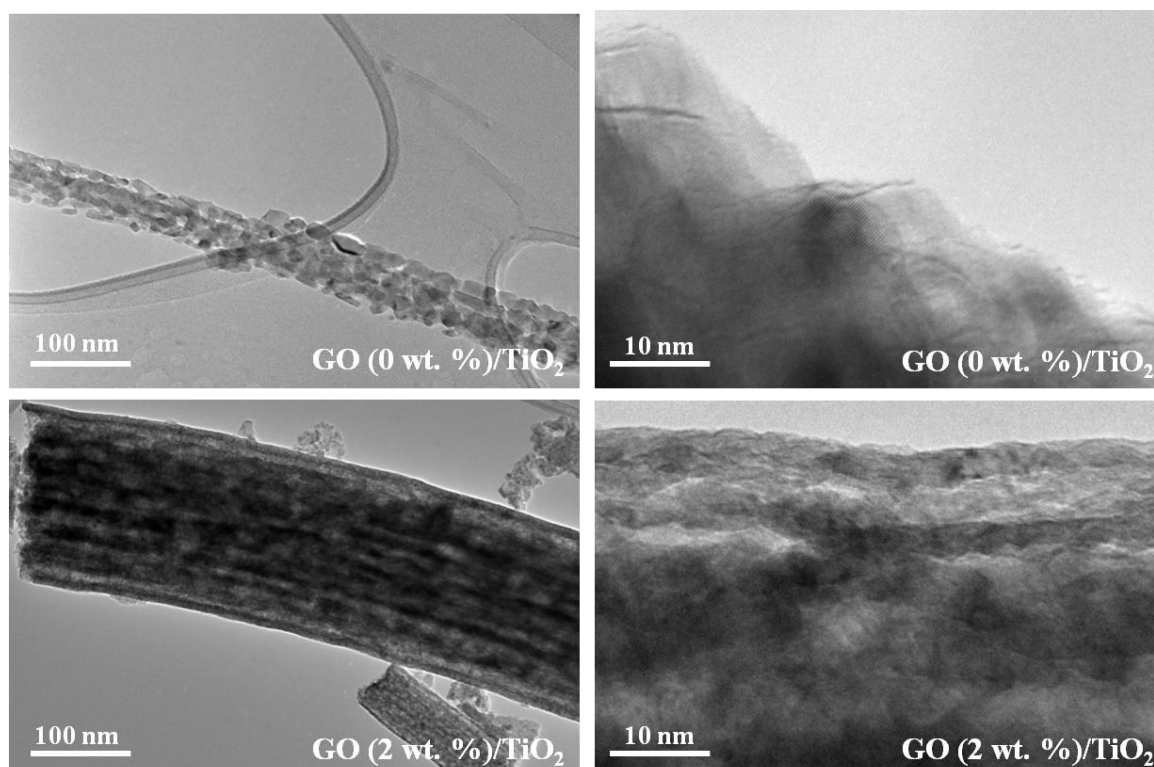
Figure 12. Transmission electron microscopy images of TiO_2 GO (2 wt. %) /TiO_2 annealed nanofibers under N_2 atmosphere for 6h at 500°C.

Figure 2.2 illustrates the TEM images of TiO_2 NFs and GO (2 wt. %) /TiO_2 composite NFs. Figure 2.2.a shows the granular aspect of the pure TiO_2, with an approximate grain diameter of 10 nm. When TiO_2 is mixed with graphene oxide, the close up morphology of the fibers appears to be more linear with the absence of apparent grains and the presence of small voids. This could be due to the dispersion of TiO_2 within the GO monosheets even though the flakes of GO do not appear in the image. We may suppose that the TiO_2 is intercalated between the layers of GO with a certain spacing that may provide a better alignment inside the fiber as shown in Figure 2.2.b. In addition, GO does not have any define structures because oxidation destroys the initial (002) peak of pristine graphite. Therefore the amorphous structure of GO (carbon based) could not be detected by selected area diffraction.

4.2. Structural properties of TiO_2 /rGO nanofibers

The crystalline phase of TiO_2, GO (2 wt. %) /TiO_2, GO (5wt. %) /TiO_2, and GO (7wt. %) /TiO_2 was analyzed by X-ray diffraction (XRD). The patterns in Figure 2.3 show the diffraction

peaks of anatase phase of TiO_2 (101), (200), (105), (211), (204) which correspond to 2θ = 25.5°, 48.2°, 54.1°, 55.3° and 64.2° and three diffraction peaks of rutile phase of TiO_2 (110), (101), (111) which correspond to 2θ = 27.7°, 35.8° and 41.6° [7]'[9]. The crystallite average sizes of TiO_2 and GO/TiO_2 with different amounts of GO were estimated using the Scherrer equation [10]. The calculated results show that the crystallite average sizes of GO/TiO_2 fibers increased as compared to pure TiO_2 fibers. The crystallite sizes were found to be 9.4, 18.4, 15.5 and 10.1 nm for the samples TiO_2, GO (2 wt. %) /TiO_2, GO (5wt. %) /TiO_2, and GO (7wt. %) /TiO_2 respectively. However, when the amount of GO exceeds 5 wt. % the crystallite size decreases which might be attributed to the agglomeration of GO sheets [11]. Evidence for stacks of graphene oxide sheets comes from the broad XRD peak of rGO (002) at around 2θ = 25° which corresponds to the d-spacing interlayer distance between the sheets [12]. It is worth noting that the diffraction peak of (rGO) cannot be distinguished in the composite, probably due to the presence of the diffraction peak of TiO_2 at the same position.
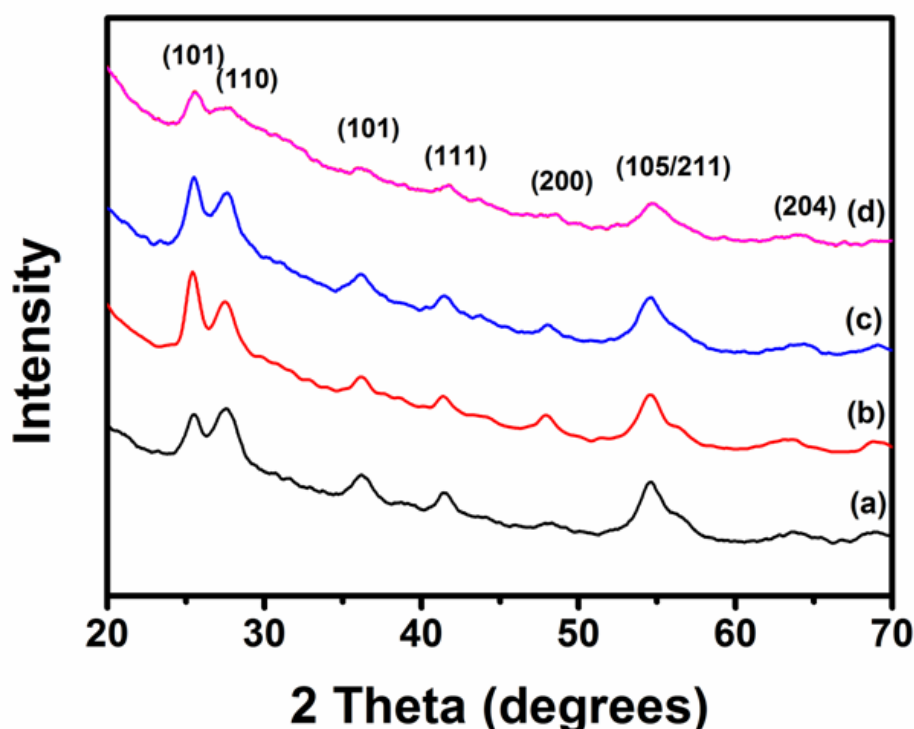
Figure 13. XRD patterns of photocatalysts: (a) TiO_2, (b) GO (2 wt. %) /TiO_2, (c) GO (5wt. %) /TiO_2, and (d) GO (7wt. %) /TiO_2 annealed nanofibers under N_2 atmosphere for 6h at 500°C.

In order to confirm the formation of the TiO_2 and rGO/TiO_2 nanofibers, the Raman spectrum was recorded in the range of 100-2000 cm^{-1}. Figure 2.4.A shows the Raman spectrum of TiO_2, GO (2 wt. %) /TiO_2, GO (5wt. %) /TiO_2, and GO (7wt. %) /TiO_2. For all samples we observe one peak corresponding to the active mode of anatase phase at 144 cm^{-1} (E_g) and three peaks corresponding to the active modes of rutile phase at 244 cm^{-1} (B_{1g}), 447 cm^{-1} (E_g) and 612 cm^{-1} (A_{1g}) [13]. More importantly, the Raman spectra of the composite GO/TiO_2 with different amounts of GO showed the broadened characteristic frequencies at 1365 cm^{-1} and 1612 cm^{-1}, which correspond to the D and G band, respectively [14]. These two bands confirm that the GO was successfully introduced into the nanofibers during electrospinning. The detected carbon comes essentially from the addition of GO and not from the initial polymer, as particularly verified by the Raman spectroscopy. In fact, the carbon in graphene oxide sheets is distributed over a honeycomb structure which exhibits a sp^2-hybridized carbon system resulting into the D and G vibration modes. The G band (1612 cm^{-1}) is due to the stretching of the C-C bond whilst the D band (1360cm^{-1}) is an in-plane vibrational mode, as clearly shown in the GO (2 wt. %) /TiO_2 sample. When the percentage of GO is increased (5 wt % and 7 wt %), the interaction between the stacked layers will change the spectrum namely by widening the D band and creating a small red shift as shown in Figure 2.4.B. These particularities are obviously not present in the pure TiO_2 sample [15]. The ratio between the intensity of D and G bands has been used as a parameter to evaluate the reduction of GO. Changes in the relative intensities of the D and G bands (D/G) indicate the modifications of the electronic conjugation state of the GO during reduction after N_2 calcination [16]. The D/G ratio can be influenced by edges, charge puddles, ripples and many other defects [17]. After calculation of the D/G ration for different GO amounts, it was found to be 1.1, 1.24, and 1.36 for GO (2 wt. %) /TiO_2, GO (5wt. %) /TiO_2, and GO (7wt. %) /TiO_2, respectively. Since the Raman D/G intensity ratio is inversely proportional to the average size of the sp^2 domains, the increase of the D/G intensity ratio suggests that smaller in-plane sp^2 domains are formed during the reduction of GO after N_2 annealing [18], which means that the GO (2 wt. %) /TiO_2 was more reduced than GO (5wt. %) /TiO_2, and GO (7wt. %) /TiO_2. This might be related to the time of the heat treatment. A larger amount of GO required a longer time of calcination for the removal of the oxygen-containing functional groups [19].
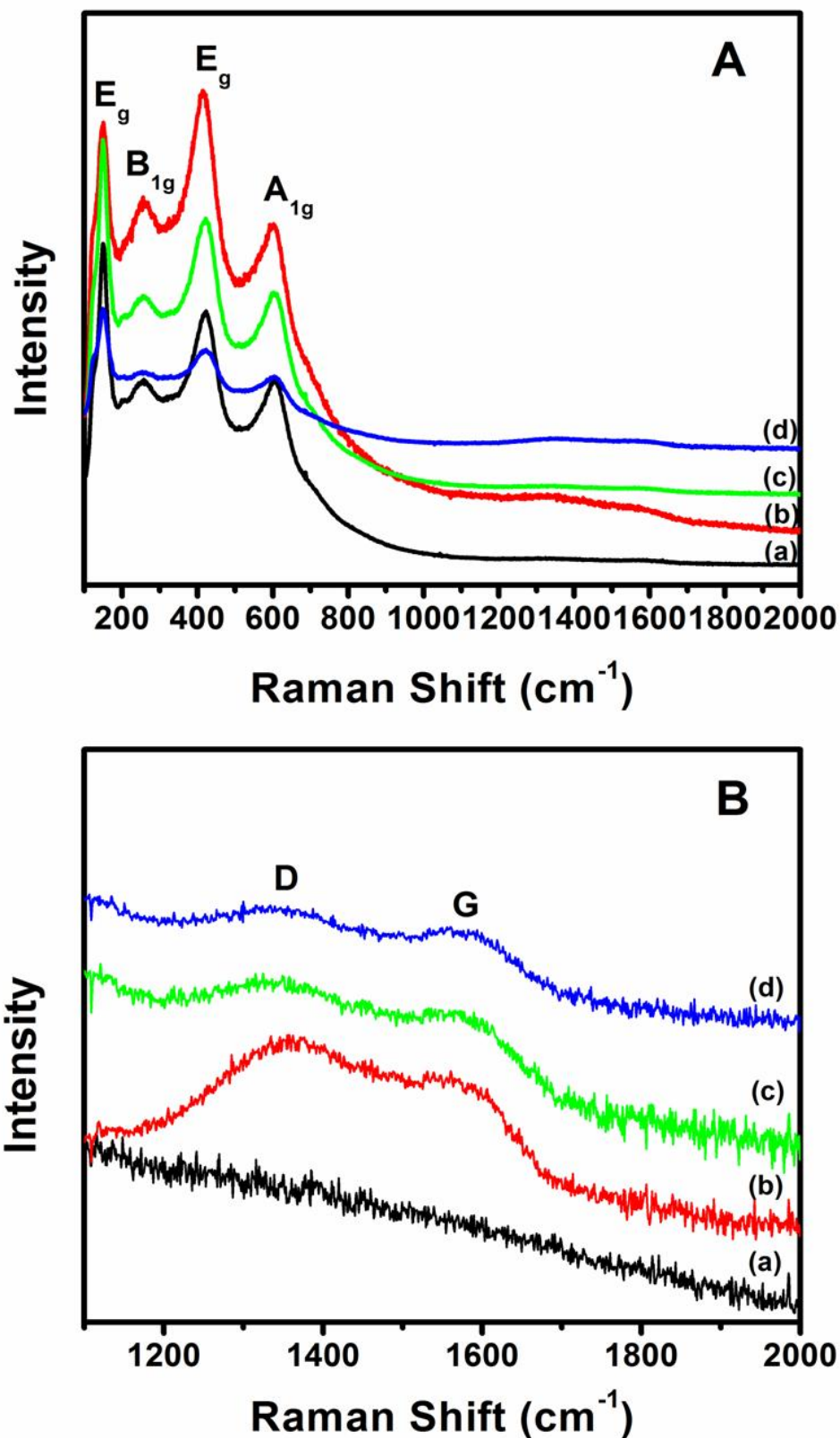
Figure 14. (A-B) Raman Shift of (a) TiO$_2$, (b) GO (2 wt. %) /TiO$_2$, (c) GO (5wt. %) /TiO$_2$, (d) GO (7wt. %) /TiO$_2$ annealed nanofibers under N$_2$ atmosphere for 6h at 500°C.

4.3. Optical properties of TiO$_2$ /rGO nanofibers

The various functional groups present in the TiO$_2$, GO and rGO/TiO$_2$ nanofibers were confirmed by using Fourier transform infrared (FTIR) spectroscopy as shown in Figure 2.5. Based on previous studies, the FTIR spectrum of GO illustrates the presence of C=O (1728 cm^{-1}) from stretching vibrations from carbonyl and carboxylic groups, C-OH (1222 cm^{-1}) from stretching vibrations, C-O (1035 cm^{-1}), and C-O (968 cm^{-1}) from carbonyl, carboxylic and epoxy groups, which confirms the presence of oxygen-containing functional groups. The peak at 1600 cm^{-1} arises due to the C-C vibrations from the graphitic domains. The broad peak at 3423 cm^{-1} is due to the adsorbed water content in the surface of GO [20]. These functional groups present in the GO renders it hydrophilic while the graphite and graphene are hydrophobic [11]. In the case of the annealed TiO$_2$ and TiO$_2$/GO (Figure 2.5.a-d), the characteristic absorption band of TiO$_2$ at 800–1200 cm^{-1} is attributed to Ti–O bond. The bands related to the carbon-containing functional groups C=C (indexed in the Figure 2.5) are observed, and increase with the GO amounts. The peak at 1730 cm^{-1} almost disappears because of the removal of C=O. This proves that many oxygen groups were removed and confirms the transformation from GO/TiO$_2$ to rGO/TiO$_2$ during the N$_2$ calcination [15].
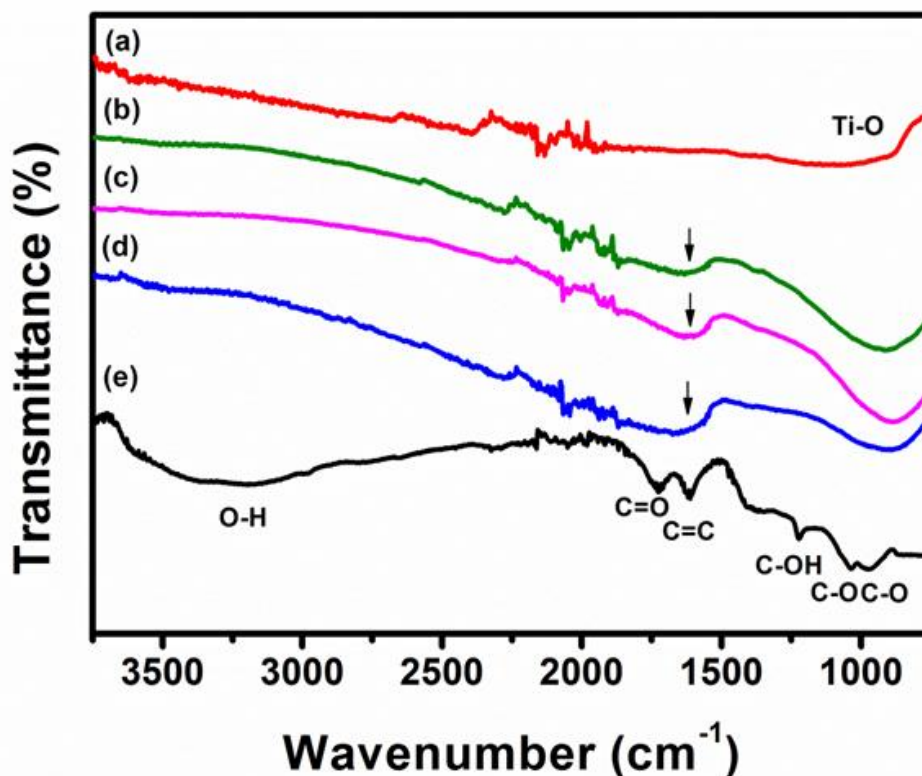
Figure 15. FTIR spectra of (a) TiO_2, (b) GO (2 wt. %) /TiO_2, (c) GO (5wt. %) /TiO_2, (d) GO (7wt. %) /TiO_2 GO annealed nanofibers under N_2 atmosphere and (e) GO.

The UV–Vis absorption spectroscopy measurement of pure TiO_2 NFs and rGO/TiO_2 composite nanofibers was carried out to investigate the optical properties of the samples and the results are shown in Figure 2.6. The UV–Vis absorption spectra of the GO (2 wt. %) /TiO_2, GO (5wt. %) /TiO_2 and GO (7wt. %) /TiO_2 nanocomposite indicates that it absorbs light at 420, 406 and 391 nm (indexed in the Figure 2.6) corresponding to a band gap of 2.95, 3.1 and 3.17 eV, respectively. Compared to the TiO_2 nanofibers (absorption edge: 386 nm, band gap energy: 3.2 eV), the absorption edges of rGO/TiO_2 composite nanofibers are red-shifted [21]. Actually, the GO (2 wt. %) has the lowest band gap since it is the most reduced sample as already confirmed by Raman analyses, and is expected to exhibit enhanced photocatalytic activity compared to other samples. The photoactivity is measured and evaluated in the next section. Thus, we can say that the incorporation of GO sheets into TiO_2 NFs creates energetic levels which decrease the band gap energy of TiO_2 and increase the visible light catalytic activity of TiO_2 nanofibers.
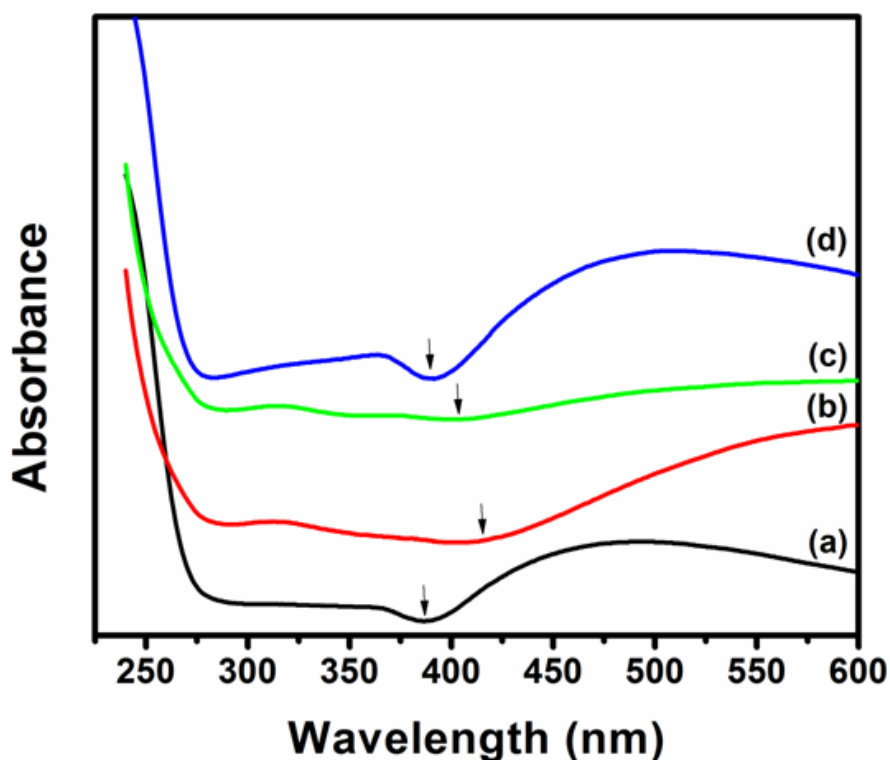
Figure 16. UV-Vis absorption spectra of (a) TiO_2, (b) GO (2 wt. %) /TiO_2, (c) GO (5wt. %) /TiO_2, (e) GO (7wt. %) /TiO_2 nanofibers.

4.4. Photocatalytic degradation of methyl orange by rGO/TiO_2 composite nanofibers

The photocatalytic activities of TiO_2/rGO NFs with different GO amounts were evaluated by degradation of methyl orange (MO) under visible light (wavelength > 400 nm). MO was selected as a model organic pollutant. Figure 2.7.a-f shows the UV-Vis absorbance spectra of MO solution (major absorption band around 462 nm) with different time intervals 0, 30, 60, 90 and 120 min after 60 min storage in dark for excluding the interference of adsorption. For comparison, the photocatalytic activities of TiO_2 NFs and commercial TiO_2-P25 were also tested under identical experimental conditions. The results indicate that MO is stable and difficult to be photodegraded in the absence of photocatalyst. After irradiation for 120 min, MO was degraded up to 40% in the presence of TiO_2 nanofibers, compared to 35% degradation by commercial granular TiO_2-P25 (Figure 2.8). Therefore, in the case of pure TiO_2, it is well known that TiO_2 NFs have a larger active surface area compared to the commercial TiO_2-P25 nanoparticles [22]. Most significant, the GO (2 wt. %) /TiO_2 and GO (5

wt. %) /TiO$_2$ NFs show remarkably enhanced photocatalytic activities, the MO degradation being 90% and 63% respectively. The GO (2 wt. %) /TiO$_2$ NFs exhibits the higher photocatalytic activity. With higher GO amount 7 wt. %, the activity of TiO$_2$/rGO NFs is gradually decreased; the MO degradation was just 26%. For the composites GO (2 wt. %) /TiO$_2$ and GO (5 wt. %) /TiO$_2$, the absorption edges are red shifted and the band gap energy decreases with the rGO incorporation. In addition, the photo electrons were quickly transferred to the rGO layers, which reduce the probability of the electron–hole recombination in TiO$_2$. Thus, more photo electrons were available compared to pure TiO$_2$ NFs, to take part in the photodegradation process. However, the use of an excessive amount of GO in the GO (7 wt. %) /TiO$_2$ composite reduced the light absorption on the TiO$_2$ surface. This leads to a decrease of photoexcited electrons [23]. This excess of GO (7wt. %) also increased the opportunity for the recombination of the photo-generated electron–hole pairs, by increasing the collision among the photogenerated electrons and holes [24].
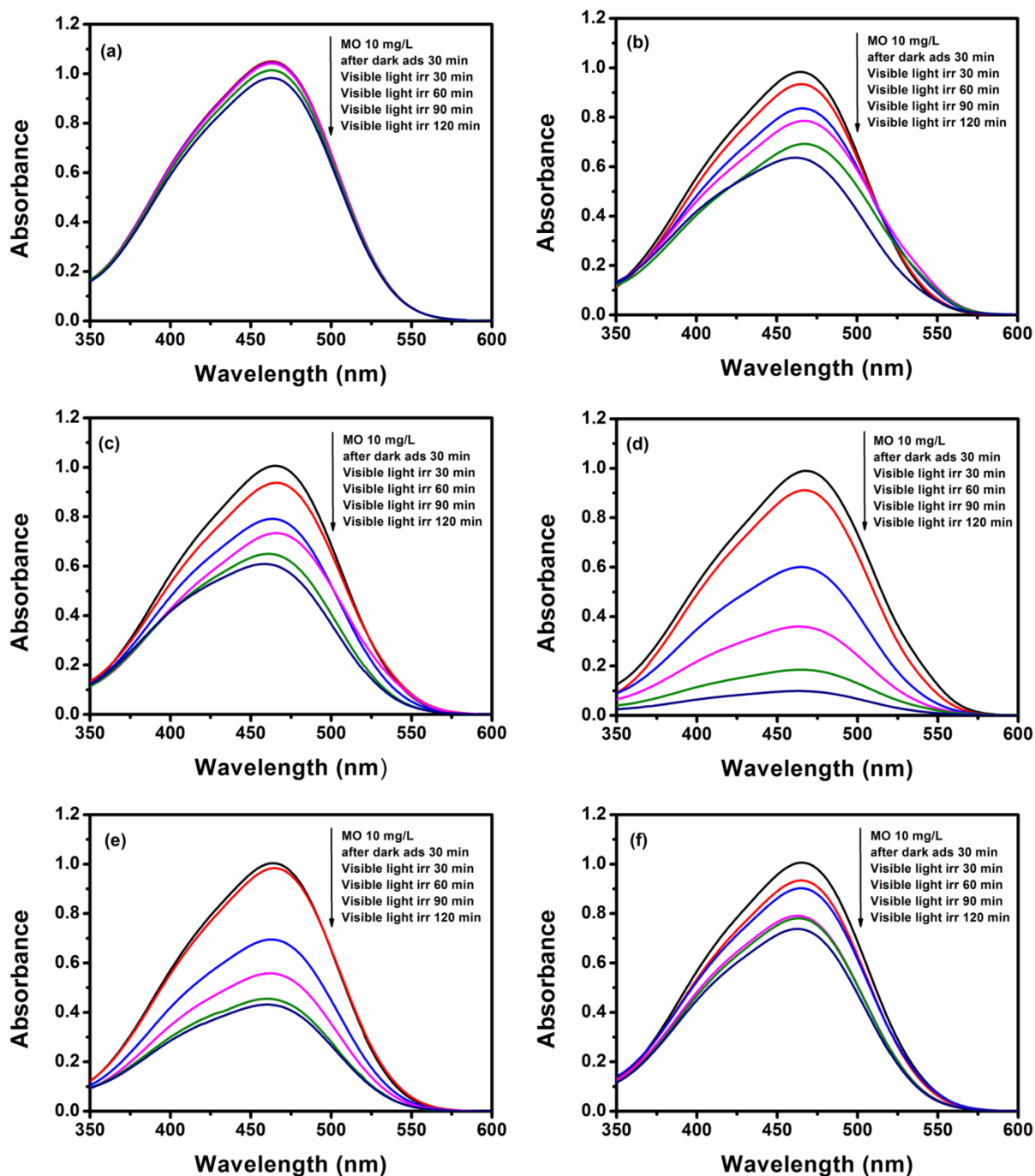
Figure 17. UV-Vis spectra of the photocatalytic degradation of MO under visible light: (a) MO without catalyst, (b) TiO_2-P25, (c) TiO_2 NFs, (d) GO (2 wt. %) /TiO_2, (e) GO (5wt. %) /TiO_2 and (f) GO (7wt. %) /TiO_2.

It was well known that the photocatalytic activity is mainly governed by crystalline phase, light absorption capacity and separation efficiency of electron–hole pairs [25]. From the XRD analysis, the crystallite average sizes of TiO_2 increased after introducing GO sheets for GO (2

wt. %) /TiO$_2$ NFs. Therefore, the relevant explanation for the high phototocatalytic activity of GO (2 wt. %) /TiO$_2$ NFs should be ascribed to the differences in the GO reduction. As confirmed by Raman analyses and UV-Vis absorption presented above, more GO in GO (2 wt. %) /TiO$_2$ NFs was reduced than that in GO (5 wt. %) /TiO$_2$ and GO (7 wt. %) /TiO$_2$ NFs which means the lowest band-gap energy (2.9 eV). These results indicate that GO (2 wt. %) /TiO$_2$ composite NFs has excellent absorption capacity of visible light and lower recombination rate of electron–hole pair.
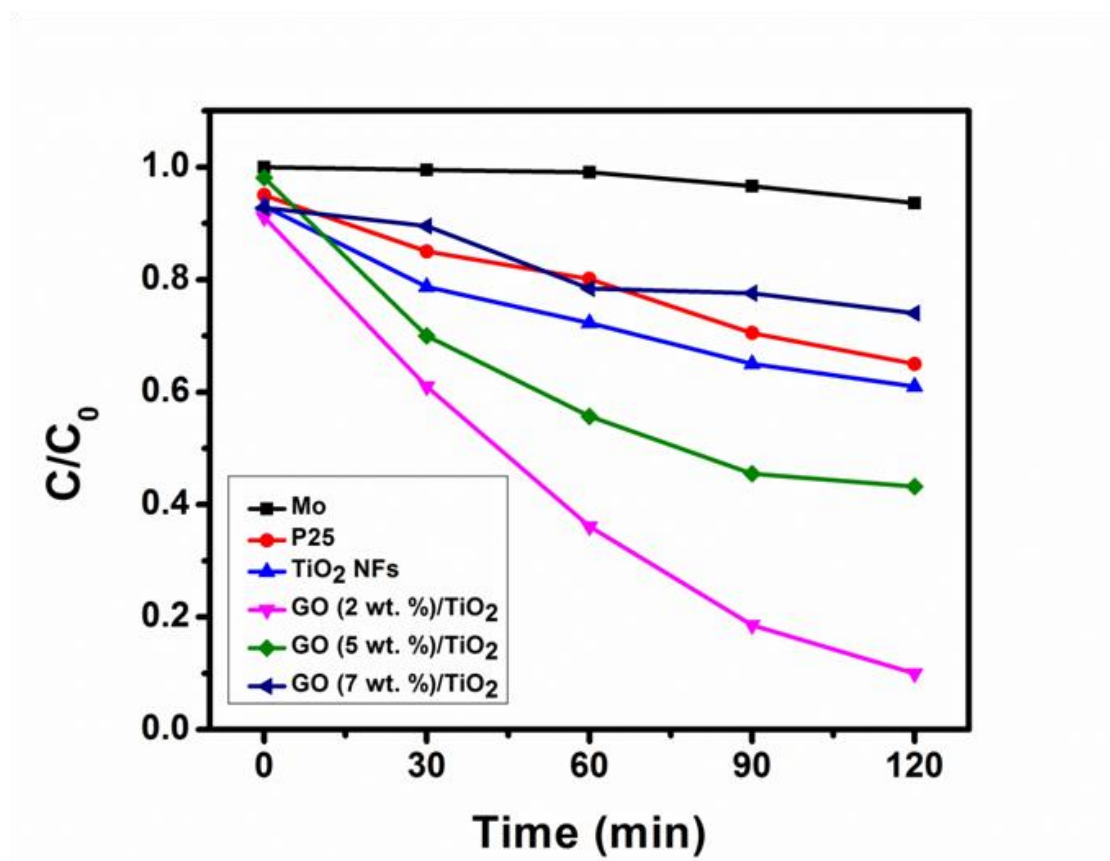
Figure 18. Photodegradation of MO by TiO$_2$-P25, TiO$_2$ NFs and rGO/TiO$_2$ composite nanofibers.

Figure 2.9 shows the different kinetic linear curves. The photodegradation reactions follow a Langmuir–Hinshelwood first-order kinetics model[26]. The explanation is described as follows:

$$r = \frac{dC}{dt} = \frac{kKC}{(1+KC)}$$ (Equation 2)

where r is the degradation rate of MO (mg (L min)$^{-1}$), C is the concentration of a MO solution (mg L^{-1}), t is the irradiation time, k is the reaction rate constant (mg (L min)$^{-1}$), and K is the adsorption coefficient of MO (mg L^{-1}). Since the initial concentrations (C_0 = 10 mg L^{-1}) of the MO solutions are very low in the present experiments, this equation can be simplified to an apparent first-order model [26]:

$$\ln (C_0/C) = kKt = k_a t \qquad \text{(Equation 3)}$$

where k_a is the apparent first-order rate constant (min^{-1}) and C is the concentration at time t. k_a obtained from the linear dependence between ln (C_0/C) and time (Figure 2.9) are reported in Table 2. The increasing order of the rate constants in the samples is: GO (2 wt. %) /TiO$_2$ < GO (5wt. %) /TiO$_2$ < TiO$_2$ NFs < TiO$_2$-P25 < GO (7wt. %) /TiO$_2$ < MO. The rate constant exhibits a maximum of 0.0186 min^{-1} for GO (2 wt. %) /TiO$_2$ nanocomposites, which is around 6 times higher than that of commercial TiO$_2$-P25 and TiO$_2$ NFS. Thus, for the more reduced sample GO (2 wt. %) /TiO$_2$ NFs as confirmed above, visible-light photocatalytic activity is significantly improved.

In the present work, the fact of using the simple electrospinning technique to synthesize composite nanofibers of rGO/TiO$_2$ for photocatalytic application is novel. The degradation efficiency (90%) obtained by using the rGO/TiO$_2$ composite nanofibers in our case is greater in comparison to what has been reported before [14],[21]. The enhancement is induced by the special morphology of the nanofibers that presents improved active surface area in comparison to rGO/TiO$_2$ nanoparticles [22].
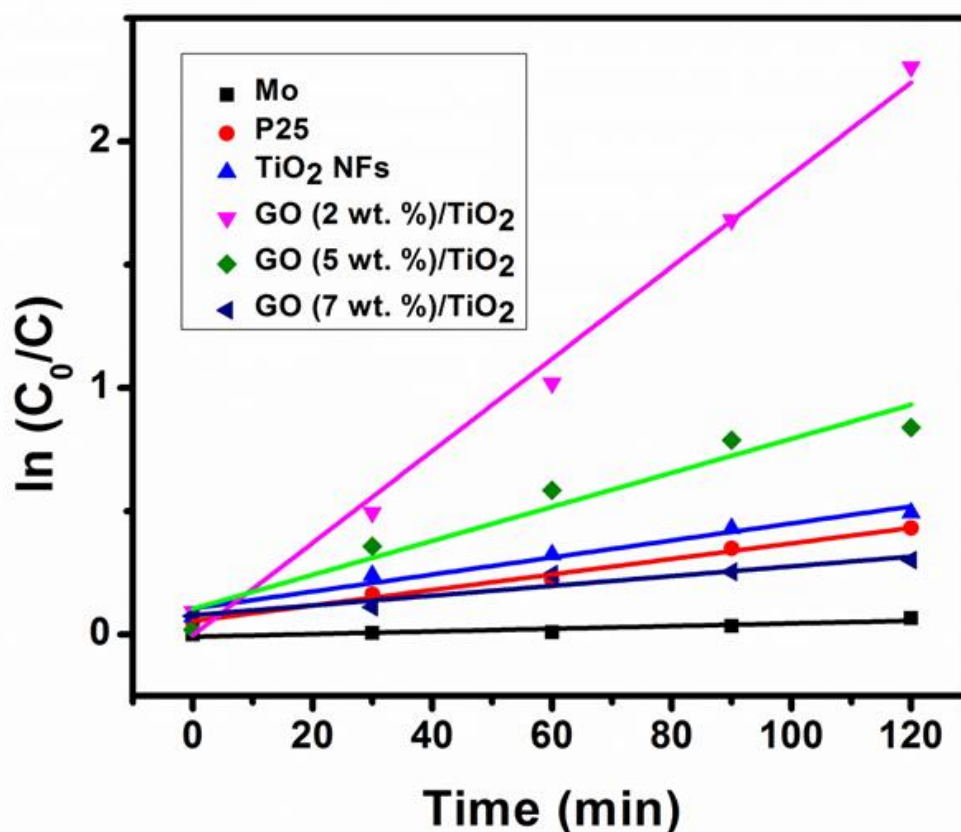
Figure 19. Kinetics of Methyl orange degradation by TiO_2-P25, TiO_2 NFs and rGO/TiO_2 composite nanofibers.

Table 2.2. Kinetic parameters for photocatalytic activities of TiO_2-P25, TiO_2 NFs and rGO/TiO_2 composite nanofibers.

	MO	TiO_2-P25	TiO_2 NFs	GO (2 wt. %) /TiO_2	GO (5wt. %) /TiO_2	GO (7wt. %) /TiO_2
k_a (min^{-1})	0.0005	0.0031	0.0034	0.0186	0.0069	0.0019
R^2	0.8146	0.9882	0.9628	0.9885	0.9230	0.8929

5. Conclusion

In summary, rGO/TiO_2 composite nanofibers with different GO amounts were successfully prepared by electrospinning. All the samples were annealed at 500°C in N_2 atmosphere for 6 hours. The SEM images showed an increase in the average diameter with the increase of rGO amount and confirmed that the one dimensional morphology was maintained. The correlation between the domain size of the TiO_2 crystalline structure and the GO incorporation effect was clearly observed in the TEM and XRD results. Raman and

FTIR confirmed the reduction of GO after calcinations in N_2 atmosphere. The decreasing of TiO_2 NFs band gap energy from 3.2 eV to 2.9 eV due to the presence of rGO sheets was confirmed by UV-Vis analysis. The incorporation of rGO significantly increases the visible light photo-response and improves the separation of the photo-induced electron–hole pairs of TiO_2. Remarkably, the optimal percentage of introducing and reducing GO is 2 wt. % / TiO_2. Under this condition, the photocatalytic degradation of methyl orange under visible light is 6 times higher than that of commercial TiO_2-P25. In addition after 120 min 90 % of MO is degraded against 35% degradation by commercial TiO_2. Thus, incorporating rGO into TiO_2 NFs is an efficient and simple way for enhancing the visible-light photocatalytic activity. As a result, we have successfully prepared rGO/TiO_2 composite nanofibers that could be used as catalysts in the degradation of different organic molecules under visible light, as well as electrolyte membrane for fuel cell application and many other membrane applications [27].

REFERENCES

1. Hummers Jr, W.S. and R.E. Offeman, Preparation of graphitic oxide. Journal of the American Chemical Society, 1958. **80**(6): p. 1339-1339.

2. Chaaya, A.A., et al., ZnO 1D nanostructures designed by combining atomic layer deposition and electrospinning for UV sensor applications. Journal of Materials Chemistry A, 2014. **2**(48): p. 20650-20658.

3. Lavanya, T., et al., Superior photocatalytic performance of reduced graphene oxide wrapped electrospun anatase mesoporous TiO 2 nanofibers. Journal of Alloys and Compounds, 2014. **615**: p. 643-650.

4. Jiang, L., Y. Huang, and T. Liu, Enhanced visible-light photocatalytic performance of electrospun carbon-doped TiO 2/halloysite nanotube hybrid nanofibers. Journal of colloid and interface science, 2015. **439**: p. 62-68.

5. Dhakal, T.P., et al., Moisture-induced surface corrosion in AZO thin films formed by atomic layer deposition. Device and Materials Reliability, IEEE Transactions on, 2012. **12**(2): p. 347-356.

6. Chuangchote, S., et al., Photocatalytic activity for hydrogen evolution of electrospun TiO2 nanofibers. ACS applied materials & interfaces, 2009. **1**(5): p. 1140-1143.

7. Kaveri, S., et al., Thiourea assisted one-pot easy synthesis of CdS/rGO composite by the wet chemical method: Structural, optical, and photocatalytic properties. Ceramics International, 2013. **39**(8): p. 9207-9214.

8. Nalbandian, M.J., et al., Synthesis and optimization of Ag–TiO 2 composite nanofibers for photocatalytic treatment of impaired water sources. Journal of hazardous materials, 2015. **299**: p. 141-148.

9. Wei, Z., et al., Hierarchical heterostructure of CdS nanoparticles sensitized electrospun TiO 2 nanofibers with enhanced photocatalytic activity. Separation and Purification Technology, 2014. **122**: p. 60-66.

10. Eid, C., et al., Tunable properties of GO-doped CoFe 2 O 4 nanofibers elaborated by electrospinning. RSC Advances, 2015. **5**(118): p. 97849-97854.

11. Wang, G., et al., Synthesis of enhanced hydrophilic and hydrophobic graphene oxide nanosheets by a solvothermal method. Carbon, 2009. **47**(1): p. 68-72.

12. Srinivas, G., et al., Synthesis of graphene-like nanosheets and their hydrogen adsorption capacity. Carbon, 2010. **48**(3): p. 630-635.

13. Nasr, M., et al., Photoluminescence: A very sensitive tool to detect the presence of anatase in rutile phase electrospun TiO 2 nanofibers. Superlattices and Microstructures, 2015. **77**: p. 18-24.

14. Pastrana-Martínez, L.M., et al., Advanced nanostructured photocatalysts based on reduced graphene oxide–TiO 2 composites for degradation of diphenhydramine pharmaceutical and methyl orange dye. Applied Catalysis B: Environmental, 2012. **123**: p. 241-256.

15. Štengl, V., et al., TiO2-graphene oxide nanocomposite as advanced photocatalytic materials. Chem. Cent. J, 2013. **7**(1): p. 41.

16. Luo, D., et al., Evaluation criteria for reduced graphene oxide. The Journal of Physical Chemistry C, 2011. **115**(23): p. 11327-11335.

17. Xue, Y., et al., Controllable synthesis of doped graphene and its applications. Small, 2014. **10**(15): p. 2975-2991.

18. Guo, Y., et al., One pot preparation of reduced graphene oxide (RGO) or Au (Ag) nanoparticle-RGO hybrids using chitosan as a reducing and stabilizing agent and their use in methanol electrooxidation. Carbon, 2012. **50**(7): p. 2513-2523.

J. Phys. Chem. C 2017, 121, 261-269

Page 84

19.   Velasco-Soto, M., et al., Selective band gap manipulation of graphene oxide by its reduction with mild reagents. Carbon, 2015. **93**: p. 967-973.

20.   Song, Y., et al., Graphene oxide: intrinsic peroxidase catalytic activity and its application to glucose detection. Advanced Materials, 2010. **22**(19): p. 2206-2210.

21.   Zhai, C., et al., Reduced graphene oxide modified highly ordered TiO 2 nanotube arrays photoelectrode with enhanced photoelectrocatalytic performance under visible-light irradiation. Physical Chemistry Chemical Physics, 2014. **16**(28): p. 14800-14807.

22.   Doh, S.J., et al., Development of photocatalytic TiO 2 nanofibers by electrospinning and its application to degradation of dye pollutants. Journal of Hazardous Materials, 2008. **154**(1): p. 118-127.

23.   Zhou, K., et al., Preparation of graphene–TiO 2 composites with enhanced photocatalytic activity. New Journal of Chemistry, 2011. **35**(2): p. 353-359.

24.   Zhang, X.-Y., et al., Graphene/TiO2 nanocomposites: synthesis, characterization and application in hydrogen evolution from water photocatalytic splitting. J. Mater. Chem., 2010. **20**(14): p. 2801-2806.

25.   Ohtani, B., Preparing articles on photocatalysis-beyond the illusions, misconceptions, and speculation. Chemistry letters, 2008. **37**(3): p. 216-229.

26.   Konstantinou, I.K. and T.A. Albanis, TiO 2-assisted photocatalytic degradation of azo dyes in aqueous solution: kinetic and mechanistic investigations: a review. Applied Catalysis B: Environmental, 2004. **49**(1): p. 1-14.

27.   Huang, S.-Y., et al., Development of a titanium dioxide-supported platinum catalyst with ultrahigh stability for polymer electrolyte membrane fuel cell applications. Journal of the American Chemical Society, 2009. **131**(39): p. 13898-13899.

Chapter 3: Enhanced Photocatalytic Performance of Novel Electrospun BN/TiO$_2$ Composite Nanofibers

Table of Contents

1. Introduction

This chapter focused on using Boron nitride (BN) nanosheets to improve the photocatalytic activity of TiO_2 under UV light. High power sonication was used to obtain the exfoliated boron nitride. This chapter is divided into 3 parts: (1) Elaboration of different BN-TiO_2 composite nanofibers with different amounts of BN nanosheets using electrospinning technique, (2) Studying the impact of BN incorporation on the morphological, structural and optical properties of TiO_2, (3) Evaluating the photocatalytic activity of BN-TiO_2 composites by the photodegradation process of methyl orange. The experiments of the photodegradation were done under UV light and under the same experimental conditions for all samples.

2. Abstract

High activity Boron nitride/Titanium dioxide (BN/TiO_2) composite nanofibers photocatalysts were successfully synthesized for the first time via the electrospinning technique. The as-spun nanofibers with controlled ratio of boron nitride nanosheets (BN) were calcined under air at 500^oC for 4 hours. Their morphological, structural and optical properties were studied by Scanning electron microscopy (SEM), X-ray diffraction (XRD), Energy-dispersive X-ray spectroscopy (EDX), BET surface area, Fourier-transform infrared (FTIR), Raman spectroscopy, UV-Visible spectrophotometer and Room temperature photoluminescence (PL). The effect of loading different BN sheets amounts on the photocatalytic degradation of methyl orange (MO) was investigated. The results indicated that the presence of BN sheets improves the separation of the photo-induced electron–hole pairs in TiO_2 and increases the band gap energy and the specific surface area compared to the pure TiO_2 nanofibers. BN/TiO_2 (wt. 10%) composite nanofibers photocatalytic activity is enhanced to 99% compared to 60% and 65% for P25 and TiO_2 nanofibers, respectively. Thus, the composites BN/TiO_2 significantly increases the UV light photo-response and improves the separation of photo-induced electron-hole pairs of TiO_2.

3. Experimental Section

3.1. Chemicals and Materials

Commercial boron nitride (95%, 325 mesh), titanium tetraisopropoxide (TTIP) Ti{OCH(CH$_3$)$_2$}$_4$ (97%), polyvinylpyrrolidone (PVP) (Mw = 13,00,000), acetic acid (98%),

Gelatine from porcine skin, methyl orange and absolute ethanol were purchased from Sigma Aldrich, and used without any further purification.

3.2. Exfoliation of Boron nitride

Boron nitride sheets were exfoliated from boron nitride powder [1], [2]. Briefly, 20g of gelatine were dissolved in 80 ml of hot water (75°C). After gelatine dissolving, 1g of boron nitride powder was added to the mixture. The solution was kept in an ultrasonic homogenizer over night at 50°C. Exfoliated BN was separated by centrifugation at 2697 G for 30 minutes and the supernatant was decanted away. The resultant precipitates were dried at 80°C for 48 hours and then calcined at 600°C in air for 2 hours in order to obtain the pure exfoliated boron nitride.

3.3. Preparation of TiO$_2$ and BN/TiO$_2$ composite nanofibers

The BN-incorporated TiO$_2$ nanofibers were synthesized by an electrospinning technique. The spun solution was prepared as follows: different amounts of boron nitride (0, 3, 5, 7 and 10 wt. % of the mass of Ti) and 2 ml of absolute ethanol were homogenized for 12h to disperse boron nitride into the ethanol solution. Titanium tetraisopropoxide was dissolved in a mixture of 2 ml of acetic acid and 3 ml of ethanol mixed with 0.3 g of polyvinylpyrrolidone (PVP). The precursor mixture was stirred for 1 h at room temperature to obtain sufficient viscosity required for electrospinning. Finally, the BN solution was added to the precursor solution under vigorous magnetic stirring (150 rpm) for 30 min. The homogeneous solution was typically extruded through a stainless steel nozzle with a diameter of 0.7 mm at a constant flow rate of 1 ml/h. The feeding rate was controlled by the syringe pump. The temperature level inside the electrospinning chamber was 38 ±5°C. Nanofibers were collected on a rotating coil covered with an aluminium foil with a rotation speed of 400 rpm. The distance between the tip of the needle and the aluminium foil was maintained at 20 cm, and a DC voltage of 25 kV was applied. In the electrospinning process, the high applied voltage was achieved by connecting the positive and ground terminals to the nozzle and collector, respectively. During electrospinning, the applied electric field overcomes the surface tension of the polymeric solution, thereby ejecting a continuous jet which upon subsequent solvent evaporation and bending produces nanofibers on the

collector surface. The electrospun BN-TiO$_2$ composite nanofibers were collected and then calcined in a tubular furnace at 500°C with a heating rate of 5°C/min for 5 h in air.

3.4. Physical and Chemical Characterization

X-ray diffraction (XRD) measurements were carried out using a PANAlytical Xpert-PRO diffractometer equipped with an X'celerator detector using Ni-filtered Cu-radiation (λ= 1.54 ˚A). Fourier-transform infrared (FTIR) spectra were recorded on a Nicolet 370 FTIR spectrometer using an ATR system. Raman spectra have been obtained from Horiba, λ= 659 nm. Scanning electron microscopy (SEM) images were taken with a Hitachi S4800, Japan. Energy-dispersive X-ray spectroscopy analysis (EDX) and elemental mapping were taken with Zeiss EVO HD15 microscope coupled with an Oxford X-MaxN EDX detector. The UV–VIS absorbance spectra were recorded by a Jasco V-570 UV–VIS-NIR spectrophotometer. The surface area of samples was determined from nitrogen adsorption-desorption isotherms at liquid nitrogen temperature using micromeritrics ASAP 2010 equipment (outgassing conditions: 200°C-12h). Room temperature photoluminescence (PL) has been measured in the range of 370-800 nm. The PL was excited with nitrogen Nd:YAG laser (266 nm, 10 mW, 1 kHz) and recorded with optical fiber spectrometer (Ocean Optics usb2000).

3.5. Photocatalytic activity measurement

Methyl orange (MO) was used as a reference of organic pollutant to evaluate the photocatalytic activity of the BN/TiO$_2$ composite nanofibers. The photocatalytic performance of the samples was evaluated by analyzing the decrease in concentration of the MO during exposure to UV light irradiation. The reaction temperature was kept constant at 25 ± 0.2 °C by circulating water in a cylindrical tube surrounding the photo-reactor during the entire experiment. The decomposition was carried out in several beakers containing a suspension of 10 mg of each sample in 25 ml of MO solution (10 mg/L) under visible light irradiation (obtained from a 48 W light source, emission wavelength < 400 nm). The distance between the lamp and the dye solution was maintained at 10 cm. First, the solution mixture was magnetically stirred for 30 min without irradiation to reach the adsorption–desorption equilibrium of MO. Then, the solution was irradiated with visible light for 75 minutes. Each 15 min, 3 ml of the sample solution was taken out and centrifuged to remove

the catalyst. The centrifuged solutions were analyzed by a UV-VIS spectrometer. The absorbance spectra of MO (major absorption band around 462 nm)[3] were recorded to measure the change in the concentration of MO[4]. After irradiation, the photocatalytic degradation efficiency has been calculated as follows:

$$\text{Degradation efficiency (\%)} = (C_0 - C)/C_0 \times 100 \qquad \text{(Equation 1)}$$

where C_0 and C are the initial concentration and the final concentration of dye before and after photo-irradiation respectively[5]. This equation shows the dye photocatalyst degradation percentage.

4. Results and discussion

4.1. Morphological properties

The TiO_2 and BN/TiO_2 NFs with different amounts of boron nitride were obtained by electrospinning of a solution of polymer with titanium tetraisopropoxide as precursor. Scanning electron microscopy was used to investigate the morphological features of TiO_2 and BN/TiO_2 nanofibers. Figure 3.1 shows the SEM images of the obtained TiO_2 and BN-containing electrospun nanofibers after calcinations in air at 500°C for 4 hours. The formation of highly interconnected networks of continuous, randomly oriented nanofibers can be clearly seen. As illustrated in Figure 3.1, the nanofibrous morphology was largely preserved after the heat treatment process. The fiber diameters were measured from the SEM images using image analysis software (Image J1.29X). The average diameter was measured on 100 randomly chosen nanofibers of each sample (Figure 3.1). After calcination, we measure average diameters of (187 ± 5 nm), (229 ± 7nm), (269 ± 10 nm), (290 ± 13 nm) and (314 ± 15 nm) for samples with BN weight amount of 0, 3, 5, 7 and 10 wt. %, respectively. In fact, the average diameter of the nanofibers increases with the increase of boron nitride amount. This can be attributed to the increase of the solution viscosity induced by inclusion of BN in the electrospinning solution [6]. This increase reveals the successful incorporation of BN in TiO_2 nanofibers.
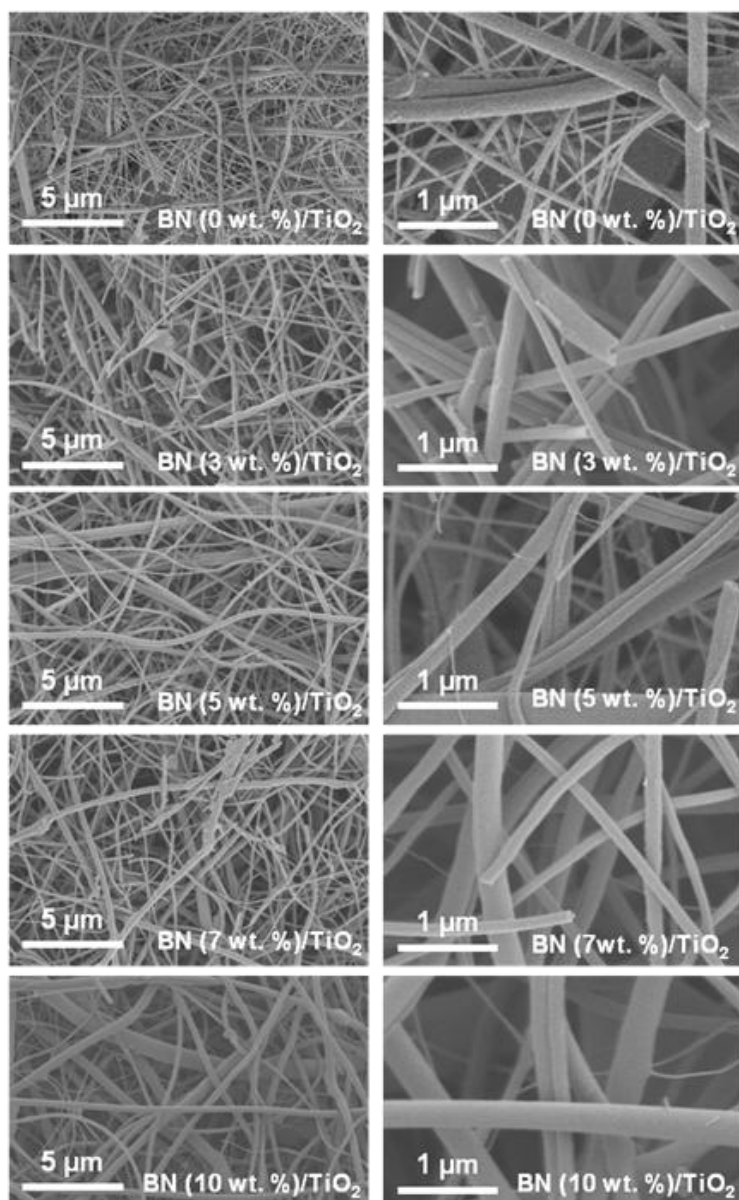
Figure 3.1. Scanning Electron Microscope images of TiO_2 and BN/TiO_2 annealed composite nanofibers in air for 4h at 500°C.

4.2. Structural properties

Table 3.1. EDX data showing the composition of TiO_2, BN (3 wt. %)/TiO_2, BN (5wt. %)/TiO_2, BN (7wt. %)/TiO_2 and BN (10 wt. %)/TiO_2 annealed nanofibers under air.

	Atomic percentages				
Samples	**Ti**	**O**	**C**	**B**	**N**
TiO₂	33.42	61.28	5.3	_	_
BN (3 wt. %)	26.59	53.67	4.16	8.4	7.18
BN (5 wt. %)	24.81	52.45	6.31	9.23	7.2

BN (7 wt. %)	23.84	48.25	5.48	10.59	11.84
BN (10 wt. %)	25.0 5	46.19	5.13	12.14	11.49

An energy dispersive X-ray spectrum (EDX) of BN/TiO$_2$ nanofibers recorded along with elemental analysis is presented in Table 3.1. The EDX analysis reveals the molar ratio of Ti and O to be 1:2 for the above described fibers, which is in good agreement with the stoichiometric ratio of TiO$_2$. Also, the BN doped fibers have a molar ratio of 1:1 for boron and nitrogen. The increase of the atomic percentages of B and N in BN (3 wt. %) /TiO$_2$, BN (5wt. %)/TiO$_2$, BN (7wt. %)/TiO$_2$ and BN (7wt. %)/TiO$_2$ can be clearly seen from table 3.1. Figure 3.2 shows elemental mapping images on BN (5wt. %)/TiO$_2$ nanofibers. These images clearly shows that Ti, O, B and N elements evenly spread over the entire area of the sample confirming the good dispersion of BN nanosheets in the TiO$_2$ nanofibers. Based on these data, the BN/TiO$_2$ composite nanofibers were successfully fabricated using the electrospinning method.
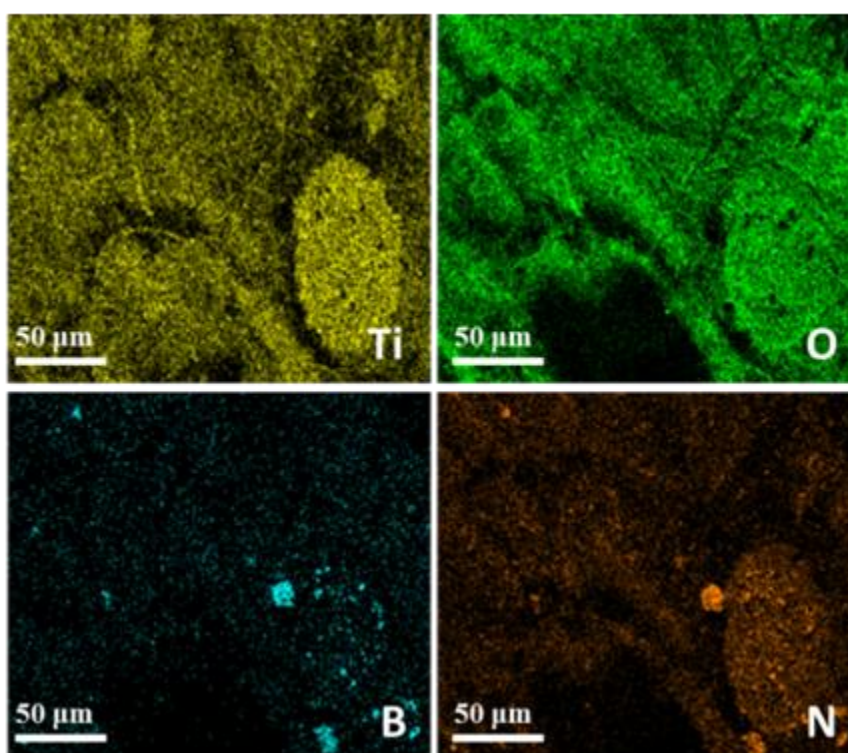
Figure 3.2. Element mapping images of the BN (5 wt.%)/TiO2 composite nanofibers.

Table 3.2 presents the specific surface area (BET) of prepared BN/TiO$_2$ nanocomposites. The specific surface area varies between 19 and 50 m^{2}g^{-1}. The increasing of the surface area with the increasing of BN sheets amount is clearly seen from Table 3.2. It is commonly accepted that TiO$_2$ with a large surface area will have superior photocatalyst activity, because a larger surface area offers more active adsorption sites [7].

Table 3.2. BET surface area of TiO$_2$ nanofibers and BN/TiO$_2$ composite nanofibers.

Samples	Surface area (m^{2}g^{-1})
TiO$_2$ NFs	19.66
BN (3wt. %)/TiO$_2$	31.75
BN (5wt. %)/TiO$_2$	34.41
BN (7wt. %)/TiO$_2$	48.31
BN (10 wt. %)/TiO$_2$	49.64

X-ray diffraction (XRD) was employed for analyzing the crystalline phase of all the obtained nanofibers. The sharp peaks in the diffraction pattern of all samples (Figure 3.3.A) can be assigned to the (101), (004), (200), (105), (211) and (204) crystal plane of pure anatase phase of TiO$_2$ which correspond to 2θ = 25.5°, 38.2°, 48.2°, 54.1°, 55.3° and 62.9°, respectively[8]. It is worth noting that the diffraction peak at 2θ = 26° of hexagonal BN related to the (002) direction is probably overlapped by the diffraction peak of TiO$_2$ at the same position [9]. The crystallite average sizes of TiO$_2$ and BN/TiO$_2$ with different amounts of BN were estimated using the Scherrer equation [10]. The calculated results show that the grain fineness numbers of BN/TiO$_2$ fibers are increasing as compared to pure TiO$_2$ fibers. The crystallite sizes for all samples are shown in Table 3.3. As shown in Figure 3.3.B, the main TiO$_2$ peak was shifted from the initial position after BN doping in all samples. We may suppose that BN incorporation increases the lattice strain in the TiO$_2$ cell and it can shift atoms from the initial position and can reduce the formation of the self-trapped excitons

(STE) localized on the TiO_6 octahedral[11]. At the same time, it might cause vacancies formation. These results will be confirmed later by photoluminescence analysis.
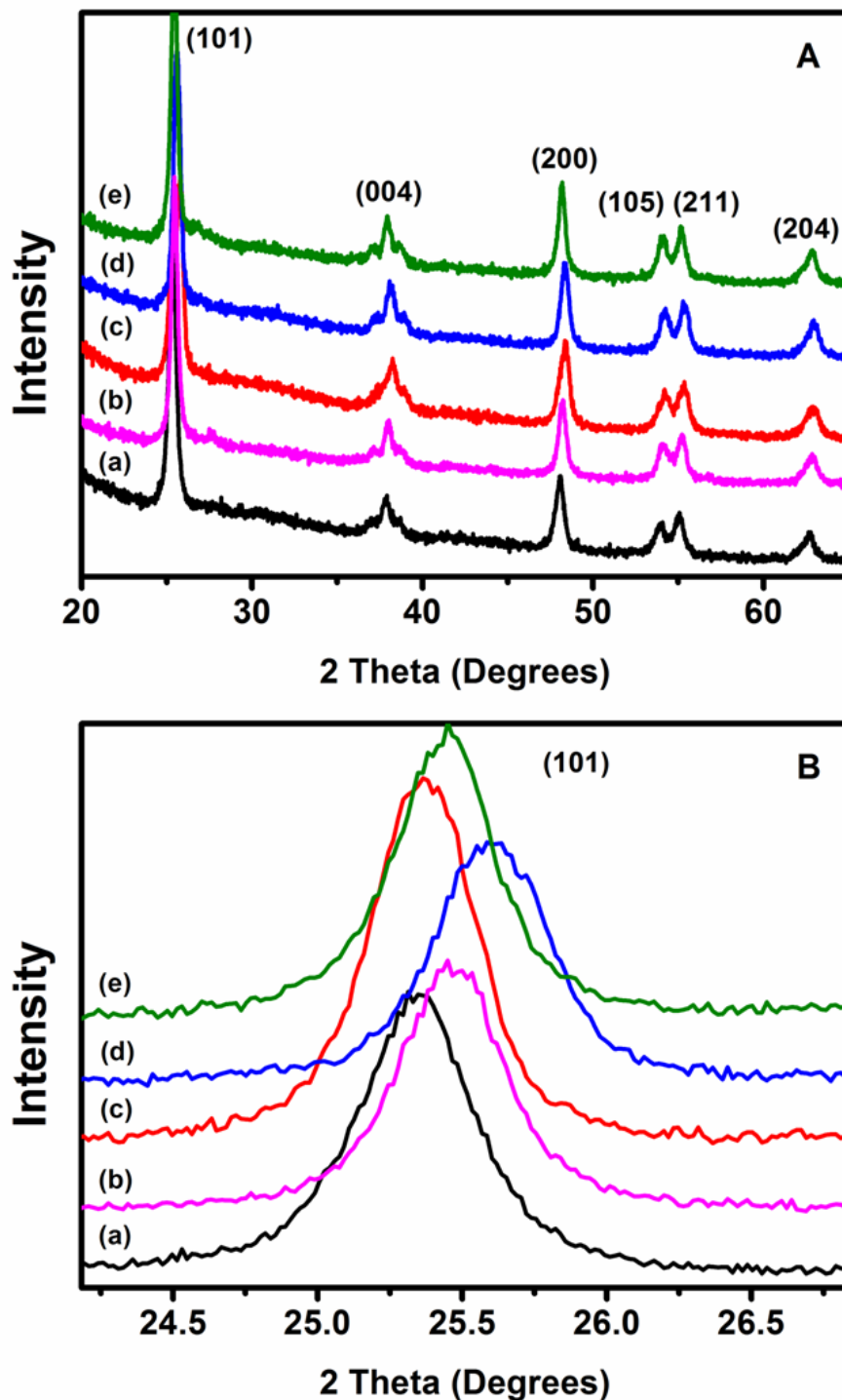
Figure 3.3. (A-B) XRD patterns of (a) TiO_2, (b) BN (3 wt. %) /TiO_2, (c) BN (5wt. %) /TiO_2, (d) BN (7wt. %) /TiO_2 and (e) BN (10wt. %) /TiO_2 annealed nanofibers in air for 4h at 500°C.

Table 3.3. Grain size of TiO_2 NFs and BN/TiO_2 composite nanofibers.

Samples	Grain size (nm)
TiO₂ NFs	16.4
BN (3wt. %)/TiO₂	24.3
BN (5wt. %)/TiO₂	25.2
BN (7wt. %)/TiO₂	26.3
BN (10wt. %)/TiO₂	28.7

Raman spectroscopy is a powerful tool to detect the molecular vibrations in order to identify our materials. As shown in Figure 3.4, the Raman spectrum of TiO_2, BN (3 wt. %)/TiO_2, BN (5wt. %)/TiO_2, BN (7wt. %)/TiO_2 and BN (10wt. %)/TiO_2 was recorded in the range of 100-1500 cm^{-1}. For all samples, we identify the six Raman active modes corresponding to the anatase phase of TiO_2 at 144 cm^{-1} (E_g), 197 cm_{-1} (E_g), 399 cm^{-1} (B_{1g}), 513 cm^{-1} (A_{1g}), 519 cm^{-1} (B_{1g}) and 639 cm^{-1} (E_g) (Figure 3.4.A) [12]. Besides, the Raman spectra of BN/TiO_2 samples shows the broadened characteristic frequency located at ~ 1365 cm^{-1} referring to the hexagonal BN related to E_{2g} mode (Figure 3.4.B) [13]. In addition, the increased intensity of the peak corresponding to h-BN with the amount of doping is visibly noticed. Thus, Raman spectroscopy confirmed the incorporation of the boron nitride in the TiO_2 nanofibers.
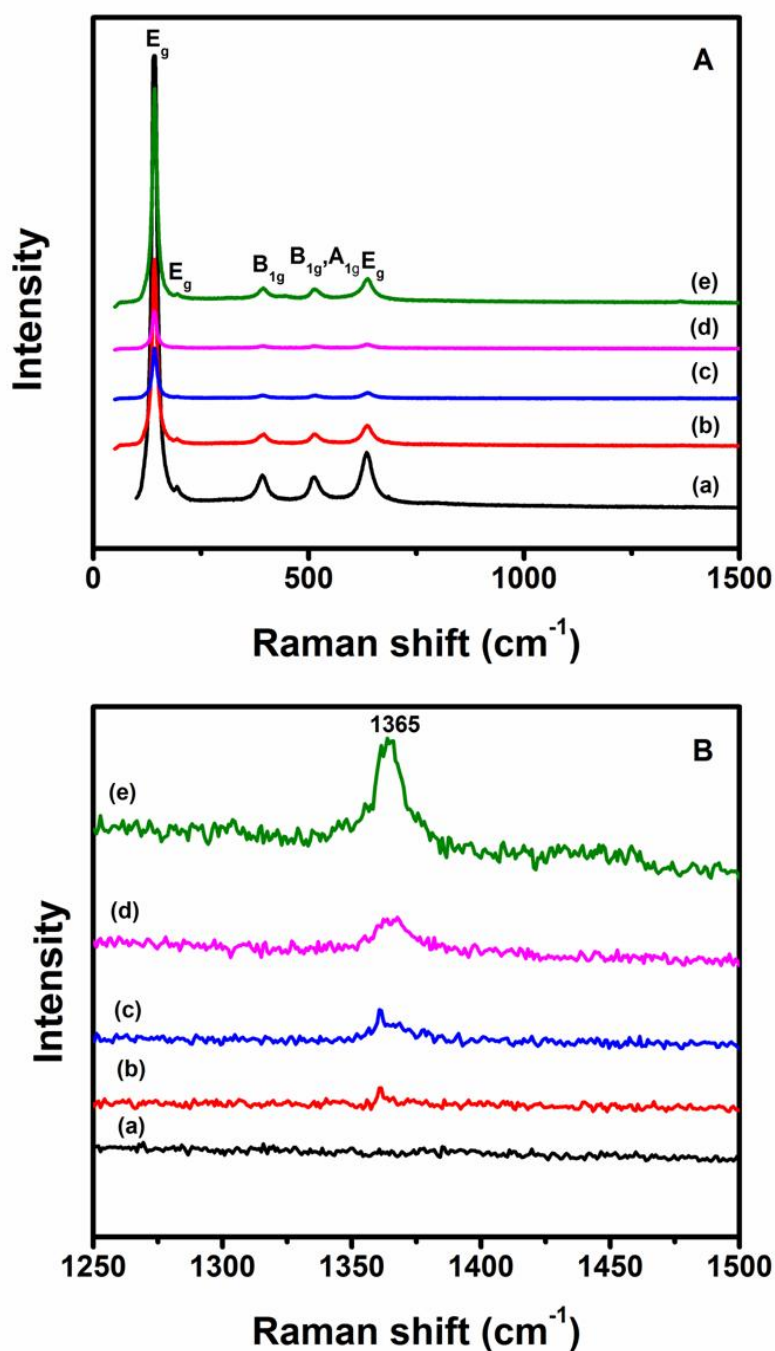
Figure 3.4. (A-B) Raman shift of (a) TiO_2, (b) BN (3 wt. %)/TiO_2, (c) BN (5wt. %)/TiO_2, (d) BN (7wt. %)/TiO_2 and (e) BN (10wt. %)/TiO_2 annealed nanofibers in air for 4h at 500°C.

4.3. Optical properties

The successful incorporation of boron nitride sheets in the TiO_2 nanofibers was revealed by the typical FTIR spectrum (Figure 3.5). For pure TiO_2 nanofibers (Figure

3.5.a), the characteristic absorption band at 650–950 cm^{-1} is attributed to Ti–O bond [14]. While for the composite BN/TiO$_2$ nanofibers with different amounts of BN sheets (Figure 3.5.b-e), two main absorption peaks of hexagonal BN were observed around 800 and 1370 cm^{-1}, ascribed to the out-of-plane bending of sp^2-bonded B-N-B and the in-plane stretching of sp^2-bonded B-N, respectively[15]. In addition, it can be clearly seen, that the intensity of these 2 peaks related to the bands B-N-B and B-N increases by increasing the BN amounts.
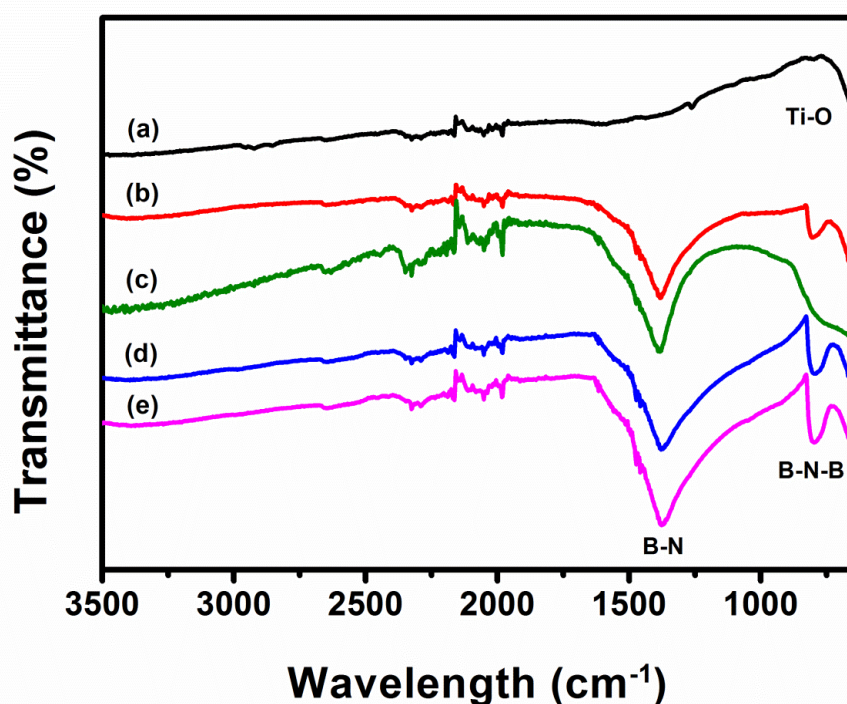
Figure 3.5. FTIR spectra of (a) TiO$_2$, (b) BN (3 wt. %)/TiO$_2$, (c) BN (5wt. %)/TiO$_2$, (d) BN (7wt. %)/TiO$_2$ and (e) BN (10wt. %)/TiO$_2$ annealed nanofibers in air for 4h at 500°C.

Figure 3.6 shows the UV–VIS absorption spectra of TiO$_2$ nanofibers and BN/TiO$_2$ composite nanofibers with different BN amounts. The energy of the band gap was calculated using the following equation:

$$E_g = hc/\lambda \qquad \text{(Equation 2)}$$

Where h is Planck's constant, c is the speed of light and λ is the cut off wavelength where the absorbance value is minimum. The UV–VIS absorption spectrum of the pure TiO_2 nanofibers, BN (3 wt. %) /TiO_2, BN (5wt. %) /TiO_2, BN (7wt. %) /TiO_2 and BN (10wt. %) /TiO_2 composite nanofibers indicates that it absorbs light at 380, 348, 345, 344 and 342 nm corresponding to a band gap of 3.2, 3.56, 3.59, 3.6 and 3.62 eV, respectively. Compared to the pure TiO_2 nanofibers, the absorption edges of BN/TiO_2 composite nanofibers are blue shifted. These facts suggest that introducing BN sheets may increase the photocatalytic activity of TiO_2 nanofibers under UV light.
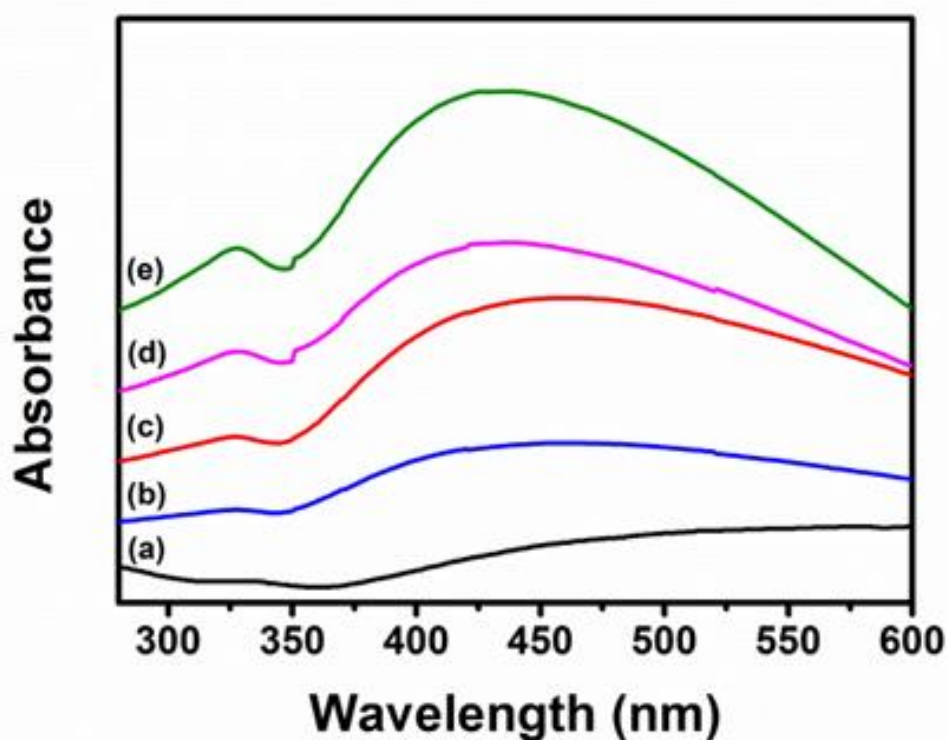
Figure 3.6. UV-VIS absorption spectra of (a) TiO_2, (b) BN (3 wt. %)/TiO_2, (c) BN (5wt. %)/TiO_2, (d) BN (7wt. %)/TiO_2 and (e) BN (10wt. %)/TiO_2 annealed nanofibers in air for 4h at 500°C.

PL spectra of TiO_2 nanofibers are shown in Figure 3.7. The significant increase of the PL intensity was observed for BN (5wt. %)/TiO_2, BN (7wt. %)/TiO_2 and BN (10wt. %)/TiO_2 samples. The PL spectrum of sample BN (3 wt. %)/TiO_2 is approximately equal to the initial TiO_2 PL spectrum. The PL spectra have been deconvoluted to individual peaks with Gaussian fitting using Origin software (Figure 3.8). We can distinguish 3 groups of peaks, centred at 415-430 nm, 544-571 nm and 688-731 nm. In our previous works, we have reported on the

detailed analysis of the PL spectra of TiO_2 based nanostructures [11], [16]. The observed peak at 415-430 nm corresponds to the self-trapped excitons (STE) localized on the TiO_6 octahedral [16],[17]. The peaks in the range of 544-571 nm correspond to oxygen vacancies, localized on the surface, and can also be considered as recombination of free electrons with trapped holes. Peaks at 688-731 nm correspond to structural defects (Ti^{3+}, Ti^{3+} interstitials, under coordinated Ti atoms) and can be related to the recombination of free holes with trapped electrons [11],[17]. It is worth saying that no peaks related to rutile phase (800-815 nm) were found.

The PL of TiO_2-BN nanostructures have not been reported before. Therefore, the analysis of the PL properties will be based on other photo-induced properties of TiO_2-BN nanostructures. M. Shanmugam *et al.* reported on BN induced passivation of the surface states on TiO_2 when BN-TiO_2 heterojunctions are formed for solar cell applications. It was discussed that BN passivates dangling bonds on the TiO_2 surface and improves the photocatalytic activity of TiO_2 nanostructures [18],[19]. The improved photocatalytic activity is based on the charge separation at the TiO_2/BN interface and the flow of holes to the BN upper layer. Thus, it is expected to get lower electron-hole recombination rate in BN doped TiO_2 nanostructures. On the basis of the above mentioned BN-TiO_2 interaction the PL intensity in the BN doped TiO_2 nanostructures should decrease [20],[7]. However, in our case, the enhancement of the TiO_2 nanofibers PL was observed when increasing of the doping level of BN.
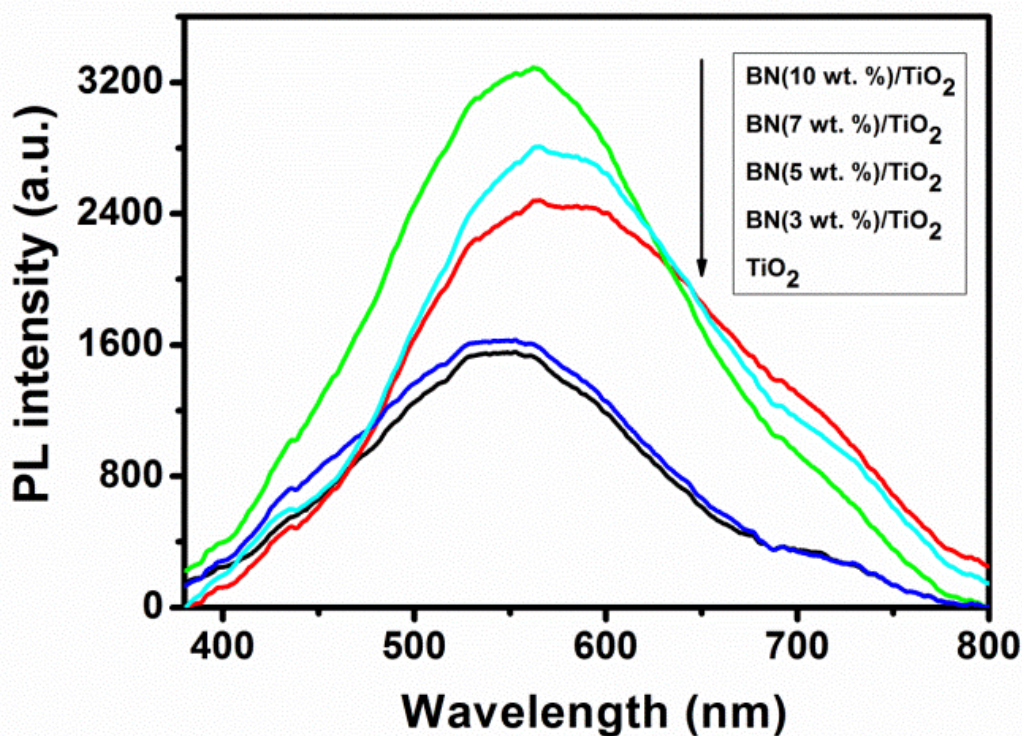
Figure3.7. Photoluminescence of TiO_2 and BN/TiO_2 NFs annealed in air at 500°C.

The mechanism of BN doping can be explained from comparison of the deconvoluted TiO_2 PL peaks (Figure 3.8). Table 3.4 shows that the normalized integrated STE peak intensity (I1) decreased with the BN doping ratio. From XRD analysis, it was found that additional lattice strain appeared in the TiO_2 lattice after BN doping. The induced strain reduces the formation of the self-trapped excitons (STE) localized on the TiO_6 octahedral and therefore quenches STE emission. The emission related to surface defects (I3) has a tendency to decrease because of the BN passivation of the dangling bonds, related to the unsaturated surface atoms and the photo-generated holes migration to BN [18],[20]. We also suppose that BN induced lattice strain in the TiO_2 lattice might cause oxygen vacancies formation. Therefore, the increase of absolute PL value of peaks, related to oxygen vacancies was observed as BN can passivate the surface state of non-radiative recombination and enhance the PL intensity of the whole spectrum. We also assume that due to charge separation on BN-TiO_2 interface, the observed PL emission is due to bulk emission centers rather than surface centers. Thus, the observed results show good

correlation between optical and structural properties of BN-TiO$_2$ nanofibers. The quantum yield of the samples was calculated as following:

$$QY = N_{em}/N_{abs} \qquad \text{(Equation 3)}$$

Where N$_{abs}$ and N$_{em}$ are numbers of absorbed and emitted photons. Taking into account that all photons are absorbed by TiO$_2$ at wavelength of 266 nm, no correlation coefficients for N$_{abs}$ were used. The N$_{abs}$ and N$_{em}$ were calculated on the basis of the obtained experimental values, such as laser power, repetition frequency, sensitivity of fiber optic spectrometer per integration time and the measured signal. The obtained values are shown in the Table 3.5. Typical QY of TiO$_2$ nanostructures is in the range of 0.001-0.2, as reported by Li et al. [21]. According to the data, obtained in the present work, the QY of TiO$_2$ nanofibers is one order lower than in other sources. It points to high ratio of charge splitting and non-radiative transitions through surface states [22] what is significantly good for photocatalytic applications.
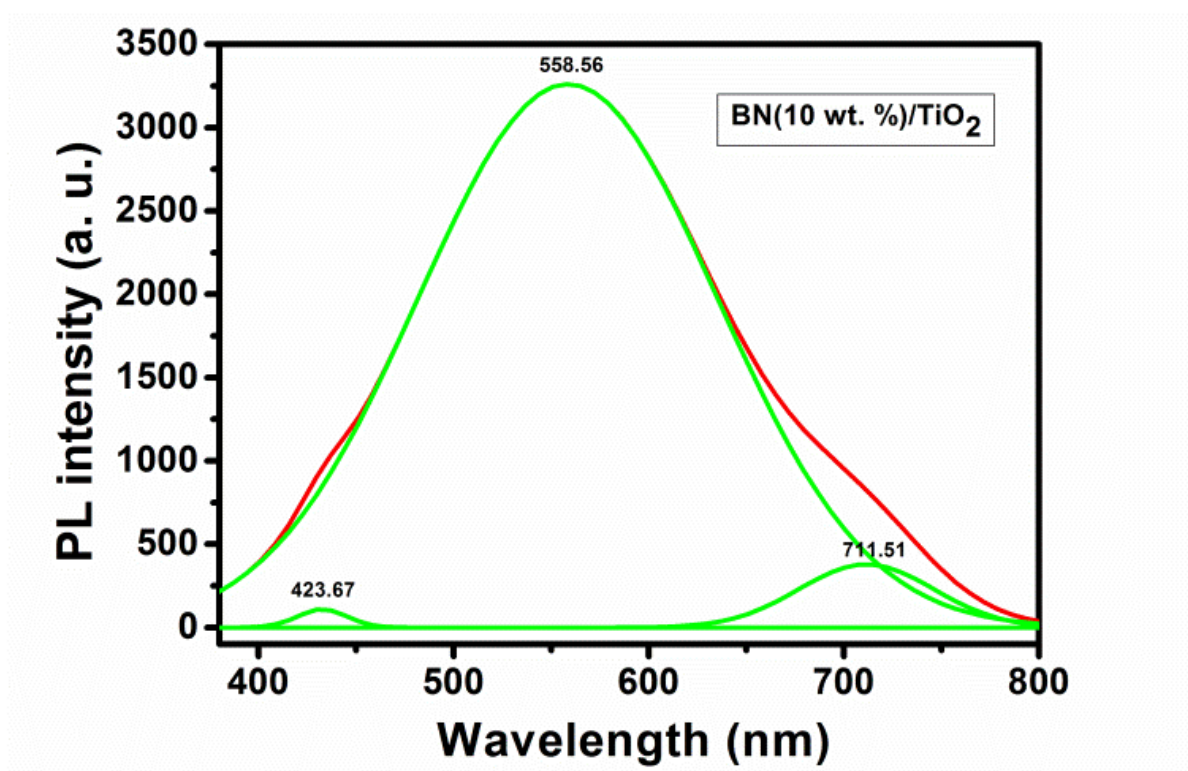
Figure 3.8. One example of a deconvoluted PL spectrum of BN/TiO$_2$ NFs annealed in air at 500°C.

Table 3.4. Normalized integrated intensity of the TiO_2 PL peaks.

Doping level	I1	I2	I3
BN (0wt. %)/ TiO_2	0.01481	1	0.05784
BN (3wt. %)/ TiO_2	0.01898	1	0.04002
BN (5wt. %)/ TiO_2	0.00841	1	0.835766
BN (7wt. %)/ TiO_2	0.01279	1	0.15328
BN (10wt. %)/ TiO_2	0.00558	1	0.05248

Table 3.5. Quantum yield of the pure TiO_2 and BN/TiO_2 composite nanofibers.

	TiO_2	BN (3wt. %)/TiO_2	BN (5wt. %)/TiO_2	BN (7wt. %)/TiO_2	BN (10wt. %)/TiO_2
QY($x10^{-6}$)	128	137	210	227	246
Error ($x10^{-5}$)	3.24	3.48	5.34	5.76	6.25
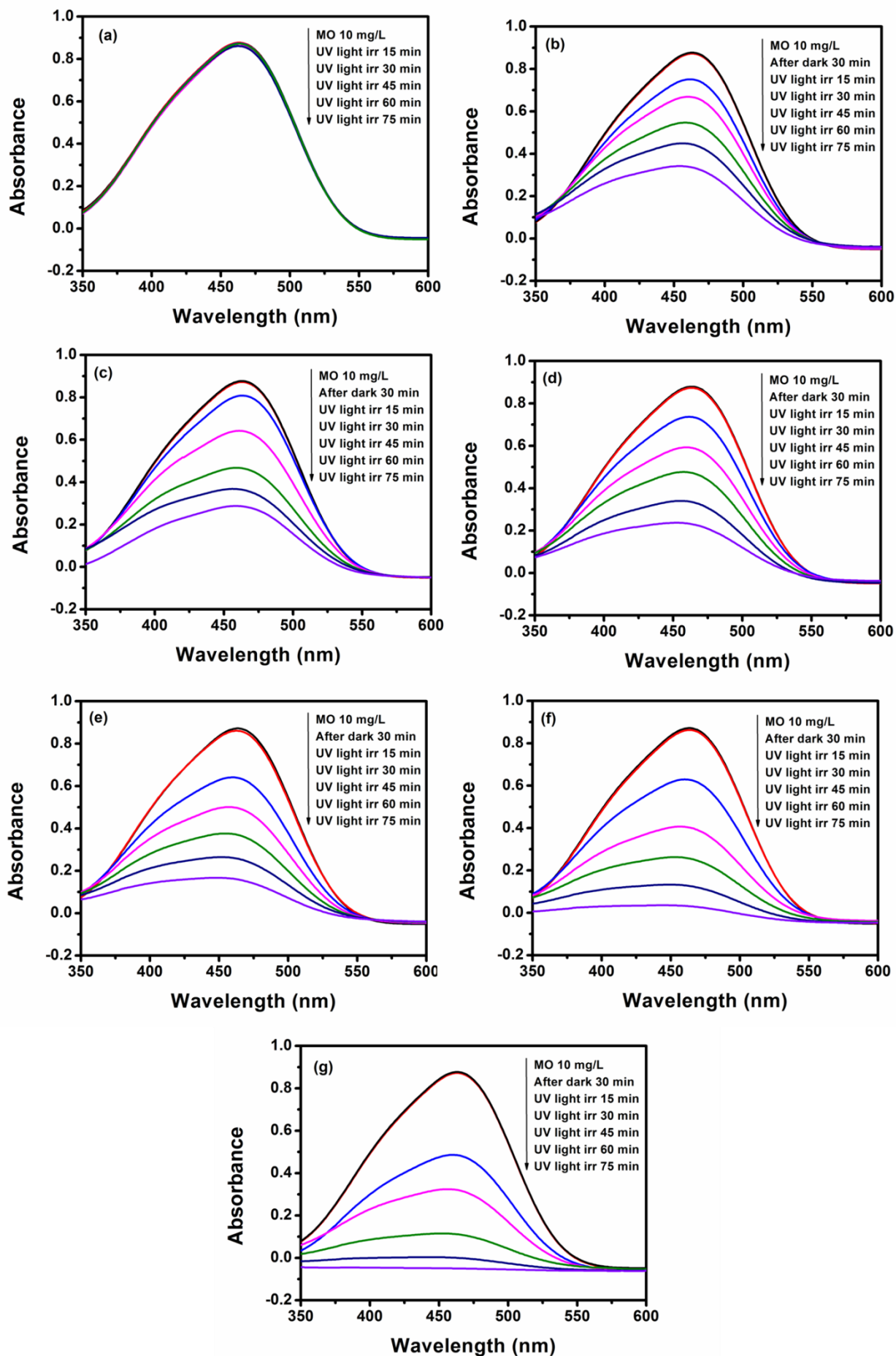
Figure 3.9. UV-Vis spectra of the photocatalytic degradation of MO under UV light: (a) MO without catalyst, (b) P 25, (c) TiO$_2$ nanofibers, (d) BN (3wt. %)/TiO$_2$, (e) BN (5wt. %)/TiO$_2$, (f) BN (7wt. %)/TiO$_2$ and (G) BN (10wt. %)/TiO$_2$ composite nanofibers.

5. Photocatalytic activity

The photocatalytic activities of BN/TiO$_2$ with different BN amounts were evaluated by degradation of methyl orange (MO) under UV light (wavelength < 400 nm). MO was selected as a model organic pollutant. Figure 3.9 (a-g) shows the UV-Vis absorbance spectra of MO solution (major absorption band around 462 nm) with different time intervals 0, 15, 30, 45, 60 and 75 min after 30 min storage in dark for excluding the interference of adsorption. For comparison, the photocatalytic activities of TiO$_2$ nanofibers and commercial TiO$_2$-P25 were also tested under identical experimental conditions. The results indicate that methyl orange is stable and difficult to be photodegraded in the absence of photocatalyst. After irradiation for 75 min, MO was degraded up to 65% in the presence of TiO$_2$ nanofibers, compared to 60% degradation by commercial granular TiO$_2$-P25 (Figure 3.10). Therefore, in case of pure TiO$_2$, it is well known that TiO$_2$ nanofibers have a larger active surface area compared to the commercial TiO$_2$-P25 nanoparticles which increases its photocatlytic activity [8]. As shown in Figure 3.10, MO was degraded up to 73%, 80%, 93% and 99% in the presence of BN (3wt. %)/TiO$_2$, BN (5wt. %)/TiO$_2$, BN (7wt. %)/TiO$_2$, BN (10wt. %)/TiO$_2$, respectively. It is well known that the photocatalytic activity is mainly governed by crystalline phase, specific surface area, light absorption capacity and separation efficiency of electron–hole pairs. Therefore, in BN/TiO$_2$ samples, owing to the pronounced electrostatic interactions, the surface naturally negative charged of boron nitride sheets could lead to the transfer of h$^+$ from the activated TiO$_2$ to the BN sheets when they are connected. Thus, more photo electrons were available compared to pure TiO$_2$ nanofibers, to take part in the photodegradation process [7],[23]. Thus, the recombination of e$^-$ and h$^+$ is inhibited as confirmed previously by photoluminescence. However, considering the specific surface area results of BN/TiO$_2$ nanofibers presented above, a large increase has been achieved compared to the pure TiO$_2$ nanofibers. From the XRD analysis, the crystallite average size of TiO$_2$ is increasing after introducing BN sheets. As confirmed by UV-VIS, compared to the pure TiO$_2$ nanofibers, the absorption edges of BN/TiO$_2$ composite nanofibers are blue shifted. From the obtained results, it is evident that BN sheets improve the separation

efficiency of e$^-$ and h$^+$ and therefore enhance the photocatalytic activity of TiO$_2$ under UV light.
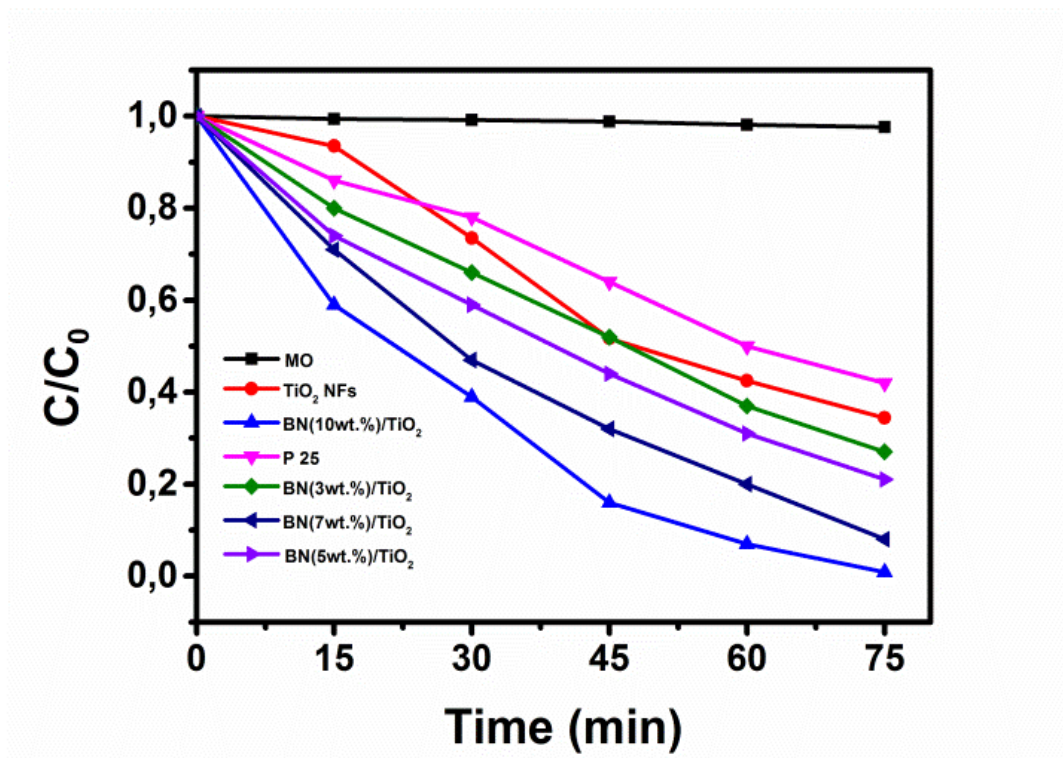
Figure 3.10. Photodegradation of MO by P25, TiO$_2$ nanofibers and BN/TiO$_2$ composite nanofibers.

Figure 3.11 shows the different kinetic linear curves. The photodegradation reactions follow a Langmuir–Hinshelwood first-order kinetics model [24]. The explanation is described as follows:

$$r= dC/dt = kKC/(1+KC) \qquad \text{(Equation 4)}$$

Where r is the degradation rate of methyl orange (MO) (mg (L min)$^{-1}$), C is the concentration of the MO solution (mg L^{-1}), t is the irradiation time, k is the reaction rate constant (mg (L min)$^{-1}$), and K is the adsorption coefficient of MO (mg L^{-1}). Since the initial concentrations (C$_0$ = 10 mg L^{-1}) of the MO solutions are very low in the present experiments, the relationship between ln(C$_0$/C) and the reaction time t shows that the decomposition of MO with different photocatalysts accords with a pseudo first order kinetic[24]:

$$\ln (C_0/C) = kKt = k_a t \qquad \text{(Equation 5)}$$

Where k_a is the apparent first-order rate constant (min^{-1}) and C is the concentration at time t. k_a is obtained from the linear dependence between ln (C_0/C) and time are reported in Table 3.6. The increasing order of the rate constants in the samples is: BN (10wt. %)/TiO_2 > BN (7wt. %)/TiO_2 > BN (5wt. %)/TiO_2 > BN (3wt. %)/TiO_2 > TiO_2 NFs > P25. The rate constant exhibits a maximum of 0.0586 min^{-1} for BN (10wt. %)/TiO_2, which is 5 and 3.8 times higher than that of P25 and TiO_2 nanofibers, respectively. In addition, all BN/TiO_2 composite nanofibers show higher photocatalytic activity than that of P25 and TiO_2 nanofibers under UV light, which is represented by larger value of k_a. Even though, in the case of BN (10wt. %), the curve of [ln (C_0/C) vs time] is not completely linear, it is still considered as approximately following the Langmuir–Hinshelwood model. This behavior is possibly due to the presence of a higher concentration of BN. When the rate of the reaction is increased with additional BN sheets, the adsorption-desorption equilibrium will be slightly disturbed and the Langmuir behavior is therefore shifting from a perfect linear first order. In our case, the disturbance is relatively small and the [ln (C_0/C) vs time] curve is still giving an acceptable value of k_a. From obtained results it is evident that the fact of introducing BN sheets improves separation of photo-induced electron-hole pairs of TiO_2 and significantly increases its photocatalytic activity under UV.

Table 3.6. Kinetic parameters for photocatalytic activities of the pure TiO_2 nanofibers and BN/TiO_2 composite nanofibers.

	k_a (min^{-1})	R^2
MO	0.00031	0.9743
P25	0.0117	0.9791
TiO_2 NFs	0.0153	0.9706
BN (3wt. %)/TiO_2	0.0173	0.9842
BN (5wt. %)/TiO_2	0.0203	0.9900
BN (7wt. %)/TiO_2	0.0319	0.9541
BN (10wt. %)/TiO_2	0.0586	0.8979
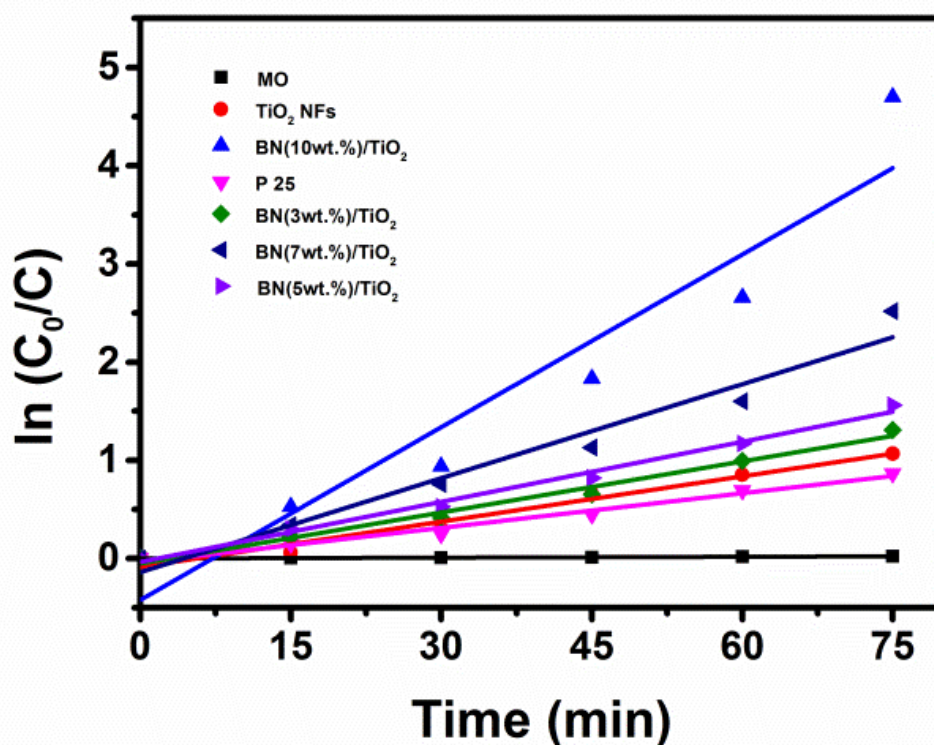
Figure 3.11. Kinetics of Methyl orange degradation by P25, TiO_2 nanofibers and BN/TiO_2 composite nanofibers.

6. Conclusion

In summary, pure TiO_2 nanofibers and BN/TiO_2 composite nanofibers with different BN nanosheets amounts were successfully prepared by electrospinning. All the samples were annealed at 500°C in air for 4 hours. The SEM images showed an increase in the average diameter with the increase of BN amount and confirmed that the one dimensional morphology was maintained. EDX, Raman and FTIR revealed the successful incorporation of the boron nitride in the TiO_2 nanofibers. The specific surface area measurements (BET) confirmed the increasing of the surface area with the increasing of BN sheets amount. A boost of the grain size from 16.4 to 28.7 nm had been recorded for the composite BN (10wt. %)/TiO_2 compared to the pure TiO_2 nanofibers. The increasing of TiO_2 nanofibers band gap energy from 3.2 eV to 3.62 eV due to the presence of BN sheets was confirmed by UV-VIS analysis. XRD and photoluminescence spectra confirmed that BN incorporation increases the lattice strain in the TiO_2 cell and reduce the formation of the self-trapped excitons. Owing to

the electrostatic interaction, BN sheets can promote the immigration of h^+ from the bulk of TiO_2 to its surface and consequently improve the photocatalytic activity of TiO_2 under UV light due to efficient charge separation and reduction of charges carriers' recombination. The photocatlytic degradation of methyl orange under UV light was 5 and 3.8 times higher than that of commercial TiO_2-P25 and TiO_2 nanofibers, respectively. In conclusion, the mixing of TiO_2-based photocatalysts with BN sheets is a challenge worth investigating to enhance efficiency in a simple and economically beneficial manner and could be used as catalysts in the degradation of different molecules for photocatalytic application.

REFERENCES

1. Biscarat, J., et al., Graphene-like BN/gelatin nanobiocomposites for gas barrier applications. Nanoscale, 2015. **7**(2): p. 613-618.
2. Thangaraj, V., et al., Fluorescence Quenching of Sulforhodamine Dye over Graphene Oxide and Boron Nitride Nanosheets. European Journal of Inorganic Chemistry, 2016.
3. Dhakal, T.P., et al., Moisture-induced surface corrosion in AZO thin films formed by atomic layer deposition. Device and Materials Reliability, IEEE Transactions on, 2012. **12**(2): p. 347-356.
4. Chuangchote, S., et al., Photocatalytic activity for hydrogen evolution of electrospun TiO2 nanofibers. ACS applied materials & interfaces, 2009. **1**(5): p. 1140-1143.
5. Du, P., et al., Photocatalytic degradation of Rhodamine B using electrospun TiO2 and ZnO nanofibers: a comparative study. Journal of Materials Science, 2013. **48**(24): p. 8386-8392.
6. Nalbandian, M.J., et al., Synthesis and optimization of Ag–TiO 2 composite nanofibers for photocatalytic treatment of impaired water sources. Journal of hazardous materials, 2015. **299**: p. 141-148.
7. Štengl, V., J. Henych, and M. Slušná, h-BN-TiO 2 nanocomposite for photocatalytic applications. Journal of Nanomaterials, 2016. **2016**: p. 22.
8. Doh, S.J., et al., Development of photocatalytic TiO 2 nanofibers by electrospinning and its application to degradation of dye pollutants. Journal of Hazardous Materials, 2008. **154**(1): p. 118-127.
9. Qiu, Y., et al., Synthesis of continuous boron nitride nanofibers by solution coating electrospun template fibers. Nanotechnology, 2009. **20**(34): p. 345603.
10. Holzwarth, U. and N. Gibson, The Scherrer equation versus the'Debye-Scherrer equation'. Nature Nanotechnology, 2011. **6**(9): p. 534-534.
11. Nasr, M., et al., Photoluminescence: A very sensitive tool to detect the presence of anatase in rutile phase electrospun TiO 2 nanofibers. Superlattices and Microstructures, 2015. **77**: p. 18-24.
12. Wang, J., et al., A high efficient photocatalyst Ag 3 VO 4/TiO 2/graphene nanocomposite with wide spectral response. Applied Catalysis B: Environmental, 2013. **136**: p. 94-102.
13. Gorbachev, R.V., et al., Hunting for monolayer boron nitride: optical and Raman signatures. Small, 2011. **7**(4): p. 465-468.
14. Thirugnanam, L., et al., Porous Tubular Rutile TiO2 Nanofibers: Synthesis, Characterization and Photocatalytic Properties. Journal of nanoscience and nanotechnology, 2014. **14**(4): p. 3034-3040.
15. Shi, Y., et al., Synthesis of few-layer hexagonal boron nitride thin film by chemical vapor deposition. Nano letters, 2010. **10**(10): p. 4134-4139.
16. Iatsunskyi, I., et al., Tailoring the structural, optical, and photoluminescence properties of porous silicon/TiO2 nanostructures. The Journal of Physical Chemistry C, 2015. **119**(13): p. 7164-7171.
17. Iatsunskyi, I., et al., Study on Structural, Mechanical, and Optical Properties of Al2O3–TiO2 Nanolaminates Prepared by Atomic Layer Deposition. The Journal of Physical Chemistry C, 2015. **119**(35): p. 20591-20599.
18. Shanmugam, M., et al., 2D layered insulator hexagonal boron nitride enabled surface passivation in dye sensitized solar cells. Nanoscale, 2013. **5**(22): p. 11275-11282.

19. Shanmugam, M., et al., Layered insulator hexagonal boron nitride for surface passivation in quantum dot solar cell. Applied Physics Letters, 2013. **103**(24): p. 243904.

20. Si, H., et al., Synthesis of Few-Atomic-Layer BN Hollow Nanospheres and Their Applications as Nanocontainers and Catalyst Support Materials. ACS applied materials & interfaces, 2016.

21. Li, Y., et al., High photoluminescence quantum yield of TiO2 nanocrystals prepared using an alcohothermal method. Luminescence, 2007. **22**(6): p. 540-545.

22. Liqiang, J., et al., Review of photoluminescence performance of nano-sized semiconductor materials and its relationships with photocatalytic activity. Solar Energy Materials and Solar Cells, 2006. **90**(12): p. 1773-1787.

23. Fu, X., et al., Ball milled h-BN: an efficient holes transfer promoter to enhance the photocatalytic performance of TiO 2. Journal of hazardous materials, 2013. **244**: p. 102-110.

24. Konstantinou, I.K. and T.A. Albanis, TiO 2-assisted photocatalytic degradation of azo dyes in aqueous solution: kinetic and mechanistic investigations: a review. Applied Catalysis B: Environmental, 2004. **49**(1): p. 1-14.

Chapter 4: High Photocatalytic and Antibacterial Activity of BN-Ag/TiO$_2$ Composite Nanofibers Under Visible Light

Table of Contents

1. Abstract

To develop material with good photocatalytic properties for organic compound degradation and bacterial removal, we produced Ag/TiO_2 and $BN-Ag/TiO_2$ composite nanofibers that included controlled amounts of boron nitride (BN) nanosheets and silver (Ag). After annealing at 500°C under air, we used scanning electron microscopy, Brunauer-Emmet-Teller analysis, X-ray diffraction, energy-dispersive X-ray spectroscopy, Raman spectroscopy, UV-visible reflectance spectroscopy and room temperature photoluminescence to investigate the morphological, structural and optical properties of all samples. The photocatalytic tests using methylene blue under visible light, in repeated and long-term applications, showed that the photodegradation activity of BN(5 wt%)-Ag(3 wt%)/TiO_2 composite nanofibers was 17.2 and 2.3 times higher than that of pure TiO_2 and Ag(3 wt%)/TiO_2 nanofibers, respectively. In antibacterial tests using Gram-negative *Escherichia coli*, 3 hours of incubation with BN(5 wt%)-Ag(3 wt%)/TiO_2 composite nanofibers killed all bacteria. These results indicate that the synthesized BN(5 wt%)-Ag(3 wt%)/TiO_2 composite nanofibers can be considered to be multifunctional material for photodegradation and antibacterial applications.

2. Introduction

This chapter was devoted to develop an effective material having photocatalytic properties for both organic compound degradation and bacterial removal. Toxic industrial chemical waste is still not properly treated and may directly pollute drinking water.[1] Therefore, it is urgent to develop effective and economic approaches to remove water contaminants, such as organic pollutants and heavy metal ions.[2] Various methods can be employed to remove biological and chemical pollutants from wastewater, such as photocatalysis, adsorption, filtration and sedimentation.[3, 4] We will report on the elaboration of Ag/TiO_2 and $BN-Ag/TiO_2$ composite nanofibers with controlled amounts of boron nitride (BN) nanosheets and silver (Ag). BN and Ag played an important role in the photodegradation process by reducing the recombination rate of electron/hole pairs. The second role of Ag was to shift the absorbance edge of TiO_2 to the visible region, thus reduce the band gap of TiO_2. For environmental applications, the long-term stability of the

photocatalytic materials is also a key property. Therefore, the photodegradation repeatability experiments of methylen blue were carried out for four cycles.

3. Experimental Section

3.1. Materials

Titanium tetraisopropoxide (TTIP) (Ti[OCH(CH$_3$)$_2$]$_4$) (97%), polyvinylpyrrolidone (PVP) (Mw = 13,00,000), acetic acid (98%), absolute ethanol (99%), silver nitrate (AgNO$_3$; 99%), MB, sodium chloride (NaCl, 99%) and gelatin from porcine skin were purchased from Sigma Aldrich. BN nanosheets were obtained from commercial BN (Combat powders, Saint Gobain, 95%, 325 mesh). The *E. coli* (K12 DSM 423) strain was from DSMZ, Germany. Lysogeny broth (LB)-Miller culture medium (ref. n°1214662) was purchased from Fischer Scientific. Ultra-pure water was produced by using the MilliQ system (Millipore). All chemicals were used without any further purification.

3.2. Boron nitride exfoliation

BN nanosheets were obtained by exfoliation of commercial BN powder with gelatin from porcine skin [5]. Briefly, 20g of gelatin was dissolved in 80 ml of hot water (75°C). Then, 1g of BN powder was added to the mixture and the solution was kept in an ultrasonic homogenizer at 50°C overnight. After centrifugation at 6000 rpm for 30 minutes, precipitates (containing exfoliated BN) were dried at 80°C for 48 hours and then calcined in a muffle furnace at 600°C in air for 2 hours to obtain pure exfoliated BN.

3.3. Preparation of Ag-TiO$_2$ and BN-Ag/TiO$_2$ composite nanofibers

Ag/TiO$_2$ and BN-Ag/TiO$_2$ composite nanofibers were prepared using the electrospinning technique. The Ag and BN content levels were calculated based on TiO$_2$ weight percentage (wt. %). The spun solution was prepared in three steps. First, different amounts of AgNO$_3$ (0.5, 1.5 and 3 wt. %) and 2 ml of acetic acid were sonicated for 12h to dissolve AgNO$_3$. Second, TTIP was dissolved in a mixture that contained 5 ml of ethanol and 0.3 g of PVP (precursor solution) and stirred at room temperature for 1h to obtain the viscosity required for electrospinning. Third, dissolved AgNO$_3$ was added to the precursor solution with vigorous magnetic stirring (150 rpm) for 30 min (Ag/TiO$_2$ solution). A similar Ag/TiO$_2$ solution but with a fixed Ag content (3 wt. %) was used to prepare BN-Ag/TiO$_2$

composite nanofibers with specific amounts of exfoliated BN (3 and 5 wt. %). The Ag/TiO_2 or BN-Ag/TiO_2 solution was transferred into a syringe with a stainless steel needle, a diameter of 0.7 mm at a constant flow rate of 1 ml/h. The feeding rate was controlled by the syringe pump. The temperature level inside the electrospinning chamber was 38 ± 5°C. A high voltage power supply was used as source of electric field. Nanofibers were collected on a rotating coil covered with aluminum foil with a rotation speed of 400 rpm. Briefly, the solution was electrospun at a DC voltage of 25 KV and 20 cm working distance (the distance between the needle tip and the collector). As the solution progressed through the system (1 ml/h), it became electrified. The tip of the resulting Taylor cone expelled an electrified jet of fibers, forming a fibrous mesh on the grounded collector.[6] Electrospun Ag/TiO_2 and BN-Ag/TiO_2 composite nanofibers were then calcined in a muffle furnace at 500°C with a heating rate of 5°C/min for 4 hours in air for polymer removal and TiO_2 crystallization. In addition, the annealing process led to the thermal decomposition of $AgNO_3$ to Ag_2O and finally to Ag.[7] Table 4.1 lists the produced nanofibers tested in this study.

Table 4.1. TiO_2, Ag/TiO_2 and BN-Ag/TiO_2 samples prepared with different weight amounts of BN nanosheets and $AgNO_3$.

Sample name	Sample description	$AgNO_3$ content (%)	BN content (%)
TiO_2	TiO_2	-	-
Ag0.5/TiO_2	Ag(0.5 wt%)/TiO_2	0.5	-
Ag1.5/TiO_2	Ag(1.5 wt%)/TiO_2	1.5	-
Ag3/TiO_2	Ag(3 wt%)/TiO_2	3	-
BN3-Ag3/TiO_2	BN(3 wt%)-Ag(3 wt%)/TiO_2	1.5	3
BN5-Ag3/TiO_2	BN(5 wt%)-Ag(3 wt%)/TiO_2	1.5	5

3.4. Chemical and structural characterizations

X-ray diffraction (XRD) measurements were carried out using a PANAlytical Xpert-PRO diffractometer equipped with an X'celerator detector using Ni-filtered Cu-radiation (λ= 1.54 ˚A). Raman spectra were obtained using a Labram 1B instrument (Jobin-Yvon S.A., Horiba, France). Spectra were taken at room temperature using a 659 nm laser line as the excitation source. All Raman spectra were recorded in the range of 100-1500 cm^{-1}. Scanning electron microscopy (SEM) images were taken with a Hitachi S4800, Japan. The average diameter of 100 randomly chosen nanofibers for each sample was measured from SEM images using the Image J1.29X software. Energy-dispersive X-ray spectroscopy analysis (EDX) and elemental mapping were performed with a Zeiss EVO HD15 microscope coupled to an Oxford X-MaxN EDX detector. Optical properties were analyzed by diffuse reflectance (Shimadzu UV-3600). The UV–visible (UV-VIS) absorbance spectra of MB were recorded with a Jasco V-570 UV–VIS-NIR spectrophotometer. Each sample surface area was determined from nitrogen adsorption-desorption isotherms at liquid nitrogen temperature using the Micromeritics ASAP 2010 system (outgassing conditions: 200°C-12h). Room temperature photoluminescence (PL) was measured in the range of 400-700 nm. After excitement with a nitrogen Nd:YAG laser (266 nm, 10 mW, 1 kHz), PL was recorded with an optical fiber spectrometer (Ocean Optics usb2000).

3.5. Photocatalytic activity

The photocatalytic activity of Ag/TiO$_2$ and BN-Ag/TiO$_2$ composite nanofibers was evaluated by monitoring the degradation of MB (used as a reference organic pollutant) under visible light. To this aim, 0.4 g/L of each photocatalyst was added to an aqueous suspension of 20 mg/L MB. After dispersion of the nanofibers by sonication in the dark for 60 min to reach the adsorption–desorption equilibrium, the solution was irradiated with visible light (obtained from a 150W light source with emission wavelength > 400 nm) for 80 minutes. The distance between the lamp and the solution (10 cm) was the same for all samples and the temperature was kept constant at 25 ± 0.2 °C by circulating water in the cylindrical tube that surrounded the photo-reactor during the entire experiment. Every 20 minutes, an aliquot of 2 ml was taken from each sample and centrifuged at 6000 rpm for 2 min in the dark to clear the supernatant because filtration resulted in the loss of some catalysts by sorption. The centrifuged solutions were analyzed with a UV/VIS spectrometer.

MB absorbance spectra (major absorption band around 664 nm) were recorded to measure the concentration changes over time. After irradiation, the photocatalytic degradation efficiency was calculated using equation 1:

$$\text{Degradation efficiency (\%)} = (C_0 - C)/C_0 \times 100 \qquad \text{(Equation 1)}$$

where C_0 and C are the MB concentrations before and after photo-irradiation, respectively. This equation gives the percentage of MB degradation by the photocatalyst. BN5-Ag3/TiO$_2$ photocatalytic activity repeatability was assessed with the same experimental set-up and after each degradation cycle, the catalyst was separated from the MB solution by centrifugation.

3.6. Antibacterial activity of TiO$_2$ nanofibers and BN-Ag/TiO$_2$ composite nanofibers

3.6.1. Bacterial strain and culture medium

LB-Miller culture medium was used for both liquid and solid bacterial cultures. The non-pathogenic and Gram-negative *E. coli* (K12 DSM 423) strain was selected as model microorganism to assess the samples' antibacterial properties because it is a common indicator of fecal contamination in water.[8]

3.6.2. Preparation of the bacterial suspensions used for the antibacterial tests

For each test, a new bacterial suspension was prepared from frozen *E. coli* aliquots stored at - 20°C. Aliquots were first rehydrated in LB-Miller medium on a rotary shaker at 110 rpm at 37°C for 3 hours. Then, they were inoculated in fresh LB-Miller medium (5% v/v) and incubated overnight at 37°C under constant stirring (110 rpm) until bacteria reached the stationary growth phase. Bacteria were centrifuged at 10°C at 3000g for 10 minutes to remove nutrients and avoid bacterial growth during the antibacterial test. Bacterial pellets were then suspended in spring water (Cristaline Sainte Cécile, France: $[Ca^{2+}]$ = 39 mg.L^{-1}, $[Mg^{2+}]$ = 25 mg.L^{-1}, $[Na^+]$ = 19 mg.L^{-1}, $[K^+]$ = 1.5 mg.L^{-1}, $[F^-]$ < 0.3 mg.L^{-1}, $[HCO_3^-]$ = 290 mg.L^{-1}, $[SO_4^{2-}]$ = 5 mg.L^{-1}, $[Cl^-]$ = 4 mg.L^{-1}, $[NO_3^-]$ < 2 mg.L^{-1}) to avoid osmotic shock and the suspension absorbance was measured at 600 nm to determine the bacterial concentration, according to calibration curves obtained previously in the laboratory. Bacteria were then diluted in spring water to obtain a bacterial suspension of about 7.0 x 10^8 CFU.mL^{-1}.

3.6.4. Assessment of the bactericidal properties of TiO$_2$ and BN5-Ag3/TiO$_2$ nanofibers

Bactericidal tests were carried out in batch mode, in glass tubes (20mL) equipped with a breathable cap. TiO$_2$, BN5-Ag3/TiO$_2$ and BN5-Ag3/TiO$_2$ nanofibers were diluted to a concentration of 10 mg.mL^{-1} in sterile ultra-pure water in the dark. One mL of bacterial suspension was mixed with 1 mL of spring water and 1 mL of each nanofiber suspension to obtain an initial bacterial concentration (C$_0$) of 2.3 ± 0.3 x 10^8 CFU.mL^{-1}. After vortexing, samples were incubated at 20°C with constant stirring (110 rpm) on a rotary shaker for 3 hours under normal light. Controls (1 mL of bacterial suspension, 1 mL of spring water and 1 mL of ultra-pure water without any material) were added to determine the initial bacterial concentration and to check that the vortex step did not affect cell viability.

3.6.5. Quantification of the bactericidal activity

After the 3-hour incubation with the different nanofiber samples, bacteria were counted using the conventional plaque assay method.[9] After decanting for 15 minutes to separate bacteria from the nanofiber-containing supernatant, bacteria were immediately ten-fold diluted in saline solution (0.9% NaCl) to neutralize the effect of any Ag that might have been desorbed, and then spread on agar plates. Negative control was a plate without bacteria. After overnight growth at 37°C, bacterial colonies were counted, knowing that each colony stemmed from one bacterium. All experiments were performed twice and the bacterial concentration in the sample was calculated as the average number of colonies divided by the inoculated volume, with the corresponding dilution factor taken into account. The quantification limit was 25 CFU.mL^{-1}. Changes in the bacterial concentrations were correlated with the bactericidal performance of the tested nanofiber sample. The concentration decrease was expressed as log-removal values, as described in the United States Environmental Protection Agency recommendations.[8] The log-removal value was defined as the logarithm (base 10) ratio of the bacterial concentration C (CFU.mL^{-1}) measured at a given time relative to the initial bacterial concentration C$_0$ (CFU.mL^{-1}). A log-removal value of -log (C$_0$) was attributed to the specific case of total removal of viable bacteria.[10] For instance, for an initial concentration C$_0$ fixed at 1.0 x 10^8 CFU/mL, a log-removal value of -8 corresponded to total removal.

4. Results and discussion

4.1. Morphological and structural properties of Ag/TiO$_2$ and BN-Ag/TiO$_2$ composite nanofibers

Pure TiO$_2$ nanofibers and Ag/TiO$_2$ and BN-Ag/TiO$_2$ composite nanofibers, with different amounts of AgNO$_3$ and BN nanosheets, were obtained using the simple electrospinning technique (Table 1). The Ag content in the TiO$_2$ nanofibers was adjusted by controlling the amount of AgNO$_3$ in the electrospun solution. After the annealing process at 500°C in air, a very light grayish tint was observed in samples with increasingly higher Ag content. Conversely, pure TiO$_2$ nanofibers were white. Analysis of their morphology by SEM (Figure 4.1) showed the nanofibrous morphology of the obtained Ag/TiO$_2$ and BN-Ag/TiO$_2$ composite nanofibers after calcination in air at 500°C for 4 hours. Although the electrospinning parameters were the same for all samples, the average diameter of composite nanofibers calculated from SEM images (Table 4.2) was significantly higher than that of pure TiO$_2$ nanofibers. As our previous findings indicate that there is an important relation between the fiber diameter and the dopant content [11], this diameter increase could be attributed to the inclusion of AgNO$_3$ and BN sheets that increase both the total metal content and the viscosity of the electrospinning solution. [12]

EDX was used to study the chemical composition and to confirm the successful production of Ag/TiO$_2$ and BN-Ag/TiO$_2$ composite nanofibers. The EDX data (Table 4.3) revealed the formation of TiO$_2$ nanofibers with the required atomic ratio of 1:2. For the Ag/TiO$_2$ composites, the progressive increase of the Ag atom percentage with the AgNO$_3$ content was clearly observed. In BN-Ag/TiO$_2$ composite nanofibers, the presence of boron progressively increased with the BN nanosheets amount. It is worth to note that due to the overlap between the energy levels of Ti and N (the L energy of Ti and the K energy of N), N could not be detected. Elemental mapping images of a BN3-Ag5/TiO$_2$ sample (Figure 4.2) clearly showed that Ti, O, Ag and B elements were well distributed over the entire area of the sample, thus confirming the good dispersion of Ag and BN nanosheets in TiO$_2$ nanofibers. In conclusion, these data indicate that BN-Ag/TiO$_2$ composite nanofibers were successfully fabricated using the electrospinning technique.
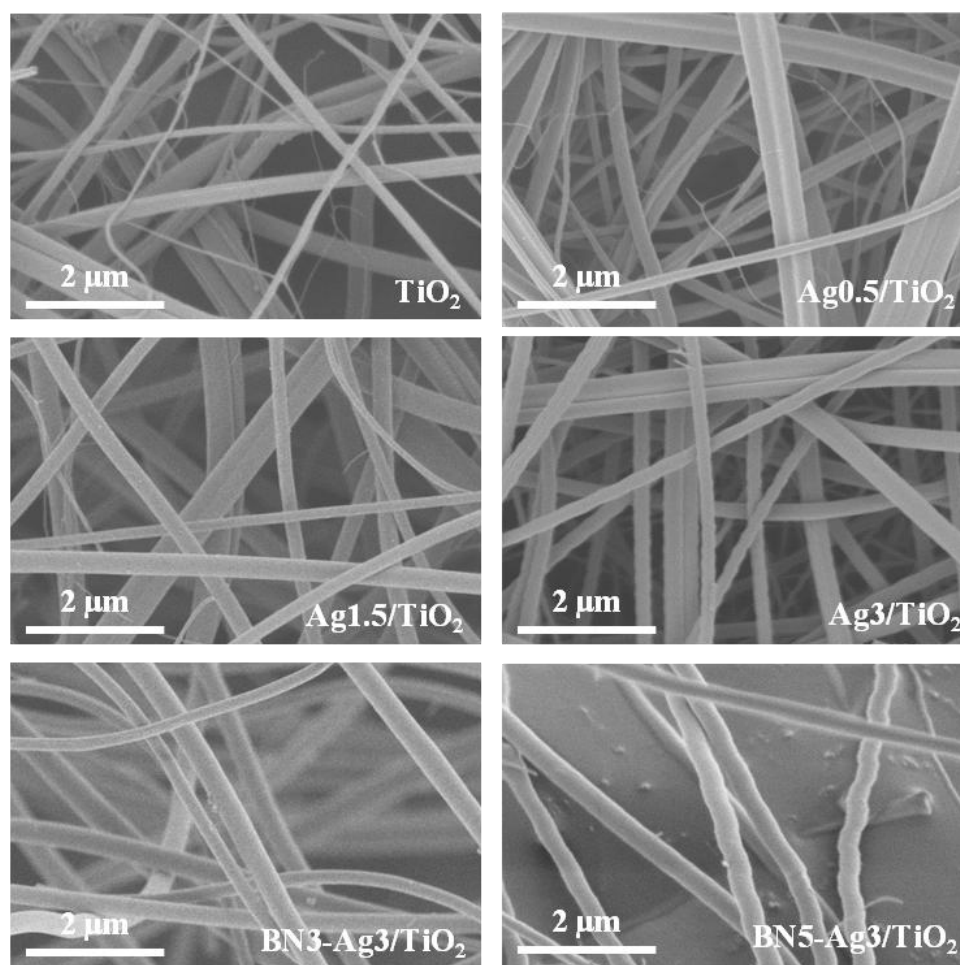
Figure 4.1. Scanning electron microscope images of pure TiO_2 nanofibers, Ag0.5/TiO_2, Ag1.5/TiO_2, Ag3/TiO_2, BN3-Ag3/TiO_2 and BN5-Ag3/TiO_2 composite nanofibers after annealing under air at 500°C for 4h.

Table 4.2. Average diameter of annealed TiO_2, Ag/TiO_2 and BN-Ag/TiO_2 nanofibers.

Sample	Average diameter (± 5 nm)
TiO_2	187
Ag0.5/TiO_2	192
Ag1.5/TiO_2	242
Ag3/TiO_2	319
BN3-Ag3/TiO_2	286
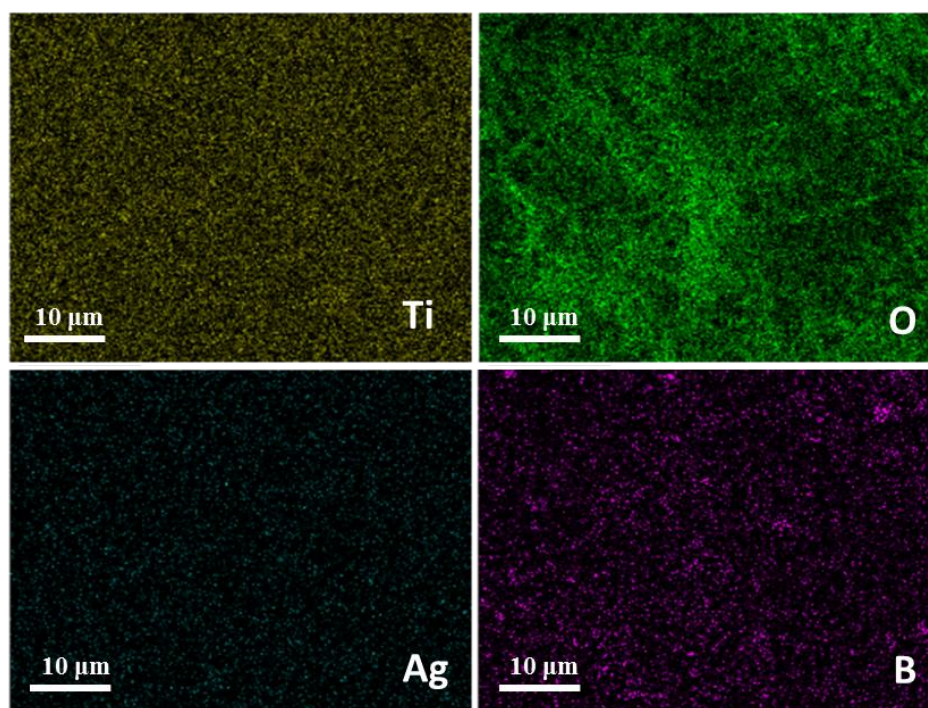
BN5-Ag3/TiO$_2$ 305

Figure 4.2. Elemental mapping images of BN5-Ag3/TiO$_2$ composite nanofibers with 5 wt% of BN and 3 wt% of Ag.

Table 4.3. EDX data showing the composition of annealed TiO$_2$, Ag/TiO$_2$ and BN-Ag/TiO$_2$ nanofibers.

	Atomic percentage				
	Ti	**O**	**Ag**	**B**	**C**
TiO$_2$	30.49	60.76	-	-	8.75
Ag0.5/TiO$_2$	30.47	64.36	0.31	-	4.86
Ag1.5/TiO$_2$	29.08	64.73	0.70	-	5.49
Ag3/TiO$_2$	34.46	62.21	0.17	-	3.16
BN3-Ag3/TiO$_2$	30.8	60.56	0.3	3.17	5.17
BN5-Ag3/TiO$_2$	29.15	58.34	0.27	9.16	3.08

Calculation of the surface area of TiO_2, Ag/TiO_2 and $BN-Ag/TiO_2$ nanocomposites using the Brunauer-Emmet-Teller (BET) method [13] (Table 4.4) showed that values varied between 19 and 35 m^2g^{-1}. The progressive increase of the surface area with the amount of BN and Ag offers more active adsorption sites and consequently should enhance TiO_2 photocatalytic activity.

Table 4.4. Surface area of TiO_2 nanofibers, and Ag/TiO_2 and $BN-Ag/TiO_2$ composite nanofibers.

Samples	Surface area ($m^2 g^{-1}$)
TiO_2	19.7
$Ag0.5/TiO_2$	19.0
$Ag1.5/TiO_2$	25.5
$Ag3/TiO_2$	31.2
$BN3-Ag3/TiO_2$	31.8
$BN5-Ag3/TiO_2$	34.4

Analysis of the XRD patterns of the synthesized TiO_2, Ag/TiO_2 and $BN-Ag/TiO_2$ nanofibers (Figure 4.3.A) indicated that all patterns had sharp diffraction peaks located at 2θ = 25.5°, 38.1°, 48.2°, 54.1°, 55.3° and 62.9° relative to the crystal planes of the pure anatase phase of TiO_2 (101), (004), (200), (105), (211) and (204), respectively.[14] The standard peaks of $AgNO_3$ and BN could not be detected by XRD due to their low amount in the samples. However, a small peak of Ag (at 2θ ~ 38°) could be seen in the XRD spectra of $Ag3/TiO_2$ and $BN3-Ag3/TiO_2$ composite nanofibers, indicating Ag presence (Figure 4.3.B) [15, 16]. Moreover, the main peak of hexagonal BN (at 2θ ~ 26°) overlapped with the sharp peak of TiO_2 (at 2θ ~ 25.5°). After Ag and BN doping, the diffraction peaks of Ag/TiO_2 and $BN-Ag/TiO_2$ composite nanofibers were shifted, compared with the peak of pure TiO_2 nanofibers (Figure 4.3.A). We suggest that the slight shifting of the TiO_2 peak is related to peak overlapping between BN and TiO_2. Alternatively, this shift could be due to Ag and BN

sheet incorporation that increases the density of surface defects and the lattice strain in the TiO_2 cell, causing vacancy formation. At the same time, it can shift atoms from the initial position and can reduce the formation of the self-trapped excitons (STE) localized on the TiO_6 octahedral.

According to Bragg's law:[17]

$$n\lambda = 2d \sin\theta \qquad \text{(Equation 2)}$$

the d spacing decreases with the increase of the $\sin\theta$ value. Therefore, we can say that the d spacing value decreased with the increase of the Ag and BN amounts. This suggests that Ag ions have diffused into the TiO_2 lattice. The average crystal size of TiO_2, Ag/TiO_2 and BN-Ag/TiO_2 samples with different amounts of $AgNO_3$ and BN was estimated using the following Scherrer-Debye equation: [18]

$$D = k\lambda/\beta\cos\theta \qquad \text{(Equation 3)}$$

where D is the average size in nm, k is the shape factor constant (0.9), λ is the X-ray wavelength (0.154 nm), β is the line broadening of the diffraction line measured by the full width at half maximum of the peak intensity (FWHM) and θ is the Bragg angle (in degrees). The results showed that the grain size of the composite nanofibers was higher than that of pure TiO_2 nanofibers (Table 4.5).
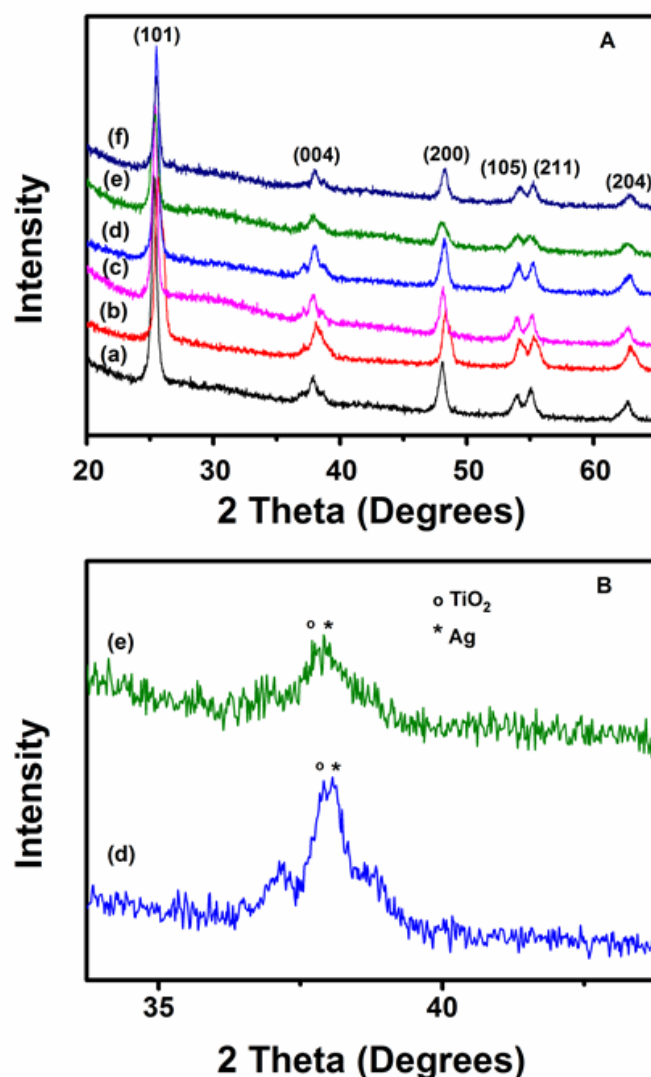
Figure 4.3. (A-B) XRD patterns of (a) TiO_2, (b) Ag0.5/TiO_2, (c) Ag1.5/TiO_2, (d) Ag3/TiO_2, (e) BN3-Ag3/TiO_2 and (f) BN5-Ag3/TiO_2 nanofibers annealed in air at 500°C for 4h.

Table 4.5. Grain size of annealed TiO_2, Ag/TiO_2 and BN-Ag/TiO_2 nanofibers.

	TiO_2	Ag0.5/TiO_2	Ag1.5/TiO_2	Ag3/TiO_2	BN3- Ag3/TiO_2	BN5- Ag3/TiO_2
Grain size (nm)	18.2	20.4	21.95	17.1	25.8	26.15

The formation of BN-Ag/TiO_2 composite nanofibers was further confirmed by Raman spectroscopy. The Raman peaks of all samples at 144 cm^{-1} (E_g), 197 cm^{-1} (E_g), 399 cm^{-1} (B_{1g}), 513 cm^{-1} (A_{1g}), 519 cm^{-1} (B_{1g}) and 639 cm^{-1} (E_g) corresponded to the pure anatase phase of

TiO_2 (Figure 4.4.A).[19] The main peak of TiO_2, located at 141 cm^{-1}, was shifted to a larger frequency after Ag and BN doping. This frequency shift could be attributed to the pressure effect induced by Ag particles and BN sheets that strongly affects the lattice vibrational characteristics of TiO_2 [20]. For BN-Ag/TiO_2 composite nanofibers, a Raman active mode located at ~ 1365 cm^{-1} was identified and was due to hexagonal BN related to the E_{2g} mode (Figure 4.4.B) [21]. In addition, an increase in the intensity of the peak corresponding to hexagonal BN with the amount of doping could be clearly observed. No peak related to silver oxide was detected in the Raman and XRD spectra. This confirmed the thermal decomposition of $AgNO_3$ and the formation of Ag nanoparticles.
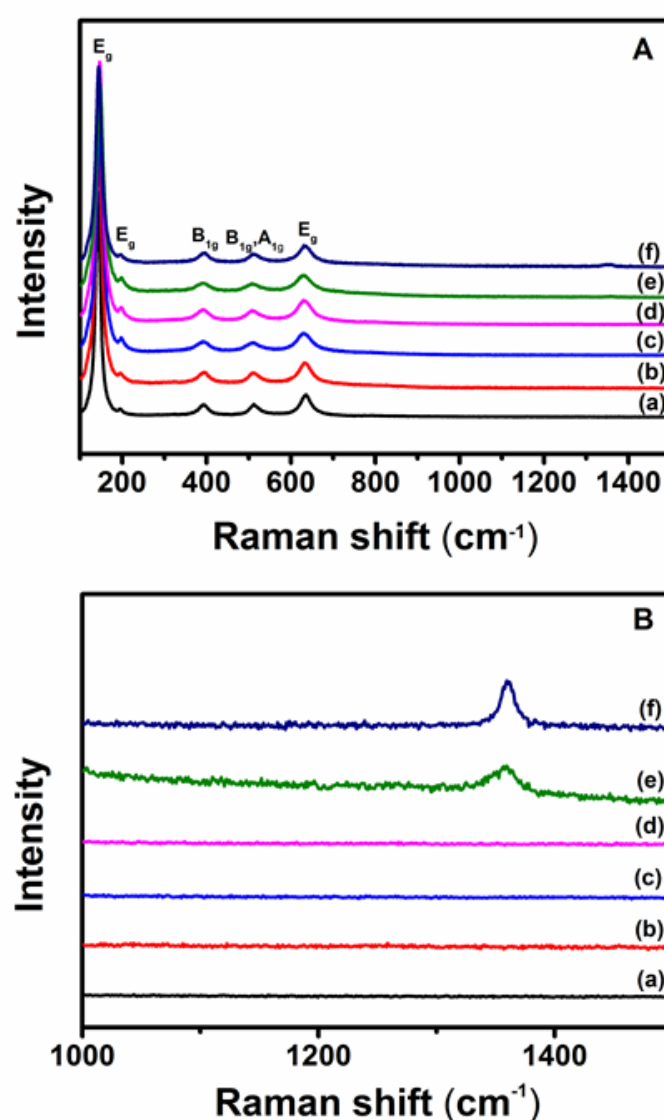
Figure 4.4. (A-B) Raman shifts of a) TiO_2, (b) Ag0.5/TiO_2, (c) Ag1.5/TiO_2, (d) Ag3/TiO_2, (e) BN3-Ag3/TiO_2 and (f) BN5-Ag3/TiO_2 nanofibers annealed in air at 500°C for 4h.

4.2. Optical properties of TiO₂, Ag/TiO₂ and BN-Ag/TiO₂ composite nanofibers

Incorporation of $AgNO_3$ and BN nanosheets strongly influenced the optical properties of the produced nanofibers. The shift of TiO_2 absorption edges was clearly seen in the reflectance spectra of the different samples (Figure 4.5). The band gap values of pure TiO_2, Ag/TiO₂ and BN-Ag/TiO₂ composite nanofibers were calculated from the reflectance spectra using the Kubelka–Munk formula [22]:

$$F = \frac{(1-R)^2}{2R} \quad \text{(Equation 4)}$$

$$(Fhv)^{1/2} \sim (hv\text{-}E_g) \quad \text{(Equation 5)}$$

where F, R, hv and E_g represent the Kubelka–Munk function, reflectance, photon energy and band gap, respectively. The E_g values were calculated from the intersection of the linear part of the curve with the hv axis. The fitting was performed automatically using the Origin 9.0 software (Figure 4.5.B). Calculation of the photo-absorption edge wavelengths and band gap values (Figure 4.5 and Table 4.6) showed that, compared with pure TiO_2 nanofibers, the absorption edges of Ag/TiO₂ and BN-Ag/TiO₂ composite nanofibers were red-shifted (from 392 to 435 nm) and the band gap values decreased remarkably with the increase of the Ag amount (from 3.16 to 2.85 eV). According to previous studies, this red shift is due to the Ag content because BN has no absorbance edge in the visible range [23]. Ag3/TiO₂, BN3-Ag3/TiO₂ and BN5-Ag3/TiO₂ composite nanofibers had the lowest band gap values. The decrease of TiO_2 band gap value with Ag doping can be explained by TiO_2 lattice changes and/or by the formation of shallow sites near the conductance band in TiO_2 band gap [24].

Table 4.6. Photo-absorption edge and band gap values of pure TiO_2 nanofibers, Ag/TiO₂ and BN-Ag/TiO₂ composite nanofibers.

Sample	Absorption edge (nm)	Band gap (eV)
TiO₂	392	3.16
Ag0.5/TiO₂	413	3.00

Ag1.5/TiO₂	417	2.97
Ag3/TiO₂	429	2.89
BN3-Ag3/TiO₂	430	2.88
BN5-Ag3/TiO₂	435	2.85
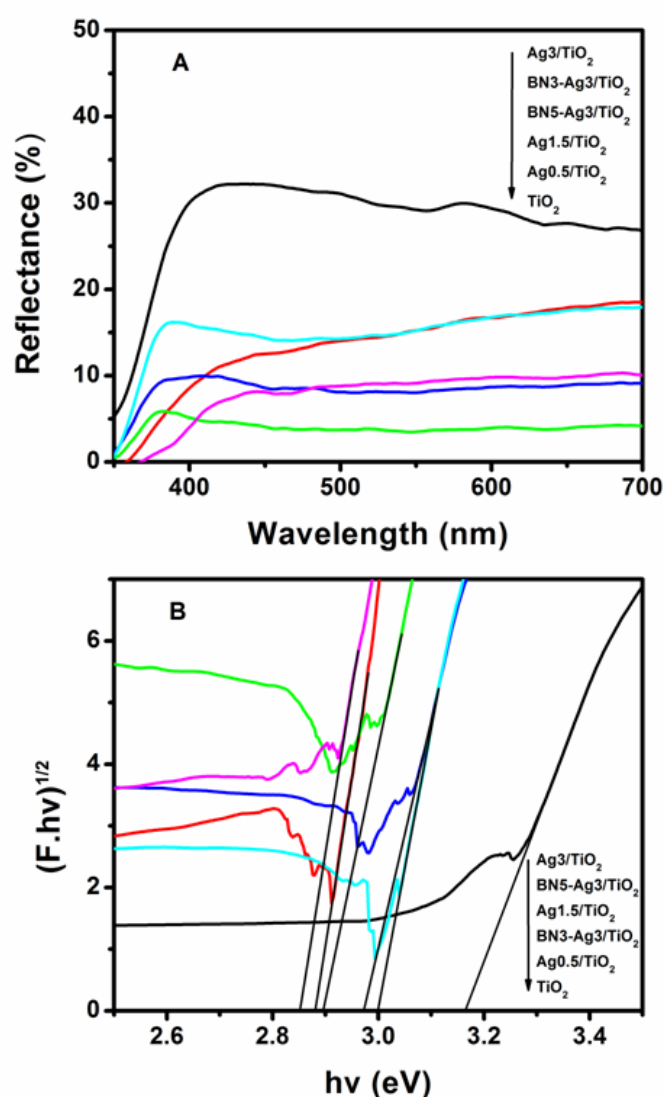
Figure 4.5. (A) Reflectance spectra and **(B)** Band gap calculation from the reflectance spectra of TiO₂, Ag/TiO₂ and BN-Ag/TiO₂ composite nanofibers.

As PL emission results from the recombination of free carriers, PL spectra have been used to investigate the efficiency of charge carrier trapping, migration and transfer in order

to understand the fate of electron–hole pairs in semiconductors.[14] In other words, a lower recombination rate or a higher transfer of electrons and holes can result in a lower PL intensity. Many studies have reported PL emissions of pure TiO_2 in photocatalysis research [25, 26]. The PL of BN/TiO_2 nanostructures was investigated for the first time by our group [27]. In this work, we report the PL emission spectra of $BN-Ag/TiO_2$ nanostructures. As photocatalytic activity improvement is based on the charge separation at the $BN-Ag/TiO_2$ interface, a lower electron–hole recombination rate in nanocomposites was expected. Consequently, the PL intensity in the $BN-Ag/TiO_2$ nanostructures should decrease. Analysis of the PL emission spectra of TiO_2, Ag/TiO_2 and $BN-Ag/TiO_2$ composite nanofibers with different Ag and BN sheets amounts (Figure 4.6) showed that pure TiO_2 nanofibers had high intensity and broad-band PL signals in the 400–700 nm region, which could be assigned to the radiative recombination of self-trapped excitons (STE) [14]. Ag and BN doping significantly reduced the PL intensities of all nanocomposites compared with pure TiO_2 nanofibers. Particularly, the $Ag1.5/TiO_2$, $Ag3/TiO_2$, $BN3-Ag3/TiO_2$ and $BN5-Ag3/TiO_2$ samples showed a very weak PL intensity, indicating that they might have the lowest photo-induced electron-hole recombination rate. XRD analysis showed that additional lattice strain appeared in the TiO_2 lattice after BN and Ag doping. This reduces STE formation on the TiO_6 octahedral and therefore, quenches their emission. PL intensity decrease can be mainly explained by the BN and Ag doping effect that leads to the formation of defects on the interface that provide non-radiative recombination and surface charge transfer.[28, 29] The surface charge separation between TiO_2 and BN is expected to improve the photocatalytic activities [27].
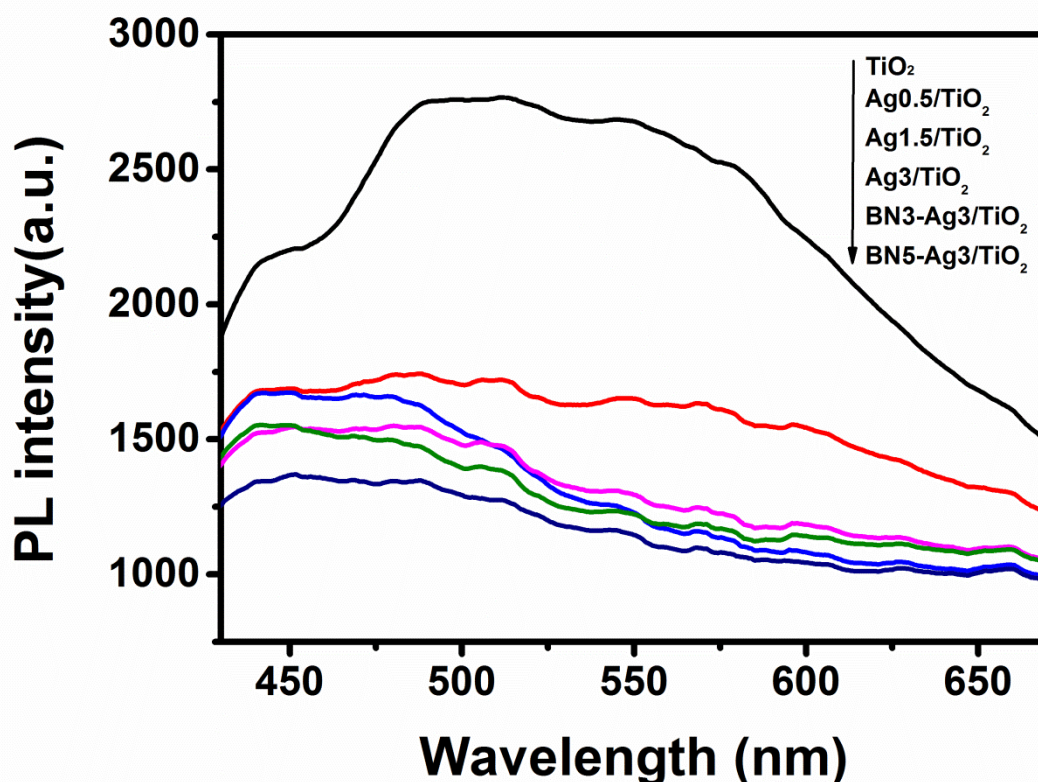
Figure 4.6. Photoluminescence spectra of pure TiO_2 nanofibers, and Ag/TiO_2 and $BN-Ag/TiO_2$ composite nanofibers.

4.3. Photocatalytic application

The photocatalytic degradation efficiency of MB by TiO_2, Ag/TiO_2 and $BN-Ag/TiO_2$ nanofibers with different Ag and BN contents was assessed by calculating the UV–VIS absorbance spectra of the MB solutions (major absorption band around 664 nm) at different time points after exposure to light (0, 20, 40, 60, and 80 min) (Figure 4.7.A for BN5-$Ag3/TiO_2$). The results obtained with the different nanofibers (Figure 4.7.B) indicated that MB was stable and difficult to be photodegraded under visible light in the absence of photocatalyst. After 80 min of exposure to light, up to 25% of MB was degraded in the presence of pure TiO_2 nanofibers. We previously reported that due to its larger active surface area, the photocatalytic activity of TiO_2 nanofibers is higher than that of commercial TiO_2-P25.[11, 27] The percentage of degraded MB increased gradually with the Ag content: 62% with $Ag0.5/TiO_2$, 73% with $Ag1.5/TiO_2$, and 77% with $Ag3/TiO_2$. It is well accepted that the photocatalytic effect in solid-state catalysis is caused by the electron - hole pairs created from photon adsorption and interaction with molecules close to the catalyst

surface.[1] The observed degradation increase could be attributed to the deposition of Ag species onto the surface of TiO_2 nanofibers that can capture the photo-induced electrons and holes. In addition, photo-induced electrons can quickly transfer to the oxygen adsorbed on TiO_2 surface [28, 30]. The improved photocatalytic activity of Ag/TiO_2 composites under visible light compared with pure TiO_2 nanofibers could mainly be ascribed to the lower band gap value, as confirmed by the diffuse reflectance spectra. MB degradation efficiency further increased to 85% with $BN3-Ag3/TiO_2$ and to 98% with $BN5-Ag3/TiO_2$ composites. The higher photocatalytic activity of $BN-Ag/TiO_2$ compared with Ag/TiO_2 composites, with the same amount of Ag, is explained by the efficient electron transfer from photo-excited Ag/TiO_2 to the BN nanosheets of the plasmonic photocatalyst. The efficient charge transfer is related to the pronounced electrostatic interactions. The naturally negatively charged surface of BN sheets could lead to h^+ transfer from the activated Ag/TiO_2 to the BN sheets when they are connected [31, 32]. Therefore, more photo-electrons are available, compared with Ag/TiO_2 samples, to take part in the photodegradation process, in agreement with the photoluminescence analysis.
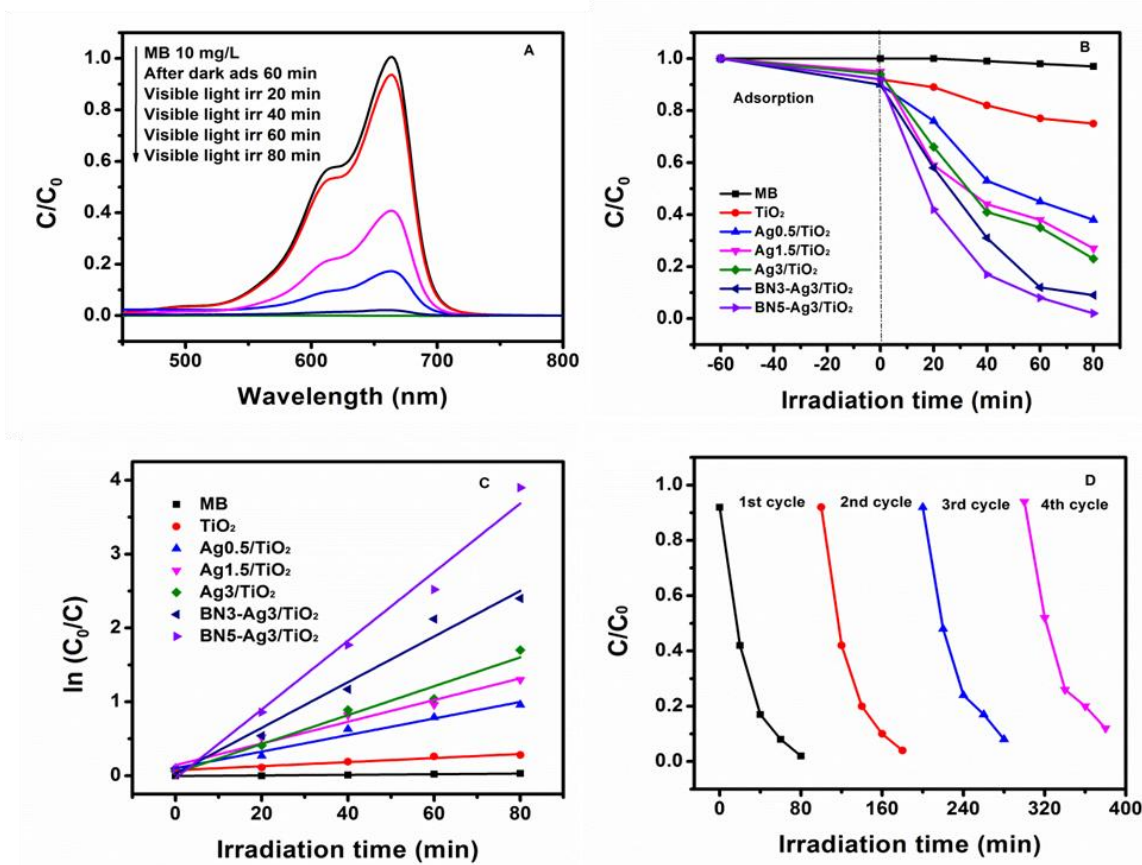
Figure 4.7. (A) Absorbance spectra of MB degradation in the presence of BN5-Ag3/TiO$_2$ composite nanofibers. **(B)** MB photodegradation by the TiO$_2$, Ag/TiO$_2$ and BN-Ag/TiO$_2$ photocatalysts under visible light. **(C)** Kinetics of MB degradation. **(D)** Long-term catalytic stability of BN5-Ag3/TiO$_2$ nanofibers in four repeated cycles of MB degradation under visible light.

The kinetic linear curves for all samples are shown in Figure 4.7.C. The photodegradation reactions followed a Langmuir–Hinshelwood first order kinetics model, as described by equation 6:

$$r = dC/dt = kKC/(1+KC) \qquad \text{(Equation 6)}$$

where r is MB degradation rate (mg (L min)$^{-1}$), C is the MB solution concentration (mg L^{-1}), t is the irradiation time, k is the reaction rate constant (mg (L min)$^{-1}$), and K is MB adsorption coefficient (mg L^{-1}). As the initial concentration (C$_0$ = 10 mg L^{-1}) of the MB solutions was very low in the present experiments, the relationship between ln(C$_0$/C) and the reaction time t showed that MB decomposition with different photocatalysts agreed with a pseudo first-order kinetic:[33]

$$\ln(C_0/C) = kKt = k_a t \qquad \text{(Equation 7)}$$

where ka was the apparent first-order rate constant (min^{-1}) and C the concentration at time t. The obtained k_a values from the linear dependence between $\ln(C_0/C)$ and time are reported in Table 4.7. The increasing order of the rate constants in the samples was: BN5-Ag3/TiO$_2$ > BN3-Ag3/TiO$_2$ > Ag3/TiO$_2$ > Ag1.5/TiO$_2$ > Ag0.5/TiO$_2$ > TiO$_2$ NFs > MB. The rate constant exhibited a maximum of 0.0465 min^{-1} for BN5-Ag3/TiO$_2$. This was 17.2 and 2.3 times higher than that of pure TiO$_2$ nanofibers and Ag3/TiO$_2$ composite nanofibers, respectively. Thus, compared with other samples, BN5-Ag3/TiO$_2$ nanocomposites showed the highest photocatalytic activity under visible light, which is represented by their larger k_a value. These results indicate that, compared with TiO$_2$ and Ag/TiO$_2$ nanofibers, the coupling effect between BN and Ag/TiO$_2$ greatly improves the photocatalytic activity under visible light.

Table 4.7. Kinetic parameters of the photocatalytic activities of pure TiO$_2$ nanofibers, and Ag/TiO$_2$ and BN-Ag/TiO$_2$ composite nanofibers.

	k_a (min^{-1})	R^2
MB	0.0004	0.9215
TiO$_2$	0.0027	0.9544
Ag0.5/TiO$_2$	0.0112	0.9707
Ag1.5/TiO$_2$	0.0147	0.9581
Ag3/TiO$_2$	0.0195	0.9622
BN3-Ag3/TiO$_2$	0.0309	0.9686
BN5-Ag3/TiO$_2$	0.0465	0.9819

The catalyst stability has always been the critical issue for long-term repeated use in practical applications [34]. Previous studies reported that TiO$_2$ nanofibers and Ag/TiO$_2$ composite nanofibers show high stability in photocatalytic repeatability experiments [28, 35]. Assessment of the photocatalytic activity repeatability in the same conditions showed

that MB degradation by BN5-Ag3/TiO$_2$ composites remained high after four cycles (Figure 4.7.D). This indicates that BN5-Ag3/TiO$_2$ is stable during the photocatalytic reaction. Also, the used nanofibers had the same light grey color as newly prepared samples. These results confirm that BN5-Ag3/TiO$_2$ nanofibers have higher photodegradation efficiency compared with pure TiO$_2$ nanofibers and Ag/TiO$_2$ composites and long-term stability in photocatalytic activity repeatability tests. As the experimental conditions are different, the photocatalytic activities of BN5-Ag3/TiO$_2$ composite nanofibers could be only broadly compared with those of previously described Ag/TiO$_2$ composites (Table 4.8). Nevertheless, BN5-Ag3/TiO$_2$ composite nanofibers showed the best visible-light photocatalytic activity compared with the other Ag/TiO$_2$ composites [15, 28, 30, 36-39].

Table 4.8. Comparison of the photocatalytic activity of different Ag/TiO$_2$ nanocomposites.

Photocatalysts	Photocatalyst concentration in dye solution (g/L)	Irradiation light source	Time (min)	Degradation efficiency (%)	Ref.
Ag(NPs) /TiO$_2$-P25 composite	0.5	Visible (125 W)	180	86	[38]
Ag/TiO$_2$ nanocomposites	–	Visible (500 W)	360	80	[39]
Ag/TiO$_2$ Composite NFs	0.1	UV (1000 W)	20	100	[15]
Ag/TiO$_2$ nanowires	0.6	UV (150 W)	80	100	[30]
Ag/TiO$_2$ nanotubes	1	Visible (500 W)	240	100	[37]
Ag(NPs)/TiO$_2$ nanofibers	1	UV (125 W)	60	98	[36]
Ag(NPs)/TiO$_2$ nanofibers	1	Visible (150 W)	120	54	[36]
Ag-AgBr(NPs)/TiO$_2$ nanofibers	1	Visible (150 W)	300	92	[28]
BN5-Ag3/TiO$_2$ composite NFs	0.4	Visible (150 W)	80	98	This work

4.4. Antibacterial properties

Besides their photocatalytic properties to degrade toxic organic compounds, BN-Ag/TiO$_2$ nanofibers should also have antibacterial effects. Antibacterial tests were carried out in liquid phase instead of using the disc diffusion method (agar phase) to favor contact [40] between *E. coli* bacteria and TiO$_2$ nanofibers and BN5-Ag3/TiO$_2$ composites (under visible light and in the dark). Control reactions without nanofibers showed that bacteria remained viable for 3 hours in the tested conditions (Table 4.9). Similarly, pure TiO$_2$ nanofibers had no bactericidal or adsorption effect after 3 hours of contact time under visible light.[10] On the other hand, total *E. coli* removal (-8 log) was observed with BN5-Ag3/TiO$_2$ under visible light, while in the dark no antibacterial activity was detected. This indicates that despite the Ag amount (3 wt. %) in the composite, Ag has no bactericidal effect. This can be explained by the fact that Ag is not deposited on the TiO$_2$ surface, but incorporated in the nanofibers, and thus cannot diffuse to the bacteria. By comparing the results obtained with BN5-Ag3/TiO$_2$ under visible light and in the dark (Table 4.9), it can be concluded that BN sheets have no antibacterial effect in the tested conditions [41]. Therefore, the high antibacterial efficiency of BN5-Ag3/TiO$_2$ composite nanofibers can be attributed to the stronger photocatalytic activity of TiO$_2$ under visible light due to Ag and BN doping, in agreement with the photocatalytic results. This study, thus, highlights the strong bactericidal activity of BN5-Ag3/TiO$_2$ composite nanofibers under visible light. Moreover, the total removal of bacteria (Table 4.9) and MB (Figure 4.7) by BN5-Ag3/TiO$_2$ under visible light demonstrates the good agreement between antibacterial activity and MB degradation.

Table 4.9. *E. coli* log-removal values after incubation with pure TiO$_2$ nanofibers or BN5-Ag3/TiO$_2$ composite nanofibers at 20°C for 3 hours (C$_0$ = 2.3 ± 0.3 x 10^8 CFU.mL^{-1}).

Samples	Removal (Log-values)
Control (3h)	0 ± 1
Pure TiO$_2$ (Light)	0 ± 1
BN5-Ag3/TiO$_2$ (Light)	-8 ± 1
BN5-Ag3/TiO$_2$ (Dark)	0 ± 1

5. Conclusion

This study shows that Ag/TiO$_2$ and BN-Ag/TiO$_2$ composite nanofibers with different amounts of Ag and BN nanosheets can be successfully prepared using the electrospinning technique. After annealing at 500°C, SEM images show an increase of the average diameter of the composite nanofibers compared with pure TiO$_2$ nanofibers. TEM images, EDX data and Raman spectra confirm the incorporation of Ag and BN nanosheets in TiO$_2$ nanofibers. BET measurements and XRD data show the higher specific surface area and grain size of BN-Ag/TiO$_2$ nanofibers compared with Ag/TiO$_2$ and TiO$_2$ nanofibers, respectively. The red shift of the absorbance edge and the decrease of the TiO$_2$ band gap value from 3.16 to 2.85 eV were confirmed by diffuse reflectance analysis. Ag/TiO$_2$ and BN-Ag/TiO$_2$ composites exhibit very weak photoluminescence intensity, and therefore low photo-induced electron-hole recombination compared with pure TiO$_2$ nanofibers. Moreover, Ag/TiO$_2$ composite nanofibers have significantly enhanced photocatalytic activity when mixed with BN nanosheets. This higher activity is due to the efficient electron transfer from photo-excited Ag/TiO$_2$ to BN nanosheets to retard TiO$_2$ charge recombination. MB degradation efficiency with BN5-Ag3/TiO$_2$ as catalyst is 17.2 and 2.3 times higher than that of pure TiO$_2$ nanofibers and Ag3/TiO$_2$ composites, respectively. Moreover, photocatalytic activity repeatability experiments confirmed the long-term stability of BN5-Ag3/TiO$_2$ composite nanofibers for MB photodegradation. Antibacterial tests showed that BN5-Ag3/TiO$_2$ composite nanofibers can kill *E. coli* cultures under visible light, indicating that this effect is related to the enhanced TiO$_2$ photocatalytic activity upon doping with BN and Ag. In conclusion, the multifunctional BN5-Ag3/TiO$_2$ composites display photodegradation and antibacterial applications. TiO$_2$-based photocatalysts doped with Ag and BN nanosheets can be considered as efficient and long-term stable antibacterial materials for biomedical use and water disinfection.

References

1. Chen, J., et al., Recent progress in enhancing photocatalytic efficiency of TiO 2-based materials. Applied Catalysis A: General, 2015. **495**: p. 131-140.
2. Jiang, L., Y. Huang, and T. Liu, Enhanced visible-light photocatalytic performance of electrospun carbon-doped TiO 2/halloysite nanotube hybrid nanofibers. Journal of colloid and interface science, 2015. **439**: p. 62-68.
3. Sofianou, M.-V., et al., Solvothermal synthesis and photocatalytic performance of Mn 4+-doped anatase nanoplates with exposed {001} facets. Applied Catalysis B: Environmental, 2015. **162**: p. 27-33.
4. Chen, C., W. Ma, and J. Zhao, Semiconductor-mediated photodegradation of pollutants under visible-light irradiation. Chemical Society Reviews, 2010. **39**(11): p. 4206-4219.
5. Thangaraj, V., et al., Fluorescence Quenching of Sulforhodamine Dye over Graphene Oxide and Boron Nitride Nanosheets. European Journal of Inorganic Chemistry, 2016.
6. Eid, C., et al., Tunable properties of GO-doped CoFe 2 O 4 nanofibers elaborated by electrospinning. RSC Advances, 2015. **5**(118): p. 97849-97854.
7. Seery, M.K., et al., Silver doped titanium dioxide nanomaterials for enhanced visible light photocatalysis. Journal of Photochemistry and Photobiology A: Chemistry, 2007. **189**(2): p. 258-263.
8. Water, O., Edition of the Drinking Water Standards and Health Advisories. EP Agency (ed.), 2012.
9. Nagarajan, S., et al., Novel biocompatible electrospun gelatin fiber mats with antibiotic drug delivery properties. Journal of Materials Chemistry B, 2016. **4**(6): p. 1134-1141.
10. Tartanson, M.-A., et al., Dynamic Mechanisms of the Bactericidal Action of an Al2O3-TiO2-Ag Granular Material on an Escherichia coli Strain. Applied and environmental microbiology, 2015. **81**(20): p. 7135-7142.
11. Nasr, M., et al., Enhanced Visible-Light Photocatalytic Performance of Electrospun rGO/TiO2 Composite Nanofibers. The Journal of Physical Chemistry C, 2016.
12. Sarlak, N., et al., Effects of electrospinning parameters on titanium dioxide nanofibers diameter and morphology: An investigation by Box–Wilson central composite design (CCD). Chemical engineering journal, 2012. **210**: p. 410-416.
13. Walton, K.S. and R.Q. Snurr, Applicability of the BET method for determining surface areas of microporous metal– organic frameworks. Journal of the American Chemical Society, 2007. **129**(27): p. 8552-8556.
14. Nasr, M., et al., Photoluminescence: A very sensitive tool to detect the presence of anatase in rutile phase electrospun TiO 2 nanofibers. Superlattices and Microstructures, 2015. **77**: p. 18-24.
15. Nalbandian, M.J., et al., Synthesis and optimization of Ag–TiO 2 composite nanofibers for photocatalytic treatment of impaired water sources. Journal of hazardous materials, 2015. **299**: p. 141-148.
16. Akhavan, O., Lasting antibacterial activities of Ag–TiO 2/Ag/a-TiO 2 nanocomposite thin film photocatalysts under solar light irradiation. Journal of Colloid and Interface Science, 2009. **336**(1): p. 117-124.

17.   Xin, B., et al., Effects of simultaneously doped and deposited Ag on the photocatalytic activity and surface states of TiO2. The Journal of Physical Chemistry B, 2005. **109**(7): p. 2805-2809.

18.   Holzwarth, U. and N. Gibson, The Scherrer equation versus the'Debye-Scherrer equation'. Nature Nanotechnology, 2011. **6**(9): p. 534-534.

19.   Yang, L., et al., Charge-transfer-induced surface-enhanced raman scattering on Ag–TiO2 nanocomposites. The Journal of Physical Chemistry C, 2009. **113**(36): p. 16226-16231.

20.   Zhang, W., et al., Raman scattering study on anatase TiO2 nanocrystals. Journal of Physics D: Applied Physics, 2000. **33**(8): p. 912.

21.   Leung, K., et al., Structural analysis of cubic boron nitride films by ultraviolet Raman spectroscopy. Applied physics letters, 2006. **88**(24): p. 241922.

22.   Baitimirova, M., et al., Tuning of Structural and Optical Properties of Graphene/ZnO Nanolaminates. The Journal of Physical Chemistry C, 2016. **120**(41): p. 23716-23725.

23.   Ide, Y., et al., h-BN nanosheets as simple and effective additives to largely enhance the activity of Au/TiO2 plasmonic photocatalysts. Physical Chemistry Chemical Physics, 2015. **18**(1): p. 79-83.

24.   Demirci, S., et al., Synthesis and characterization of Ag doped TiO 2 heterojunction films and their photocatalytic performances. Applied Surface Science, 2016. **390**: p. 591-601.

25.   Li, Y., et al., High photoluminescence quantum yield of TiO2 nanocrystals prepared using an alcohothermal method. Luminescence, 2007. **22**(6): p. 540-545.

26.   Liqiang, J., et al., Review of photoluminescence performance of nano-sized semiconductor materials and its relationships with photocatalytic activity. Solar Energy Materials and Solar Cells, 2006. **90**(12): p. 1773-1787.

27.   Nasr, M., et al., Enhanced photocatalytic performance of novel electrospun BN/TiO 2 composite nanofibers. New Journal of Chemistry, 2017. **41**(1): p. 81-89.

28.   Sui, Y., et al., Ag-AgBr nanoparticles loaded on TiO 2 nanofibers as an efficient heterostructured photocatalyst driven by visible light. Journal of Molecular Catalysis A: Chemical, 2015. **410**: p. 226-234.

29.   Jaafar, N., et al., Direct in situ activation of Ag 0 nanoparticles in synthesis of Ag/TiO 2 and its photoactivity. Applied Surface Science, 2015. **338**: p. 75-84.

30.   Yao, Y.-C., et al., Synthesis of Ag-decorated porous TiO 2 nanowires through a sunlight induced reduction method and its enhanced photocatalytic activity. Applied Surface Science, 2016. **387**: p. 469-476.

31.   Fu, X., et al., Ball milled h-BN: an efficient holes transfer promoter to enhance the photocatalytic performance of TiO 2. Journal of hazardous materials, 2013. **244**: p. 102-110.

32.   Tang, C., et al., Improved TiO2 photocatalytic reduction by the intrinsic electrostatic potential of BN nanotubes. Chemistry–An Asian Journal, 2010. **5**(5): p. 1220-1224.

33.   Konstantinou, I.K. and T.A. Albanis, TiO 2-assisted photocatalytic degradation of azo dyes in aqueous solution: kinetic and mechanistic investigations: a review. Applied Catalysis B: Environmental, 2004. **49**(1): p. 1-14.

34.   Nasr, M., et al., Synthesis of novel ZnO/ZnAl 2 O 4 multi co-centric nanotubes and their long-term stability in photocatalytic application. RSC Advances, 2016. **6**(105): p. 103692-103699.

35. Kawahara, T., et al., A Patterned TiO2 (Anatase)/TiO2 (Rutile) Bilayer-Type Photocatalyst: Effect of the Anatase/Rutile Junction on the Photocatalytic Activity. Angewandte Chemie, 2002. **114**(15): p. 2935-2937.

36. Zhang, F., et al., Controllable synthesis of Ag@ TiO 2 heterostructures with enhanced photocatalytic activities under UV and visible excitation. RSC Advances, 2016. **6**(3): p. 1844-1850.

37. Yang, D., et al., Synthesis of Ag/TiO2 nanotube heterojunction with improved visible-light photocatalytic performance inspired by bioadhesion. The Journal of Physical Chemistry C, 2015. **119**(11): p. 5827-5835.

38. de Souza, M.L. and P. Corio, Effect of silver nanoparticles on TiO 2-mediated photodegradation of Alizarin Red S. Applied Catalysis B: Environmental, 2013. **136**: p. 325-333.

39. Zhang, H., et al., Tuning photoelectrochemical performances of Ag– TiO2 nanocomposites via reduction/oxidation of Ag. Chemistry of Materials, 2008. **20**(20): p. 6543-6549.

40. Goei, R. and T.-T. Lim, Ag-decorated TiO 2 photocatalytic membrane with hierarchical architecture: photocatalytic and anti-bacterial activities. Water research, 2014. **59**: p. 207-218.

41. Gao, G., et al., Designing nanoscaled hybrids from atomic layered boron nitride with silver nanoparticle deposition. Journal of Materials Chemistry A, 2014. **2**(9): p. 3148-3154.

Chapter 5: Optical and structural properties of Al$_2$O$_3$ doped ZnO nanotubes by ALD and their photocatalytic application

Table of Contents

1. Abstract

Al_2O_3 doped ZnO nanotubes with controlled ratio of Al_2O_3 were successfully designed by combining the two techniques of atomic layer deposition (ALD) and electrospinnig. In order to study the effect of Al_2O_3 doping on optical and structural properties of Al_2O_3 doped ZnO nanotubes, the prepared samples were analyzed by scanning electron microscopy (SEM), X-ray diffraction (XRD), energy-dispersive X-ray spectroscopy (EDX), Fourier-transform infrared (FTIR), reflectance emission and room temperature photoluminescence (PL). The photocatalytic activity of these materials under UV light was studied by the photodegradation of methyl orange (MO). The results indicate that Al_2O_3 doping increases the disorder (defects and oxygen vacancies formation) in the ZnO nanostructure which improves the separation efficiency of electron-hole pairs and therefore enhances the photocatalytic activity (5 times higher) of Al_2O_3 doped ZnO in comparison to pure ZnO nanotubes.

2. Introduction

This chapter focused on the synthesis of ZnO and Al_2O_3 /ZnO nanotubes by combining the two techniques electrospinning and atomic layer deposition (ALD). The morphological, structural and optical properties were analyzed with different characterization techniques. Different parameters have been calculated such as nanofibers' average diameter, grain size, lattice constants, interplane distance, strain values, Urbach energy and band gap. After evaluating the photocatalytic activity of the nanotubes under UV light, the impact of the optical properties on the photocatalytic activity was analyzed.

The green technology, "photocatalysis", is one of the less expensive and more efficient methods for wastewater treatment. In recent years, the attention of the researchers has been given to the semiconducting oxide photocatalysts due to their potential applications in solar energy conversion[1] and environmental purification [2]. Zinc oxide (ZnO) with a wide band gap (3.3 eV) is one of the most effective photocatalysts under UV light due to its high activity, low cost and environmental safety [3]. However, the fast electron-hole pairs' recombination in ZnO limits the high efficiency of the photocatalytic reaction [4]. In previous studies, many efforts have been developed to improve the separation efficiency of the photogenerated pairs, including doping ZnO with other oxides

(In_2O_3, SnO_2, NiO …).[5-7] It is well known that doping ZnO with Aluminum oxide (Al_2O_3) improves its optical and structural properties which will influence its photocatalytic activity [8]. Therefore, in order to study the effect of the optical properties on the photocatalytic activity, Al_2O_3 doped ZnO nanotubes were synthesized by combining the two techniques of Atomic Layer Deposition (ALD) and Electrospinning. ALD is a unique and powerful vapor-phase deposition technique to fabricate different oxides materials. The ALD technique ensures a precise thickness control, chemical composition, high quality conformal and homogenous deposited layers [9]. Electropsinning is a simple and cost effective technique that took much attention because of its capability in generating large amounts of nanofibers with the use of high electrical field [10]. In the present work, as a first step, PAN nanofibers were synthesized by electrospinning technique [11]. The second step is metal oxides deposition by ALD [12]. After the heat treatment, the prepared samples were characterized in order to study their structural, morphological and optical properties. The photodegradation of methyl orange under UV was investigated to study the photocatalytic activity of the ZnO and Al_2O_3/ZnO nanotubes.

3. Experimental section

3.1. Chemicals and materials

Diethyl zinc {(DEZ), Zn $(CH_2CH_3)_2$, 95%} and trimethylaluminum {(TMA), Al $(CH_3)_3$, 97%} were used as precursors for ZnO and Al_2O_3 respectively. N,N-dimethylformamide (DMF; 99.8%) and polyacrylonitrile (PAN; MW = 500 000) were used to elaborate PAN nanofibers. Methyl orange (MO) was used as a pollutant to evaluate the photocatalytic activity of the samples. All chemicals were purchased from Sigma Aldrich and used without any further purification.

3.2. Preparation of PAN nanofibers

The electrospinning process was used to synthesize PAN nanofibers. The polymer solution was prepared by dissolving 10 wt% of polyacrylonitrile in dimethylformamide. The mixture was maintained under agitation for 4 hours and then was loaded into a plastic syringe having a stainless steel needle with a diameter of 0.7 mm. The electrospinning process was performed at 38 ± 5°C with an applied voltage of 25 kV. The flow rate was fixed at 1 ml.h^{-1} and the distance between the tip of the needle and the aluminum foil was

maintained at 20 cm. Nanofibers were collected on a rotating coil covered with an aluminum foil with a rotation speed of 400 rpm.

3.3. ALD sequences

A homemade ALD reactor was used for the synthesis of ZnO and AL_2O_3/ZnO nanotubes. All the ALD depositions were performed at 60°C using the following sequence mentioned in Table 5.1. The precursor pulses were coupled with 25 sccm Ar flow as a gas vector; purge was performed with 100 sccm Ar flow as a gas vector. PAN nanofibers were heated at 500°C after the ALD deposition with a heating rate of $1°C.min^{-1}$ for 8 hours in air to eliminate the core of carbon in order to obtain ZnO and Al_2O_3/ZnO nanotubes. As shown in Table 5.2, Al_2O_3 doped ZnO nanotubes with different ratios of Zn/Al were obtained by alternating the deposition sequences of Al_2O_3 and ZnO cycles on the PAN nanofibers.

Table 5.1. Step time investigation of Al_2O_3 and ZnO deposition on PAN nanofibers.

	Pulse	Exposure	Purge	Water Pulse	Exposure	Purge
	Al_2O_3 (TMA)					
Time	0.2s	30s	40s	2s	30s	40s
	ZnO (DEZ)					
	0.4s	20s	40s	2s	30s	40s

Table 5.2. Deposition sequences of Al_2O_3 and ZnO cycles on the PAN nanofibers.

Samples	Deposition sequences		
	ZnO cycle	Al_2O_3 cycle	Repetition
ZnO	1	0	100
Al_2O_3/ZnO (5 wt%)	20	1	5
Al_2O_3/ZnO (10 wt%)	10	1	10

Al$_2$O$_3$/ZnO (20 wt%)	5	1	20

3.4. Chemical and structural characterization

Scanning electron microscopy (SEM) images were taken with a Hitachi S4800, Japan. Energy-dispersive X-ray spectroscopy analyses (EDX) were taken with a Zeiss EVO HD15 microscope coupled with an Oxford X-MaxN EDX detector. X-ray diffraction (XRD) measurements were carried out using a PANAlytical Xpert-PRO diffractometer equipped with an X'celerator detector using Ni-filtered Cu-radiation (λ= 1.54 ˚A). Optical properties were analyzed by diffuse reflectance (Shimadzu UV-3600). Photoluminescence (PL) spectra of Al$_2$O$_3$/ZnO nanotubes were measured in the range of 350-850 nm using HR2000+ Ocean Optics spectrometer (USA). Excitation of photoluminescence was performed by nitrogen laser LGI (Russia) (λ=337 nm, output power 2.5 mW, 100 Hz).

3.5. Measurement of photocatalytic activity

The photocatalytic activity of ZnO and Al$_2$O$_3$ doped ZnO nanotubes was evaluated by the degradation of methyl orange (MO) solution under UV light irradiation (obtained from a 400 W light source, emission wavelength < 380 nm). The reaction temperature was kept constant at 25 ± 2°C by circulating water in a cylindrical tube surrounding the photo-reactor during the entire experiment. MO was used as a reference for organic pollutants. The decomposition was carried out in several beakers containing a suspension of 10 mg from each photocatalyst and 25 mL of MO solution (20 mg.L^{-1}). Prior to light irradiation, the suspension was stirred for 1 h in the dark to obtain a good dispersion and to reach the adsorption-desorption equilibrium. Then, the solution was irradiated with UV light for 45 minutes. The distance between the lamp and the dye solution was maintained at 10 cm. Every 15 min, 3 ml of the sample solution was taken out and centrifuged to remove the catalyst. The centrifuged solutions were analyzed by a UV-VIS spectrometer in order to evaluate the decrease in the dye concentration. After irradiation, the photocatalytic degradation efficiency percentage has been calculated as follow [13]:

$$\text{Degradation efficiency (\%)} = (C_0 - C)/C_0 \times 100 \qquad \text{(Equation 1)}$$

Where C_0 is the initial concentration and C is the final concentration of dye before and after photo-irradiation respectively.

4. Results and discussion

4.1. Morphological and Structural properties of ZnO and Al$_2$O$_3$/ZnO nanotubes

The nanotubes of ZnO and Al$_2$O$_3$ doped ZnO were elaborated by combining the two techniques: Electrospinning and ALD. After the heat treatment, the morphological properties of the as-prepared samples were analyzed by scanning electron microscopy. The SEM images in Figure 5.1 show the well-defined nanotubes morphology of ZnO, Al$_2$O$_3$/ZnO (5 wt%), Al$_2$O$_3$/ZnO (10 wt%) and Al$_2$O$_3$/ZnO (20 wt%). The average diameter was measured on 100 randomly chosen nanotubes of each sample. The diameters were measured from the SEM images using image analysis software (Image J1.29X). No significant changes were detected in the average diameter of the prepared nanotubes; the obtained value was 300 ± 20 nm for all samples. EDX data of ZnO and Al$_2$O$_3$/ZnO nanotubes reported in table 5.3 show the presence of the three elements Zn, Al and O without detection of any impurities. In addition, the increase of the atomic percentage of Al with the doping amount of Al$_2$O$_3$ can be clearly seen from table 5.3.
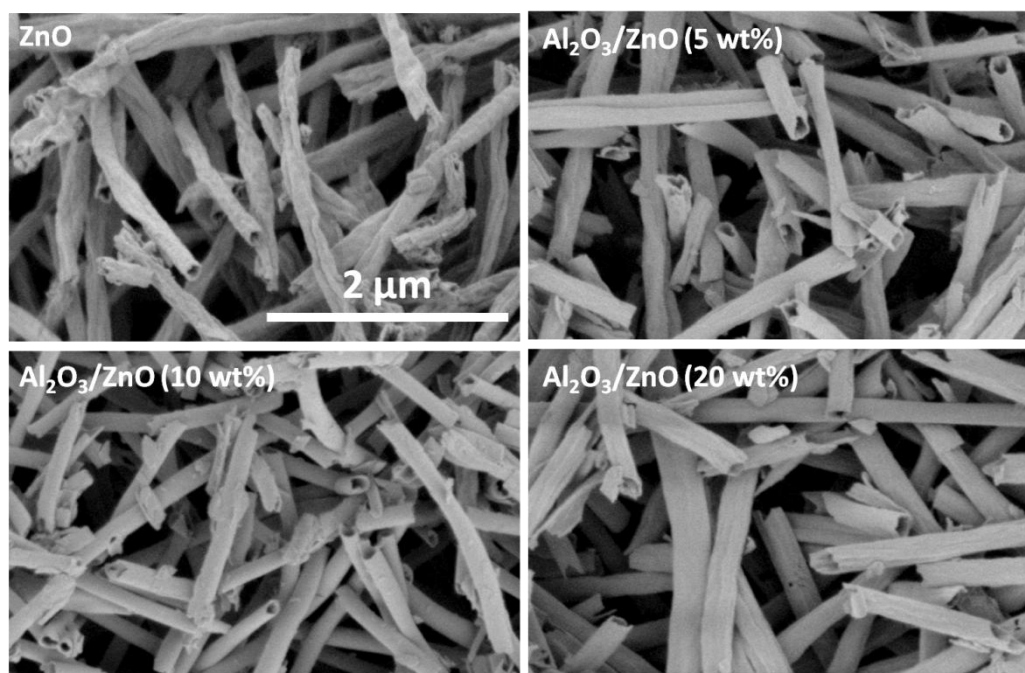
Figure 5.1. Scanning Electron Microscope images of ZnO and Al_2O_3 doped ZnO annealed nanotubes in air for 8h at 500°C.

Table 5.3. EDX data showing the atomic percentage composition of ZnO and Al_2O_3/ZnO prepared samples.

Samples	Atomic percentage		
	Zn	**Al**	**O**
ZnO	48.24	-	51.76
Al_2O_3/ZnO (5 wt%)	48.92	3.70	47.37
Al_2O_3/ZnO (10 wt%)	36.66	7.98	55.35
Al_2O_3/ZnO (20 wt%)	36.34	13.62	50.03

The XRD patterns of the prepared samples presented in Figure 5.2 show the diffraction peaks of the hexagonal wurtzite crystalline phase of zinc oxide (100), (002), (101), (102), (110), (103), (200), (112) and (201) corresponding to 2θ = 31.7°, 34.4°, 36.2°, 47.5°, 56.5°, 62.8°, 66.3°, 67.9° and 69.0°, respectively.[14] The peak shift towards higher values of 2θ and the peak widening were observed with the increase of Al_2O_3 concentration. Lattice

constants (a and c), and interplane distances (d) were calculated from XRD data (Table 5.4). The increase of Al_2O_3 concentration results in a decrease of the lattice constants and interplane distances. The mechanism of these structural changes is related to the substitution of Zn^{2+} ions with Al^{3+} ions. As the radius of Al^{3+} ion (0.053 nm) is much lower than the radius of Zn^{2+} ion (0.074 nm), a decrease of lattice constants is expected with an increase of Al_2O_3 dopant concentration [15]. The average grain size D (nm) was calculated using Debye-Scherrer equation [16]:

$$D = k\lambda/\beta cos\vartheta \qquad \text{(Equation 2)}$$

where k is the shape factor constant (0.9), λ is the X-ray wavelength (0.154 nm), β is the line broadening of the diffraction line measured by the full width at half maximum of the peak intensity (FWHM) and θ is the Bragg angle (in degrees).The obtained grain size values were 16 nm, 10 nm, 9 nm and 9 nm for ZnO, Al_2O_3/ZnO (5 wt%), Al_2O_3/ZnO (10 wt%) and Al_2O_3/ZnO (20 wt%), respectively. The decrease of the crystalline structure of ZnO with Al_2O_3 doping amount is due to the amorphous state of Al_2O_3. Thus, the growth of ZnO crystals is stopped by the amorphous Al_2O_3 layers. [8] Strain values (ε) were calculated due to the following equation:

$$\varepsilon = \beta/4tan(\vartheta) \qquad \text{(Equation 3)}$$

where θ and β are diffraction angle and full width of half maximum, respectively. The obtained strain values were 0.0068, 0.01, 0.011 and 0.012 for ZnO, Al_2O_3/ZnO (5 wt%), Al_2O_3/ZnO (10 wt%) and Al_2O_3/ZnO (20 wt%), respectively.
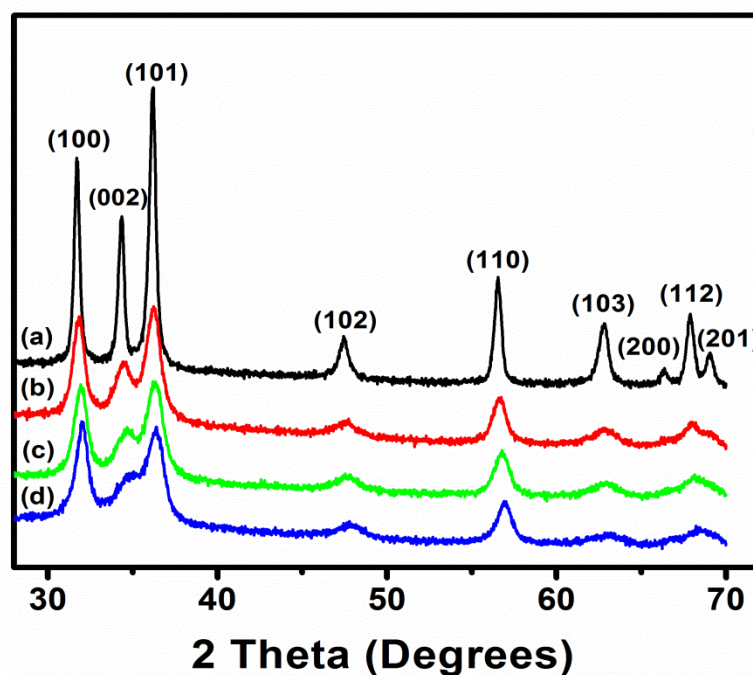
Figure 5.2. XRD spectra of (a) ZnO, (b) Al_2O_3/ZnO (5 wt%), (c) Al_2O_3/ZnO (10 wt%) and (d) Al_2O_3/ZnO (20 wt%) annealed nanotubes.

Table 5.4. Lattice constants and interplane distances of the prepared nanotubes.

	a (nm)	c (nm)	d (100)	d (002)	d (101)
ZnO	0.325	0.521	0.282	0.261	0.248
Al_2O_3/ZnO (5 wt%)	0.324	0.519	0.281	0.260	0.247
Al_2O_3/ZnO (10 wt%)	0.323	0.517	0.280	0.258	0.246
Al_2O_3/ZnO (20 wt%)	0.322	0.516	0.279	0.258	0.245

4.2. Optical properties of ZnO and Al_2O_3/ZnO nanotubes

Reflectance spectra of ZnO and Al_2O_3/ZnO nanotubes samples are shown in Figure 5.3. A blue shift of the absorption edge of Al_2O_3/ZnO samples was found with the increase of Al_2O_3 doping concentration compared to ZnO nanotubes. Band gap energies of the samples were calculated from the reflectance spectra:[9]

$$(Fhv)^2 \sim (E_g - hv) \qquad \text{(Equation 4)}$$

where hv and E_g are the photon energy and the band gap, respectively. Parameter F, related to the absorption coefficient of the sample, was calculated as follow:[9]

$$F = \frac{(1-R)^2}{2R} \qquad \text{(Equation 5)}$$

where R is diffuse reflectance of the sample. The calculated band gap values are shown in Table 5.5. The increase of band gap of Al_2O_3/ZnO samples was observed with the increase of Al_2O_3 dopant amount. Previously, we have reported on optical properties of Al_2O_3/ZnO nanolaminates [17]. It was shown that Al_2O_3 sublayers changed the growth of ZnO nanolayers. Analysis of XRD and optical constants (refractive index and extinction coefficient) showed that Al_2O_3 do not dope ZnO during the growth. The blue shift of the band gap was supposedly due to the quantum confinement effect. In the present work, doping of ZnO with Al_2O_3 was proved by XRD data. The obtained grain size values are much higher than Bohr radius for ZnO (2.37 nm). Therefore, the blue shifted band gap value is due to Burstein-Moss effect [18]. The band gap of Al_2O_3/ZnO nanotubes (E_g) depends on the concentration of free electrons (n) as follow [15]:

$$E_g = E_{g0} + \frac{h^2}{8 \cdot m^*} \cdot \left(\frac{3}{\pi}\right)^{2/3} \cdot n^{2/3} \qquad \text{(Equation 6)}$$

where, E_{g0}, h and m^* are the band gap of undoped ZnO nanotubes, the Plank's constant and the effective mass of electron, respectively. The obtained dependence of n vs Al_2O_3 dopant concentration is plotted in Figure 5.4. The concentration of free electrons linearly increased with Al_2O_3 doping. Therefore more electrons are available to take part in the photodegradation process compared to pure ZnO nanotubes. Urbach tail energy is an important parameter, which can assist the analysis of disorder in metal oxide nanostructure. It can be calculated from absorption spectrum using the following equation [17]:

$$F = F_0 \cdot e^{\frac{hv - E_0}{E_u}} \qquad \text{(Equation 7)}$$

F_0 and E_0 are specific parameters of the material; hv and E_u are the photon energy and Urbach energy, respectively. Parameter F was calculated using equation 7. The obtained E_u values are plotted in Figure 5.4. The increase of Al_2O_3 dopant concentration resulted in an

increase of E_u, which can be related to the formation of defect states in the band gap of ZnO (Al^{3+} states, zinc interstitials, zinc vacancies …). From the obtained results, the photocatalytic activity under UV irradiation of Al_2O_3 doped ZnO is expected to be enhanced compared to pure ZnO nanotubes.
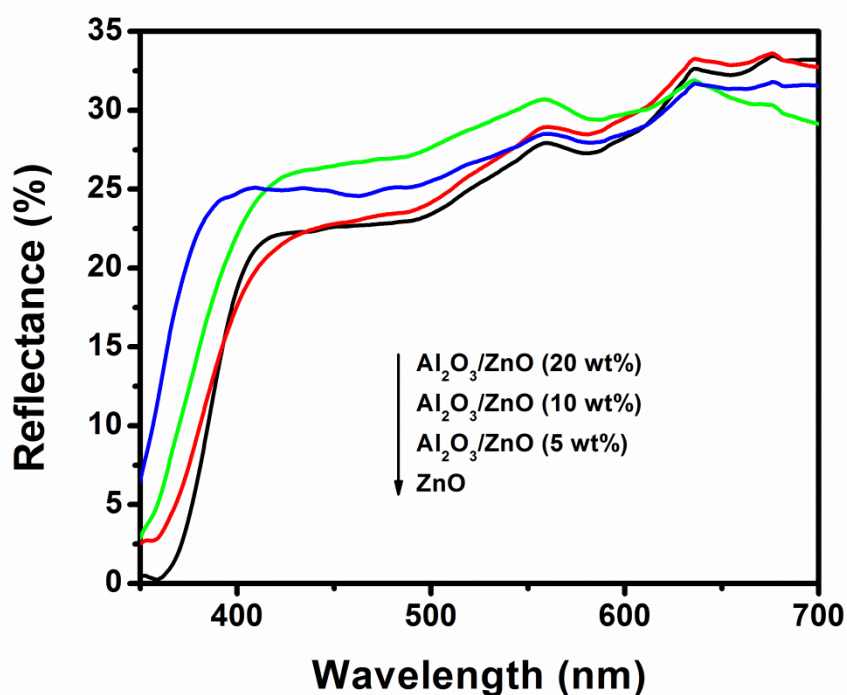
Figure 5.3. Reflectance spectra of ZnO, Al_2O_3/ZnO (5 wt%). Al_2O_3/ZnO (10 wt%) and Al_2O_3/ZnO (20 wt%) nanotubes.

Table 5.5. Band gap energies of ZnO and Al_2O_3/ZnO nanotubes.

Nanotubes	ZnO	Al_2O_3/ZnO (5 wt%)	Al_2O_3/ZnO (10 wt%)	Al_2O_3/ZnO (20 wt%)
E_g (eV)	3.18	3.24	3.31	3.42
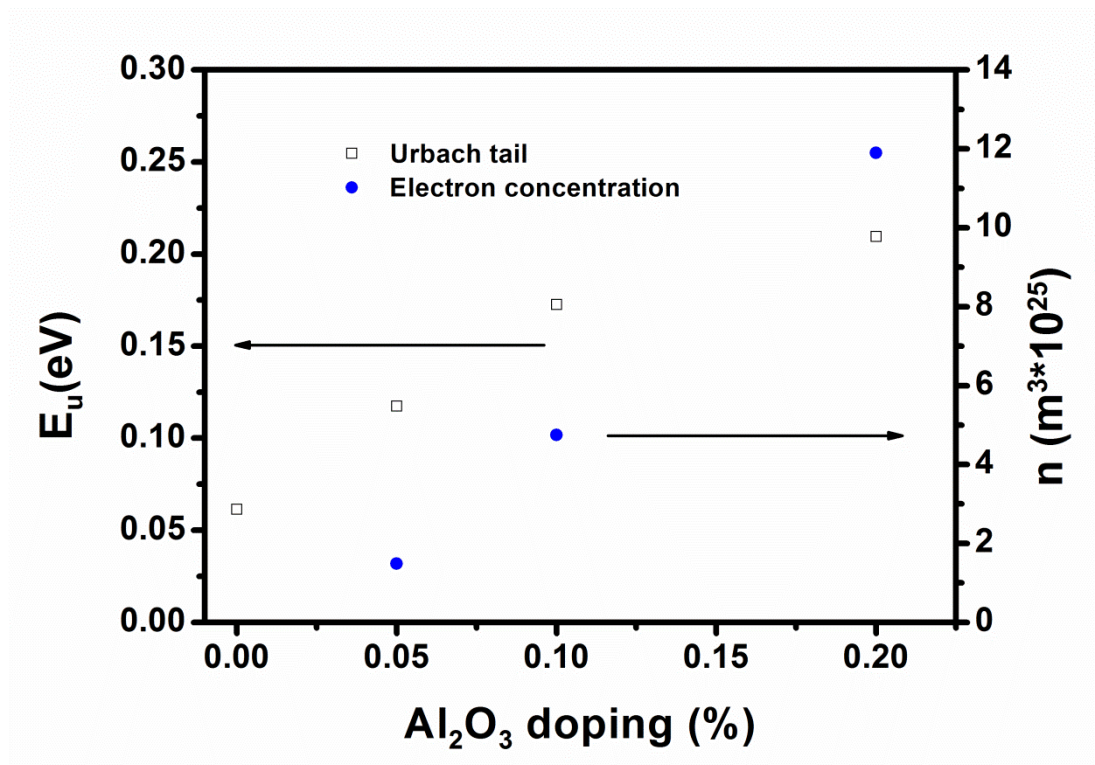
Figure 5.4. Evaluation of Urbach tail and free electron concentration with Al_2O_3 doping amounts.

Photoluminescence spectra of ZnO and Al_2O_3/ZnO nanotubes are shown in Figure 5.5. ZnO nanotubes showed PL spectrum with two emission bands in UV and Visible regions, centred at 385 and 570 nm, respectively. Al_2O_3 doped ZnO resulted in a change of the PL spectra. The wide emission bands were found at 420-440 nm and 490-560 nm for doped ZnO nanotubes with different concentration of Al_2O_3. Deconvolution of the PL spectra was performed with Gauss fitting using Origin software and the calculated peak positions are summarized in Table 5.6. For undoped ZnO, the PL peaks correspond to exciton emission (385 nm), shallow defects (406 nm), oxygen vacancies (502 and 550 nm) and oxygen interstitials (621 nm) [19]. PL spectra of Al_2O_3/ZnO drastically depend on Al_2O_3 dopant concentration. At low doping concentration (5 wt%) a new peak related to Zn interstitials was observed at 416 nm. PL peaks in the range of 425-436 could correspond to Zn vacancies. PL peaks in the range of 470-595 nm correspond to oxygen vacancies with different charge states (neutral, single and double ionized). PL peaks in the range of 630-710 nm correspond to donor-acceptor pairs, formed by Al^{3+} donor level and acceptor sites.[20, 21] As shown in Figure 5.5, PL spectra shift towards IR region when Al_2O_3 dopant amount

increases. It was shown that Al_2O_3 dopant induced compressive strain and therefore defect formation. Oxygen vacancies are mostly formed within Al_2O_3 doping as discussed by Jule et al. [20] Therefore, IR shift of PL for highly doped ZnO is related to oxygen vacancies. Appearance of new peaks in the region of 634-710 could be due to the optical transitions between Al^{3+} donor sites and ionized oxygen vacancies.
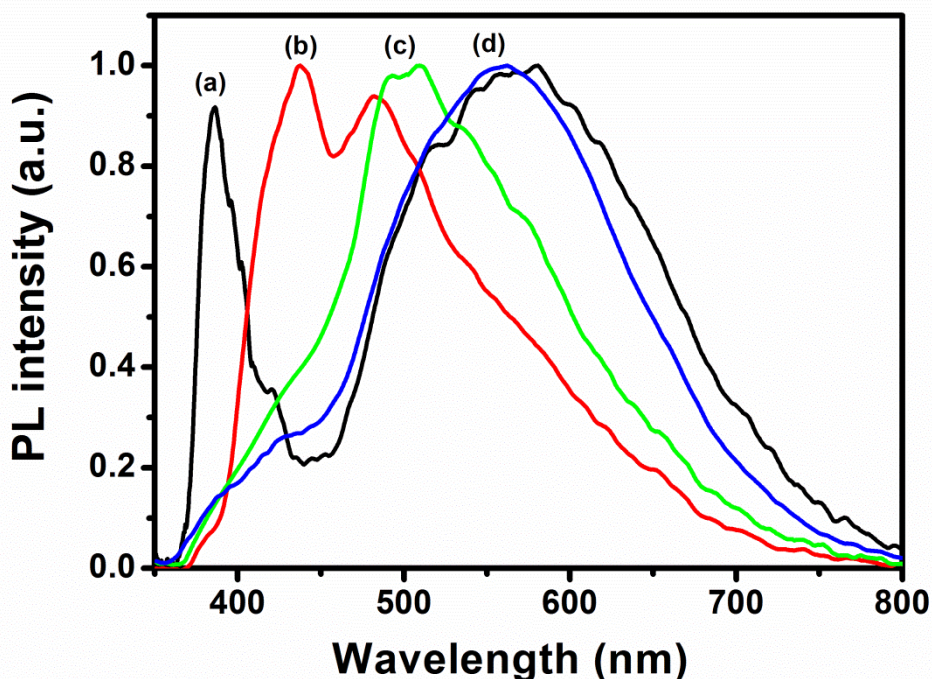
Figure 5.5. Photoluminescence spectra of (a) ZnO, (b) Al_2O_3/ZnO (5 wt %), (c) Al_2O_3/ZnO (10 wt%) and (d) Al_2O_3/ZnO (20 wt%) nanotubes.

Table 5.6. Peak positions of ZnO and Al_2O_3/ZnO nanotubes with different Al_2O_3 amounts.

		ZnO	Al_2O_3/ZnO (5 wt%)	Al_2O_3/ZnO (10 wt%)	Al_2O_3/ZnO (20 wt%)
Peak positions (nm)		385	416	434	425
		406	439	496	498
		502	475	536	546

550	521	560	595
621	604	634	653
-	-	709	680

The infrared spectrum of Al_2O_3 doped ZnO with different amounts of Al_2O_3 in the range 400–3500 cm^{-1} are represented in Figure 5.6. The FTIR analysis allows us to observe two bands around 656 cm^{-1} and 715 cm^{-1}. The first one can be assigned to the Al-O stretching mode in octahedral structure and the second one corresponds to the tetrahedral Al-O bonds.[22] As we can note, the intensity of these bands is slightly increasing with Al_2O_3 amount deposited by ALD. Thus, the presence of Al_2O_3 phase in the prepared samples was detected as well by IR spectroscopy.
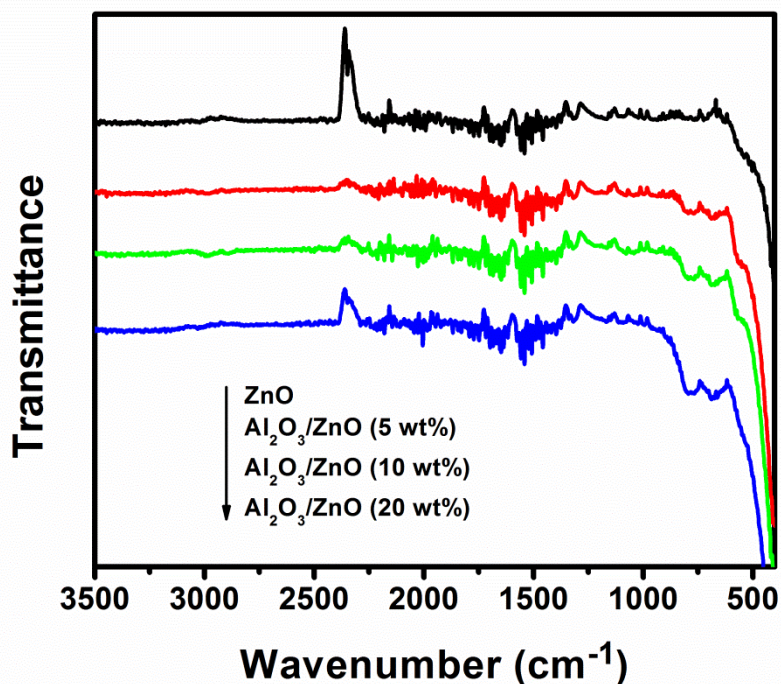
Figure 5.6. FTIR spectra of ZnO, Al_2O_3/ZnO (5 wt%). Al_2O_3/ZnO (10 wt%) and Al_2O_3/ZnO (20 wt%) nanotubes.

4.3. Photocatalytic activity

To evaluate the photodegradation efficiency of the as prepared samples under UV light (< 380 m), MO (major absorption band around 462 nm) was selected as model pollutant. Figure 5.7 shows the photodegradation curves of MB after 45 minutes with ZnO and Al_2O_3/ZnO nanotubes as catalysts. As results, it was found that in the absence of photocatalysts, MB was stable and difficult to be photodegraded under UV light. Under identical experimental conditions, the photodegradation percentages of Methylene blue were 57%, 80%, 89% and 98% in the presence of ZnO, Al_2O_3/ZnO (5 wt%), Al_2O_3/ZnO (10 wt%) and Al_2O_3/ZnO (20 wt%) nanotubes, respectively. As confirmed above by optical and structural analysis, the concentration of free electrons and the defects formation linearly increased with Al_2O_3 doping amount, thus the recombination of electron-hole pairs decreased. Therefore, the photodegradation activity of Al_2O_3/ZnO under UV light is increased with Al_2O_3 doping concentration. As shown in Figure 5.8, the photocatalytic reactions follow a Langmuir–Hinshelwood first order kinetics model [23]:

$$r = dC/dt = kKC/(1+KC) \qquad \text{(Equation 8)}$$

where r, C, t, k and K are the degradation rate of MB (mg $(L\ min)^{-1}$), the concentration of the MB solution (mg L^{-1}), the irradiation time, the reaction rate constant (mg $(L\ min)^{-1}$), and the adsorption coefficient of MB (mg L^{-1}), respectively. The relationship between $\ln(C_0/C)$ and reaction time t is presented as follow:

$$\ln(C_0/C) = kKt = k_a t \qquad \text{(Equation 9)}$$

where k_a and C are the apparent first-order rate constant (min^{-1}) and the concentration at time t, respectively. The k_a and R square value are reported in Table 5.7. The maximum rate constant (0.0884 min^{-1}) correspond to Al_2O_3/ZnO (20 wt%) sample which is 5, 3 and 2 times higher than that of pure ZnO, Al_2O_3/ZnO (5 wt%) and Al_2O_3/ZnO (10 wt%), respectively. Thus the Al_2O_3 doping effect improves the photocatalytic activity of ZnO under UV light.
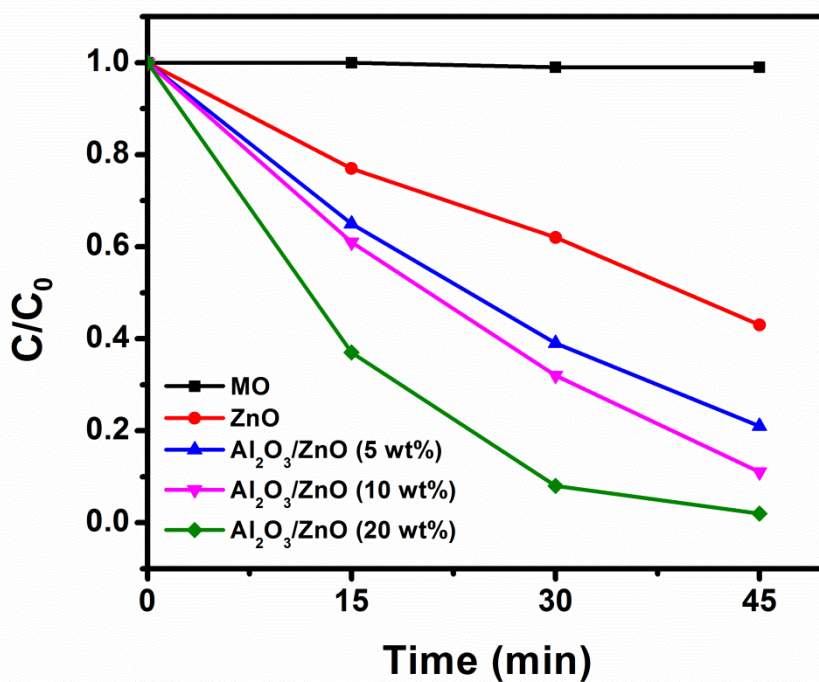
Figure 5.7. Photodegradation of MO by ZnO, Al$_2$O$_3$/ZnO (5 wt%). Al$_2$O$_3$/ZnO (10 wt%) and Al$_2$O$_3$/ZnO (20 wt%) photocatalysts under UV light.
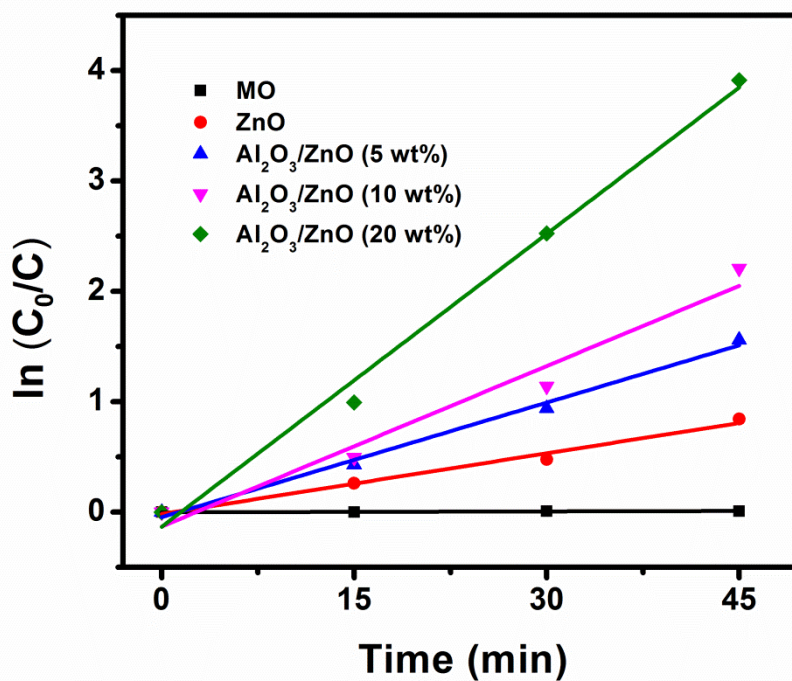
Figure 5.8. Kinetics of methyl orange degradation by the prepared samples.

Table 5.7. Kinetic parameters of ZnO and Al$_2$O$_3$/ZnO nanotubes.

	k$_a$ (min^{-1})	R^2
MO	0.0002	0.9428
ZnO	0.0183	0.9819
Al$_2$O$_3$/ZnO (5 wt%)	0.0346	0.9901
Al$_2$O$_3$/ZnO (10 wt%)	0.0484	0.9527
Al$_2$O$_3$/ZnO (20 wt%)	0.0884	0.9895

5. Conclusion

ZnO and Al$_2$O$_3$/ZnO nanotubes with controlled doping ratio of Al$_2$O$_3$ are successfully prepared by elecrospinning and atomic layer deposition techniques. All prepared samples were annealed at 500°C in air. After calcination, SEM images showed the nanotubes' morphology of ZnO and Al$_2$O$_3$/ZnO samples. EDX data confirmed the increase of Al atomic percentage with the increasing of Al$_2$O$_3$ doping amount. The decrease of the crystalline structure due to the amorphous structure of Al$_2$O$_3$ and the increase of the strain values with Al$_2$O$_3$ doping concentration were detected from XRD data. The blue shift of Al$_2$O$_3$/ZnO band gap value due to the Burstein-Moss effect and the defect formation was confirmed by diffuse reflectance analysis. PL spectra analysis revealed that oxygen vacancies results in the IR shift of doped ZnO nanotubes. The photocatalytic degradation of methyl orange under UV light by Al$_2$O$_3$/ZnO (20 wt%) was 5 times higher than that of ZnO nanotubes. In conclusion, the defects formation and oxygen vacancies due to Al$_2$O$_3$ doping increase the charge separation efficiency of ZnO, thus enhancing its photoactivity under UV light. Therefore, the photocatalytic activity is greatly depending on the optical and structural properties of the material. The ability to tune the optical and structural properties of our synthesized materials could be promising in different applications such as the production of optical sensors and biosensors [24-27].

References

1.   Elias, J., et al., Electrochemical growth of ZnO nanowires on atomic layer deposition coated polystyrene sphere templates. Electrochimica Acta, 2013. **110**: p. 387-392.

2.   Chen, J., et al., Recent progress in enhancing photocatalytic efficiency of TiO 2-based materials. Applied Catalysis A: General, 2015. **495**: p. 131-140.

3.   Bechelany, M., et al., ZnO nanotubes by template-assisted sol–gel route. Journal of Nanoparticle Research, 2012. **14**(8): p. 980.

4.   Georgekutty, R., M.K. Seery, and S.C. Pillai, A highly efficient Ag-ZnO photocatalyst: synthesis, properties, and mechanism. The Journal of Physical Chemistry C, 2008. **112**(35): p. 13563-13570.

5.   Zheng, L., et al., Network structured SnO2/ZnO heterojunction nanocatalyst with high photocatalytic activity. Inorganic Chemistry, 2009. **48**(5): p. 1819-1825.

6.   Wang, Z., et al., Highly photocatalytic ZnO/In2O3 heteronanostructures synthesized by a coprecipitation method. The Journal of Physical Chemistry C, 2009. **113**(11): p. 4612-4617.

7.   Hameed, A., et al., Photocatalytic decolourization of dyes on NiO–ZnO nano-composites. Photochemical & Photobiological Sciences, 2009. **8**(5): p. 677-682.

8.   Viter, R., et al., Enhancement of electronic and optical properties of ZnO/Al2O3 nanolaminate coated electrospun nanofibers. The Journal of Physical Chemistry C, 2016. **120**(9): p. 5124-5132.

9.   Baitimirova, M., et al., Tuning of Structural and Optical Properties of Graphene/ZnO Nanolaminates. The Journal of Physical Chemistry C, 2016. **120**(41): p. 23716-23725.

10.   Nasr, M., et al., Photoluminescence: A very sensitive tool to detect the presence of anatase in rutile phase electrospun TiO 2 nanofibers. Superlattices and Microstructures, 2015. **77**: p. 18-24.

11.   Selloum, D., et al., A highly efficient gold/electrospun PAN fiber material for improved laccase biocathodes for biofuel cell applications. Journal of Materials Chemistry A, 2014. **2**(8): p. 2794-2800.

12.   Cabello-Aguilar, S., et al., Slow translocation of polynucleotides and their discrimination by α-hemolysin inside a single track-etched nanopore designed by atomic layer deposition. Nanoscale, 2013. **5**(20): p. 9582-9586.

13.   Konstantinou, I.K. and T.A. Albanis, TiO 2-assisted photocatalytic degradation of azo dyes in aqueous solution: kinetic and mechanistic investigations: a review. Applied Catalysis B: Environmental, 2004. **49**(1): p. 1-14.

14.   Nasr, M., et al., Synthesis of novel ZnO/ZnAl 2 O 4 multi co-centric nanotubes and their long-term stability in photocatalytic application. RSC Advances, 2016. **6**(105): p. 103692-103699.

15.   Zhai, C.-H., et al., Effects of Al Doping on the Properties of ZnO Thin Films Deposited by Atomic Layer Deposition. Nanoscale Research Letters, 2016. **11**(1): p. 407.

16.   Nasr, M., et al., Enhanced photocatalytic performance of novel electrospun BN/TiO 2 composite nanofibers. New Journal of Chemistry, 2017. **41**(1): p. 81-89.

17.   Chaaya, A.A., et al., Tuning optical properties of Al2O3/ZnO nanolaminates synthesized by atomic layer deposition. The Journal of Physical Chemistry C, 2014. **118**(7): p. 3811-3819.

18.   Chaaya, A.A., et al., Optical and structural properties of Al2O3/ZnO nanolaminates deposited by ALD method. Physica status solidi (c), 2014. **11**(9-10): p. 1505-1508.

19.   Chaaya, A.A., et al., Evolution of microstructure and related optical properties of ZnO grown by atomic layer deposition. Beilstein journal of nanotechnology, 2013. **4**(1): p. 690-698.

20.   Jule, L., et al., Defect-induced room temperature ferromagnetic properties of the Al-doped and undoped ZnO rod-like nanostructure. Materials Letters, 2017.

21.   Sandeep, K., S. Bhat, and S. Dharmaprakash, Structural, optical, and LED characteristics of ZnO and Al doped ZnO thin films. Journal of Physics and Chemistry of Solids, 2017.

22.   Djebaili, K., et al., XPS, FTIR, EDX, and XRD analysis of Al2O3 scales grown on PM2000 alloy. Journal of Spectroscopy, 2015. **2015**.

23.   Nasr, M., et al., Enhanced Visible-Light Photocatalytic Performance of Electrospun rGO/TiO2 Composite Nanofibers. The Journal of Physical Chemistry C, 2016.

24.   Tereshchenko, A., et al., Optical biosensors based on ZnO nanostructures: advantages and perspectives. A review. Sensors and Actuators B: Chemical, 2016. **229**: p. 664-677.

25.   Tereshchenko, A., et al., ZnO films formed by atomic layer deposition as an optical biosensor platform for the detection of Grapevine virus A-type proteins. Biosensors and Bioelectronics, 2016.

26.   Choi, A., et al., ZnO nanowire biosensors for detection of biomolecular interactions in enhancement mode. Sensors and Actuators B: Chemical, 2010. **148**(2): p. 577-582.

27.   Joshi, A.G., et al., Valence band and core-level analysis of highly luminescent ZnO nanocrystals for designing ultrafast optical sensors. Applied Physics Letters, 2010. **96**(12): p. 123102.

Chapter 6: Synthesis of Novel ZnO/ZnAl$_2$O$_4$ Multi Co-Centric Nanotubes and their Photocatalytic Application

Table of Contents

1. Abstract

Based on the Kirkendall effect, novel double, triple and quadruple co-centric nanotubes of ZnO/ZnAl$_2$O$_4$ have been successfully fabricated by combining the two techniques of Electrospinning and Atomic Layer Deposition. The as-prepared samples were annealed at 900°C under air. Their morphological, structural and optical properties were studied by Scanning Electron Microscopy (SEM), X-ray Diffraction (XRD), Energy-Dispersive X-ray spectroscopy (EDX), UV-Visible spectrophotometry and Raman spectroscopy. The performances and long-term stability of these multi co-centric nanotubes for photocatalytic applications have been evaluated under the same conditions. As result, the triple and quadruple co-centric nanotubes of ZnO/ZnAl$_2$O$_4$ exhibit a higher activity (94% and 99%, respectively) compared to the pure ZnO reported in previous studies (28%) in the photodegradation of methyl orange (MO) under UV irradiation. Thus, the fact of coupling these two semiconductors ensured a high photocatalytic activity and long term stability.

2. Introduction

Zinc aluminate (ZnAl$_2$O$_4$) is a spinel type oxide, which has high chemical and thermal stability, low surface acidity and high mechanical resistance as a bulk [1]-[2]. Zinc aluminate was considered as an attractive material for different applications, such as optical coating or host matrix, high temperature ceramic material, catalyst and catalyst support [3]-[4]. ZnAl$_2$O$_4$ is a naturally available mineral commonly called gahnite with a normal spinel structure having all zinc cations in the tetrahedral and all aluminum cations in the octahedral sites of the cubic face-centered lattice of oxygen anions [5]. ZnAl$_2$O$_4$ is also a semiconductor material suitable for ultraviolet (UV) photoeletronic application due it wide energy bandgap (about 3.8 eV) [6]. Few studies involving the degradation of organic dyes using ZnO/ZnAl$_2$O$_4$ as a photocatalyst are reported in the literature [4]-[7]-[8]. Zhang et al. [9] prepared ZnO/ZnAl$_2$O$_4$ composite hollow microspheres using hydrothermal method. Zhao et al. [10] dispersed the ZnAl$_2$O$_4$ nanoparticles inside a network of ZnO. They reported that the effect of coupling both ZnO and ZnAl$_2$O$_4$ phase in the ZnO/ZnAl$_2$O$_4$ nanocomposite ensured the efficient separation of photogenerated e$^-$ and h$^+$ pairs, which was prerequisite for the enhancement of the photocatalytic performance.Therefore, in order to enhance the

photocatalytic activity and the long term stability, novel $ZnO/ZnAl_2O_4$ multi co-centric nanotubes were synthesized by combining the two techniques: electrospinning and atomic layer deposition (ALD).

In this chapter, we report the fabrication of a novel morphology of multi co-centric nanotubes of $ZnO/ZnAl_2O_4$ and we study for the first time their long term stability in photocatalytic performance. Herein, we combine the electrospinning and ALD techniques to elaborate double, triple and quadruple co-centric nanotubes of $ZnO/ZnAl_2O_4$ based on the kirkendall effect between aluminum oxide and zinc oxide [11]. Electrospun PAN was used as template for the multi co-centric nanotubes of $ZnO/ZnAl_2O_4$. The structural, morphological and optical properties of the prepared samples were analyzed. The re-use of photocatalysts is so important, therefore the performances of these materials for long term stability and the photocatalytic degradation of methyl orange (MO) under UV have also been evaluated.

3. Experimental Section

3.1. Chemicals and Materials

Diethyl Zinc {(DEZ), Zn $(CH_2CH_3)_2$, 95%}, Trimethylaluminum {(TMA), Al $(CH_3)_3$, 97%}, N, N-Dimethylformamide (DMF; 99.8%), Polyacrylonitrile (PAN; MW= 500 000) and methyl orange (MO) were purchased from Sigma Aldrich. All chemicals were used without any further purification.

3.2. Preparation of PAN nanofibers

Electrospinning solution was prepared by dissolving 10 wt. % of polyacrilonitrile in dimethylformamide [12]. The solution was maintained under agitation for 4 hours. The polymer solution was loaded into a plastic syringe having a stainless steel needle with a diameter of 0.7 mm at a constant flow rate of 1 ml/h. The electrospinning process was performed at 38 ± 5°C in an ambient atmosphere under an applied voltage of 25 kV. Nanofibers were collected on a rotating coil covered with an aluminum foil with a rotation speed of 400 rpm. The distance between the tip of the needle and the aluminum foil was maintained at 20 cm.

3.3. ALD sequences

The ALD was performed using a homemade reactor [13]. All the ALD depositions were performed at 60°c using the following sequence mentioned in Table 6.1. All precursor pulses were coupled with 25 Sccm Ar flow as gas vector; purge was performed with 100 Sccm Ar flow as gas vector. After ALD deposition PAN fibers were heated at 450°C with a heating rate of $1°C.min^{-1}$ for 8 h in air to eliminate the core of carbon, and then calcined at 900°C for 12 h in order to obtain $ZnO/ZnAl_2O_4$ co-centric nanotubes. As shown in Table 6.2, double, triple and quadruple co-centric nanotubes of $ZnO/ZnAl_2O_4$ were obtained by alternating the deposition sequences of Al_2O_3 and ZnO cycles on the PAN nanofibers.

Table 6.1. Step time investigation of Al_2O_3 and ZnO deposition on PAN nanofibers.

	Pulse	Exposure	Purge	Water Pulse	Exposure	Purge
Time	Al_2O_3 (TMA)					
	0.1s	30s	40s	2s	30s	40s
	ZnO (DEZ)					
	0.2s	20s	40s	2s	30s	40s

Table 6.2. Deposition sequences of Al_2O_3 and ZnO cycles on the PAN nanofibers.

$ZnO/ZnAl_2O_4$ co-centric nanotubes	Deposition sequences
Double	$100Al_2O_3/200ZnO/100Al_2O_3$
Triple	$100Al_2O_3/200ZnO/100Al_2O_3/200ZnO/100Al_2O_3$
Quadruple	$100Al_2O_3/200ZnO/100Al_2O_3/200ZnO$ $/100Al_2O_3/200ZnO/100Al_2O_3$

3.4. Chemical and Structural Characterization

X-ray diffraction (XRD) measurements were carried out using a PANAlytical Xpert-PRO diffractometer equipped with an X'celerator detector using Ni-filtered Cu-radiation (λ= 1.54 ˚A). Scanning electron microscopy (SEM) images were taken with a Hitachi S4800, Japan. The UV–Vis absorbance spectra of methyl orange were recorded by a Jasco V-570 UV–VIS-NIR spectrophotometer. Raman spectra have been obtained with a Horiba spectrometer, λ= 659 nm. Energy-Dispersive X-ray spectroscopy analysis (EDX) was taken with Zeiss EVO ED15 microscope coupled with an Oxford X-MaxN EDX detector. Photoluminescence and reflectance measurements have been performed using fiber optic technique measurement system. Nitrogen laser (340 nm, 0.4 mW, 100 Hz) has been used as excitation source. The emission spectra have been measured with Ocean Optic spectrometer HR2000+, equipped with optical fiber and collecting lenses. The SpectraSuit software was used for collecting spectra in MSExcel files. Reflectance spectra were measured using reflectance Y-probe and UV-Vis Ocean Optics light source (DT-MINI-2-GS). The PL and reflectance spectra were recorded in the range of 360-750 nm and 380-800 nm, respectively.

3.5. Photocatalytic activity measurement

Methyl orange (MO) was used as a reference for organic pollutant to evaluate the photocatalytic activity of the ZnO/ZnAl$_2$O$_4$. The photocatalytic performance of the samples was evaluated by analyzing the decrease in concentration of the MO during exposure to UV light irradiation. The reaction temperature was kept constant at 25 ± 0.2 °C by circulating water in a cylindrical tube surrounding the photo-reactor during the entire experiment. The decomposition was carried out in many beakers containing a suspension of 10 mg of each sample in 25 ml of MO solution (10 mg/L) under UV light irradiation (obtained from a 400 W light source, emission wavelength 300 - 400 nm). The distance between the lamp and the dye solution was maintained at 10 cm. The solution was irradiated with UV light for 3 hours. Each 1 hour, 3 ml of the sample solution was taken out and centrifuged to remove the catalyst. The centrifuged solutions were analyzed by a UV/Vis spectrometer. The absorbance spectra of MO (major absorption band around 462 nm) were recorded to measure

the change in the concentration of MO [14]. After irradiation, the photocatalytic degradation efficiency has been calculated using equation 1 [15]:

$$\text{Degradation efficiency (\%)} = (C_0 - C) / C_0 \times 100 \qquad \text{(Equation 1)}$$

Where C_0 is the initial concentration and C is the final concentration of dye before and after photo-irradiation respectively. This equation shows the dye photocatalyst degradation percentage.

4. Results and discussion

4.1. Morphological, Structural and Optical properties of ZnO/ZnAl$_2$O$_4$ multi co-centric nanotubes

SEM has been used to insure the feasibility of multi co-centric nanotubes of ZnO/ZnAl$_2$O$_4$ by combining the two techniques, Electrospinning and ALD. As shown in Figure 6.1, the new morphology of ZnO/ZnAl$_2$O$_4$ double (3 sequences), triple (5 sequences) and quadruple (7 sequences) co-centric nanotubes is well-defined. The nanotubes are separated by voids due to the Kirkendall effect and surface diffusion as will be explained later in the section dedicated to the mechanism. The nanotubes thickness was measured from the SEM images using image analysis software (Image J1.29X). The average thickness was measured on 50 randomly chosen nanotubes of each sample. After calcination, we measured an average thicknesses of (100 ± 5 nm), (150 ± 7 nm) and (200 ± 9 nm) for double, triple and quadruple co-centric nanotubes of ZnO/ZnAl$_2$O$_4$, respectively. Also a uniform thickness of (50 ± 5) nm for each individual nanotube in all samples was measured. Therefore, we can assume that the increase of the thickness may cause an increase of the surface area. A larger surface area provides more surface active sites for the adsorption of reactants molecules, making the photocatalytic process more efficient. An energy dispersive X-ray spectrum (EDX) of all multi co-centric nanotubes recorded along with elemental analysis is presented in Table 6.3. The EDX analysis reports the Al, Zn and O presence without any residual carbon confirming the ALD complete reaction and the polymer removal with the setup mentioned above in Table 6.1.
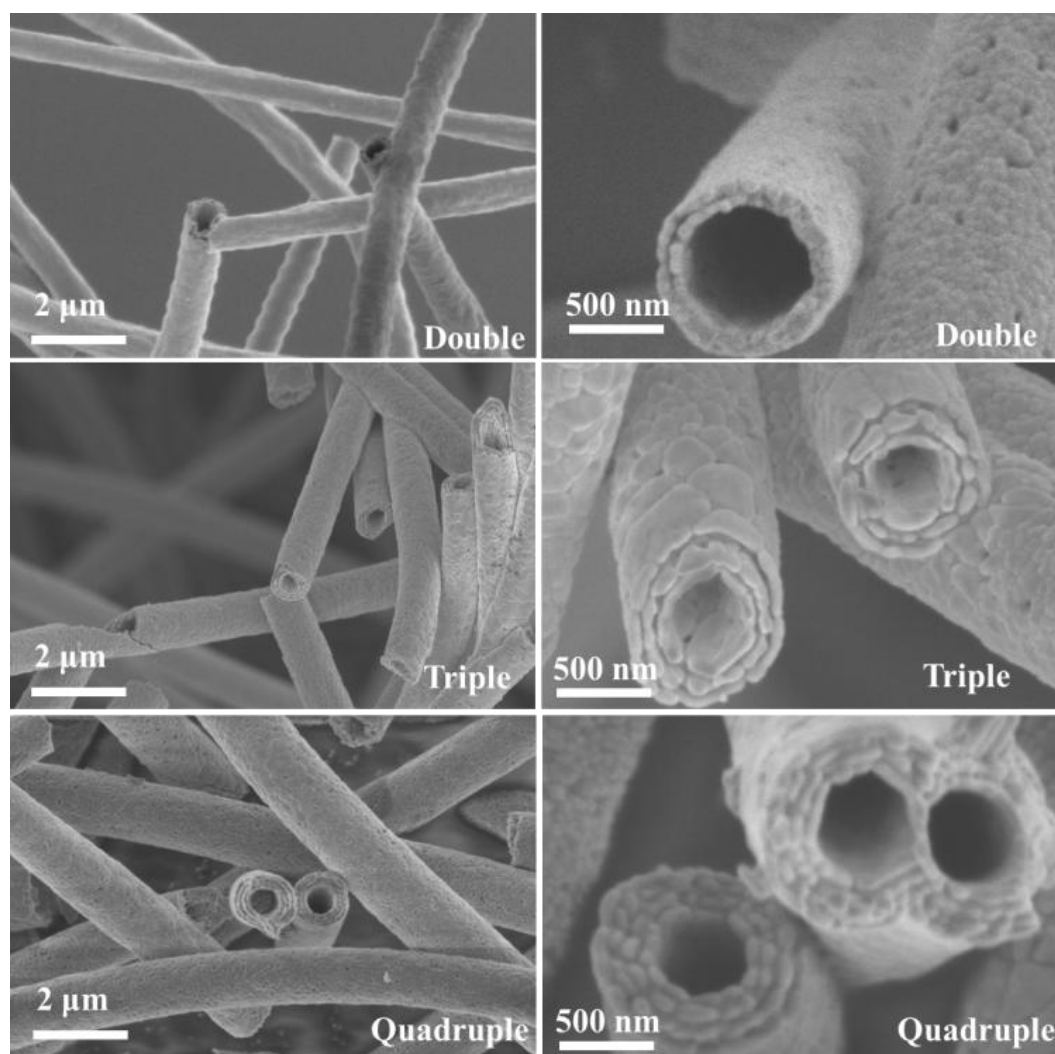
Figure 6.1. Scanning Electron Microscope images of ZnO/ZnAl$_2$O$_4$ double, triple and quadruple co-centric nanotubes annealed in air at 900°C.

Table 6.3. EDX data showing the composition of multi co-centric nanotubes of ZnO/ZnAl$_2$O$_4$ annealed under air.

Samples	Atomic percentages		
	Zn	**Al**	**O**
Double	20.52	30.4	49.08
Triple	22.1	29.06	48.84
Quadruple	22.77	27.96	49.27

Figure 6.2 illustrates the TEM images of double, triple and quadruple co-centric nanotubes of ZnO/ZnAl$_2$O$_4$. These images reveal that both ZnO and ZnAl$_2$O$_4$ phase are highly crystallized and all the nanotubes were composed of nanosized grains. The grain size was measured using ImageJ, a Java-based image processing program. It was found to be (30 ± 3 nm), (40 ± 5nm) and (50 ± 5 nm) for the double, triple and quadruple co-centric nanotubes of ZnO/ZnAl$_2$O$_4$, respectively. In addition, the increased darkness of the nanotubes with the number of layers can be clearly seen in Figure 6.2.
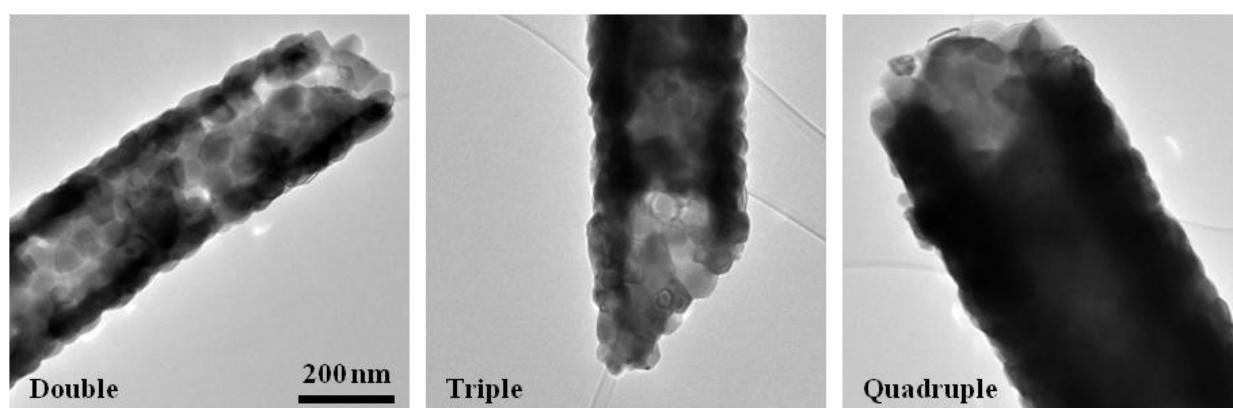
Figure 6.2. Transmission Electron Microscope images of ZnO/ZnAl$_2$O$_4$ double, triple and quadruple co-centric nanotubes.

The crystal structure was examined by X-ray diffraction. Figure 6.3 (A-B) shows XRD patterns of ZnO/ZnAl$_2$O$_4$ multi co-centric nanotubes prepared by combining the two techniques electrospinning and ALD. The XRD patterns of Figure 6.3.a-c are very similar. They show the diffraction peaks of the hexagonal wurtzite crystalline phase of zinc oxide (100), (002), (101), (102), (110), (103), (200), (112) and (201) corresponding to 2θ = 31.7, 34.4, 36.2, 47.5, 56.5, 62.8, 66.3, 67.9 and 69.0, respectively [16]. In addition to the ZnO peaks, we can observe seven diffraction peaks of the spinel ZnAl$_2$O$_4$ (220), (331), (400), (311), (422), (333/511) and (440) corresponding to 2θ = 31.4, 37, 45, 49.2, 55.7, 59.5 and 65.3, respectively. This is in good agreement with what have been reported before [17]. The average crystalline size of ZnO and ZnAl$_2$O$_4$ in the four samples was estimated by the Scherrer equation [18]. The high grain fineness numbers of both ZnO and ZnAl$_2$O$_4$ in all samples are

clearly seen in Table 6.4. Thus, XRD analysis confirmed the successful synthesis and the good crystalline structure of $ZnO/ZnAl_2O_4$ multi co-centric nanotubes by combining electrospinning and ALD.
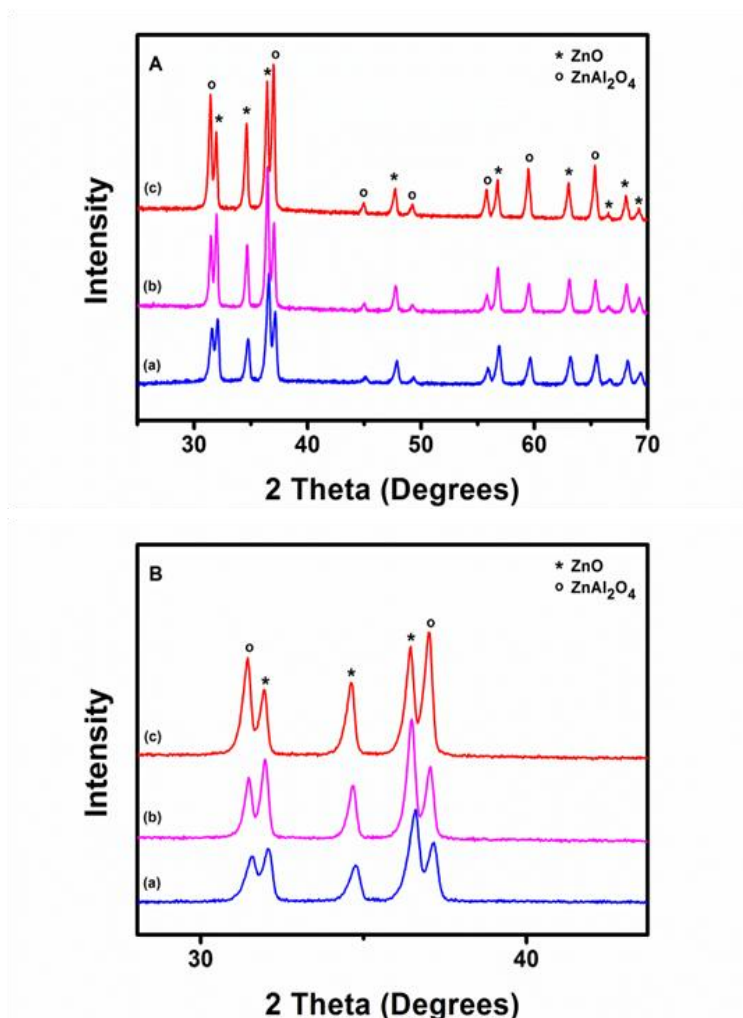
Figure 6.3. (A-B) XRD patterns of (a) Double, (b) Triple and (c) Quadruple co-centric nanotubes of $ZnO/ZnAl_2O_4$.

Table 6.4. Grain size of ZnO and $ZnAl_2O_4$ multi co-centric nanotubes.

		Double	Triple	Quadruple
Grain size (nm)	ZnO	29	35	47
	$ZnAl_2O_4$	31	42	50

It is well known that Raman spectroscopy is a characterization method to measure the frequencies of the long-wavelength lattice vibrations (phonons). Raman spectroscopy can provide useful information on crystal symmetry, impurity, grain size, residual stress, disorder etc [17]. The Raman spectra shown in Figure 6.4 were measured at room temperature. Raman signals are sensitive to the crystal structures and the defects. For all the samples, we observed 3 peaks corresponding to the active modes of ZnO. A dominant sharp peak was observed at 432 cm^{-1} corresponding to the Raman active optical phonon mode E_2 which is the characteristic of hexagonal wurtzite ZnO. Other small peaks were also observed at 327 cm^{-1} and 578 cm^{-1}. The peak at 327 cm^{-1} (E_{2H-2L}) is due to multiple phonons scattering, and the small peak at 578 cm^{-1} (E_{1L}) is observed due to structural defects like oxygen deficiency [19]. The intensity of the peak at 432 cm^{-1} as compared to other peaks is very high which indicates high crystal quality for all samples. In particular, it can be seen that the intensity of this peak is increasing going from double (a) to quadruple tubes (c) which is consistent with the XRD results presented above. As shown in Figure 6.4.a-c corresponding to the Raman spectra of ZnO/ZnAl$_2$O$_4$ double, triple and quadruple co-centric nanotubes respectively, two peaks located at 414 and 654 cm^{-1} are clearly observed. Based on our knowledge, there is no previous study on the Raman spectroscopy of ZnAl$_2$O$_4$. Thus, these two peaks may correspond to the active modes of ZnAl$_2$O$_4$ since they are not observed in the previous study of the pure ZnO.
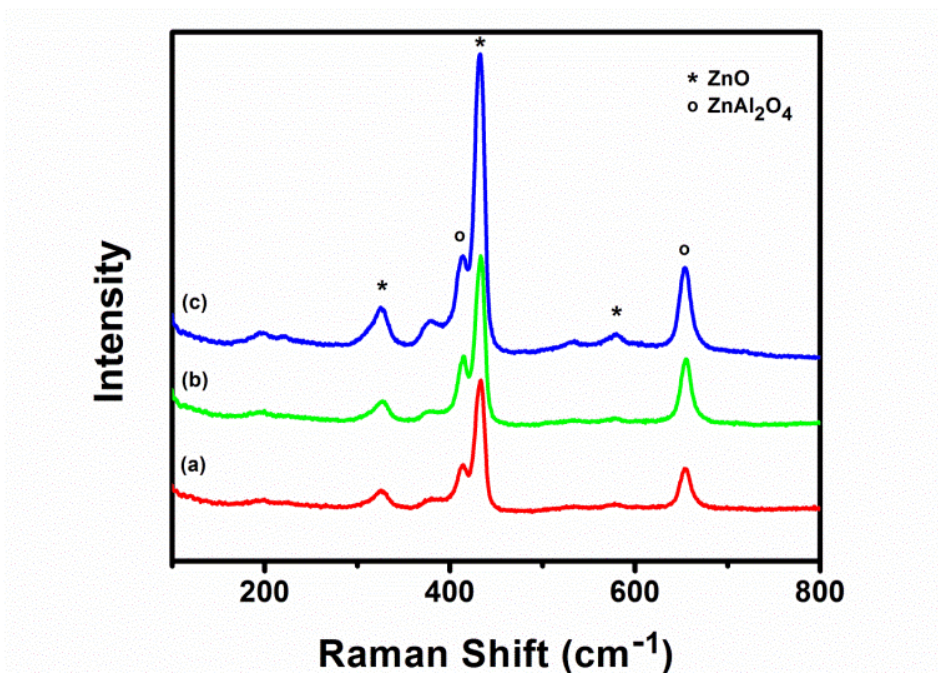
Figure 6.3. Raman Shift of (a) Double, (b) Triple and (c) Quadruple co-centric nanotubes of ZnO/ZnAl$_2$O$_4$

Reflectance spectra of the samples are shown in Figure 6.5. Due to restrictions of the light source, the absorption of ZnAl$_2$O$_4$ phase (310-330 nm) was not detected.[20] Only ZnO absorption has been revealed. The band gap value of ZnO in bare ZnO, double, triple and quadruple ZnO/ZnAl$_2$O$_4$ nanotubes have been calculated according to the following equations [20]:

$$2F = (1 - R)^2/2.R \qquad \text{(Equation 2)}$$

$$(hv.F)^2 \sim (hv - E_g) \qquad \text{(Equation 3)}$$

Where F, R, hv and E$_g$ are Kubelka-Munk function, reflectance, photon energy and band gap, respectively. The calculations of band gap showed almost no change in band gap for ZnO, D, T and Q samples) (E$_g$= 3,21 ± 0.008 eV).
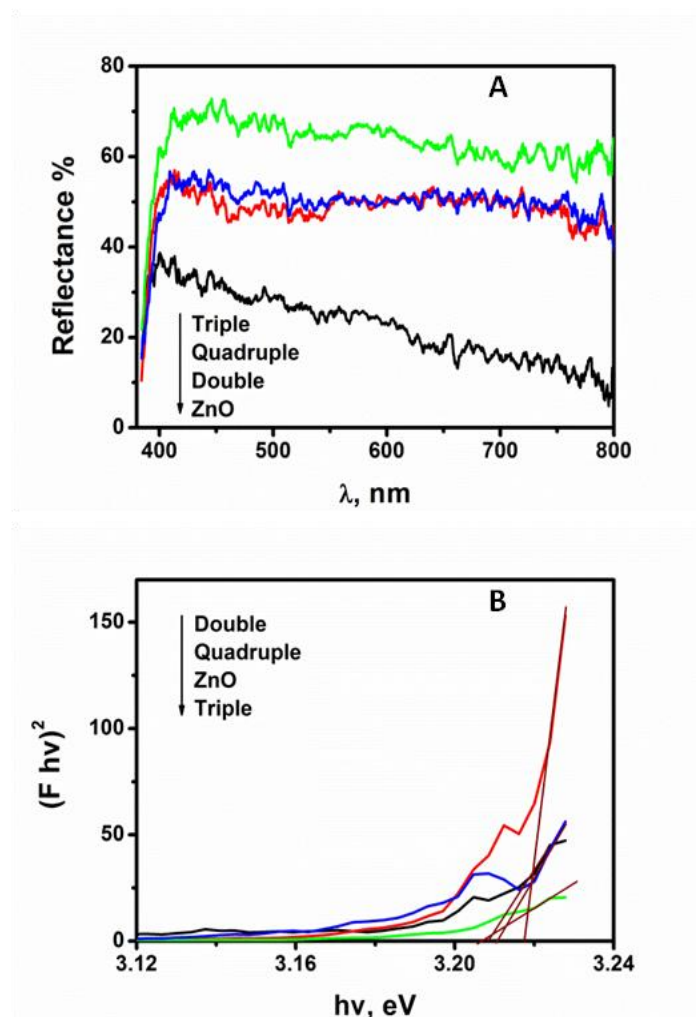
Figure 6.4. (A) Reflectance spectra and **(B)** band gap calculation from reflectance spectra of ZnO nanotubes and double, triple, quadruple co-centric nanotubes of ZnO/ZnAl$_2$O$_4$.

Table 6.5. Ratio of intensities of visible and UV emissions.

Sample	I(DLE)/I(NBE)
ZnO	0.15 ± 0.03
Double	0.2 ± 0.05
Triple	0.26 ± 0.1
Quadruple	0.97 ± 0.08

PL spectra of ZnO and nanotubes are shown in Figure 6.6. ZnO has demonstrated high intensive UV peak and broad band in visible range with significantly lower intensity,

related to exciton (near band NBE) and defect (deep level DLE) emission.[21] According to Chaya at al.,[22] the observed results point to high crystalline structure and high emission rate, due to lower rate of non radiative recombination through surface states and other defects. Development of double, triple and quadruple nanowires resulted in significant quenching of photoluminescence. It is known that the band gap of $ZnAl_2O_4$ is over 3.77 eV and it cannot be seen using the excitation source applied in the present work [23]. The first obvious reason is a reduction of ZnO ratio and therefore, the emission intensity. However, due to low laser power the most significant factor could be a charge separation due to complex structure on the surface. Chen et al. [23] has reported that the decrease of UV peak in $ZnO/ZnAl_2O_4$ could be due to additional forming defects on the interface which provide non radiative recombination. Ratio of intensities of visible and UV is shown emissions in Table 6.5. It is clearly seen that with increase of the number of $ZnO/ZnAl_2O_4$ layers the concentration of defects increased similarly as described in Chaya at al. [22] Thus, the forming of double, triple and quadruple $ZnO/ZnAl_2O_4$ nanotubes results in defect formation, stimulation of nano radiative recombination and/or surface charge transfer.
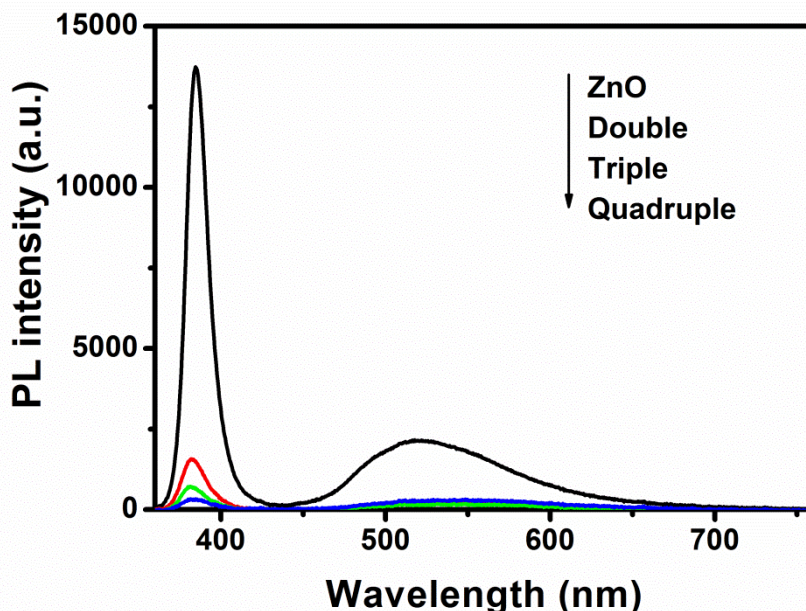
Figure 6.5. Photoluminescence spectra of ZnO and double, triple, quadruple co-centric nanotubes of $ZnO/ZnAl_2O_4$.

5.2. Mechanism of ZnO/ZnAl$_2$O$_4$ formation
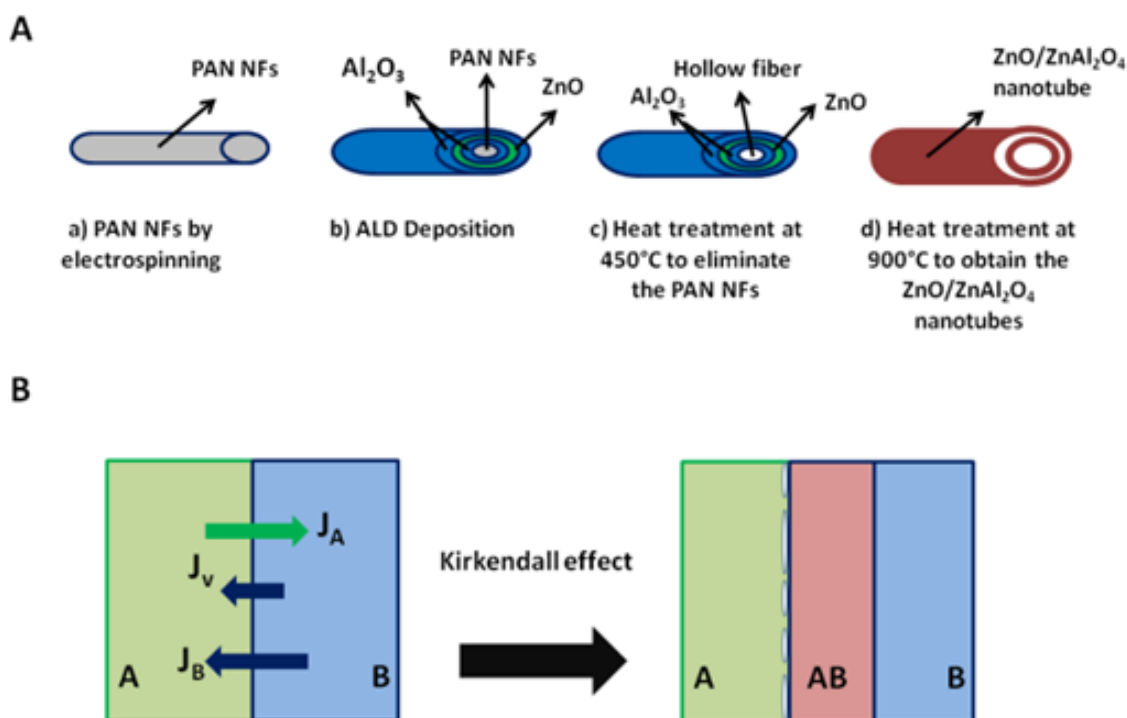
Figure 6.6. (A) Different steps of ZnO/ZnAl$_2$O$_4$ nanotubes formation. **(B)** Kirkendall effect and surface diffusion process, where J$_A$, J$_B$, and J$_v$ are diffuse flux of metal A, B, and void, respectively.

Based on the Kirkendall effect, multi co-centric nanotubes of ZnO/ZnAl$_2$O$_4$ were elaborated. All the steps for the ZnO/ZnAl$_2$O$_4$ elaboration were described in Figure 6.7.A. The Kirkendall effect is a classical phenomenon in metallurgy [24]. It basically refers to a non-equilibrium mutual diffusion process through an interface of two metals A and B (in our case A and B refer to ZnO and Al$_2$O$_3$, respectively) so that vacancy diffusion occurs to compensate for the unequal material flow [25]-[26]. In planar metallic bi-layers, this effect can give rise to void formation near the bond interface and within the fast-diffusion side, thus deteriorating the bonding strength of the interface [11]. Figure 6.7.B shows schematically the generalized model for hollow structure formation based on the kirkendall effect and surface diffusion. For the diffusion flux, we assume J$_A$ > J$_B$. In the initial stage, Kirkendall voids are generated near the A/AB interface during vacancy assisted exchange of material via bulk inter-diffusion. The voids are the sinks for subsequent inward flux of vacancies (J$_V$ = J$_A$ - J$_B$) and thus grow in size. The voids coalesce into bigger ones and touch

the compound layer AB, in one sense breaking the connection for lattice diffusion and in the other sense establishing new bridges as fast transport paths for the remaining material A [27]-[28]-[29]. Herein, we synthesized photocatalysts multi co-centric nanotubes of ZnO/ZnAl$_2$O$_4$ with relatively high surface area. The hollow nanotubes allow multiple reflections of UV light within the interior cavity that facilitates more efficient use of the light source. Moreover, the void between ZnO and ZnAl$_2$O$_4$ allows more efficient transport for the reactant molecules to get to the active sites and inhibiting charge recombination, hence enhancing the efficiency of photocatalysis.

4.3. Photocatalytic degradation of methyl orange by multi co-centric nanotubes of ZnO/ZnAl$_2$O$_4$
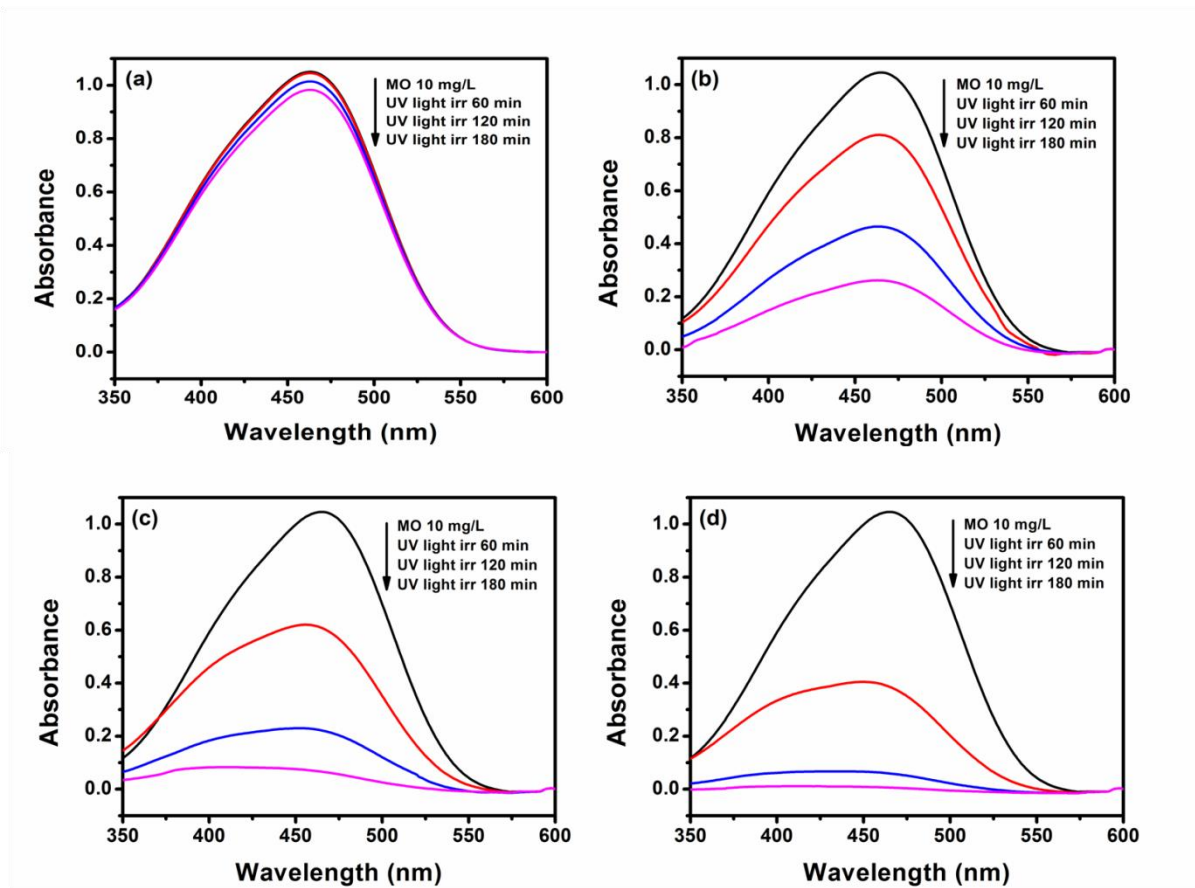
Figure 6.7. UV-Vis spectra of the photocatalytic degradation of MO under UV light: (a) MO without catalyst, (b) Double, (c) Triple and (d) Quadruple co-centric nanotubes of ZnO/ZnAl$_2$O$_4$.

The photocatalytic activities of the $ZnO/ZnAl_2O_4$ multi co-centric nanotubes were evaluated by the photodegradation of methyl orange (MO) under UV light (wavelength < 360 nm). MO was chosen as a model organic pollutant. Figure 6.8 shows the dye adsorption without catalysts under UV irradiation and photocatalytic degradation of organic dye in the presence of catalysts under UV irradiation at different periods of time (0, 60, 120, 180 min). The major absorption peak of MO is positioned at 462 nm. As shown in Figure 8.6.a, the concentration of MO without any catalysts almost does not change for every measurement under UV irradiation. Thus, light irradiation in the absence of any catalysts does not work in the photocatalysis of MO, indicating that the photodegradation of MO can be neglected. As shown in Figure 6.8.b-d, after 3 hours and under identical experimental conditions, MO was degraded up to 70%, 94% and 99% in the presence of $ZnO/ZnAl_2O_4$ double, triple and quadruple co-centric nanotubes respectively (Figure 6.9). When ZnO and $ZnAl_2O_4$ are coupled together, photons may be absorbed in both ZnO and $ZnAl_2O_4$ and form the electron-hole pairs. The electrons at the bottom of the Conduction Band (CB) of $ZnAl_2O_4$ would migrate to that of the ZnO; whereas holes at the Valence Band (VB) at the top of $ZnAl_2O_4$ would remain there. On the other hand, the holes at the VB at the top of the ZnO would migrate to that of $ZnAl_2O_4$, with electrons at the CB bottom of ZnO remaining there [16]-[10]. Such process, which is energetically favorable and reduces the probability of the electron-hole recombination, is regarded as the key factor for the enhancement of photocatalytic activities of the $ZnO/ZnAl_2O_4$ nanotubes compared to the pure ZnO [9]. According to the EDX results presented above, in the case of double co-centric nanotubes (photodegradation: 70%) when the content of ZnO decreases (Zn: 20 at. %), ZnO will reduce the catalytic efficiency of $ZnO/ZnAl_2O_4$, which is attributed to complete or sparse coverage of ZnO on the $ZnAl_2O_4$. It displays low photocatalytic activity of ZnO or $ZnAl_2O_4$ itself, which can only use about 3–5% of UV light in sunlight.

Also, it was well known that the photocatalytic activity is mainly governed by crystalline phase, light absorption capacity and active surface area [30]. For comparison, the $ZnO/ZnAl_2O_4$ quadruple and triple co-centric nanotubes exhibit the higher photocatalytic activity (99% and 94%, respectively) compared to the $ZnO/ZnAl_2O_4$ double co-centric nanotubes (70%). From SEM results, we assume a

bigger active surface area with a bigger number of layers so $S_{Quadruple} > S_{Triple} > S_{Double}$. From the XRD analysis, the grain fineness number of both ZnO and $ZnAl_2O_4$ is increasing as follow $D_{Quadruple} > D_{Triple} > D_{Double}$. Therefore, the important reason for the high phototocatalytic activity under UV light should be ascribed to the UV-Vis absorption presented above. The ZnO/$ZnAl_2O_4$ triple and quadruple co-centric nanotubes have the two highest band gap (3.39 and 3.25 eV, respectively). These results indicate that ZnO/$ZnAl_2O_4$ triple and quadruple co-centric nanotubes have excellent absorption capacity of UV light, large active surface area, high crystallite sizes and lower recombination rate of electron–hole pair.
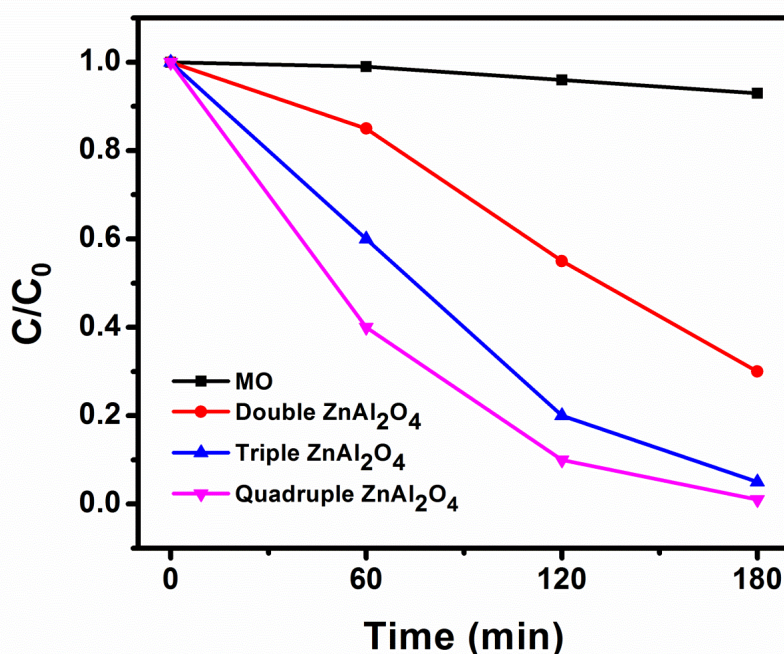
Figure 6.8. Photodegradation of MO by Double, Triple and Quadruple co-centric nanotubes of ZnO/$ZnAl_2O_4$.

Table 6.6. Kinetic parameters for photocatalytic activities of ZnO/$ZnAl_2O_4$ double, triple and quadruple co-centric nanotubes.

	MO	Double	Triple	Quadruple
k_a (min^{-1})	0.00035	0.0067	0.0167	0.0253
R^2	0.9538	0.9113	0.9436	0.9386

Figure 6.9 shows the different kinetic linear curves. The photodegradation reactions follow a Langmuir–Hinshelwood first-order kinetics model. The explanation is described as follows [31]:

$$r = dC/dt = kKC/1+KC \qquad \text{(Equation 4)}$$

Where r is the degradation rate of MO (mg (L min)$^{-1}$), C is the concentration of the MO solution (mg l^{-1}), t is the irradiation time, k is the reaction rate constant (mg (L min)$^{-1}$), and K is the adsorption coefficient of MO (mg L^{-1}). Since the initial concentrations (C_0 = 10 mg L^{-1}) of the MO solutions are very low in the present experiments, the relationship between ln(C_0/C) and reaction time t shows that the decomposition of MO with different photocatalysts accords with a pseudo first order kinetic [31]:

$$\ln (C_0/C) = kKt = k_a t \qquad \text{(Equation 5)}$$

Where k_a is the apparent first-order rate constant (min^{-1}) and C is the concentration at time t. k_a obtained from the linear dependence between ln (C_0/C) and time are reported in Table 6.6. The increasing order of the rate constants in the samples is: ZnO/ZnAl$_2$O$_4$ quadruple > ZnO/ZnAl$_2$O$_4$ triple > ZnO/ZnAl$_2$O$_4$ double > MO. The rate constant exhibits a maximum of 0.0253 min^{-1} for ZnO/ZnAl$_2$O$_4$ quadruple co-centric nanotube, which is 3.7 and 1.5 times higher than that of ZnO/ZnAl$_2$O$_4$ double and ZnO/ZnAl$_2$O$_4$ triple co-centric nanotubes, respectively. Thus, compared with other samples, the ZnO/ZnAl$_2$O$_4$ quadruple co-centric nanotubes show higher photocatalytic activity under UV light, which is represented by larger value of k_a. All these results indicate that compared with single phase ZnO material reported in previous studies (MO photodegradation: 28%) [9], the coupling effect between ZnO and ZnAl$_2$O$_4$ increases the life time of charge carriers which leads to the enhancement of its photocatalytic activity.
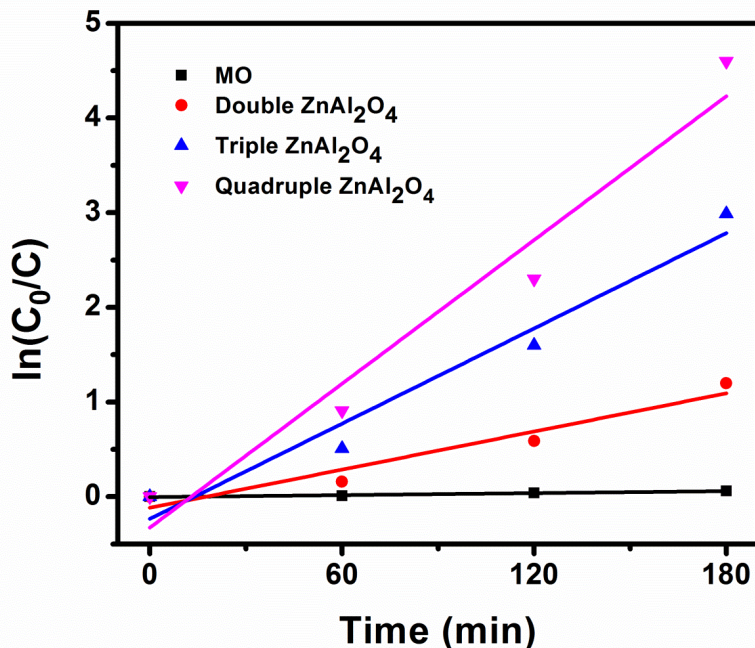
Figure 6.9. Kinetics of Methyl orange degradation by Double, Triple and Quadruple co-centric nanotubes of $ZnO/ZnAl_2O_4$.

The re-use of catalysts is very important. However to our knowledge, there is no study concerning the long term stability of $ZnO/ZnAl_2O_4$.Therefore, we performed for the first time the photocatalytic repeatability test of each catalyst. Repetitive degradation of MO by Double, Triple and Quadruple co-centric nanotubes of $ZnO/ZnAl_2O_4$ under UV light irradiation was conducted to study their long-term stability and the results are shown in Figure 6.10. After each cycle, the catalyst was separated from the solution by centrifugation. From Table 6.7, it can be seen that after 180 min of UV light irradiation and in the presence of the same $ZnO/ZnAl_2O_4$ samples, MO has been degraded in four repeated cycles. The loss of efficiency was only 6% after the fourth cycle, which can be attributed to the loss of catalyst during centrifugation after each cycle. In addition, the used nanotubes show the same off-white color as the newly prepared catalyst. These results suggest that the multi co-centric nanotubes of $ZnO/ZnAl_2O_4$ have higher photodegradation efficiency in repeated and long-term applications compared to the pure ZnO which has very low long-term photocatalytic stability [32].
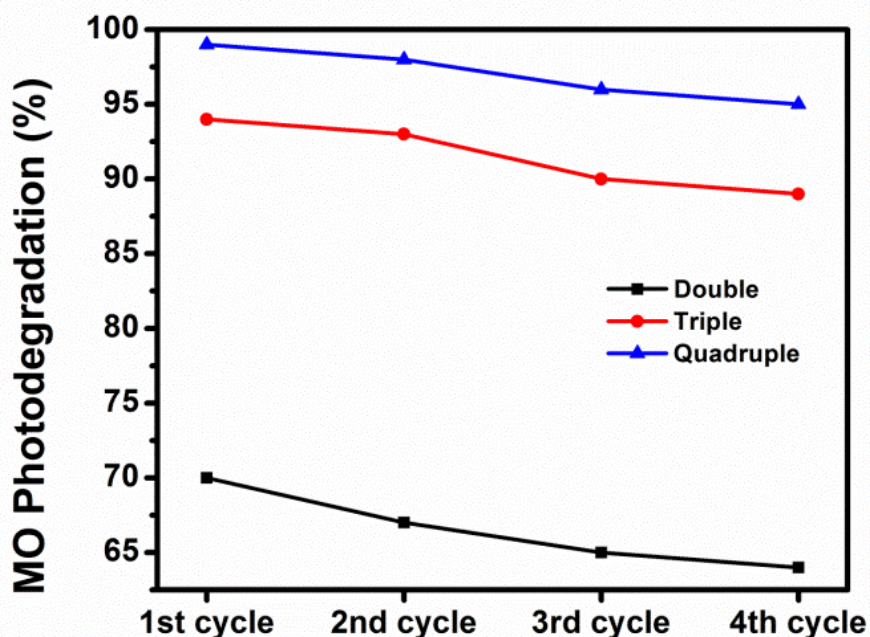
Figure 6.10. Long-term catalytic stability of Double, Triple and Quadruple co-centric nanotubes of ZnO/ZnAl$_2$O$_4$ in four repeated cycles of MO degradation under UV irradiation.

Table 6.7. MO photodegradation percentages by Double, Triple and Quadruple co-centric nanotubes of ZnO/ZnAl$_2$O$_4$ in four repeated cycles.

	Double	Triple	Quadruple
First cycle	70%	94%	99%
Second cycle	67%	93%	98%
Third cycle	65%	90%	96%
Fourth cycle	64%	89%	95%

5. Conclusion

In summary, novel multi co-centric nanotubes of ZnO/ZnAl$_2$O$_4$ have been fabricated by combining the two techniques of Electrospinning and Atomic Layer Deposition (ALD). The photocatalytic activity of the resultant nanotubes has been investigated in details. All the samples were annealed at 900°C in air for 12 hours. The new morphology of double, triple and quadruple co-centric nanotubes of

ZnO/ZnAl$_2$O$_4$ was shown by SEM images. The successful synthesis of ZnO/ZnAl$_2$O$_4$ multi co-centric nanotubes and ALD was confirmed by EDX, XRD and Raman results. The UV-Vis analysis showed the band gap energy of the different samples. Photocatalysis results confirmed that the coupling of the band gap structure in the novel ZnO/ZnAl$_2$O$_4$ nanotubes ensured the efficient separation of the photogenerated e$^-$ and h$^+$ pairs, which leads to a high photocatalytic performance for the degradation of MO (99% and 94%) and a long-term photocatalytic stability compared to the pure ZnO. The fact of combining the two techniques, Electrospinning and ALD might open a new route for new design and controlled fabrication of semiconductor nanocomposites in the development of future photocatalysts.

References

1. El-Nabarawy, T., A. Attia, and M. Alaya, Effect of thermal treatment on the structural, textural and catalytic properties of the ZnO-Al 2 O 3 system. Materials letters, 1995. **24**(5): p. 319-325.

2. Le Peltier, F., et al., In situ FT-IR and kinetic study of methanol synthesis from CO 2/H 2 over ZnAl 2 O 4 and Cu–ZnAl 2 O 4 catalysts. Journal of Molecular Catalysis A: Chemical, 1998. **132**(1): p. 91-100.

3. Schneider, R., et al., Perovskite-type oxide monolithic catalysts for combustion of chlorinated hydrocarbons. Catalysis today, 1999. **47**(1): p. 429-435.

4. Zhu, Z., et al., Photocatalytic performances and activities of ZnAl 2 O 4 nanorods loaded with Ag towards toluene. Chemical engineering journal, 2012. **203**: p. 43-51.

5. Grabowska, H., et al., A method for obtaining thymol by gas phase catalytic alkylation of m-cresol over zinc aluminate spinel. Applied Catalysis A: General, 2001. **220**(1): p. 207-213.

6. Dixit, H., et al., Electronic structure and band gap of zinc spinel oxides beyond LDA: ZnAl2O4, ZnGa2O4 and ZnIn2O4. New Journal of Physics, 2011. **13**(6): p. 063002.

7. Ragul, G., et al., Synthesis, Characterization and Photocatalytic Study of Zinc Aluminate Nanopowders against Rhodamine–B and Crystal Violet Dyes. International Journal of Applied Engineering Research, 2013. **8**(19): p. 2013.

8. Battiston, S., et al., Synthesis of zinc aluminate (ZnAl2O4) spinel and its application as photocatalyst. Materials Research, 2014. **17**(3): p. 734-738.

9. Zhang, L., et al., Fabrication and photocatalytic properties of spheres-in-spheres ZnO/ZnAl 2 O 4 composite hollow microspheres. Applied Surface Science, 2013. **268**: p. 237-245.

10. Zhao, X., et al., Fabrication and photocatalytic properties of novel ZnO/ZnAl2O4 nanocomposite with ZnAl2O4 dispersed inside ZnO network. AIChE Journal, 2012. **58**(2): p. 573-582.

11. Yang, Y., et al., Influence of temperature on evolution of coaxial ZnO/Al2O3 one-dimensional heterostructures: From core-shell nanowires to spinel nanotubes and porous nanowires. The Journal of Physical Chemistry C, 2008. **112**(11): p. 4068-4074.

12. Bechelany, M., et al., Highly crystalline MOF-based materials grown on electrospun nanofibers. Nanoscale, 2015. **7**(13): p. 5794-5802.

13. Chaaya, A.A., et al., ZnO 1D nanostructures designed by combining atomic layer deposition and electrospinning for UV sensor applications. Journal of Materials Chemistry A, 2014. **2**(48): p. 20650-20658.

14. Dhakal, T.P., et al., Moisture-induced surface corrosion in AZO thin films formed by atomic layer deposition. Device and Materials Reliability, IEEE Transactions on, 2012. **12**(2): p. 347-356.

15. Chuangchote, S., et al., Photocatalytic activity for hydrogen evolution of electrospun TiO2 nanofibers. ACS applied materials & interfaces, 2009. **1**(5): p. 1140-1143.

16. Huo, R., et al., Enhanced photocatalytic performances of hierarchical ZnO/ZnAl 2 O 4 microsphere derived from layered double hydroxide precursor spray-dried microsphere. Journal of colloid and interface science, 2013. **407**: p. 17-21.

17. Ciupina, V., I. Carazeanu, and G. Prodan, Characterization of ZnAl2O4 nanocrystals prepared by coprecipitation and microemulsion techniques. Journal of Optoelectronics and Advanced Materials, 2004. **6**(4): p. 1317-1322.

18. Nasr, M., et al., Photoluminescence: A very sensitive tool to detect the presence of anatase in rutile phase electrospun TiO 2 nanofibers. Superlattices and Microstructures, 2015. **77**: p. 18-24.

19. Singh, P., K. Mondal, and A. Sharma, Reusable electrospun mesoporous ZnO nanofiber mats for photocatalytic degradation of polycyclic aromatic hydrocarbon dyes in wastewater. Journal of colloid and interface science, 2013. **394**: p. 208-215.

20. Motloung, S., et al., Effect of annealing temperature on structural and optical properties of ZnAl 2 O 4: 1.5% Pb 2+ nanocrystals synthesized via sol-gel reaction. Journal of Alloys and Compounds, 2016. **677**: p. 72-79.

21. Viter, R., et al., Application of room temperature photoluminescence from ZnO nanorods for Salmonella detection. IEEE Sensors Journal, 2014. **14**(6): p. 2028-2034.

22. Chaaya, A.A., et al., Evolution of microstructure and related optical properties of ZnO grown by atomic layer deposition. Beilstein journal of nanotechnology, 2013. **4**(1): p. 690-698.

23. Chen, X., et al., The formation and acceptor related emission behavior of ZnO/ZnAl 2 O 4 core–shell structures. Journal of Alloys and Compounds, 2013. **571**: p. 114-117.

24. Fan, H.J., et al., Influence of surface diffusion on the formation of hollow nanostructures induced by the Kirkendall effect: the basic concept. Nano Letters, 2007. **7**(4): p. 993-997.

25. Schröder, H., K. Samwer, and U. Köster, Micromechanism for metallic-glass formation by solid-state reactions. Physical review letters, 1985. **54**(3): p. 197.

26. Radi, Z., P. Barna, and J. Labar, Kirkendall voids and the formation of amorphous phase in the Al-Pt thin-film system prepared by high-temperature successive deposition. Journal of applied physics, 1996. **79**(8): p. 4096-4100.

27. Yin, Y., et al., Colloidal synthesis of hollow cobalt sulfide nanocrystals. Advanced Functional Materials, 2006. **16**(11): p. 1389-1399.

28. Li, Q. and R.M. Penner, Photoconductive cadmium sulfide hemicylindrical shell nanowire ensembles. Nano Letters, 2005. **5**(9): p. 1720-1725.

29. Wang, Y.-l., L. Cai, and Y.-n. Xia, Monodisperse spherical colloids of Pb and their use as chemical templates to produce hollow particles. Advanced Materials, 2005. **17**(4): p. 473-477.

30. Ohtani, B., Preparing articles on photocatalysis-beyond the illusions, misconceptions, and speculation. Chemistry letters, 2008. **37**(3): p. 216-229.

31. Konstantinou, I.K. and T.A. Albanis, TiO 2-assisted photocatalytic degradation of azo dyes in aqueous solution: kinetic and mechanistic investigations: a review. Applied Catalysis B: Environmental, 2004. **49**(1): p. 1-14.

32. Kim, J.K., et al., Nano carbon conformal coating strategy for enhanced photoelectrochemical responses and long-term stability of ZnO quantum dots. Nano Energy, 2015. **13**: p. 258-266.

General Conclusion

The strategies to improve the photocatalytic activity of the semiconductors under UV and visible light for wastewater treatment are still remaining the interest of researchers for future studies in energy and environmental field. In this work, we succeeded to enhance the photocatalytic efficiency of TiO_2 under UV and visible light by metal and non metal doping. Also, we improved the photocatalytic stability of ZnO by designing novel nanostructures using atomic layer deposition and electrospinning techniques. The morphological, structural and optical properties of the prepared samples were analyzed using several characterizations techniques. In order to modify the properties of TiO_2 and ZnO, different strategies have been investigated and reported as follow:

- (1) Reduced GO/TiO_2 composite nanofibers with different GO nanosheets amounts were successfully prepared by electrospinning. The GO was reduced under a heat treatment at 500^oC in N_2 atmosphere for 6 hours. The band gap energy of TiO_2 NFs was decreased from 3.2 eV to 2.9 eV due to the presence of rGO sheets. The incorporation of rGO with an amount of (2 wt %)/TiO_2 significantly increases the visible light photo-response and improves the separation of the photo-induced electron–hole pairs of TiO_2. The photocatalytic degradation of methyl orange under visible light was 6 times higher than that of commercial TiO_2-P25. Thus, incorporating rGO into TiO_2 NFs is an efficient and simple way for enhancing the visible-light photocatalytic activity.

- (2) Elaboration of BN/TiO_2 composite nanofibers with different BN nanosheets amounts was performed using electrospinning technique. The successful incorporation of boron nitride in TiO_2 nanofibers was confirmed by SEM, EDX, Raman and FTIR. An increase of crystal sizes and specific surface area of BN (10wt. %)/TiO_2 compared to the pure TiO_2 nanofibers was found. A blue shift of the band gap energy from 3.2 eV to 3.62 eV due to the presence of BN sheets was confirmed by UV-VIS analysis. XRD and photoluminescence spectra confirmed that BN incorporation increases the lattice strain in the TiO_2 cell. As result, BN sheets can promote the migration of h^+ from the bulk of TiO_2 to its surface due to the electrostatic interaction and consequently improve the photocatalytic activity of TiO_2 under UV light due to efficient charge separation. The photocatlytic degradation of methyl orange under UV light was 5 and 3.8 times higher than that of commercial TiO_2-P25 and TiO_2 nanofibers, respectively.

- (3) To develop an effective material having photocatalytic properties for both organic compound degradation and bacterial removal, we report on the elaboration of Ag/TiO_2 and $BN-Ag/TiO_2$ composite nanofibers with controlled amounts of BN nanosheets and Ag. The photocatalytic tests using methylene blue under visible light, in repeated and long term applications, showed that the photodegradation efficiency of BN(5 wt %)-Ag (3 wt %)/TiO_2 was 17.2 and 2.3 times higher than that of pure TiO_2 nanofibers and Ag (3 wt %)/TiO_2 respectively. This higher activity is due to the efficient electron transfer from photo-excited Ag/TiO_2 to BN nanosheets to retard the charge recombination. Antibacterial tests against gram-negative *Escherichia coli* indicate that BN (5 wt %)-Ag (3 wt %)/TiO_2 resulted in a total removal of cultivable bacteria within a short time. The prepared samples can be nominated as multifunctional materials for photodegradation and antibacterial applications.

- (4) Al_2O_3 doped ZnO nanotubes with controlled doping ratio of Al_2O_3 were designed by combining the two techniques of atomic layer deposition and electrospinning. The effects of Al_2O_3 doping on optical and structural properties of Al_2O_3 doped ZnO nanotubes were discussed and the photocatalytic activity of these materials under UV light was studied by the photodegradation of methyl orange as model pollutant. As a result, the Al_2O_3 doping increases the disorder (defects and oxygen vacancies formation) in the ZnO nanostructure which improves the separation efficiency of electron-hole pairs. Therefore, the photocatalytic degradation of methyl orange by Al_2O_3/ZnO (20 wt%) was 5 times higher than that of ZnO nanotubes.

- (5) Novel double, triple and quadruple co-centric nanotubes of $ZnO/ZnAl_2O_4$ have been successfully designed by combining the two techniques of atomic layer deposition and electrospinning. After a heat treatment at 900°C under air, morphological, structural and optical analysis confirmed the elaboration of multi co-centric nanotubes of $ZnO/ZnAl_2O_4$ based on Kirkendall effect. Photoluminescence results showed that the coupling of the band gap structure in the novel $ZnO/ZnAl_2O_4$ nanotubes ensured the efficient separation of the photogenerated e^- and h^+ pairs and leads therefore, to a high photocatalytic performance for the degradation of methyl orange (99% and 94%) and a long-term photocatalytic stability compared to the pure ZnO.

The results presented in this work are hoped to contribute to the development of the green photocatalysis for wastewater treatment in the near future. The prepared photocatalysts could be used for other photocatalytic applications such as the hydrogen production, water disinfection, degradation of heavy metals and pharmaceutical products. Even though great progresses have been achieved in the photocatalysis under visible light at a laboratory scale, future research should be devoted to further improve the efficiency of these photocatalysts for large scale applications (industrial use). In addition, the photocatalyst must be removed after treatment. A post treatment will therefore be necessary; it consists of a solid-liquid separation step. Thus, future studies should be focused in this area.

Scientific Contributions

Publications

1. **Maryline Nasr**, Adib Abou Chaaya, Nadine Abboud, Mikhael Bechelany, Roman Viter, Cynthia Eid, Antonio Khoury, Philippe Miele, Photoluminescence: A very sensitive tool to detect the presence of anatase in rutile phase electrospun TiO_2 nanofibers, Superlattices and Microstructures 77 (2015) 18–24.

DOI: 10.1016/j.spmi.2014.10.034

2. **Maryline Nasr**, Sébastien Balme, Cynthia Eid, Roland Habchi, Philippe Miele, Mikhael Bechelany, Enhanced Visible-Light Photocatalytic Performance of Electrospun rGO/TiO_2 Composite Nanofibers, J. Phys. Chem. C 2017, 121, 261–269.

DOI: 10.1021/acs.jpcc.6b08840

3. **Maryline Nasr**, Roman Viter, Cynthia Eid, Roland Habchi, Philippe Mielea, Mikhael Bechelany, Enhanced photocatalytic performance of novel electrospun BN/TiO_2 composite nanofibers, NewJ.Chem., 2017, 41, 81.

DOI: 10.1039/c6nj03088b

4. **Maryline Nasr**, Roman Viter, Cynthia Eid, Fabienne Warmont, Roland Habchi, Philippe Mielea, Mikhael Bechelany, Synthesis of novel $ZnO/ZnAl_2O_4$ multi co-centric nanotubes and their long-term stability in photocatalytic application, RSC Adv., 2016, 6, 103692.

DOI: 10.1039/c6ra22623j

5. **Maryline Nasr**, Roman Viter, Cynthia Eid, Roland Habchi, Philippe Miele, Mikhael Bechelany, Optical and structural properties of Al_2O_3 doped ZnO nanotubes by ALD and their photocatalytic application, Applied Materials & Interfaces, 2017.
Submitted (Manuscript ID: am-2017-07712b).

6. **Maryline Nasr**, Laurence Soussan, Roman Viter, Cynthia Eid, Roland Habchi, Philippe Miele, Mikhael Bechelany, High photocatalytic and antibacterial activity of $BN-Ag/TiO_2$ composite nanofibers under visible light, The Journal of Physical Chemistry C, 2017.
Submitted (Manuscript ID: jp-2017-05976g).

7. **Maryline Nasr**, Cynthia Eid, Roland Habchi, Philippe Miele, Mikhael Bechelany, Recent progress in enhancing visible light photocatalytic activity of TiO$_2$: Review (In progress).

8. Amr A. Nada, **Maryline Nasr**, Mikhael Bechelany, Stéphanie Roualdes, Enhancing the photocatalytic properties of mesoporous TiO$_2$@ZnFe$_2$O$_4$ nanofiber via PECVD (In progress).

Conferences

➤ **Oral Communcations**

1. <u>**Maryline Nasr**</u>, Cynthia Eid, Philipe Miele, Roland Habchi, Mikhael Bechelany, Oxides membranes by electrospinning for photocatalytic applications, 3rd International Conference on Bioinspired and Biobased Chemistry & Materials, October 16-19, 2016 Nice, France.

2. <u>**Maryline Nasr,**</u> Roman Viter, Cynthia Eid, Philipe Miele, Roland Habchi, Mikhael Bechelany, Synthesis of novel ZnO/ZnAl$_2$O$_4$ multi co-centric nanotubes and their long-term stability in photocatalytic application, E-MRS Spring Meeting, May 21-26, 2017 Strasbourg, France.

3. <u>**Maryline Nasr**</u>, Roman Viter, Cynthia Eid, Philipe Miele, Roland Habchi, Mikhael Bechelany, Enhanced photocatalytic performance of novel electrospun BN/TiO$_2$ composite nanofibers, E-MRS Spring Meeting, May 21-26, 2017 Strasbourg, France.

4. <u>**Maryline Nasr**</u>, Sébastien Balme, Cynthia Eid, Roland Habchi, Philippe Miele, Mikhael Bechelany, Enhanced Visible-Light Photocatalytic Performance of Electrospun rGO/TiO$_2$ Composite Nanofibers, Le 5ème Forum Doctoral, le 18 et 19 Mai 2016. Ecole Doctorale en Sciences et Technologie (EDST), Unversite Libanaise, Liban.

➤ **Posters**

1. <u>**Maryline Nasr**</u>, Sébastien Balme, Cynthia Eid, Roland Habchi, Philippe Miele, Mikhael Bechelany, Synthèse des nanofibres de TiO$_2$ dopées avec des monofeuillets de GO pour des applications photocatalytiques, la 22ème Conférence Scientifique Internationale (LAAS22), les 14 et 15 Avril 2016 - USEK campus Kaslik – Liban.

2. <u>**Maryline Nasr**</u>, Adib Abou Chaaya, Nadine Abboud, Mikhael Bechelany, Roman Viter, Cynthia Eid, Antonio Khoury, Philippe Miele, Elaboration des membranes d'oxydes par

electrospinning pour des applications photocatalytiques, Troisièmes Journées Franco-Libanaises JFL3, le 29 et 30 octobre 2015. Ecole Doctorale en Sciences et Technologie (EDST) et la Faculté des Sciences, Unversite Libanaise, Liban.

3. **<u>Maryline Nasr</u>**, Sébastien Balme, Cynthia Eid, Roland Habchi, Philippe Miele, Mikhael Bechelany, Enhanced Visible-Light Photocatalytic Performance of Electrospun rGO/TiO$_2$ Composite Nanofibers, les 12ème Journées de l'Ecole Doctorale, les 5 et 6 décembre 2016 - Institut Botanique, Montpellier – France.

Annex

Photoluminescence: a very sensitive tool to detect the presence of anatase in rutile phase electrospun TiO$_2$ nanofiber

1. Abstract

This paper reports on the synthesis and the characterization of titanium dioxide (TiO$_2$) nanofiber sprepared by electrospinning. The samples were annealed at various temperatures in air for 4h.The as-spun and annealed TiO$_2$/PVP composite nanofibers were characterized by scanning electron microscopy (SEM), Energy-dispersive X-ray spectroscopy analysis (EDX), X-ray diffraction (XRD), Raman spectroscopy and photoluminescence (PL). The results show that the heat treatment has an effect on the crystallization process. Even if the XRD data shows a complete anatase-to-rutile transition in the TiO$_2$ nanofibers at 900°C, photoluminescence shows a small portion of anatase in rutile sample. This observation proved that photoluminescence is a very sensitive tool to detect the presence of anatase in rutile phase TiO$_2$ nanostructures.

2. Introduction

In the last decade, the attention of researchers is paid to design new nanoscale materials such one-dimensional nanostrcutures [1-6]. Different methods have been used to produce one-dimensional nanomaterials such as thermal evaporation,[7] freeze-drying method,[8] physical vapor deposition,[9] and chemical vapor deposition.[10] Among these methods, the simplest technique to design nanofibers is the electrospinning. This method was first introduced by Formhals [11]. It is a versatile and cost-effective technique for the production of multi-functional nanofibers from various polymers, polymer blends, composites, sol-gels, and ceramics [12]. The fibers are rather uniform in diameter ranging from tens of nanometers to several micrometers [13, 14]. The basic principle of this technique is based on generating the direct movement of charged molecules by applying a high voltage. The droplets coming from the polymer solution, through the spinneret, would then be ejected in the form of a liquid jet forming the nanofibers on the collector.

Among the different types of oxide semiconductors produced by this method, Titanium oxide (TiO$_2$) is one of the most extensively studied materials because of its remarkable optical and electronic properties along with its chemical and thermal stability [15]. Due to

these outstanding properties, TiO_2 has been used in wide range of applications such as chemical sensors,[16, 17] catalytic filters,[18, 19]and solar cells [20, 21]. TiO_2 has three crystalline phases: anatase, rutile, and brookite. Rutile is a stable phase at high temperature, where anatase and brookite would transform to rutile when treated at high temperatures.

In addition, TiO_2 nanostructures demonstrate room temperature photoluminescence in visible (440-570 nm) and IR (800-860 nm) intervals of the wavelength spectrum, in particular for anatase and rutile phases respectively [22-25]. The emission of anatase nanostructures has usually two bands, related to self-trapped excitons luminescence (440-510 nm) and deep levels formed by oxygen vacancies (515-560 nm) [26-28]. Photoluminescence in rutile phase concerns deep levels, related to Ti^{3+} states [15, 25]. It was mentioned that photoluminescence in TiO_2 is sensitive to ambient conditions and thermal treatment [24, 25]. PL in TiO_2 nanostructures is ruled by the surface charge and could be changed by the adsorption of gas and biomolecules on TiO_2 surface [29, 30], what makes an impact on some application if the TiO_2 is used in optical sensors or biosensors for instance.

In the present paper we report the fabrication of TiO_2 nanofibers by electrospinning method and detailed optical and structural characterization of the obtained nanostructures. The structural and optical changes induced by high temperature annealing will be discussed. The high sensitivity of the photoluminescence technique for detecting anatase trace in rutile phase will be also highlighted.

3. Experimental section

3.1. Materials

In this study titanium tetraisopropoxide [Ti(OiPr)4; 97%,], PVP (Mw = 1 300 000), ethanol (98%) and acetic acid (100%) were purchased from Sigma–Aldrich.

3.2. Preparation of TiO_2 nanofibers

Fabrication of the TiO_2nanofibers was achieved by electrospinning. The TiO_2 sol was prepared by hydrolyzing 3 ml of titanium tetraisopropoxide with a mixture of 2 mL of ethanol and 2 mL of acetic acid. 0.3g of PVP was separately dissolved in 3 mL of ethanol and then added to the TiO_2 sol solution. The precursor mixture was stirred for 2h at room temperature to obtain sufficient viscosity required for electrospinning. The electrospinning

solution was placed into a 22 ml syringe with a 25 gauge stainless steel needle at the tip. The syringe was placed on a syringe pump which was adjusted to 0.4 ml/h of feeding rate. Then the electric voltage of 25 kV was applied between the needle and the collector. The distance between the tip of the syringe needle and the collector (Al plate) was fixed to 10 cm. The as-spun nanofibers were left overnight in air to fully hydrolyze. To remove the polymer and achieve crystallinity, the composite fibers were then treated in air at different temperatures 500°C, 700°C and 900°C for 4h with a heating rate of 5°C/min.

3.3. Structural characterizations

The microstructures, the phase and the crystal structure of the synthesized nanofibers were investigated using scanning electron microscopy (SEM, Hitachi S-4800), X-ray diffraction (PANAlytical Xpert-PRO diffractometer equipped with a X'celerator detector using Ni-filtered Cu-radiation), Raman (Horiba xplora, 532 nm) and Energy-dispersive X-ray spectroscopy analysis (Ametek, EDX). Photoluminescence of TiO_2 nanostructures was measured at room temperature using the experimental setup, described elsewhere by Abou Chaaya *et al.*.[31] The PL was excited by solid state laser (355 nm) and the emission spectra were recorded in the range 360-800 nm.

4. Results and discussion

The morphology of the nanofibers was examined by scanning electron microscopy (SEM). Figure1a shows the SEM images of the fibers before annealing. The average diameter of the fibers is 300 nm. The composite nanofibers were then treated in air at different temperatures 500°C (Figure 1b), 700°C (Figure 1c) and 900°C (Figure 1d). As shown in the Figure1b and Figure1c the nanofibers have uniform surfaces with an average diameter of 170 nm and 140 nm, respectively, smaller than the as-spun nanofibers because of the loss of PVP and the decomposition of titanium tetraisopropoxide. After calcination at 900°C (Figure1d), the average diameter (190 nm) increased and this can be explained by the process of crystallization. The average diameter of TiO_2 nanofibers increases with the increasing of crystallinity therefore with the increasing of calcination temperature [28]. The EDX data (Table 1) confirms the removal of polymer and show the formation of stoichiometric TiO_2 nanofibers.
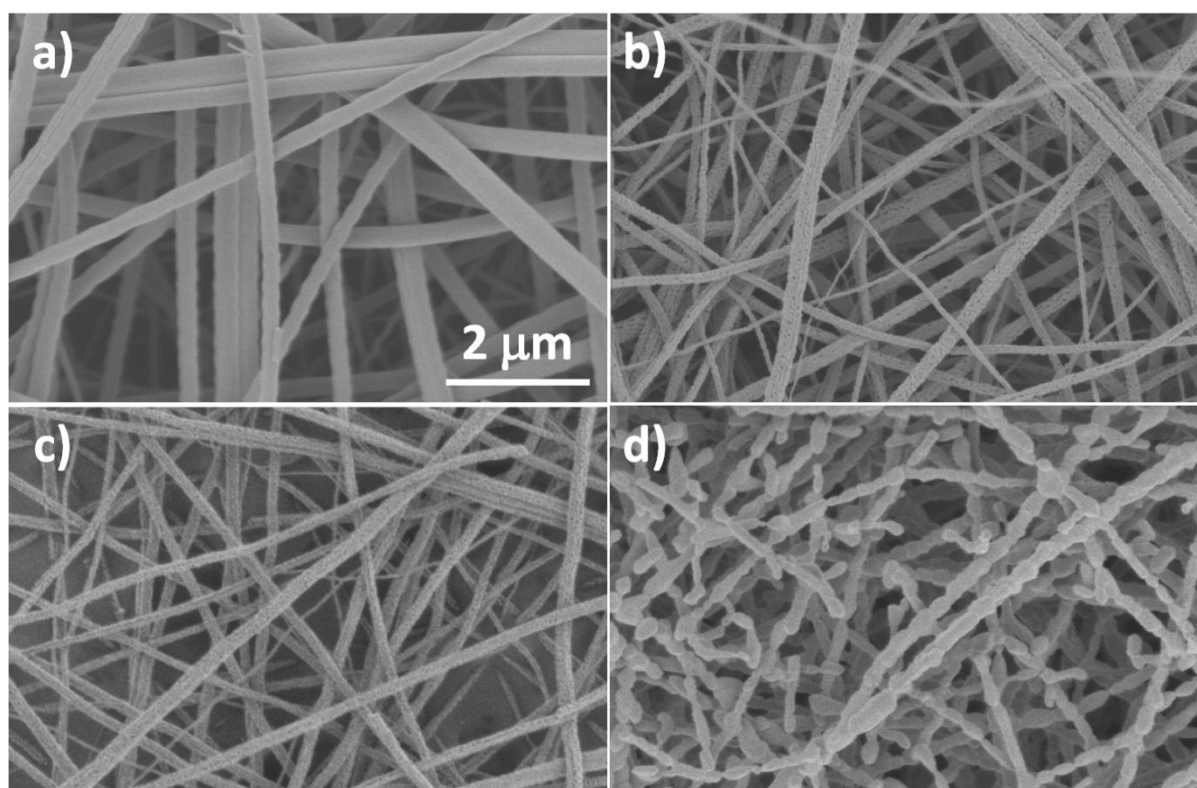
Figure 1. Scanning electron microscope images of the (a) as-spun TiO_2-PVP composite nanofibers and TiO_2 nanofibers annealed in air at various temperatures for 4h: (b) 500˚C, (c) 700˚C, and (d) 900˚C.

Table 1. EDX data showing the composition of TiO_2 nanofibers annealed at 500, 700 and 900˚C

Element	Atomic percentage		
	500˚C	**700˚C**	**900˚C**
Ti	31.76	37.75	33.11
O	68.24	62.25	66.89

The XRD analysis (Figure 2) confirms the change of the crystalline structures when the annealing temperature increases. At 500°C, five peaks appear at 2θ = 25.5°, 38.2°, 48.2°, 54.1° and 55.3° which correspond to (101), (004), (200), (105), (211) respectively of the crystallized anatase-structured TiO_2. The Debye-Scherrer equation was used to calculate the crystal size of TiO_2 nanofibers. The grain size obtained at 500°C is 16 nm. At 700°C, the rutile phase is observed with the two diffraction peaks at 2θ = 27.7° and 35.8° that correspond to (110) and (101) respectively. An increasing of the average grain size to 30 nm is also observed. With the increasing of annealing temperature to 900°C, we have an increasing of the grain size to 45 nm and the anatase phase disappears and pure rutile-structured TiO_2 is observed with the diffraction peaks at 2θ = 27.7°, 35.8°, 38.9°, 54.1° and 56.4° which correspond to (110), (101), (111), (210), (211) respectively.[26] The XRD results show a clear evolution of TiO_2 anatase-to-rutile when the temperature rises as well as an improvement in the crystalline structures.
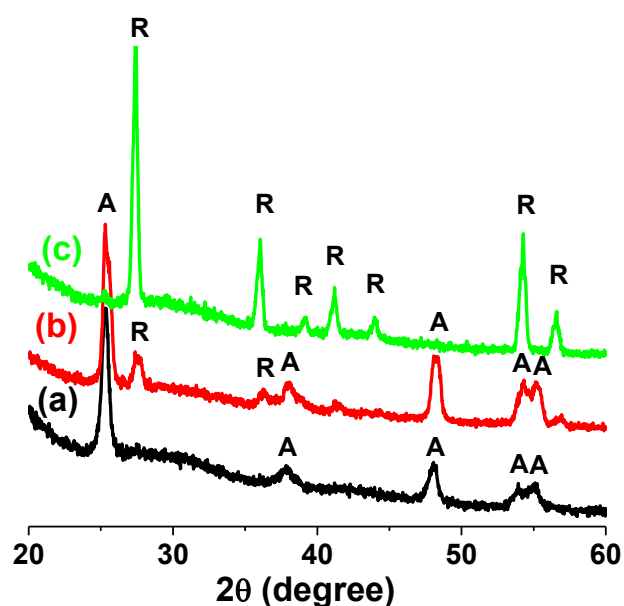
Figure 2. X-ray diffraction patterns of TiO_2 nanofibers treated at (a) 500, (b) 700, and (c) 900°C in air for 4h (A: anatase, R: rutile)

The formation of TiO_2 nanofibers and the anatase -to- rutile phase transition was confirmed by Raman spectroscopy because the two phases have two different spectra. The

spectra were taken at room temperature using a 532 nm laser line as the excitation source. Figure 3 shows Raman spectra of the TiO_2/PVP composite nanofibers calcined at 500˚C, 700˚C, and 900˚C.We identify that anatase has six Raman active modes at 144 cm^{-1} (E_g), 197 cm^{-1} (E_g), 399 cm^{-1} (B_{1g}), 513 cm^{-1} (A_{1g}), 519 cm^{-1} (B_{1g}) and 639 cm^{-1} (E_g).[27] The Raman spectra of anatase phase were observed in the nanofibers treated at 500°C. At 700˚C the very small peak at around 449 cm^{-1}wich is E_g mode of the rutile phase indicates the presence of rutile phase. Rutile has four Raman active modes detected at 244 cm^{-1} (B_{1g}), 447 cm^{-1}(E_g), 612 cm^{-1} (A_{1g}) and 826 cm^{-1} (B_{2g}).[32]After treated at 900˚C the intensity of the peaks at around 449 cm^{-1} (E_g) and at around 612 cm^{-1}(A_{1g}) increased relative to the anatase peaks at around 400 cm^{-1} (B_{1g}) and 639 cm^{-1}(E_g), respectively, which confirm the anatase-to-rutile transformation. A small peak corresponding to E_g (144 cm^{-1}) which indicate the presence of anatase phase in the rutile sample even after annealing at 900°C is still observed.
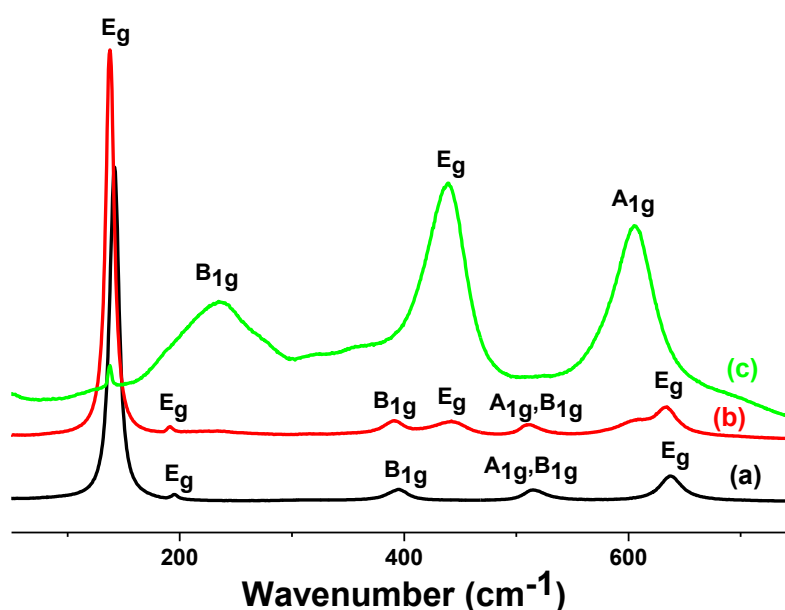
Figure 3. Raman spectra of TiO_2 nanofibers annealed at (a) 500, (b) 700, (c) 900˚C
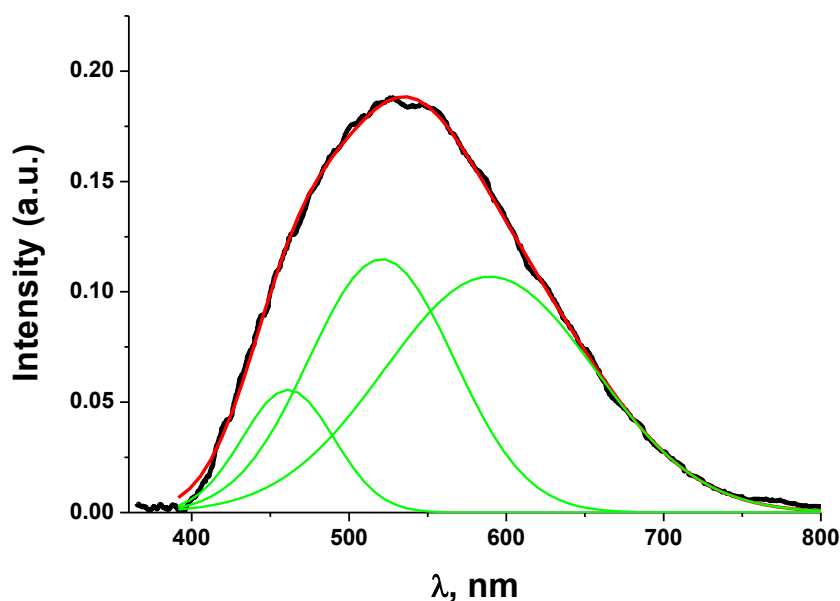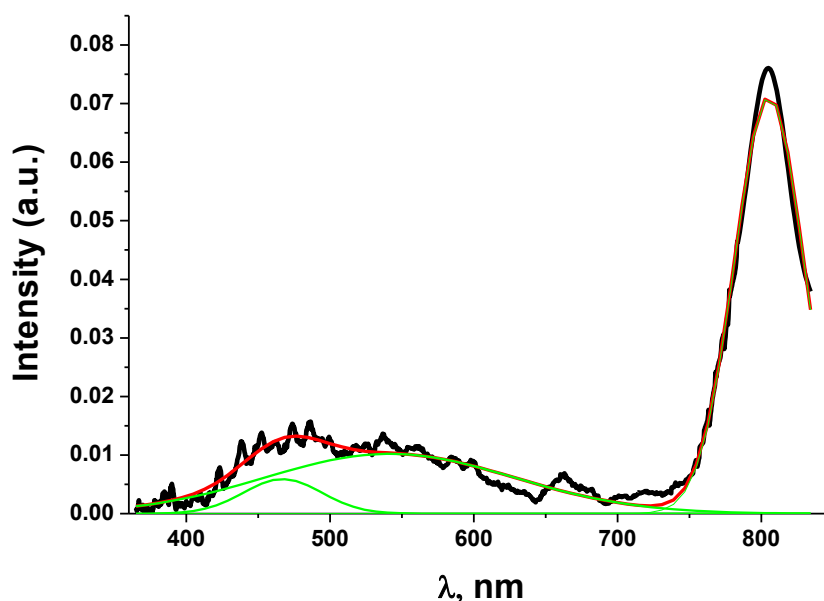
Figure4. Photoluminescence of TiO$_2$nanofibers annealed at 500˚C

The photoluminescence spectrum of TiO$_2$ nanofibers, annealed at 500˚C is shown in Figure 4. The analysis of the spectrum was performed with Gaussian function fitting in Origin 7.5. Three emission bands were found: peak at 461 nm (related to self-trapped excitons)[24], peak at 520 nm (related to oxygen vacancies)[24] and peak at 589 nm. Room temperature emission at 580 nm was observed for TiO$_2$ nanofibers by J. Liu *et* al. [33], however no explanation of the peak was proposed. Knorr *et al.*[34] proposed that in anatase nanostructures two types of luminescence centers (traps) are possible: oxygen vacancies (hole traps) and electron traps (structural defects: Ti^{3+}, Ti^{3+} interstitials, undercoordinated Ti atoms).[25, 35] According to Knorr *et al.*[34], the emission assisted by oxygen vacancies was blue shifted in comparison to the emission, assisted by electron traps. Candy Mercado *et al.[36]* generalized visible photoluminescence (~530 nm) in TiO$_2$ as recombination of free electrons with trapped holes and red emission (600 nm) as recombination of free holes with trapped electrons. Wang *et al.* [15] proposed donor-acceptor mechanism of photoluminescence in TiO$_2$ nanostructures. According to Wang *et al.*[15], singly ionized oxygen vacancies capture photogenerated electrons whereas the surface hydroxyl groups capture generated holes. The formed donor-acceptor couple induces electron-hole recombination with energy lower than free hole-donor recombination. As the samples were treated at high temperatures in air, the hydroxyl groups were removed or transformed to

molecular surface oxygen. Therefore, emission mechanisms proposed by Mercado *et al.*[36] are more possible.

Figure 5. Photoluminescence of TiO_2 nanofibers, annealed at 900˚C

The photoluminescence spectrum of TiO_2 nanofibers, annealed at 900˚C is shown in Figure 5. The analysis of the spectrum with Gaussian function fitting showed 3 peaks: at 467 nm, 541 nm and 805 nm. It was found that PL emission of rutile phase of TiO_2 is located in IR range of the wavelengths.[25, 34, 36] It is associated with Ti^{3+} states and can be shown as recombination of free holes with trapped electrons.[25, 34, 36] According to XRD data, no anatase peaks were observed. Therefore, peak centered at 805 nm is attributed with Ti^{3+} states in TiO_2 rutile nanofibers. However, two weak peaks were observed at 467 and 541 nm. These peaks are well fit with anatase phase of TiO_2. The red shift is associated with annealing induced grain growth. Although XRD did not show the presence of anatase, Raman spectroscopy showed weak peak, corresponding to Eg (144 cm^{-1}). The small portion of anatase in rutile sample can explain the presence of anatase related PL peaks on emission spectrum of TiO_2 nanofibers, annealed at 900˚C.

5. Conclusion

In conclusion, TiO_2 nanofibers with uniform diameters have been fabricated via electrospinning followed by calcination at different temperature in air for 4h. The SEM measurements indicate that the average diameter of nanofibers calcined at 500°C and 700°C is smaller than the as-spun nanofibers. At 900°C, the average diameter increases relative to 500°C and 700°C due to the increasing of the domain size of the crystal structure which is confirmed by XRD analysis. The Raman spectra and the XRD analysis show clearly the anatase phase at 500°C, the anatase-rutile mixed phase at 700°C and the complete anatase-to-rutile transformation at 900°C. Even if the XRD data shows a complete anatase-to-rutile transition in the TiO_2 nanofibers at 900°C, photoluminescence shows a small portion of anatase in rutile sample. This observation proved that photoluminescence could be a very sensitive tool to detect the presence of anatase in rutile phase TiO_2 nanostructures.

References

1. Formo, E., et al., Functionalization of electrospun TiO2 nanofibers with Pt nanoparticles and nanowires for catalytic applications. Nano Letters, 2008. **8**(2): p. 668-672.

2. Li, H., W. Zhang, and W. Pan, Enhanced Photocatalytic Activity of Electrospun TiO2 Nanofibers with Optimal Anatase/Rutile Ratio. Journal of the American Ceramic Society, 2011. **94**(10): p. 3184-3187.

3. Bechelany, M., et al., Chemical surface transformation of SiC-based nanocables. Journal of Optoelectronics and Advanced Materials, 2006. **8**(2): p. 638-642.

4. Bechelany, M., et al., New Silicon Architectures by Gold-Assisted Chemical Etching. Acs Applied Materials & Interfaces, 2011. **3**(10): p. 3866-3873.

5. Bechelany, M., et al., CNT-Encapsulated beta-SiC Nanocrystals: Enhanced Migration by Confinement in Carbon Channels. Crystal Growth & Design, 2011. **11**(5): p. 1891-1895.

6. Elias, J., et al., Urchin-inspired zinc oxide as building blocks for nanostructured solar cells. Nano Energy, 2012. **1**(5): p. 696-705.

7. Ma, D., et al., Preparation and structure investigation of nanoparticle-assembled titanium dioxide microtubes. Applied Physics Letters, 2003. **83**(9): p. 1839-1841.

8. Xiang, B., et al., Field-emission properties of TiO 2 nanowire arrays. Journal of Physics D: Applied Physics, 2005. **38**(8): p. 1152.

9. Ozaki, N., Y. Ohno, and S. Takeda, Silicon nanowhiskers grown on a hydrogen-terminated silicon {111} surface. Applied Physics Letters, 1998. **73**(25): p. 3700-3702.

10. Chen, Y.-j., J.-b. Li, and J.-h. Dai, Si and SiOx nanostructures formed via thermal evaporation. Chemical Physics Letters, 2001. **344**(5–6): p. 450-456.

11. Anton, F., Process and apparatus for preparing artificial threads, 1934, Google Patents.

12. Selloum, D., et al., A highly efficient gold/electrospun PAN fiber material for improved laccase biocathodes for biofuel cell applications. Journal of Materials Chemistry A, 2014. **2**(8): p. 2794-2800.

13. Dassler, A., et al., CHARACTERIZATION OF RUTILE AND ANATASE POWDERS BY THERMAL-ANALYSIS. Journal of Thermal Analysis, 1988. **33**(3): p. 803-809.

14. Sigmund, W., et al., Processing and Structure Relationships in Electrospinning of Ceramic Fiber Systems. Journal of the American Ceramic Society, 2006. **89**(2): p. 395-407.

15. Wang, X., et al., Trap states and carrier dynamics of TiO2 studied by photoluminescence spectroscopy under weak excitation condition. Physical Chemistry Chemical Physics, 2010. **12**(26): p. 7083-7090.

16. Shu, X., et al., H2O2 Sensor Based on the Room-Temperature Phosphorescence of Nano TiO2/SiO2 Composite. Analytical Chemistry, 2007. **79**(10): p. 3695-3702.

17. Wang, P., et al., Water-Assisted Synthesis of Anatase TiO2 Nanocrystals: Mechanism and Sensing Properties to Oxygen at Room Temperature. The Journal of Physical Chemistry C, 2008. **112**(17): p. 6648-6652.

18. Albu, S.P., et al., Self-Organized, Free-Standing TiO2 Nanotube Membrane for Flow-through Photocatalytic Applications. Nano Letters, 2007. **7**(5): p. 1286-1289.

19. Yurdakal, S., et al., Nanostructured Rutile TiO2 for Selective Photocatalytic Oxidation of Aromatic Alcohols to Aldehydes in Water. Journal of the American Chemical Society, 2008. **130**(5): p. 1568-1569.

20. Mor, G.K., et al., Use of Highly-Ordered TiO2 Nanotube Arrays in Dye-Sensitized Solar Cells. Nano Letters, 2005. **6**(2): p. 215-218.

21. Snaith, H.J. and L. Schmidt-Mende, Advances in Liquid-Electrolyte and Solid-State Dye-Sensitized Solar Cells. Advanced Materials, 2007. **19**(20): p. 3187-3200.

22. Li, G., et al., Effect of calcination temperature on the morphology and surface properties of TiO2 nanotube arrays. Applied Surface Science, 2009. **255**(16): p. 7323-7328.

23. Mali, S.S., et al., Nanocoral architecture of TiO2 by hydrothermal process: Synthesis and characterization. Applied Surface Science, 2011. **257**(23): p. 9737-9746.

24. Preclikova, J., et al., Nanocrystalline titanium dioxide films: Influence of ambient conditions on surface- and volume-related photoluminescence. Journal of Applied Physics, 2010. **108**(11).

25. Jeanne, L.M. and J.K. Fritz, Photoluminescence and Carrier Transport in Nanocrystalline TiO2, in Handbook of Luminescent Semiconductor Materials. 2011, CRC Press. p. 365-390.

26. Doh, S.J., et al., Development of photocatalytic TiO2 nanofibers by electrospinning and its application to degradation of dye pollutants. Journal of Hazardous Materials, 2008. **154**(1–3): p. 118-127.

27. Ohsaka, T., TEMPERATURE-DEPENDENCE OF THE RAMAN-SPECTRUM IN ANATASE TIO2. Journal of the Physical Society of Japan, 1980. **48**(5): p. 1661-1668.

28. Zhao, J., et al., Structural properties and photoluminescence of TiO2 nanofibers were fabricated by electrospinning. Journal of Alloys and Compounds, 2008. **461**(1–2): p. 447-450.

29. Stevanovic, A., et al., Photoluminescence of TiO2: Effect of UV Light and Adsorbed Molecules on Surface Band Structure. Journal of the American Chemical Society, 2012. **134**(1): p. 324-332.

30. Viter, R., et al., Novel Immune TiO2 Photoluminescence Biosensors for Leucosis Detection. 26th European Conference on Solid-State Transducers, Eurosensor 2012, 2012. **47**: p. 338-341.

31. Abou Chaaya, A., et al., Tuning Optical Properties of Al2O3/ZnO Nanolaminates Synthesized by Atomic Layer Deposition. Journal of Physical Chemistry C, 2014. **118**(7): p. 3811-3819.

32. Porto, S.P.S., P.A. Fleury, and T.C. Damen, Raman Spectra of Ti. Physical Review, 1967. **154**(2): p. 522-526.

33. Liu, J., et al., Structure and Photoluminescence Study of TiO(2) Nanoneedle Texture along Vertically Aligned Carbon Nanofiber Arrays. Journal of Physical Chemistry C, 2008. **112**(44): p. 17127-17132.

34. Knorr, F.J., C.C. Mercado, and J.L. McHale, Trap-state distributions and carrier transport in pure and mixed-phase TiO2: Influence of contacting solvent and interphasial electron transfer. Journal of Physical Chemistry C, 2008. **112**(33): p. 12786-12794.

35. Mercado, C.C., F.J. Knorr, and J.L. McHale, Observation of Charge Transport in Single Titanium Dioxide Nanotubes by Micro-Photoluminescence Imaging and Spectroscopy. Acs Nano, 2012. **6**(8): p. 7270-7280.

36.   Mercado, C., et al., Photoluminescence of Dense Nanocrystalline Titanium Dioxide Thin Films: Effect of Doping and Thickness and Relation to Gas Sensing. Acs Applied Materials & Interfaces, 2011. **3**(7): p. 2281-2288.